UNIVERSITÀ DEGLI STUDI DI NAPOLI FEDERICO II

Dipartimento di Scienze della Terra, dell'Ambiente e delle Risorse

PhD in Dinamica interna dei sistemi vulcanici e rischi idrogeologico-ambientali

XXVI Ciclo

V_s CRUSTAL MODELS IN CAMPI FLEGREI AND ISCHIA ISLAND

Supervisor
Prof.ssa Concettina Nunziata

PhD Coordinator
Prof. Benedetto De Vivo

PhD student
Roberta Strollo

UNIVERSITÀ DEGLI STUDI DI NAPOLI FEDERICO II

Dipartimento di Scienze della Terra, dell'Ambiente e delle Risorse

PhD in Dinamica interna dei sistemi vulcanici e rischi idrogeologico-ambientali

XXVI Ciclo

V_S crustal models in Campi Flegrei and Ischia island

Supervisor
Prof.ssa Concettina Nunziata

PhD student
Roberta Strollo

PhD Coordinator
Prof. Benedetto De Vivo

To you, my angels,
my guides

Science is but a perversion of itself
unless it has as its ultimate goal the betterment of humanity.
(Nikola Tesla)

Table of Contents

Introduction

The aim of this research project is the definition of 1-D shear wave velocity (V_S) models in the upper crust of Campi Flegrei and Ischia volcanic areas (southern Italy).
This target is achieved by the non-linear inversion of the group velocity dispersion curves of Rayleigh surface waves fundamental mode obtained by the application of the seismic noise cross-correlation method to data recorded at Campi Flegrei and Ischia.

The volcanic field of Campi Flegrei and the island of Ischia belong to the Phlegraean Volcanic District, a volcanic complex located in the southwestern part of the Campanian Plain (southern Italy). This area is included in a large graben formed as a result of the Pliocene-Quaternary extensional domain of NE-SW- and NW-SE-trending normal faults of the Tyrrhenian margin of the Appennine thrust belt (Ippolito et al., 1973; D'Argenio et al., 1973; Finetti and Morelli, 1974; Bartole, 1984; Bartole et al., 1984).
Alkali-potassic magmas, in particular products belonging to the potassic series (trachybasalts, latites, trachytes and phonolites) have been erupted at Campi Flegrei and Ischia (Kastens et al., 1986; 1988).
Campi Flegrei consists in a caldera which origin is inferred to be caused by the two greatest eruptions of the Campanian area, i.e. Campanian Ignimbrite (39 ka B.P.) (De Vivo et al., 2001) and Neapolitan Yellow Tuff eruptions (15 ka B.P.) (Deino et al., 2004), which caused two collapses, so there are two calderas, one nested in the other one (Rosi and Sbrana, 1987; Fisher et al., 1993; Orsi et al., 1996a). Other authors (De Vivo et al., 2001; Rolandi et al., 2003), instead, assert that only the Neapolitan Yellow Tuff eruption occurred in Campi Flegrei causing the calderic collapse. After this event numerous explosive and phreato-magmatic eruptions occurred inside the caldera originating tuff-rings and tuff-cones: the features of these volcanic structures testify an intense volcanic activity interacting with seawater. The last eruption occurred in 1538 A.D. at Monte Nuovo (Di Vito et al., 1987).
Seismicity, bradyseism, fumaroles and hydrothermal activities are also present at Campi Flegrei, demonstrating that the volcanic area is still active, in fact during 1969-1972 and 1982-1984 two intense crises caused an uplift that reached the maximum value of 3.5 m in the town of Pozzuoli.
The geological and structural setting of the Phlegraean area is very complex, being the result of the interaction between volcano-tectonic events and sea level variations. Stratigraphies of ~3 km deep boreholes at Mofete and San Vito (AGIP, 1987) show the

presence of partially hydrothermally altered volcanic and sedimentary rocks at shallow depth, and their thermometamorphic equivalents at greater depth. The deep wells have indicated the presence of a saline water-dominated geothermal field with multiple reservoirs (Carella and Guglielminetti, 1983).

The Phlegraean area is characterized by the presence of a marked Bouguer gravity minimum (Nunziata and Rapolla, 1981; AGIP, 1987) centred in the Gulf of Pozzuoli, which has been related to the collapsed area. High V_P/V_S values have been retrieved in the central part of the Phlegraean area at 1 km depth, which can be interpreted with the presence of fractured rocks, saturated with liquid water (Aster and Meyer, 1988; Vanorio et al., 2005; Battaglia et al., 2008).

The island of Ischia is the westernmost active volcanic complex of the Campanian Plain. The most ancient known volcanic products are dated prior to 150 ka B.P. (Gillot et al., 1982; Vezzoli, 1988). The main eruptive event is the Mt. Epomeo Green Tuff eruption occurred 55 ka B.P., which formed a caldera depression in the central part of the island (Gillot et al., 1982; Vezzoli, 1988). After that products emplaced by following eruptions filled the caldera and, around 33 ka B.P., a 800-1,000 m uplift affected the Mt. Epomeo resurgent block (Gillot et al., 1982; Vezzoli, 1988). Recent volcanism concentrated in the last 10 ka in the eastern part of the island (Vezzoli et al., 2009) along both resurgence-related faults and regional NNW- and NE-striking faults. The most recent eruption is the Arso lava flow occurred in 1302 A.D..

Strong heat flow and hydrothermal manifestations are present at Ischia island (Penta, 1954): the occurrence of two distinct hydrothermal aquifers at ~400 m and ~900 m with temperatures of ~250° C and ~300° C is hypothesized (Chiodini et al., 2004). According to Penta and Conforto (1951), the hydrothermal circulation concentrates in the highly fractured lavas underlying the Green Tuff.

Ischia island is also affected by seismic hazard mainly concentrated in the northern sector. The most important seismic events occurred in 1881 and 1883, causing several damages in the town of Casamicciola.

The definition of V_S models in active volcanic areas allows to point out anomalous thermal conditions, that is low velocity zones, related to partial fusion of rocks, being V_S strongly affected by temperature variations. Moreover the volcanic areas of Campi Flegrei and Ischia are densely inhabited, so they are characterized by high volcanic and seismic risks. In this contest improving the knowledge of the physical parameters of the buried geological structures in these two volcanic areas is fundamental.

In this research project V_S profiles vs. depth have been defined through the analysis of seismic noise data, recorded at Campi Flegrei and Ischia, by the cross-correlation method. This technique has been successfully applied both at global and local scale. It represents a very suitable method for urban areas, where active seismic experiments are prohibitive. Moreover, it allows to obtain seismic data in those areas where earthquake recordings are rarely available, because of their scarcity and the seismic waves attenuation.

The theory of this method has been explained by Lobkis and Weaver (2001) who demonstrated that cross-correlation function computed on the seismic noise recorded by a pair of receivers allows to obtain Green's function of the medium between the two stations. If seismic noise is registered during a time interval long enough to consider the medium scattering a repeatable phenomenon, the registered signals contain coherent information. This means that, in diffuse wavefield condition, all the possible paths that a seismic ray can travel have been sampled; one of these rays has been recorded by the first receiver and, after a time interval, by the second one. So the cross-correlation function can be seen as the signal which one station would receive when the other one is given an impulsive excitation.

Cross-correlation functions computed at Campi Flegrei and Ischia have been analysed by the FTAN (Frequency-Time Analysis) method, which is a multiple filter technique that allows to extract the group velocity dispersion curve of the fundamental mode (Dziewonski et al., 1969; Levshin et al., 1972; 1992; Nunziata, 2005).

1-D V_S models have been obtained by the Hedgehog non-linear inversion (Valyus et al., 1968; Panza, 1981) of the average group velocity dispersion curves of Rayleigh surface waves fundamental mode.

The analysis has been performed along 50 paths crossing Campi Flegrei and 14 paths crossing Ischia. Seismic noise data have been recorded in February-April 2010 by 11 stations belonging to the INGV-OV seismic network located in the Phlegraean area and by 2 stations of the Osservatorio Geofisico - sez. Sismologia (www.ogsism.unina.it) of the Dipartimento di Scienze della Terra, dell'Ambiente e delle Risorse (University of Napoli Federico II), and during two field surveys executed in June 2011 and September-October 2012 at Ischia.

This thesis is subdivided into seven chapters:

- the first is dedicated to the geological and geophysical setting of Campi Flegrei and Ischia;

- the second chapter presents the used methods to compute the cross-correlation functions, to extract the group velocity dispersion curves of Rayleigh surface waves fundamental mode (FTAN method), and to perform the non-linear inversion (Hedgehog method);
- the third and fourth chapters contain the results of the computed NCFs and average group velocity dispersion curves obtained along the analysed paths crossing Campi Flegrei and Ischia, respectively;
- the fifth and sixth chapters present the V_S models obtained from the inversion of the dispersion data at Campi Flegrei and Ischia, respectively;
- the seventh chapter is the conclusive chapter with discussion of the results and comparison with literature data.

Chapter 1

GEOLOGICAL AND GEOPHYSICAL SETTING OF CAMPI FLEGREI AND ISCHIA

The Phlegraean Volcanic District is a volcanic complex located in the southwestern part of the Campanian Plain (southern Italy) and includes the volcanic field of Campi Flegrei, the islands of Procida and Ischia and numerous submarine vents in northwestern Gulf of Napoli (Fig.1.1). It is situated in a Pliocene-Quaternary extensional domain of NE-SW and NW-SE trending normal faults of the Tyrrhenian margin of the Apennine thrust belt (Ippolito et al., 1973; D'Argenio et al., 1973; Finetti and Morelli, 1974; Bartole, 1984; Bartole et al., 1984). A large graben, which includes the Campanian Plain, formed as a result of this tectonic activity (Fig.1.1).

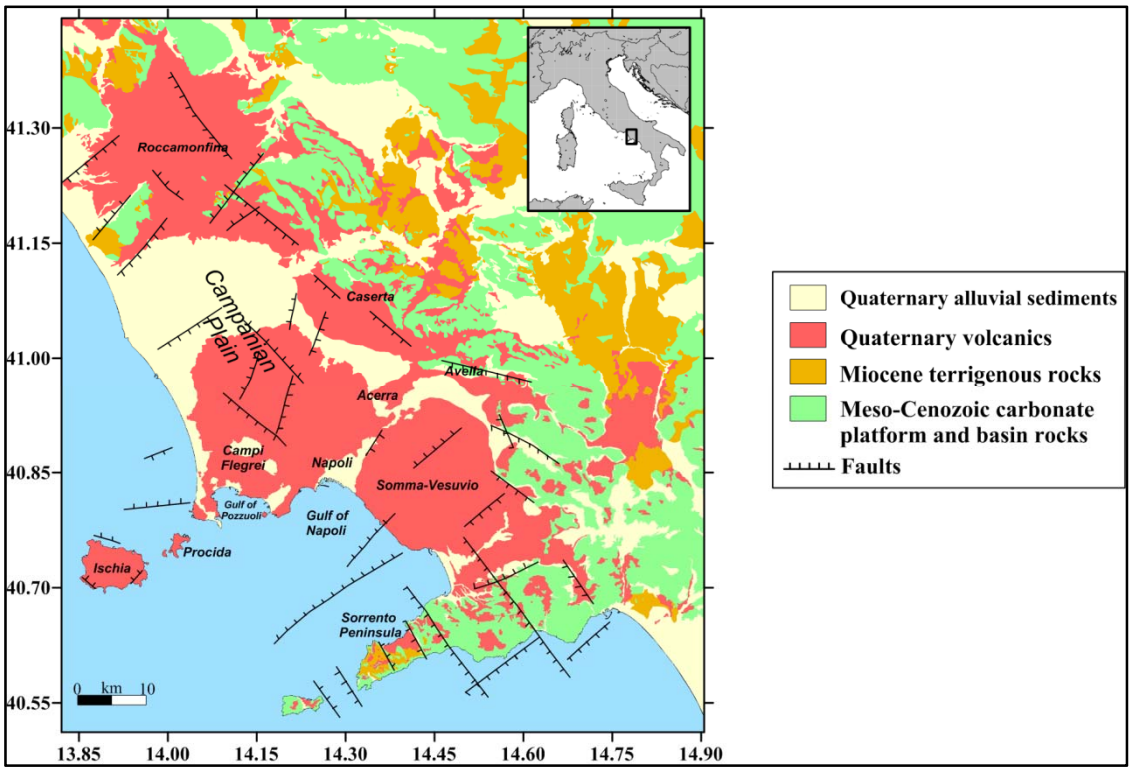

Fig.1.1 *– Simplified geological map of the Campanian Plain (modified after Costanzo and Nunziata, 2014 in press).*

In particular, a NW-SE extensional tectonics was responsible between 700 ka and 400 ka of the formation of deep basins, one of which was the Campi Flegrei (Milia and Torrente, 1999). During the late-Quaternary uplifting areas and E-W left lateral strike slip faults were documented along the margin simultaneously with the activity of normal faults. The faults and folds documented in the Campanian margin area are compatible with block

rotation resulting from a trans-tensional shear zone, characterized by east-trending left lateral and NW-trending extensional movements, active along the eastern Tyrrhenian Sea margin during the Late Quaternary (Milia and Torrente, 2003; Lima et al., 2009).
The graben that includes the Campanian Plain is broken into smaller horst-and-graben structures (Carrara et al., 1973; 1974; Finetti and Morelli, 1974; Agip, 1981). In particular the Phlegraean Volcanic District is related to a NE-SW trending horst-type structure that connects south-eastward, through a graben, to another horst below the Somma-Vesuvio volcano (Orsi et al., 1996a) (Fig.1.1).

The volcanic areas of Campi Flegrei, Ischia, Procida and Vivara islands share the same tectonic setting and a common origin of their alkali-potassic magmas, which characterize the volcanoes of the Campanian region. These magmas are subdivided into an ultra-potassic series (leucitites and leucitic phonolites, in the Somma-Vesuvio volcano) and a potassic series (trachybasalts, latites, trachytes and phonolites, in the Ischia and Procida islands and in Campi Flegrei). The whole region pertains to the eastern Tyrrhenian margin, located on a thinned continental lithosphere, transitional with respect to the oceanic sectors of the Tyrrhenian bathyal plain (Kastens et al., 1986; 1988).
The lithospheric extension, accompanying the opening of the Tyrrhenian basin from Pliocene to recent times, has controlled a strong vertical kinematic and translational tectonics in the upper crust, where the uprising of highly differentiated magmas occurred, mostly along Apenninic (NW-SE) and anti-Apenninic (NE-SW) structural lineaments.
This evidence among others is testified by the drilling of andesitic rocks in the subsurface northward of the Phlegrean area (Ortolani and Aprile, 1978; Aiello et al., 2011).

1.1. Campi Flegrei volcanic field

1.1.1 Geological setting of Campi Flegrei

In the Campanian margin the stratigraphic architecture, depositional environments and rate of subsidence and sediment supply are controlled by normal fault activity (Milia and Torrente, 1999). In particular in the Phlegraean area morphological setting and stratigraphic sequences are very complex, being the results from alternating, sometimes coeval, constructive and destructive volcanic and/or volcano-tectonic events. Variation in time and space of the relationship between sea and earth-surface level has also greatly contributed to the present geomorphic setting (Orsi et al., 1996a).

The Phlegraean volcanic area includes a subaerial and a submerged part: the former corresponds to the horse-shaped area centred on the Gulf of Pozzuoli (Fig.1.2).

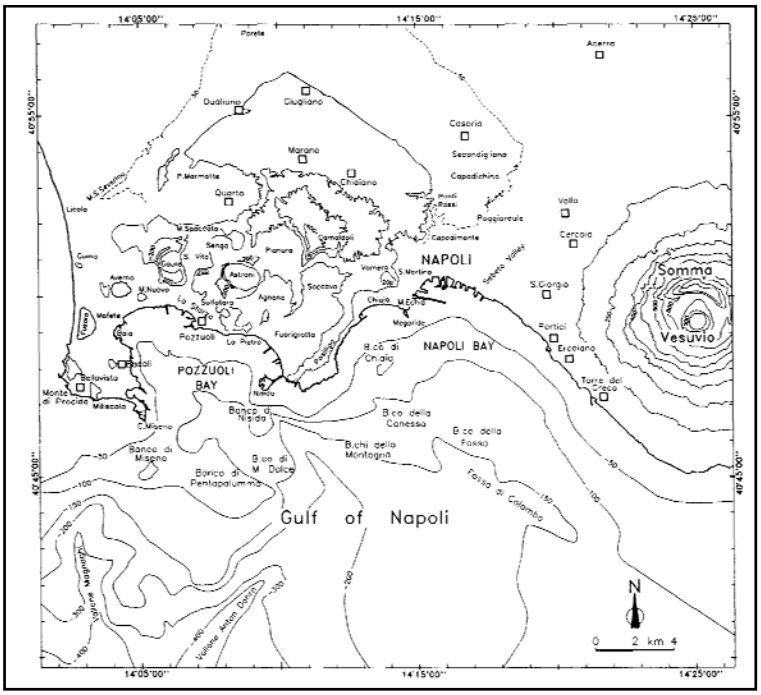

Fig.1.2 *– Morphological map of Campi Flegrei and Gulf of Napoli (from Orsi et al., 1996a).*

The central part of Campi Flegrei is characterized by the presence of rugged terrain of many tuff-rings and tuff-cones, bounded to the west, north and east by lowlands. In the south La Starza marine terrace (Cinque et al., 1984) occurs few hundreds of meters from the Gulf of Pozzuoli. To the west the peripheral lowland merges with a flat littoral plain broken by the morphological heights of Monte di Procida and Cuma. The Quarto, Pianura and Soccavo plains are bordered to the north by steep cliffs. To the east the Fuorigrotta plain is interrupted by the NE-SW elongated Posillipo hill, bordered by steep scarps to the west and gently dipping coast to the east. This hill extends north-eastward into a chain of morphological heights which includes the Camaldoli, Vomero, San Martino, Capodimonte and Capodichino hills. The Campi Flegrei highland merges toward the north and east with the Campanian Plain through the San Martino hill. The Megaride islet and the Monte Echia, San Martino, Capodimonte and Poggioreale hills describe a southward concave arc which borders to the west and north a large plain. This plain includes the Sebeto valley, extends eastward up to the Somma-Vesuvio volcano and merges southward with the Gulf of Napoli (Orsi et al., 1996a) (Fig.1.2).

The Campi Flegrei - Gulf of Napoli area corresponds to a half-graben basin, bounded by NE-trending normal faults (Milia et al., 2003) (Fig.1.3).

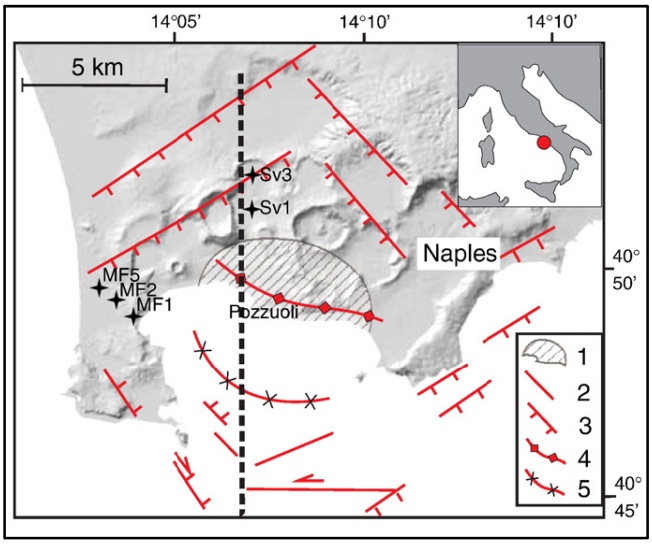

Fig.1.3 *- Structural map of Campi Flegrei and Gulf of Pozzuoli (from Milia and Torrente, 2000; Milia et al., 2003). 1. Area affected by an uplift of 100-50% during the 1982-1984 bradyseism; 2. Fractures and lateral faults; 3. Normal faults; 4. Pozzuoli anticline; 5. Gulf of Pozzuoli syncline. Black stars indicate the location of deep geothermal wells in Mofete area (MF1, MF2, MF5) and in San Vito area (SV1, SV3). The dashed line is the location of the geologic cross section shown in Fig.1.4 (modified after Lima et al., 2009).*

The structural setting of the studied area is characterized by high angle faults that affect the boundary of the Campi Flegrei area onshore and offshore. In the Gulf of Pozzuoli active folding is occurring (Milia et al., 2000; Milia and Torrente, 2000). The main fold is an anticline culminating near the city of Pozzuoli and a syncline located in the Gulf of Pozzuoli (Figs.1.3-1.4-inset A). Structural and stratigraphic analyses yield quantitative data on the timing of fold inception, kinematics, and the amount and rates of uplift. The rate of fold uplift ranges from 1 to 20 mm/yr. The structures show limb rotation kinematics and decreasing uplift rates. The uplift rates and geometry of the Gulf of Pozzuoli folds suggest that they are of tectonic origin, a product of detachment folding (Lima et al., 2009).

The correlation between the seismic units recognized in the Gulf of Napoli with outcrops and well logs, and with dated successions and dated fault activity, enables reconstruction of the stratigraphic succession along the Campanian margin (Milia and Torrente, 1999; Milia et al., 2003). The basement corresponds to the Mesozoic-Cenozoic carbonate succession forming the Apennine thrust belt. Terrigenous conglomerates overlie carbonates. A marine succession of siltstones and calcarenites of Lower Pleistocene age lies above the conglomerates. Following the Campi Flegrei - Gulf of Napoli half-graben formation, a tectonically enhanced unconformity formed on the shelf area and relatively thick debris flows were deposited in the basins. A Middle Pleistocene stratigraphic succession characterized by a transgressive-regressive cycle rests above the debris flow unit. The transgressive succession (Unit B), deposited between 0.7 and 0.4 Ma,

corresponds to claystone-siltstone composed of fine-grained pelagic and hemipelagic sediments, characteristic of deepwater environments associated with transgressions and high stands of sea level. The regressive succession (Unit C) is mainly composed of coarser grained clastic sediments interlayered within the hemipelagic succession. In the upper part of the Unit C, numerous ignimbrites and volcanic units are deposited (Milia and Torrente, 2007). Offshore Campi Flegrei, numerous monogenetic volcanoes and volcanoclastic deposits fill the marine basin (Milia et al., 2006; Lima et al., 2009) (Fig.1.4).

An extensive exploration and drilling programs was resumed in 1978 as a joint venture of AGIP and ENEL and the Italian Geodynamic Project (Rosi and Sbrana, 1987). Several wells have been drilled to depth of 3 km (Carella and Guglielminetti, 1983) concentrated in two inner areas of Campi Flegrei: Mofete, in the western sector and San Vito, in the central sector (Figs.1.2-1.3). At shallow depth, partially hydrothermally altered volcanic, volcanoclastic and sedimentary rocks are encountered; at greater depth, their thermometamorphic equivalents are encountered. The deep wells have indicated the presence of a saline water-dominated geothermal field with multiple reservoirs (Carella and Guglielminetti, 1983).

The remnants of the Mofete cone are located in the northwestern end of the Gulf of Pozzuoli, where numerous occurrences of hydrothermal manifestations are present between Lucrino Lake, Baia and Fusaro Lake (Fig.1.2). The stratigraphic sequence penetrated by Mofete 1 (MF1), Mofete 2 (MF2) and Mofete 5 (MF5) wells (Fig.1.3) is quite uniform. In the first 250 m recent pyroclastics with yellow tuffs at the base are found. From 250 m to 800 m, the sequence consists of chaotic marine tuffites with trachytic-type lava at the bottom. From 800 m to 1,300 m there is a homogeneous trachytic lava complex probably corresponding to a lava dome. From 1,300 m to 2,000 m pyroclastic products alternating with lavas and subordinate siltites of marine environment are found. Below 2,000 m, the lithology is quite heterogeneous with sedimentary rocks alternating with trachylatitic lava layers. The primary rock types were difficult to recognize at this depth because of the pervasive thermometamorphic recrystallization (De Vivo et al., 1989) (Fig.1.5).

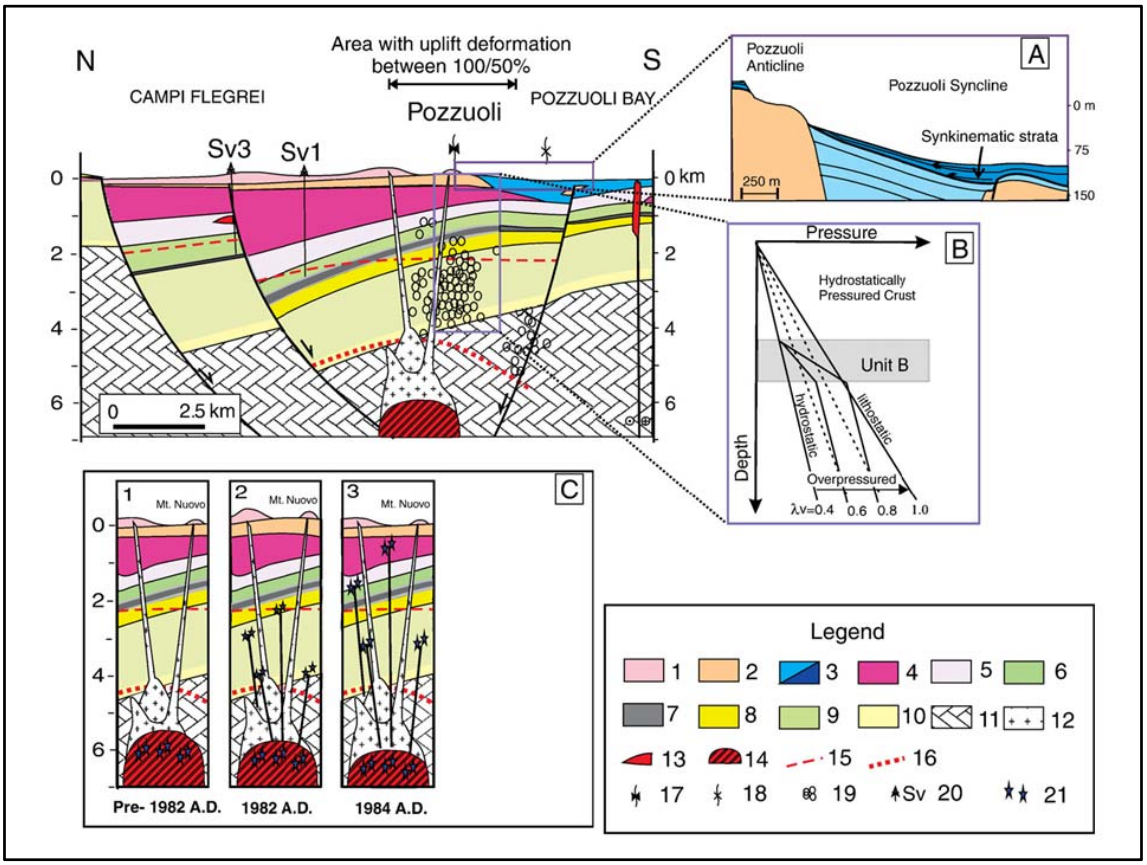

Fig.1.4 *- Geologic section across Campi Flegrei – Gulf of Pozzuoli (as dashed line in Fig.1.3). 1. Holocene volcanics; 2. Neapolitan Yellow Tuff; 3. Main sediments post 39 ka; 4. Campania Ignimbrite and pre-CI tuffs; 5. Middle Pleistocene sandstones, siltstones and volcanics; 6. Middle Pleistocene marine sediments (sandstones and siltstones - Unit C in text); 7. Fine grained Middle Pleistocene marine sediments (claystones and siltstones - Unit B in text); 8. Middle Pleistocene deep water debris flows; 9. Lower Pleistocene marine sediments; 10. Continental deposits and conglomerates; 11. Meso-Cenozoic substrate; 12. Crystallized magma; 13. Volcanic bodies; 14. Magma body; 15. Thermometamorphic boundary; 16. Impermeable zone surrounding the crystallizing magma body. 17. Pozzuoli Anticline; 18.Gulf of Pozzuoli Syncline; 19. 1983–84 earthquake hypocenters; 20. Deep geothermal wells; 21. Magmatic fluids.*
Inset A: North-South cross section showing Pozzuoli Anticline-Syncline and the synkinematic strata.
Inset B: Pressure-depth relationships across the relatively impermeable layer (Unit B) shown in terms of the pore-fluid factor, λ_v, with hydrostatic gradients preserved in the relatively high permeability rock above and below the claystones and siltstones of Unit B. Maximum overpressure is governed by the local compressional stress regime, the prevailing level of differential stress, and the absence of inherited brittle structures.
Inset C: Schematic interpretation of subsurface magmatic-hydrothermal activity at Campi Flegrei (1) Following the 1538 eruption, the magma body became a closed system, and magmatic volatiles accumulated below impermeable crystallized carapace. (2) In 1982, the carapace confining the magmatic system fractured, allowing magmatic fluids to enter the overlying rocks beneath the low-permeability cap rock (Unit B), causing vertical ground deformation. (3) Ground deformation that began in 1982 ended and deflation began when fractures penetrated the low-permeability cap rock, allowing the deep fluids to migrate into the shallow hydrostatic aquifers and flow toward the surface (modified after Lima et al., 2009).

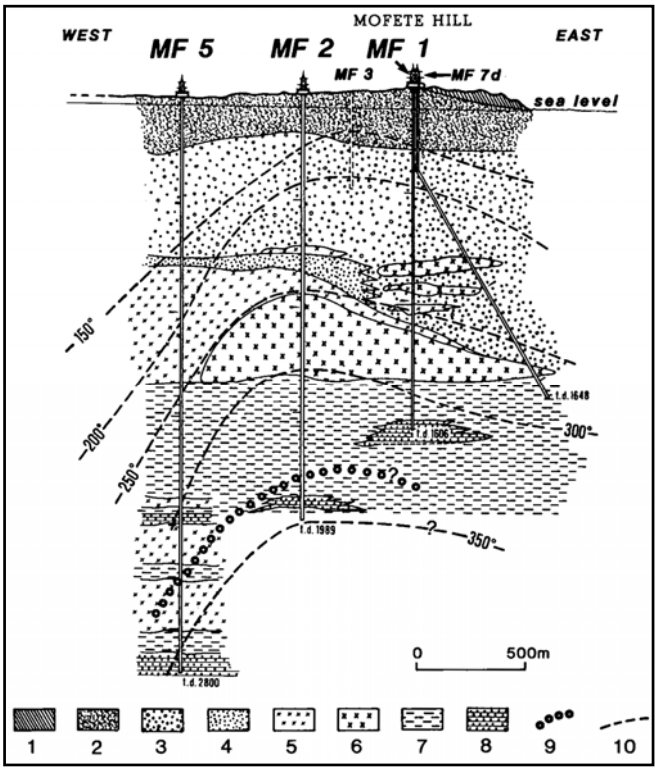

Fig.1.5 *– Cross-section including wells MF5, MF2 and MF1 in the Mofete geothermal field. Well MF3 is projected onto the cross-section and the oblique well MF7d is also shown. MF5, MF2 and MF1 are vertical. Total depth (t.d.) is indicated at the bottom of each well (meters). 1= pyroclastics from Baia (~8.4 ka B.P.); 2= yellow tuff; 3= chaotic tuff; 4= subaerial tuffs; 5= trachytic lavas; 6= latitic lavas (lava domes); 7= interbedded tuffites, tuffs and lavas (submarine environment); 8= interbedded shales, siltstones and sandstones (marine); 9= top of thermometamorphism; 10= isotherms (°C) from measured down-hole well temperature. No vertical exaggeration (from De Vivo et al., 1989).*

The San Vito plain, located in the central portion of Campi Flegrei, formed as a result of volcano-tectonic collapse that occurred after the building of the Gauro tuff-cone (10-11 ka B.P.) (Fig.1.2). The geology of the plain is characterized by a deep pyroclastic cover formed in the recent subaerial post-caldera period. The pyroclastics filled up the collapse structure (Bruni et al., 1985). The stratigraphy of the uppermost 1,000 m of the San Vito 1 (SV1) and San Vito 3 (SV3) wells (Fig.1.3) consists of a rather chaotic sequence of pyroclastic products of pumice and cinder tuffs, tuffaceous breccias and chaotic tuffites belonging to the post-caldera period. From 1,000 m to 1,350 m of depth homogeneous trachytic rocks occur. Below this lava body, down to 1,900 m there are again chaotic tuffites alternating with trachytic volcanics and a complex sequence containing siltites and subordinate volcanics. Below 1,900 m the effects of thermometamorphism are observed; the thermometamorphism obliterates completely the primary structure of the rocks in the deepest portions of San Vito 1 well (De Vivo et al., 1989) (Fig.1.6).

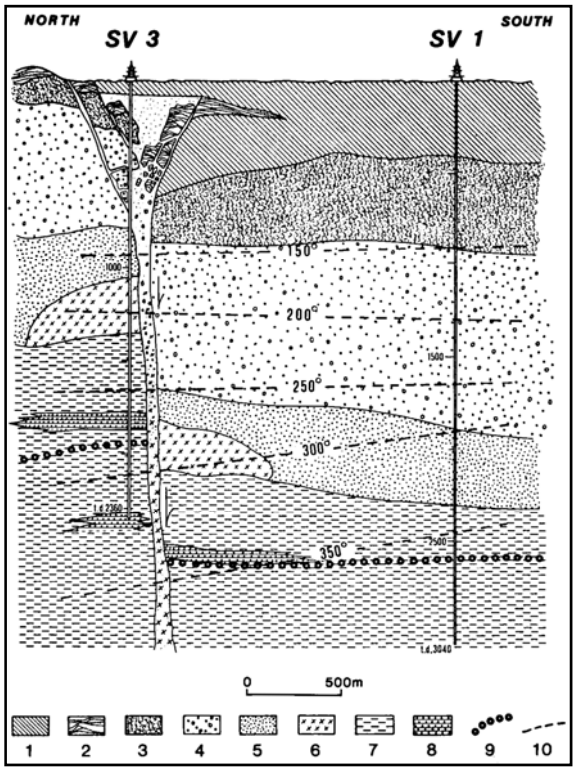

Fig.1.6 *- Cross-section including wells SV3 and SV1 in the San Vito geothermal field. Well SV3 (total depth=2,360 m) and well SV1 (total depth=3,040 m) are vertical. 1= inchoerent pyroclastic rocks; 2= latitc scoriae and pumices; 3= yellow tuffs (post-caldera submarine activity); 4= chaotic tuffites; 5= chaotic tuffs (subaerial environment); 6= trachytic lavas - lava domes (pre-caldera period); 7= interbedded tuffites, tuffs and lavas (submarine environment); 8= interbedded siltstones and sandstones (marine); 9= top of the thermometamorphism; 10= isotherms (°C) from measured well temperature. No vertical exaggeration (from De Vivo et al., 1989).*

1.1.2 Volcanic history of Campi Flegrei

The Campi Flegrei volcanic complex represents a typical caldera system in both size and development (Smith and Bailey, 1968).

The volcanic rocks of Campi Flegrei belong to the potassic series of the Roman Province and range in composition from rare trachybasalts to latites, trachytes, alkali trachytes and peralkaline phonolitic trachytes. Most of the Campi Flegrei rocks are undersaturated in silica and the degree of silica undersaturation is very low from trachybasalts to trachytes, but increases in alkali trachytes and especially in peralkaline phonolitic trachytes. Armienti et al. (1983) interpreted the magma evolution in the area as low-pressure (1-5 kbar) fractional crystallization from a trachybasalt parent where only the more evolved products have reached the surface (De Vivo et al., 1989). No volcanic rocks possibly representative of primary mafic magmas occur; however, it is likely that the mantle-derived parental magmas feeding the volcanism of Campi Flegrei should be similar

in composition to the high-K basaltic lava xenoliths found at Procida (Solchiaro eruption; D'Antonio et al. 1999a).

The beginning of the volcanic activity of Campi Flegrei is not defined as yet. The volcanic history of the complex has been reconstructed using the products of the two greatest volcanic events occurred in the Campanian area as marker: the Campanian Ignimbrite (CI) eruption (39 ka B.P.) (De Vivo et al., 2001) and the Neapolitan Yellow Tuff (NYT) eruption (12 ka B.P. according to ^{14}C dating by Alessio et al. (1973), recently dated at 15 ka B.P. by Deino et al. (2004) using $^{40}Ar/^{39}Ar$ method). So the volcanic history of Campi Flegrei has been subdivided in four different periods: volcanism older than CI, the CI eruption, volcanism between CI and NYT eruptions, the NYT eruption, volcanism younger than NYT (Orsi et al., 1996a).

The most ancient products found in the Phlegraean area are lava domes of Punta Marmolite and Cuma, emplaced 47 ka and 37 ka B.P. respectively (Cassignol and Gillot, 1982) and the Tufi di Torre Franco older than 42 ka (Alessio et al., 1973) (Fig.1.7). Only a few of the eruptive vents of the recognized deposits are visible at the present time (Fig.1.8A). Exposed and cored pyroclastic sequences generally have sedimentological characteristics of proximal deposits. In particular at Trefola (Fig.1.7) impact sags indicate that the vents were located toward east and northeast. This is an evidence that before the CI eruption volcanism was active also outside of Campi Flegrei depression (Orsi et al., 1996a). Some evidences of a widespread volcanic activity going beyond the Phlegraean area are the products of three periods of trachytic ignimbrite volcanism (289-246 ka, 157 ka and 106 ka) identified in the Apennine area in the last 300 ka. The whole Campanian area has been recognized as a region volcanologically active in the last 600 ka, since it has been identified as the Campanian Volcanic Zone (CVZ) (Rolandi et al., 2003). These deposits probably represent distal ash flow units of ignimbrite eruptions which occurred throughout the CVZ. Deep exploration holes allowed to document that the ignimbrite activity alternated with periods of marine sedimentation within the CVZ. Ignimbrite formation probably documents important phases of the CVZ structural evolution, as ignimbrite eruptions producing trachytic magmas preceded the additional graben collapse of the Apennine sedimentary basement (Rolandi et al., 2003).

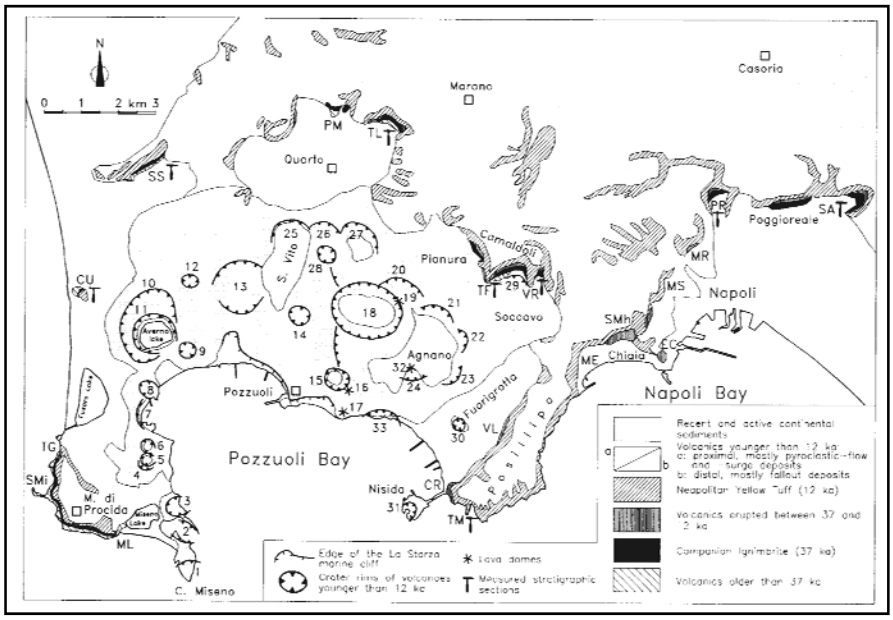

Fig.1.7 *– Distribution of the volcanic products in the Phlegraean area settled during the four periods of volcanic activity.*
ML=Miliscola; SMi=isolotto San Martino; TG=Torregaveta; CU=Cuma; SS=San Severino;PM=Punta Marmolite; TL=Trefola; TF=Torre di Franco; VR=Verdolino; PR=Ponti Rossi; SA=Sant'Arpino; MR=Moiariello; MS=Montesanto; ME=Mergellino; SMh=collina San Martino; EC=Monte Echia; TM=Trentaremi; CR=Coroglio; VL=Villanova.
Location of vents is indicated by numbers on the map: 1=Capo Misero; 2=Punta Pennata; 3=Bacoli; 4=Bellavista; 5=Fondi di Baia I; 6=Fondi di Baia II; 7=Baia; 8=Mofete; 9=Monte Nuovo; 10=Archiaverno; 11=Averno; 12=Fondo Riccio; 13=Gauro; 14=Cigliano;15=Solfatara; 16=Accademia; 17=Monte Olibano; 18=Astroni; 19=Caprara; 20=Sartania; 21=Pigna San Nicola; 22=Monte Sant'Angelo; 23= Grotta del Cane; 24=Agnano-Monte Spina; 25=Montagna Spaccata; 26=Pisani; 27=San Martino; 28=Senga; 29=Minopoli; 30=Santa Teresa; 31=Nisida; 32=Cupola di Monte Spina; 33=La Pietra (from Orsi et al., 1996a).

The Campanian Ignimbrite eruption, dated 39 ka B.P. using $^{40}Ar/^{39}Ar$ method (De Vivo et al., 2001), produced the largest pyroclastic deposit of the Campanian region (Barberi et al., 1978) covering an area of about 30,000 km^2 with about 150 km^3 of erupted magma ranging in composition from trachyte to phonolitic-trachyte (Civetta et al., 1997). The CI eruption has been the subject of intensive investigations for over two centuries, yet its source and eruptive history remain unclear. Some researchers assumed that the CI source is the Campi Flegrei caldera (Fig.1.8B) (Rosi and Sbrana, 1987; Fisher et al., 1993), some others hypothesized that the CI source was localized along fissures, parallel to the main trends of post-orogenic South Apennine extensional tectonics (Di Girolamo, 1968; 1970; De Vivo et al., 2001). Scandone et al. (1991) located the CI source in the so called Acerra depression, a graben located 15 km NE of Napoli (Fig.1.1).

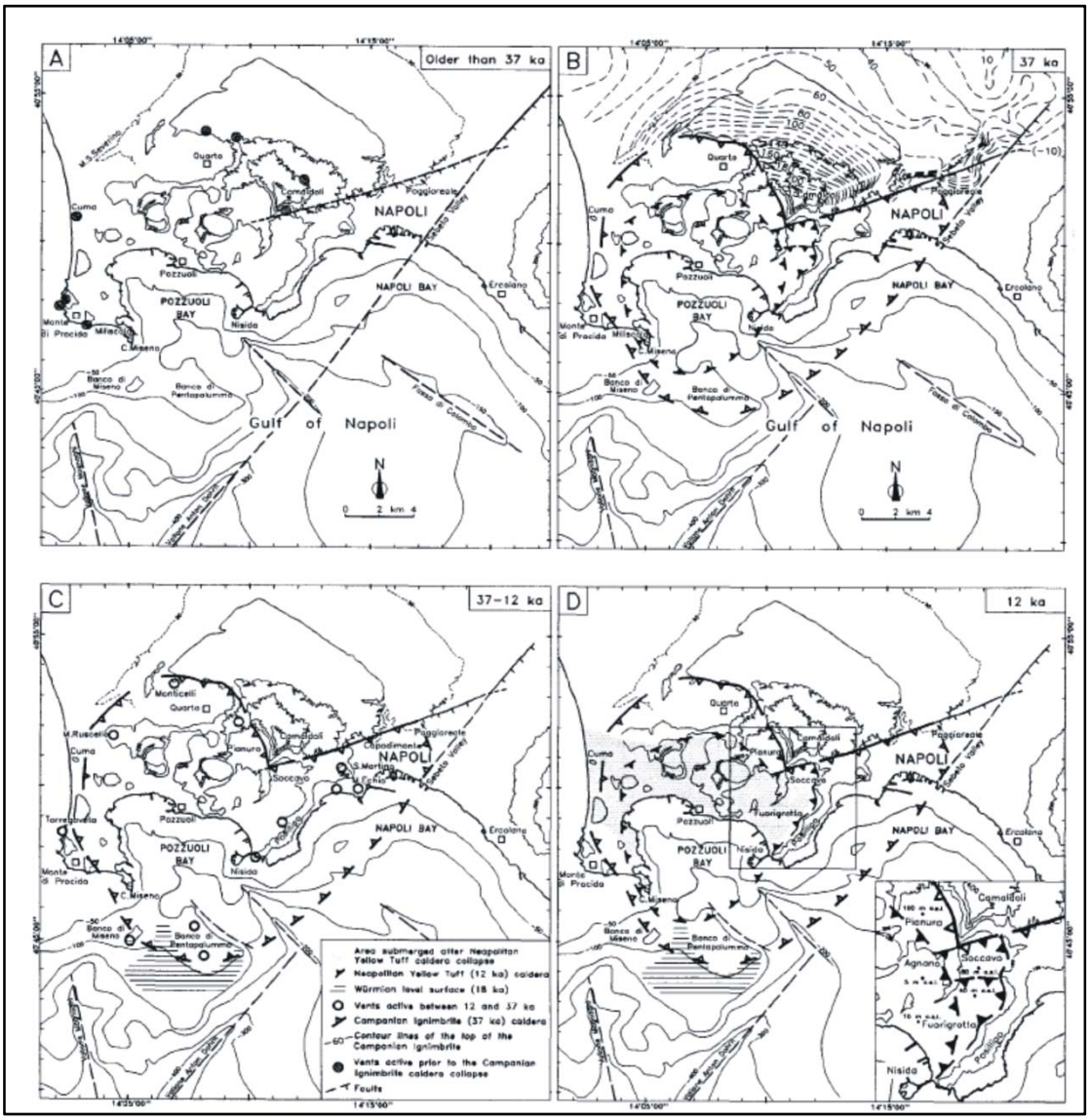

Fig.1.8 *– Structural sketch maps of the Phlegraean area showing time-space evolution of volcanism and deformation between 37 and 12 ka B.P. (modified after Orsi et al., 1996a).*

According to some authors (e.g. Rosi and Sbrana, 1987; Fisher et al., 1993; Orsi et al., 1996a) the Campi Flegrei volcanic complex underwent two different collapses both during the CI and NYT eruptions. They hypothesize two calderas, one nested in the other one (Fig.1.9). Orsi et al. (1996a) examined many shallow drill cores and the correlation with exposed allowed them to reconstruct the top of the CI (Fig.1.10): CI proximal deposits are exposed along the scarps bordering to the west and north the Campi Flegrei depression and extend eastward along the Camaldoli-Poggioreale alignment. The distribution of the top of the CI shows that inside the Campi Flegrei depression and south of the Camaldoli-Poggioreale alignment the tuff occurs at depth not shallower than few hundreds of meters.

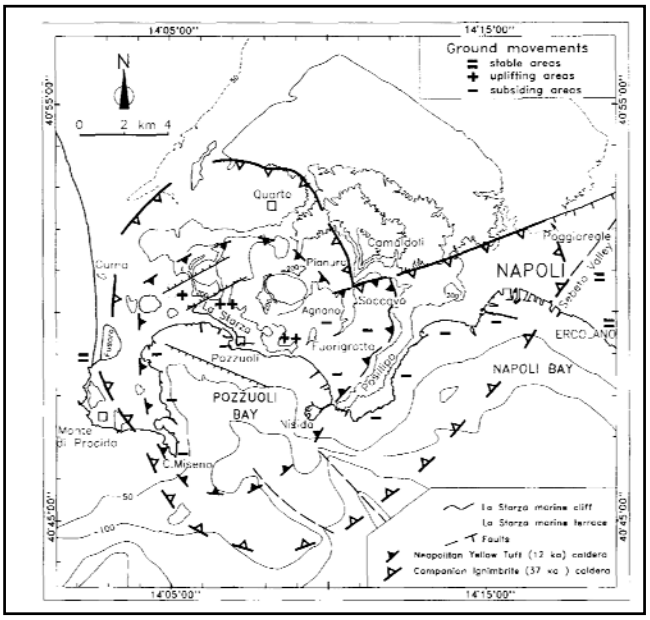

Fig.1.9 *– Structural sketch map of the two nested calderas in Campi Flegrei (from Orsi et al., 1996a).*

Civetta et al. (1997) and Rosi et al. (1996) hypothesized that the vent migrated and a caldera began to collapse during the course of the CI eruption by means of new faults and the reactivation of parts of earlier regional faults. The topographic rim is visible inland, in particular in the western (Monte di Procida and Cuma) and in the northern (Monte San Severino and Camaldoli-Poggioreale alignment) parts of Campi Flegrei, while its submerged part (in the southern part) is inferred on the basis of structural, morphological and geophysical features (Fig.1.9). Inland it is marked by high-angle surfaces unconformably overlain by thick sequences of rocks younger than CI (Orsi et al., 1996a).

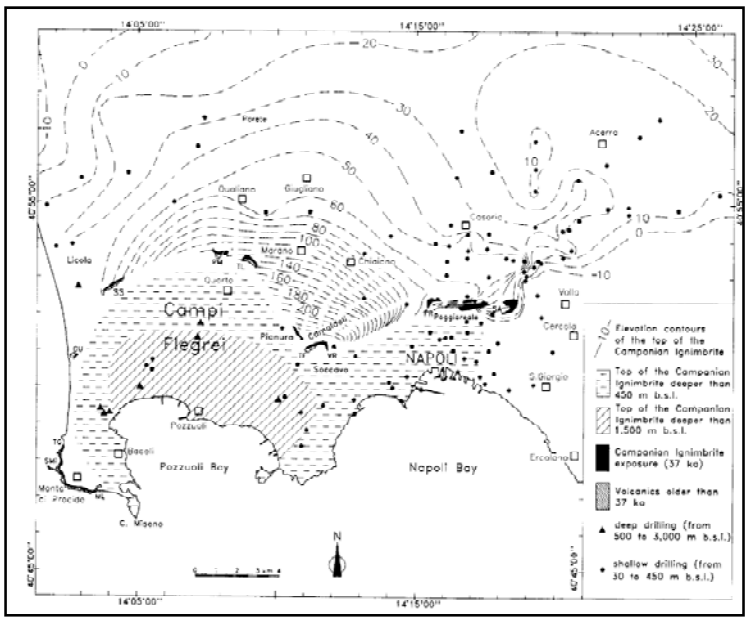

Fig.1.10 *– Map of isobaths of the Campanian Ignimbrite in meters a.s.l. (from Orsi et al., 1996a).*

In contrast with these studies, the existence of such a large caldera is not supported by gravity, seismic and magnetic data (Fusi et al., 1991; Berrino et al., 1998; Milia, 1999; Florio et al., 1999).

Moreover, the analysis of stratigraphic data let to recognize ignimbrite eruptions in the CVZ at least in the last 300 ka (Rolandi et al., 2003). These findings suggested to hypothesize that the Campanian Ignimbrite was fed by tectonically controlled fissure eruptions across the CVZ (Rolandi et al., 2003).

These fissures appear to have been located along the grabens and their location has been determined by preexisting NE-SW, NW-SE and E-W trending tectonic faults associated with the evolution of the Apennine chain. Within such an extensional tectonic regime, the eruption of hundreds of cubic kilometres of magma is likely to have induced additional collapse. This interpretation is supported by the absence of local ring faults, which must be expected for caldera collapse. Moreover geochemical and volcanological evidences suggest that volcanic products were initially erupted and deposited in the CVZ and northeastern Apennine area over a wide area (Fig.1.11). Additional rifting was induced by eruptions in the Acerra-Gulf of Napoli graben and a shift in position of the fault-controlled eruption vents then occurred along the depression (Rolandi et al., 2003) (Fig.1.12).

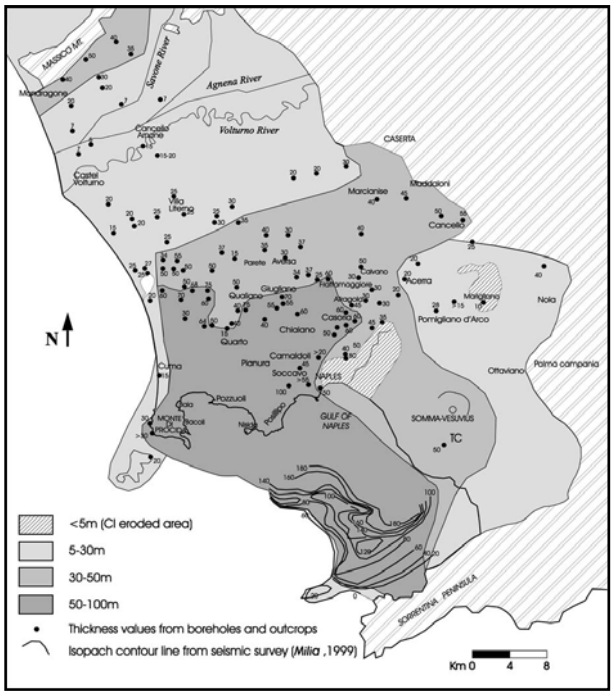

Fig.1.11 *- Location map of CVZ showing the distribution of thickness values of the CI units. Dots indicate localities where boreholes and exposed stratigraphic columns were measured. In the Gulf of Napoli CI thickness values are inferred from the isopach map of Milia (1999) (from Rolandi et al., 2003).*

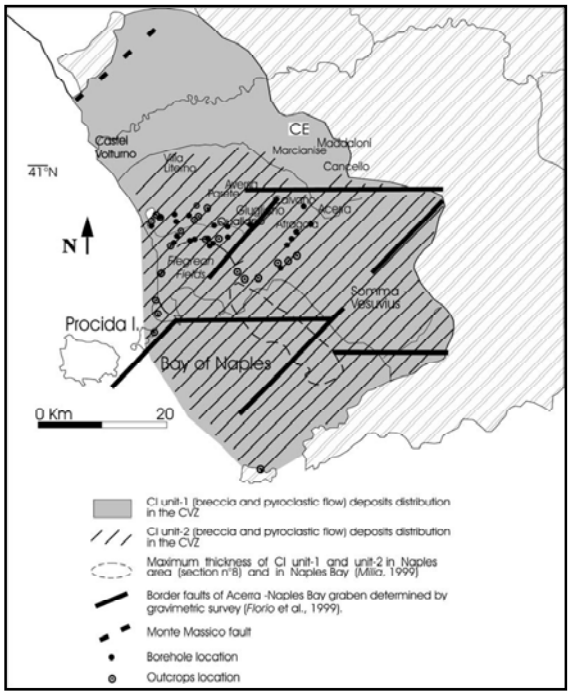

Fig.1.12 *- Relationship of faulting and some vent positions of CI units in the Acerra – Gulf of Napoli graben (from Rolandi et al., 2003).*

Little is known about the volcanic activity in Campi Flegrei between CI and NYT eruptions (Fig.1.8C). Mostly submarine activity is indicated by stratigraphic and deep borehole data (Figs.1.5-1.6). Rocks erupted during this time span can be inferred at the southern edge of the Gulf of Pozzuoli from seismic data (Pescatore et al., 1984; Fusi et al., 1991; Fevola et al., 1993). Volcanic products of this period are exposed only along the scarps that represent the topographic rim of the inferred CI caldera (Orsi et al., 1996a), in scattered outcrops across the central part of the city of Napoli and along the northwestern and southwestern scarps of the Posillipo hill (Fig.1.7). They have been penetrated by many boreholes inland (Fig.1.10). Outside the inferred CI caldera they occur always above sea level, while inside the caldera and south of the eastern prolongation of Camaldoli-Poggioreale alignment they are below sea level (Orsi et al., 1996a).

The Neapolitan Yellow Tuff eruption, dated at 12 ka B.P. according to ^{14}C dating by Alessio et al. (1973) and recently dated at 15 ka B.P. by Deino et al. (2004) using $^{40}Ar/^{39}Ar$ method, is the second largest volcanic event of the Campanian region, covering an area of about 1,000 km^2 with a volume of erupted magma, ranging in composition from alkali-trachyte to latite, of about 40 km^3. The eruption was phreatoplinian to phreatomagmatic with a very complex history (Orsi et al., 1991a; 1992; 1995; Wohletz et al., 1995). Its eruptive dynamics changed during the course of the eruption according to the variations of the efficiency water/magma interaction and to caldera collapse. Although the vent of this

eruption was unquestionably in Campi Flegrei (Fig.1.8D), different hypotheses about the location of the source have been proposed. According to Rittmann et al. (1950) and Rosi et al. (1983) the NYT is the results of eruptions from several different centres; whereas Di Vito et al. (1985) suggest that the main source area was located on the eastern sector of Campi Flegrei.

Using stratigraphical, sedimentological and compositional characteristics of the NYT sequence, Orsi and Scarpati (1989), Orsi et al. (1991a; 1992), Scarpati et al. (1993), Orsi et al. (1995) and Wohletz et al. (1995) concluded that a caldera began to collapse during the eruption. Although these strong geological and volcanological evidences, the rim of the caldera is poorly exposed as only its northeastern sector has a morphological expression inland (Figs.1.2-1.9). Orsi et al. (1996a) based the location of the structural rim of the NYT caldera mostly on gravimetric and magnetic data (Barberi et al., 1991), distribution of vents younger than 12 ka, distribution of dated level surfaces in the submerged portion of Campi Flegrei (Pescatore et al., 1984; Fusi et al., 1991; Fevola et al., 1993) and interpretation of shallow and deep boreholes (AGIP, 1987). The western scarps of the Camaldoli, San Martino and Posillipo hills have been interpreted as the morphological evolution of the marginal caldera faults. The northern border of the Soccavo plain results from partial reactivation of the regional fault system. The displacement between the Soccavo (80 m a.s.l.) and Fuorigrotta (20 m a.s.l.) plains, separated by a ENE-WSW trending scarp, is related to differential vertical movements inside the collapsed area (Figs.1.8D-1.9). A circular alignment of gravimetric positive anomalies (Barberi et al., 1991) is interpreted by Orsi et al. (1996a) as coincident with the faults bordering the most depressed part of the NYT caldera along which most of the later magma migrated toward the surface.

The NYT eruption was followed by sea ingression in the southern part of the present Campi Flegrei. Shallow water marine sediments, intercalated with younger pyroclastic deposits were found in the boreholes and also reported from deep boreholes in the Campi Flegrei (Rosi and Sbrana, 1987) (Figs1.4-1.5-1.6). These sediments overlie a few hundred meters of zeolitized yellow tuff (D'Erasmo, 1931; Rosi and Sbrana, 1987) mostly NYT.

After NYT eruption about 30 volcanic events occurred in Campi Flegrei, concentrated in two different periods: from 10.5 to 8.0 ka B.P. and from 4.5 to 3.7 ka B.P. (Rosi and Sbrana, 1987).

During the first period of activity almost all the eruptive vents were located along the margin of the most depressed area. Only the Minopoli eruption (Fig.1.7) took place along

the NE-SW trending regional fault system partially reactivated during the caldera collapse. The volcanoes formed in this period were dominantly tuff-rings and tuff-cones, suggesting that the eruptions were mostly triggered by efficient water/magma interactions. The compositions of the erupted magmas range from trachyte to alkali-trachyte; only the Minopoli eruption emitted trachybasaltic magma (Armienti et al., 1983; Civetta et al., 1991a). The largest tuff-cone of this period is the Gauro volcano (Fig.1.7), formed about 10 ka B.P.. One of the largest eruption of the past 12 ka generated the Pomici Principali (Scherillo and Franco, 1960) and is occurred 10.7 ka B.P.. This deposit is composed of pumice-fallout beds and is interpreted as the product of a plinian eruption that occurred in the Agnano area (Lirer et al., 1987) (Fig.1.7).

After 2,000 years of quiescence volcanism resumed. The vents of this second period were mostly located in the northern and eastern sector of the NYT caldera, still partially submerged, and subordinately along the Averno-Capo Miseno alignment (Fig.1.7). The composition of the erupted magmas ranges from trachyte to alkali-trachyte. Most of the eruptions were explosive with phreatomagmatic phases. Only few effusive eruptions took place and generated the Monte Olibano-Accademia lava domes, located south of the Solfatara volcano (Rosi et al., 1983; Di Girolamo et al., 1984) (Fig.1.7). The largest eruptions generated the Astroni tuff-ring (Di Filippo et al., 1991) (age constrained between 4.1 and 3.8 ka B.P.) (Isaia et al., 2004) and the complex Agnano-Monte Spina tephra (4.1 ka B.P.) (Rosi and Santacroce, 1984; de Vita et al., 1999) (Fig.1.7). This period of volcanism ended with the Senga and Averno eruptions about 3.7 ka B.P. (Alessio et al., 1971; 1973; Di Girolamo et al., 1984; Rosi and Sbrana 1987) (Fig.1.7).

The subsequent and most recent eruption of Campi Flegrei formed the Monte Nuovo tuff-cone (Di Vito et al., 1987) (Fig.1.7) in 1538 A.D. after a quiescence of about 3,000 years. It is one of the smallest eruption of Campi Flegrei and lasted one week. The erupted products are mostly pyroclastic-surge and -flow beds distributed within 1 km around the vent. This eruption strongly changed the physiography of the Gulf of Pozzuoli, transforming the sea branch of the Averno Bay into the Averno Lake (Di Vito et al., 1987) (Fig.1.2). Moreover the eruption was preceded by ground deformation and seismicity, also felt in the city of Napoli (Parascandola, 1947).

The spatial and temporal migration of the volcanic activity in the past 12,000 years toward the centre of the caldera, plus a major reduction in the volumes and an evolution in the chemistry of the erupted products, suggests that the more recent activity phases represent the evolution of a large cooling magma chamber (Armienti et al., 1983).

1.1.3 The feeding system of Campi Flegrei

The structure and location of the magma feeding system at Campi Flegrei is still a matter of debate in the scientific community.

From the modeling of P-to-S conversions of teleseismic waves, a magma chamber was hypothesized at 4-5 km depth by Ferrucci et al. (1992).

Some geochemical and petrological evidences indicate that the feeding system of Campi Flegrei should have a deeper source. A study on melt inclusions of Minopoli I and Fondo Riccio products (located in Fig.1.7) allowed Cannatelli et al. (2007) to conclude that the two eruptive events were the products of the same magma batch that had experienced different residence times in a shallow reservoir during which olivine and clinopyroxene fractionation dominated. Further melt inclusions studies on Minopoli 2 and Fondo Riccio (located in Fig.1.7) mafic products (Mangiacapra et al., 2008), however, let to infer that volatile concentrations within the melt inclusions require gas-melt equilibria between 8 and 9 km depth and closed-system degassing in the presence of the ascending CO_2-rich fluids of deep origin, and later magmas equilibration at 2-3 km depth. Recent melt inclusions studies on Solchiaro eruption, at Procida island (Esposito et al., 2009), indicate that volatile undersaturated magma originated at great depth at the crust-mantle boundary. These parental magmas generate, by fractional crystallization and assimilation processes, magmas saturated in volatiles (H_2O-CO_2), with pressure of trapping ranging from 0.6 to 1.7 kbar, corresponding to 2.3 to 6.3 km depth. Danyushevsky and Lima (2001), on the basis of melt inclusions data in clinopyroxene phenocrysts from xenoliths found at Campi Flegrei, suggest that Campi Flegrei and Vesuvio volcanic systems are genetically very similar and possibly linked. They speculate that the link was established prior to eruption of the NYT.

Isotopic ratios have been frequently used to constrain the possible magma source for Campi Flegrei. Pappalardo et al. (2002), Rosi and Sbrana (1987) and Signorelli et al. (1999) identified four groups of magmas involved in the feeding system of Campi Flegrei: trachytic magmas erupted before the CI eruption; trachytic magmas erupted during the CI eruption; latitic to trachytic magmas erupted during the NYT eruption; shoshonitic magmas erupted for the first time about 10 ka B.P.. Mixing and mingling among these four components and limited assimilation of crust combined with fractional crystallization are used to explain all the geochemical and isotopic variations observed in the post NYT products (D'Antonio et al., 2007).

D'Antonio (2005) proposed a feeding system scheme, in which mantle derived high K-basaltic magmas stagnate in deep reservoirs, differentiating and partly assimilating Hercynian basement (Civetta et al., 2004; D'Antonio et al., 2007). These magmas ascend and then rest in large shallow reservoirs which fed the high VEI caldera giving events after different durations of residence times. According to this scheme, the magma chambers that fed CI and NYT eruptions were fully independent at least up to the end of the NYT eruption (D'Antonio et al., 1999b; Pappalardo et al., 2002). The explosive events after the NYT eruption could have been fed by even shallower magma pockets where the complex interaction between mafic magma coming from the deepest reservoirs and some batches of magmas left behind by the high VEI events occurred (D'Antonio et al., 2007). Bellucci et al. (2006) used the pattern of soil deformation at Campi Flegrei recorded from Roman times to hypothesize a two-magma reservoir system beneath the volcanic field. Recently Pabst et al. (2008) proposed a model of several small magma chambers occurring below Campi Flegrei before the CI and NYT eruptions which coalesced into a large reservoir only a few ka before those events.

A low V_S layer has been detected at ~9 km depth from the inversion of local and regional surface wave tomography (Guidarelli et al., 2006). Wide and extended magma sills, having approximate thickness of 1 km and V_S of 1 km/s, have been inferred at about 8 km beneath Campi Flegrei (Zollo et al., 2008) and Vesuvio (e.g. Auger et al., 2001) from active seismic experiments. The low V_S layer, also detected below Vesuvio at the depth of about 10 km, has been associated with the presence of partial melting and, therefore, may represent a quite diffused crustal magma reservoir which is fed by a deeper reservoir, that is regional in character and located in the uppermost mantle (Guidarelli et al., 2006; Nunziata et al., 2006).

A similar result has been obtained by Nunziata (2010) below the Neapolitan area between Campi Flegrei and Vesuvio volcanic areas.

1.1.4 Campi Flegrei bradyseism

The phenomenon of slow, vertical, ground movements in Campi Flegrei has been known since before Roman times (Parascandola, 1947). The ground movement is named bradyseism from the Greek words meaning, literally, "slow movement". The main example is given by the Macellum at Pozzuoli, an ancient Roman market incorrectly known as Serapeum (Temple of Serapis) which shows the record of the oscillations of the ground

level, since it contains Roman columns with evidence of submersion provided by holes of lithodomes molluscs (Lithodomus lithophagus) occurring at heights of about 7 m (Parascandola, 1947).

Morhange et al. (2006) documented three relative sea level high stands using radiocarbon dating of biological materials at Serapis (Fig.1.13A). A strong ground uplift of about 7 m occurred before the 1538 A.D. Monte Nuovo eruption (starting from 1500 A.D.) and a progressive ground deflation started slightly after the eruption, so that in 1822 the Serapeum floor was submerged again. The slow sinking of the ground continued until 1968 (Fig.1.13A). In the periods 1970-1972 and 1982-1984, two important episodes of inflation occurred in the Pozzuoli area (Berrino et al., 1984) (Fig.1.13B), interrupted by a subsidence of 0.2 m in the period 1972-1975. These two episodes produced an uplift of 1.7 m and 1.82 m (Fig.1.13B), respectively, at the points of maximum deformation located in Pozzuoli (Fig.1.3). The inflation had a circular symmetry around Pozzuoli and regularly decreased toward the margin of the caldera. The episodes of inflation were accompanied by seismic crises (Corrado et al., 1977; Barberi et al., 1984, De Natale et al., 1995).

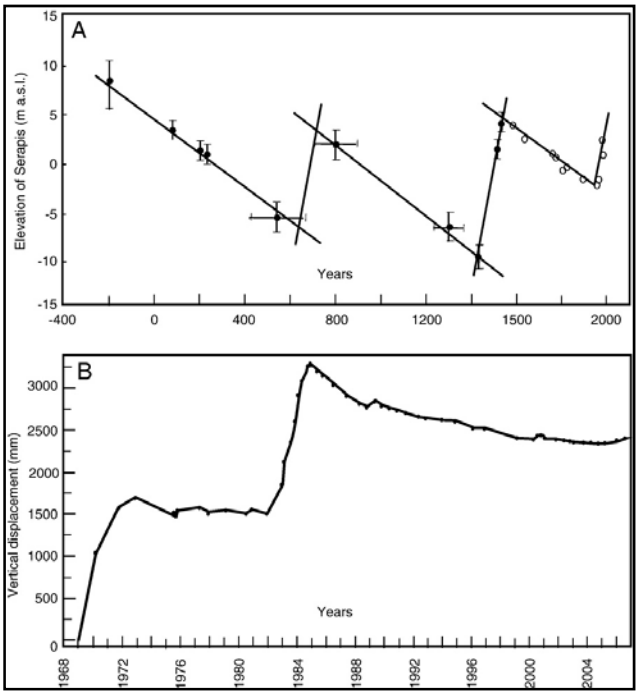

Fig.1.13 *– A) Schematic vertical movements history at the Temple of Serapis in Pozzuoli. Black circles represent the constraints found from radiocarbon and archaeological measurements by Bellucci et al. (2006); white circles (post-1538 A.D.) represent inference from Dvorak and Mastrolorenzo (1991). B) Vertical ground displacements recorded at Pozzuoli harbour by levelling data in the period 1969-2006 (Macedonio and Tammaro, 2005; Del Gaudio et al., 2005; Pingue et al., 2006) (from Lima et al., 2009).*

As a matter of fact, secular deformations and intense unrests are typical manifestations of activity at calderas and a distinctive feature of such deformation episodes is that they are

generally not followed by magma eruptions (Dzurisin and Newhall, 1984; Newhall and Dzurisin, 1988).

In fact within the past 2,000 years, there have been many phases of ground deformation at Campi Flegrei not associated with volcanic eruptions. Only the unrest episode occurred at the beginning of the 16th century preceded a volcanic eruption (i.e. the Monte Nuovo eruption in 1538 A.D.). This is true not only at Campi Flegrei but also in other regions characterized by significant bradyseism such as at Yellowstone (Pierce et al., 2002; Lowenstern and Hurwitz, 2007) and the Long Valley caldera (Hill et al., 2002; Foulger et al., 2003). Although bradyseism is restricted to volcanic regions, bradyseism and volcanic eruptions imperfectly correlate.

Seismicity at Campi Flegrei occurs only during unrest episodes (Corrado et al., 1977; De Natale et al., 1995): in particular the subsidence has never been accompanied by earthquakes, while seismicity did accompany the uplifts (Orsi et al., 1996a) (Fig.1.14).

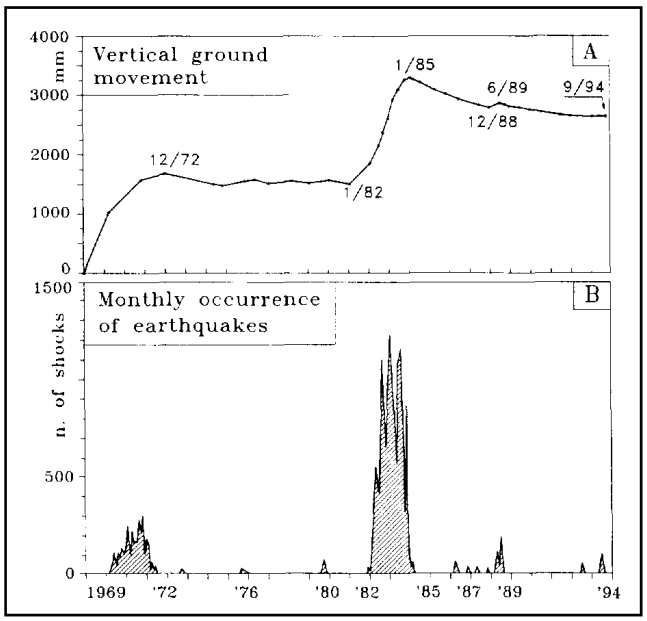

Fig.1.14 *– Vertical ground movement since 1969 at the most uplifted part of the caldera, near Pozzuoli, (A) and related seismicity (B) (from Orsi et al., 1996a).*

The bradyseismic crisis occurred in 1970-1972 was accompanied by seismicity with epicentres concentrated in the northern part of the Gulf of Pozzuoli and in the area between Averno and Agnano (Fig.1.15A). During the 1982-1984 crisis more than 16,000 earthquakes occurred, ranging from 0.4 to 4.0 in magnitude (Aster et al., 1992). Some epicentres were located in the northern part of the Gulf of Pozzuoli, but most of them concentrated in the area between Solfatara and Monte Nuovo (Fig.1.15B) that is located northeastward respect to the most uplifted part of the caldera during the 1982-1984 crisis

(Aster and Meyer, 1988; Orsi et al., 1996a) (Fig.1.3). This area is located approximately at the centre of the Campi Flegrei, where low values of shear wave velocity (Aster and Meyer, 1988; Guidarelli et al., 2002), high values of V_P/V_S ratio (Aster and Meyer, 1988; Vanorio et al., 2005; Battaglia et al., 2008) and a pronounced gravity low (Nunziata and Rapolla, 1981; AGIP; 1987) have been retrieved. So this area has been described as an extremely weak region, such as it deformed aseismically, and characterized by the presence of highly fractured rocks, essentially saturated with liquid water (Aster and Meyer, 1988).

The foci of the earthquakes occurred during the 1982-1984 bradyseismic crisis are located at very shallow depth: most of them occurred between 2 and 4 km in depth (Aster and Meyer, 1988; Vanorio et al., 2005; Battaglia et al., 2008) (Fig.1.4). Earthquakes location are mostly distributed on the top of a region characterized by velocity reversal (Vanorio et al., 2005) (Fig.1.29) and within a region marked by a low V_P/V_S anomaly at 4 km in depth (Vanorio et al., 2005; Battaglia et al., 2008) (Figs.1.28-1.30). These signatures were interpreted by Vanorio et al. (2005) and Battaglia et al. (2008) as related to the presence of gas under supercritical conditions, and hypothesized that seismicity might be induced by overpressured fluids (see the following section for more details). However, no specific seismicity analysis was made with regard to this issue. Nevertheless, a phenomenological correlation among uplift rate, seismicity and increase of the H_2O/CO_2 ratio in fumaroles as a function of time is noted in the Campi Flegrei caldera (Chiodini et al., 2001; 2003). Such a correlation suggests that the observed phenomena may have a common origin.

After the two major crises, the ground slowly subsided till the present stationary phase with occasional renewal of minor uplift episodes accompanied by a few felt earthquakes (Del Gaudio et al., 2010). In fact the general subsidence phase started in 1985 has been interrupted by minor, short duration uplifts in 1989, 1994 and 2000. In August 2000, subsidence renewed and stopped in November 2004 with the onset of a new uplift episode, reaching a level of about 4 cm by the end of October 2006 (Troise et al., 2007) (Fig.1.13B).

The origin of the bradyseismic phenomenon is still debated in the scientific community and various models have been proposed to explain the uplift at Campi Flegrei. All models ultimately depend on the presence of a magma body at depth, but the role of magma in driving bradyseism is quite different (Lima et al., 2009).

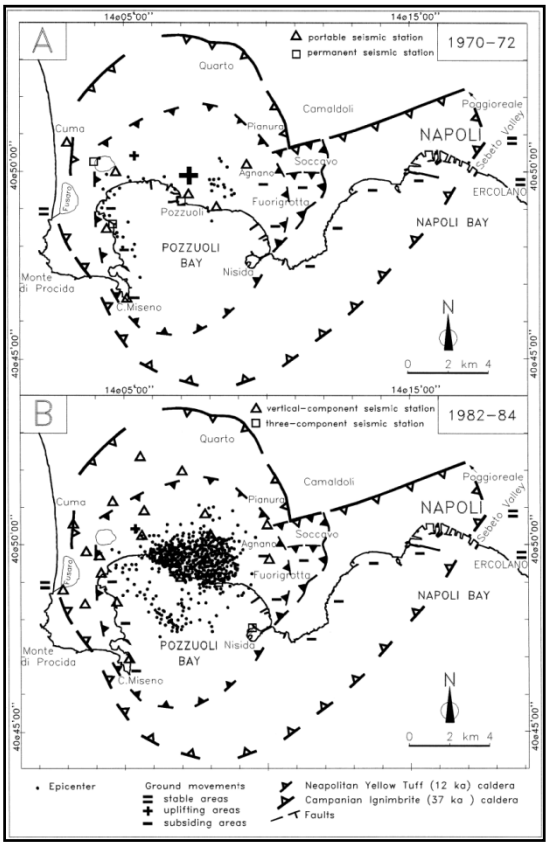

Fig.1.15 *- Distribution of the earthquake epicentres recorded during the bradyseismic crises occurred in 1970-1972 (A) and 1982-1984 (B) (from Orsi et al., 1999a).*

One scenario relates ground surface deformation directly to emplacement of a fresh batch of magma at shallow depth. In this model the ground deformation is the response of the crust acting as an elastic or viscoelastic medium into which magma has been emplaced (Mogi, 1958; Corrado et al., 1977; Barberi et al., 1984; Berrino et al., 1984; Bonafede et al., 1986; Bianchi et al., 1987). The deflation is, on the contrary, due to a compaction of the pore space in the buried loose pyroclastic deposits (Scandone et al., 1991). Recently, Bellucci et al. (2006), in the light of new calculation of uplift and subsidence rates at Campi Flegrei from Roman times, proposed again this model interpreting the behaviour in terms of the intermittent ascent of magma between a reservoir of ~10^2-10^3 km^3 at depths of 8-15 km or greater, to a much smaller, shallower system at depths of about 3-4 km.

A second class of models also involves fresh magma input to trigger bradyseism and explains ground surface deformation as due to the injection of magmatic fluids into overlying crust, rather than as response to pressurized magma. Injection of high temperature magmatic fluid into the shallow hydrothermal reservoir system induces fluid overpressures that may cause the host rocks to inflate depending on the mechanical properties of the local crust (Fournier, 1999). In this model, subsidence results from a

decrease in the flux of magmatic fluid entering the hydrothermal system or as a response to rapid permeability increases and hence pore pressure decreases that occur when the fluid pressure exceeds the local strength of the crustal host, a condition generally easily achieved at shallow depths. Some authors (Cortini et al., 1991; Cortini and Barton, 1993; Cubellis et al., 2002) proposed more generalized nonlinear dynamic models based on chaos theory, some others (Casertano et al., 1976; Bonafede, 1991; Gaeta et al., 1998) suggested that the inflation episodes are due to a pressure increase in the fluids circulating in the hydrothermal system of Campi Flegrei.

More recently, models based on the interaction of magmatic fluids with hydrothermal systems dominated by non magmatic fluids have been proposed by Battaglia et al. (2006), De Natale et al. (2006), Caliro et al. (2007) and Troise et al. (2007). In particular, according to the mixed magmatic-geothermal model proposed by De Natale et al. (2006), large amounts of uplift (up to 3.5 m in 15 years), sometimes followed by partial subsidence, are explained in terms of an initial magma input followed by pressurization of the geothermal system, which then progressively deflates by water outflow. The water deflation phase, associated with the subsidence following large uplift episodes, is strongly constrained by gravity and ground deformation data, which uniquely indicate that the subsidence source is a shallow (about 2 km), vertically elongated zone, with fluid densities in the range 500-1,000 kg/m^3.

Scandone et al. (2006) tried to reconcile the two hypotheses (magmatic vs. hydrothermal) through a comprehensive model of the recent dynamics of Campi Flegrei by considering the problem on different timescales. On the shorter timescale, deflation and inflation episodes provide evidence of a deformation of the floor of the caldera almost as an elastic plate bounded by a circular discontinuity. On a longer timescale involvement of a structural source in the origin of inflation-deflation phenomena is postulated.

De Vivo and Lima (2006), Bodnar et al. (2007) and Lima et al. (2009) supported the pioneering hypothesis of Oliveri del Castillo and Quagliariello (1969) by attributing an active role for the deformations at Campi Flegrei to hydrothermal fluids, both of magmatic and/or meteoric/seawater origin, and not to the magma. Their results are supported by data obtained from fluid inclusions from geothermal boreholes at Campi Flegrei (De Vivo et al., 1989), as well as data from fluid inclusions and melt inclusions in the nearby sub-volcanic systems of the Pontine Islands (De Vivo et al., 1995; Belkin et al., 1996) and Vesuvio (Lima et al., 2003; 2006). In such model, magma plays only the role of a “furnace” to heat the system, and bradyseism results from the complex interplay of two dominant processes

operating on very different timescales: aqueous fluid exsolution during magma solidification on a slow timescale (10^3-10^4 yr) is superimposed upon the episodic expulsion of fluid from a deep (~3-5 km) lithostatically pressured low-permeability reservoir to an overlying hydrostatic reservoir occurring on a shorter (1-10^2 yr) timescale (Bodnar et al., 2007; Lima et al., 2009) (Fig.1.4-inset C). The fluids exsolving from an underlying crystallizing magma, under lithostatic pressure for long periods of time, generate overpressure (volatile accumulation) in the upper, apical, part of the magma chamber that, confined by an impermeable ring or layer, causes uplift of the overlying rocks (positive bradyseism) (Fig.1.4-inset C-1). A seismic crisis occurs when the conditions change from lithostatic to hydrostatic pressure, with consequent boiling, hydraulic fracturing (De Vivo et al., 1989), seismic tremor and then pressure release. At this point, the area experiences the maximum degree of inflation (Fig.1.4-inset C-2), which is then followed by pressure release and beginning of subsidence (negative bradyseism) (Fig.1.4-inset C-3). Afterwards, the system, saturated with boiling fluids, begins to seal again due to the precipitation of newly formed minerals. The beginning of a new positive bradyseism phase occurs only after a period of time (years) during which the system "reloads" under new lithostatic pressure conditions.

The timescale of the episodic expulsion process depends on the rate of generation of magmatic volatiles and most significantly on the anisotropy, magnitude and temporal variations of the permeability field characterizing the hydrothermal system. At Campi Flegrei there is an overall permeability structure imposed by the sedimentary and metasedimentary rocks of the crust in which, with increasing depth, the ordering is permeable to impermeable back to permeable and then in the deepest part of the system (~5 km) impermeable (contact metamorphic rocks) (Fig.1.4). Of special significance are the low permeability fine grained Middle Pleistocene marine claystones and siltstones at about 2 km depth that make up Unit B (Fig.1.4). This unit acts as the throttling valve between the hydrothermal and the intermediate lithostatic-hydrostatic reservoirs with distinct vertical gradients in fluid pressure (Lima et al., 2009) (Fig.1.4-inset B).

According to this model, as the magma body cools and crystallizes and the H_2O-saturated carapace migrates to greater depth, the energy and volume exchange associated with volatile exsolution decreases and the magnitude of future events is likewise expected to decrease (De Vivo et al., 2010).

1.1.5 Structural models of Campi Flegrei

The intense volcanological history of Campi Flegrei, the tectonic activity and the variation of the sea level generated a very complex structure. Several geophysical studies have been performed in order to define the structural setting.

A milestone in the literature is the seismic reflection survey made by Finetti and Morelli (1974) in the Gulfs of Napoli and Pozzuoli. They recognized three main stratigraphic sequences constituted from the top to the bottom by the Quaternary-Pliocene, the pre-Pliocene Tertiary and the carbonate Mesozoic series. The deepest reflecting horizon, called "K" horizon, crops out in the Sorrento Peninsula (Fig.1.1) and deepens to the west, reaching a depth of about 2.7 km near the island of Nisida. Further west, although this horizon can be followed with less confidence, it seems to rise gently reaching a depth of about 2.2 km in the western part of the Gulf of Pozzuoli. Two main faults were detected in the Gulf of Pozzuoli with NNW-SSE orientation: the first one is located in the western part of the bay extending to the south near Capo Miseno; the second one is located in the eastern part of the bay extending to the north toward the Posillipo hill and the Gulf of Napoli. Intense volcanic activity and shallow earthquakes occurred (Guerra et al., 1972; Rampoldi, 1972) along these two faults (mainly along the western fault).

Moreover, the buried volcanic edifice of Nisida was recognized, active since the Late Pliocene-Early Quaternary. After an intense volcanic activity, a quiescence period and a subsidence of a few hundred meters occurred, so a 300 m thick layer of sediments cover the volcano. In the Recent epoch the volcanic activity started again forming the Banco of Nisida (Fig.1.2) that is isolated from the buried volcano of Nisida (Finetti and Morelli, 1974).

Bouguer anomalies in Campi Flegrei (Ciani et al., 1960; Maino et al., 1964; Amadei et al., 1971; Calligaris et al., 1972) are characterized by a number of gravity highs, separated by a low centred in the Gulf of Pozzuoli (Fig.1.16). A caldera shaped structure, filled of loose volcanics, resulted from the interpretation of the gravity low (Nunziata and Rapolla, 1981). Regarding the nature of the basement, both the hypotheses of carbonate and lava are possible and cannot be discriminated as density and seismic velocity ranges of lavas are fairly equal to those of carbonate rocks.

After drillings in the Mofete area (Fig.1.3), a similar model was proposed by AGIP (1987). The edges of the caldera are defined by numerous gravity highs surrounding the minimum (Fig.1.16) and by a series of positive magnetic anomalies (Fig.1.17) which have been

interpreted as pericalderic lava bodies (Figs.1.18-1.19). The gravity highs defining a ring-like trend are located in Agnano, Astroni, Senga, Cigliano and Accademia areas (Fig.1.16). They have been related to the recent volcanic activity which is concentrated inside the collapsed area. These gravity highs have been interpreted as due to the occurrence of hydrothermal alteration, the presence of shallow lava bodies and structural high of hydrothermalized lava (AGIP, 1987) (Fig.1.18).

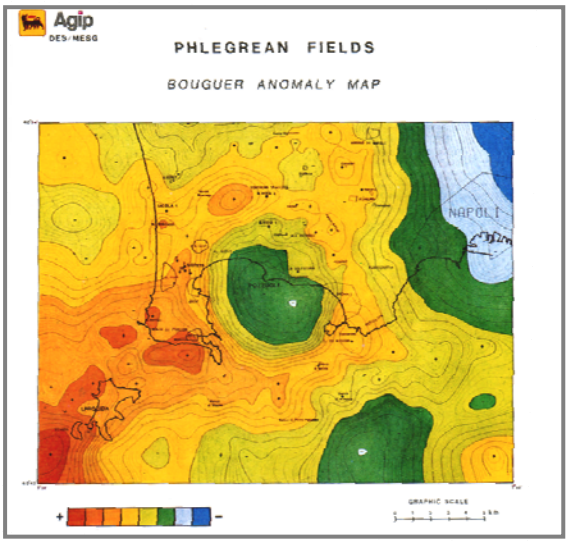

Fig.1.16 *– Bouguer anomaly map of Campi Flegrei performed by AGIP (1987) (from AGIP, 1987).*

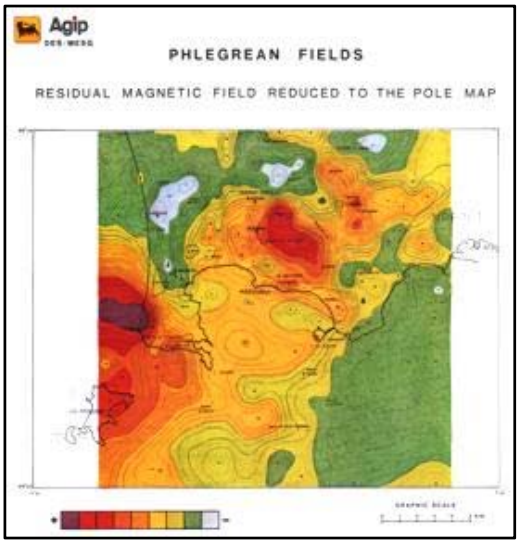

Fig.1.17 *– Residual magnetic field reduced to the pole map performed by AGIP (1987) (from AGIP, 1987).*

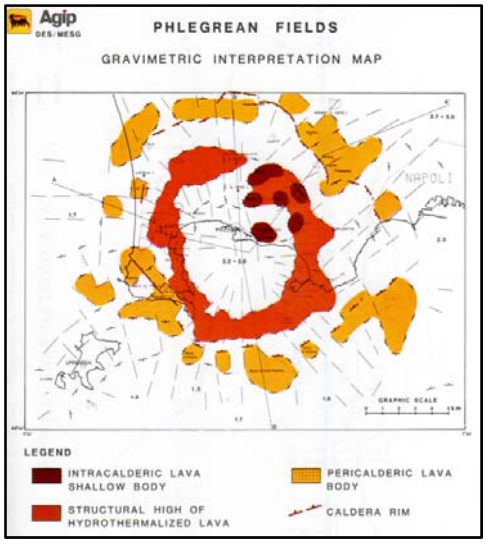

Fig.1.18 *– Structural model of Campi Flegrei based on the interpretation of gravimetric data proposed by AGIP (1987) (from AGIP, 1987).*

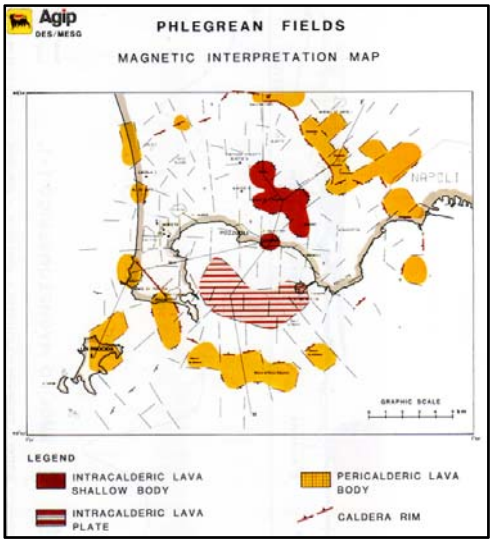

Fig.1.19 *– Structural model of Campi Flegrei based on the interpretation of magnetic data proposed by AGIP (1987) (from AGIP, 1987).*

The reconstructed geological setting along a profile from Mofete area to Pianura area (Fig.1.20) is characterized, from the top, by: shallow layers of tuff material with increasing

density (ρ=2.0 g/cm^3 and ρ=2.2 g/cm^3); hydrothermalized lavas (ρ=2.4 g/cm^3) and thermometamorphic rocks (ρ=2.6 g/cm^3). The latter ones are at depth of about 2 km below Mofete and Pianura and of about 3 km below the Accademia area (Fig1.20). The density increase with depth could be due to the lithostatic load and to the effect of the hydrothermal weathering (Barberi et al., 1991).

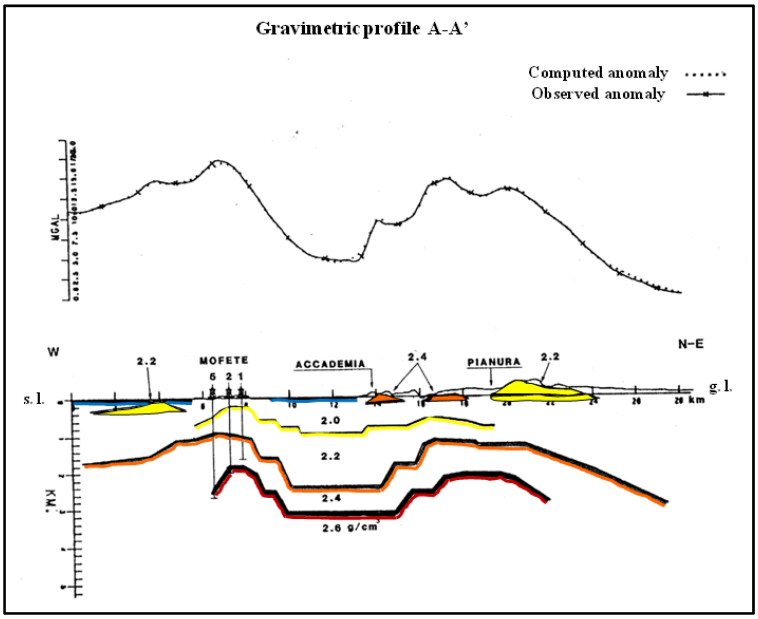

Fig.1.20 *- Density model provided by AGIP (1987) along the gravimetric profile A-A' located in Fig.1.18 from Mofete area to Pianura (modified after Agip, 1987).*

The resulting model proposed by AGIP (1987) is a caldera structure characterized by a basal geometry in the form of a truncated pyramid with a -0.2 g/cm^3 density contrast. On the contrary Fedi et al. (1991) applied the E.P.D. (Equivalent Prism Densities) method to fit the gravity anomaly of the Campi Flegrei obtaining a funnel-shaped caldera model with a lateral -0.22 g/cm^3 density contrast between the caldera filling material and the surrounding rocks (Fig.1.21b). The depressed area reaches the maximum depth of about 3 km south of Pozzuoli, where the relative gravity minimum is located (Fig.1.21a).

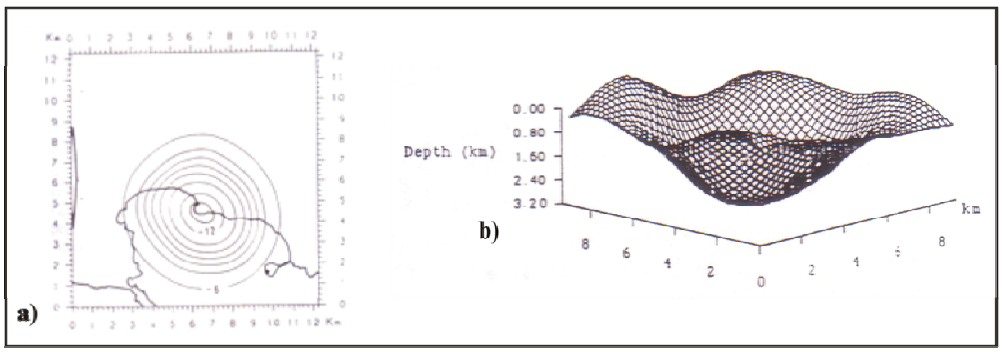

Fig.1.21 *- 3-D funnel-shaped model of Campi Flegrei caldera (from Fedi et al., 2009).*

The aeromagnetic map of Campi Flegrei (Scarascia, 1972) is characterized by three main anomalies: the first has maximum west of Capo Miseno Peninsula and minimum on Fusaro Lake; the second has maximum east of the Gulf of Pozzuoli, near the Solfatara-Astroni craters, and minimum near Quarto; the third has maximum on Procida island and minimum just north of it. These anomalies are superimposed on and tend to mask a wider negative anomaly (Fig.1.22).

These three anomalies are well justified by very shallow magnetized bodies with a thickness of 200 m (Fig.1.22). These bodies should be seen as a schematic representation of lava flows, domes and scoriae, which here and there crop out at Agnano, Astroni, Solfatara, Capo Miseno and Procida (Rittman et al., 1950). Subtracting these three anomalies from the observed magnetic field, Nunziata and Rapolla (1981) obtained a residual anomaly field characterized by a large and intense low centred in the southwestern area of the Gulf of Pozzuoli. The interpretative model along a NE-SW profile consisted in a low magnetized body, because of the high thermal state, with its top at depths varying from about 0.6 km on the western side of the Gulf of Pozzuoli to about 0.3 km in the centre and about 1 km on the eastern side (Fig.1.23).

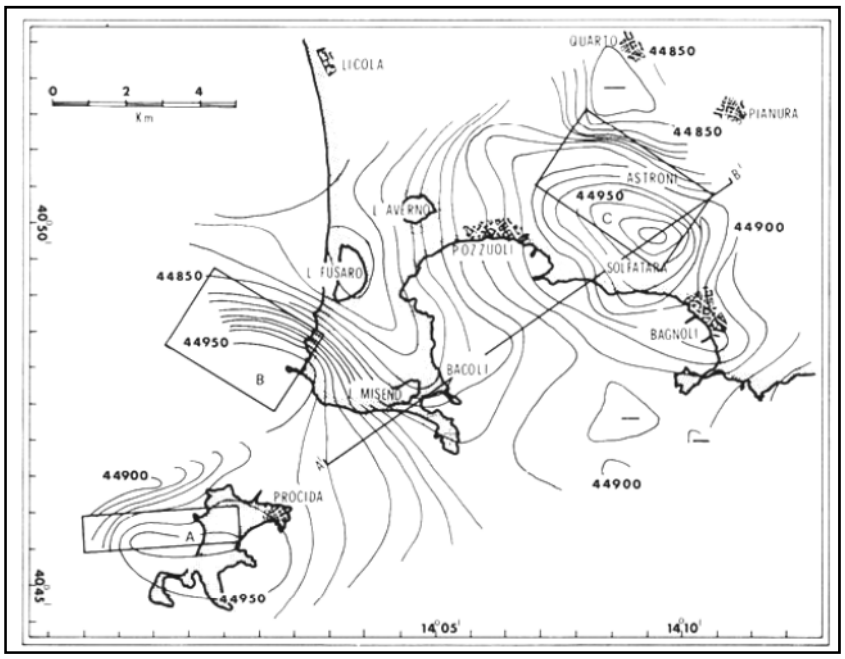

Fig.1.22 *– Aeromagnetic map of Campi Flegrei (after Scarascia, 1972) and location of the three interpretative parallelepipedic magnetized bodies (from Nunziata and Rapolla, 1981).*

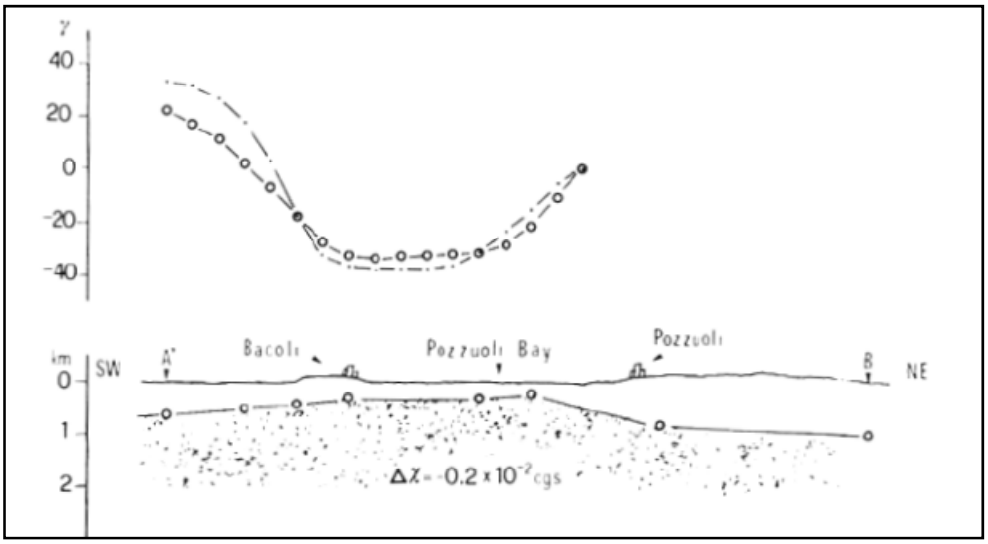

Fig.1.23 *– Interpretation of the residual magnetic anomaly in the Gulf of Pozzuoli carried out by Nunziata and Rapolla (1981) along the NE-SW profile (see Fig.1.21). Dots=observed anomaly; open circles=computed anomaly (from Nunziata and Rapolla, 1981).*

Aster and Meyer (1988), using P- and S-pick times on recordings of earthquakes occurred in the Phlegraean area during the 1982-1984 bradyseismic crisis, proposed a three-dimensional model for the velocity structure within the uppermost 3 km of the crust in the Campi Flegrei caldera. This model evidences low values of compressional (V_P) and shear (V_S) wave velocities and high-V_P/V_S anomaly in the central area of Campi Flegrei (Fig.1.24). In this region the V_P model shows the highest resolution within the whole explored thickness, while the V_S and V_P/V_S models have generally lower resolution and the anomaly in the central area is well resolved within the first kilometre only, where V_S reaches a minimum value of 1.35 km/s and V_P/V_S ratio reaches its maximum value of 2.2 (Fig.1.24).

This anomaly is roughly coincident with the region of greatest uplift (Fig.1.3) and spatially correlated with the Bouguer gravity low (Fig.1.16), but is about 1 km south of the zone of greatest seismicity observed from 1982 through 1985. This anomaly has been interpreted by the authors as an incompetent, highly fractured zone of liquid water-filled cracks.

In the northwestern sector of Campi Flegrei a shallow region of low-V_P, low-V_S and low V_P/V_S ratio (Fig.1.24) is recognized and is spatially correlated with the prominent yellow tuff cone of Gauro volcano (see the location of this vent in Fig.1.7). This anomaly is well resolved within the first kilometre, where V_S reaches a minimum value of 1.36 km/s and V_P/V_S ratio reaches its minimum value of 1.6 (Fig.1.24). It may represent a region of dry or partially saturated cracks (lack of fumarole activity makes it unlikely that there is shallow steam here) (Aster and Meyer, 1988).

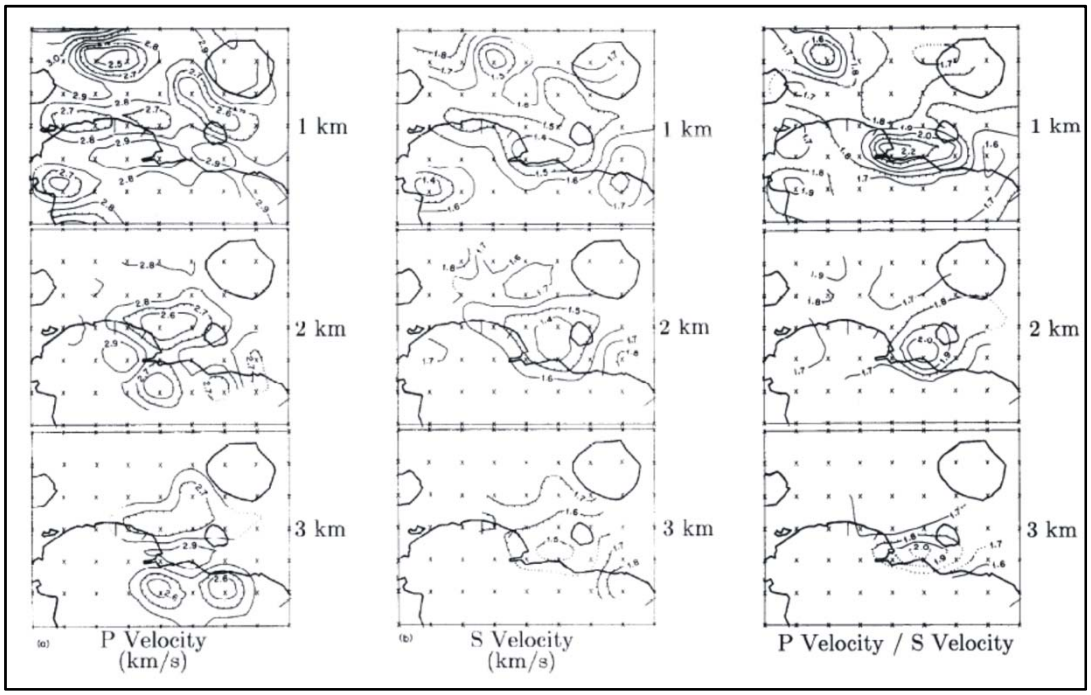

Fig.1.24– *Contoured 3-dimensional V_P, V_S and V_P/V_S models for depth 1, 2 and 3 km performed by Aster and Meyer (1988). The contour interval is 0.1 km/s for V_P and V_S maps, 0.1 for V_P/V_S map; the grid spacing is 1 km (modified after Aster and Meyer, 1988).*

Guidarelli et al. (2002) analyzed a set of events recorded during March 1984 in Phlegraean area and performed a surface wave tomography at fixed periods of 0.3, 0.5 and 1.5 s. Three negative anomalies of Rayleigh wave group velocities resulted, being one located in the Gulf of Pozzuoli, approximately corresponding to the central part of the caldera where the Bouguer anomaly minimum is centred (Fig.1.16) and the other two are located in correspondence of the Astroni and Gauro volcanoes. The inland negative anomalies correlate well with the low V_S regions singled out by Aster and Meyer (1988; 1989) within the uppermost 2 km of the crust, and the low Q_P areas retrieved by De Lorenzo et al. (2001a, b) interpreted by the authors as caused by an increase of permeability and fluid circulation.

Guidarelli et al. (2002) obtained shear wave velocity models for the uppermost 2 km of the crust from the inversion of the group velocity dispersion curves relative to the three low velocity regions identified through the surface wave tomography (Fig.1.25a). All the models are characterised by V_S lower than 1 km/s within the first kilometre; but only the V_S model representative of the Gauro region shows a low velocity layer, thick about 0.22 km, characterized by a V_S value of 0.57 km/s (Fig.1.25b). At depth of about 1.8 km, V_S is about 1.9 km/s in Golfo and Gauro regions and 1.35 km/s in the Astroni area (Fig.1.25).

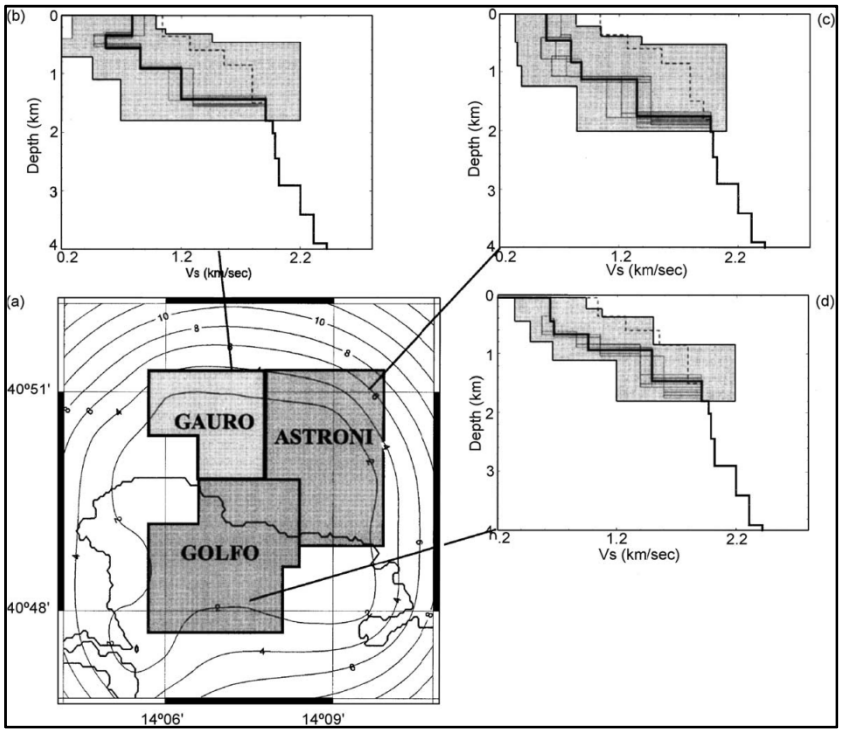

Fig.1.25 *– Three regions characterized by negative anomalies of Rayleigh wave group velocities (a); V_S models obtained from inversion of dispersion curves relative to Gauro (b), Astroni (c) and Golfo (d) tomographic areas (from Guidarelli et al., 2002).*

A 3-D velocity model of the Campi Flegrei caldera has been proposed by Judenherc and Zollo (2004) from the analysis of first P-wave arrival times relative to an active seismic survey in the Gulfs of Napoli and Pozzuoli. The modelled velocity distribution shows the presence of a ring-like high-velocity structure at 0.75-1 km below sea level extending down to 2 km of depth from Capo Miseno to Nisida island (Fig.1.26). This high-velocity ring has been associated to the southern rim of the Campi Flegrei caldera (Zollo et al., 2003). Below this structure, the high velocity disappears and the central portion of the Gulf of Pozzuoli is characterized by low velocities. This area approximately coincides with the low gravity centred in the Gulf of Pozzuoli; the southern edge of this minimum is surrounded by a relative high gravity which fits the high-velocity arc. At 2.5-3 km of depth a sharp velocity increase is recognized, probably due to the occurrence of the carbonatic layer (Judenherc and Zollo , 2004) (Fig.1.26).

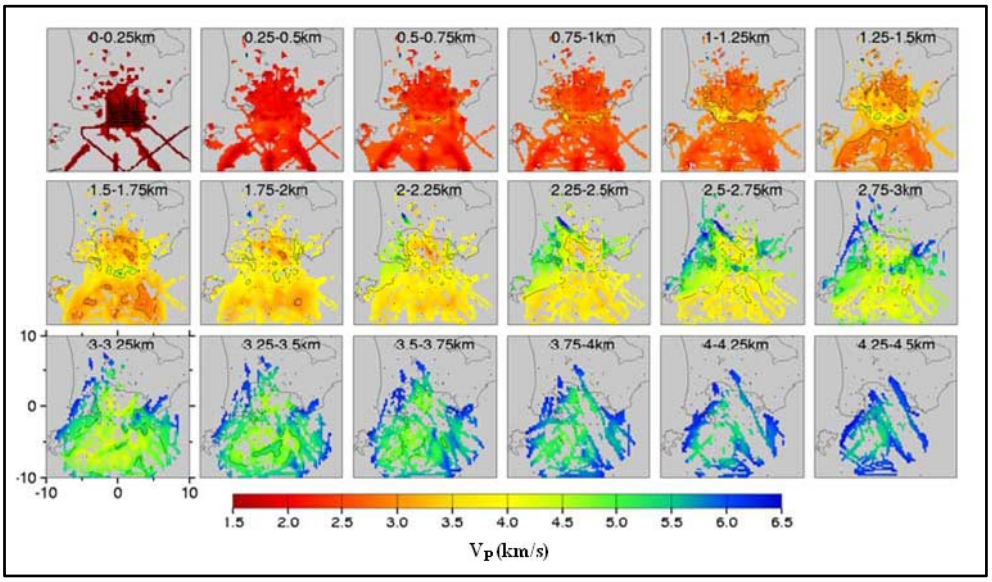

Fig.1.26 *- Plane views of the velocity model of the Gulf of Pozzuoli obtained by Judenherc and Zollo (2004). For each layer the top and bottom depths of the layer are indicated. In the first layer acquisition profiles are located (from Judenherc and Zollo, 2004).*

Correlating the 1 km vertical offset retrieved from the gravity modeling (AGIP, 1987) on the land side of the rim with that observed in the velocity distribution on the sea side, the V_P model provided by Judenherc and Zollo (2004) along a profile crossing the Gulf of Pozzuoli (Fig.1.27) shows that the vertical velocity gradient along the rim of the Campi Flegrei caldera is shifted upward by about 1 km with respect to the gradient in the inner and outer parts of the caldera. In particular, the depths and shapes of the 3 and 3.5 km/s isolines (Fig.1.27) correlate very well with the depths and shapes of the top of the 2.2 and 2.4 g/cm^3 bodies, respectively, in the density model provided by AGIP (1987) (Fig.1.20). Moreover, the 2.2-2.4 g/cm^3 transition corresponds to the transition from the tuff-dominated to the lava-dominated units (Rosi and Sbrana, 1987). Consequently, Judenherc and Zollo (2004) suggest that the tomographic velocities <3 km/s are associated with the volcanic filling material (incoherent pyroclastic rocks, tuffs and chaotic tuffites), while the higher velocities (>3.5 km/s) represent more coherent units (trachytic lavas and tuffites or tuffs with interbedded lavas).

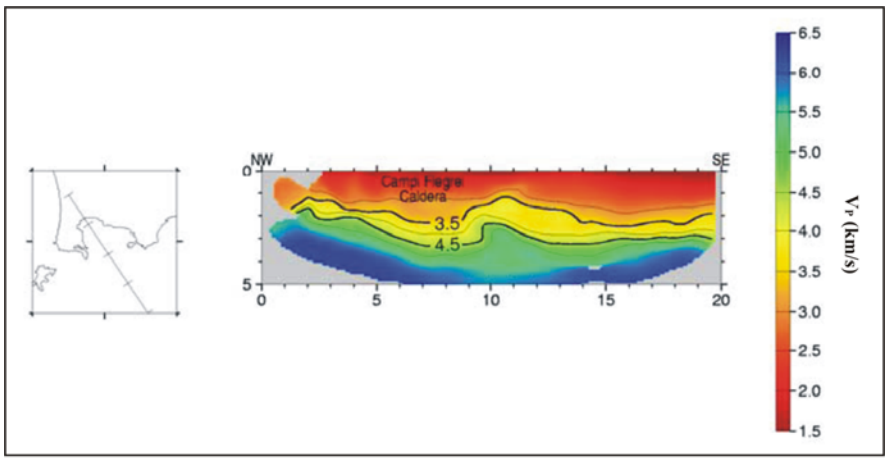

Fig.1.27 *- V_P model provided by Judenherc and Zollo (2004) along a NW-SE profile crossing the Gulf of Pozzuoli (modified after Judenherc and Zollo, 2004).*

Vanorio et al. (2005) computed a 3-D velocity model by inverting P-wave and S-wave first-arrival times picked on the recordings of earthquakes occurred during the 1982-1984 bradyseismic crisis. The deduced V_P/V_S ratio distribution in Campi Flegrei presents a high V_P/V_S anomaly centred on Pozzuoli and located at about 1.5 km depth (also noted by Aster and Meyer (1988)) surrounded by a low V_P/V_S anomaly which shows a flat feature at 4 km depth beneath the city of Pozzuoli (Fig.1.28).

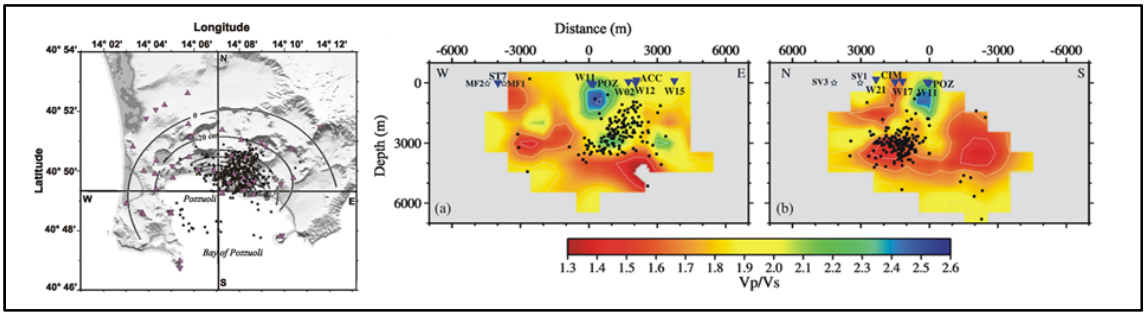

Fig.1.28*- Vertical cross sections describing the variation of the V_P/V_S ratio and earthquake distribution (black points) along the (a) E-W and (b) N-S directions reported in the map of Campi Flegrei on the left. Black stars and triangles indicate well and station locations (from Vanorio et al., 2005).*

Several P-wave and S-wave velocity profiles are characterised by velocity values decreasing between 2 and 4 km of depth (Fig.1.29).

Vanorio et al. (2005) performed also laboratory measurements on tuffite samples in order to study the variation of V_P/V_S ratio as a function of the porosity. The agreement with laboratory experiments (Ito et al., 1979) and effective medium modeling (Dvorkin et al., 1999) allowed Vanorio et al. (2005) to interpret the low V_P/V_S anomaly, occurring at 4 km depth beneath the centre of the caldera and below the reversal velocity zone, as evidence of overpressured gas-bearing rocks at supercritical conditions (temperatures of ~400° C were reported in the San Vito well at 3 km depth (AGIP, 1987)). Instead, the shallower higher

V_P/V_S anomaly at 1 km depth is attributed to the presence of rocks containing brine, probably due to steam condensation as a result of lower temperatures, in agreement with Aster and Meyer (1988).

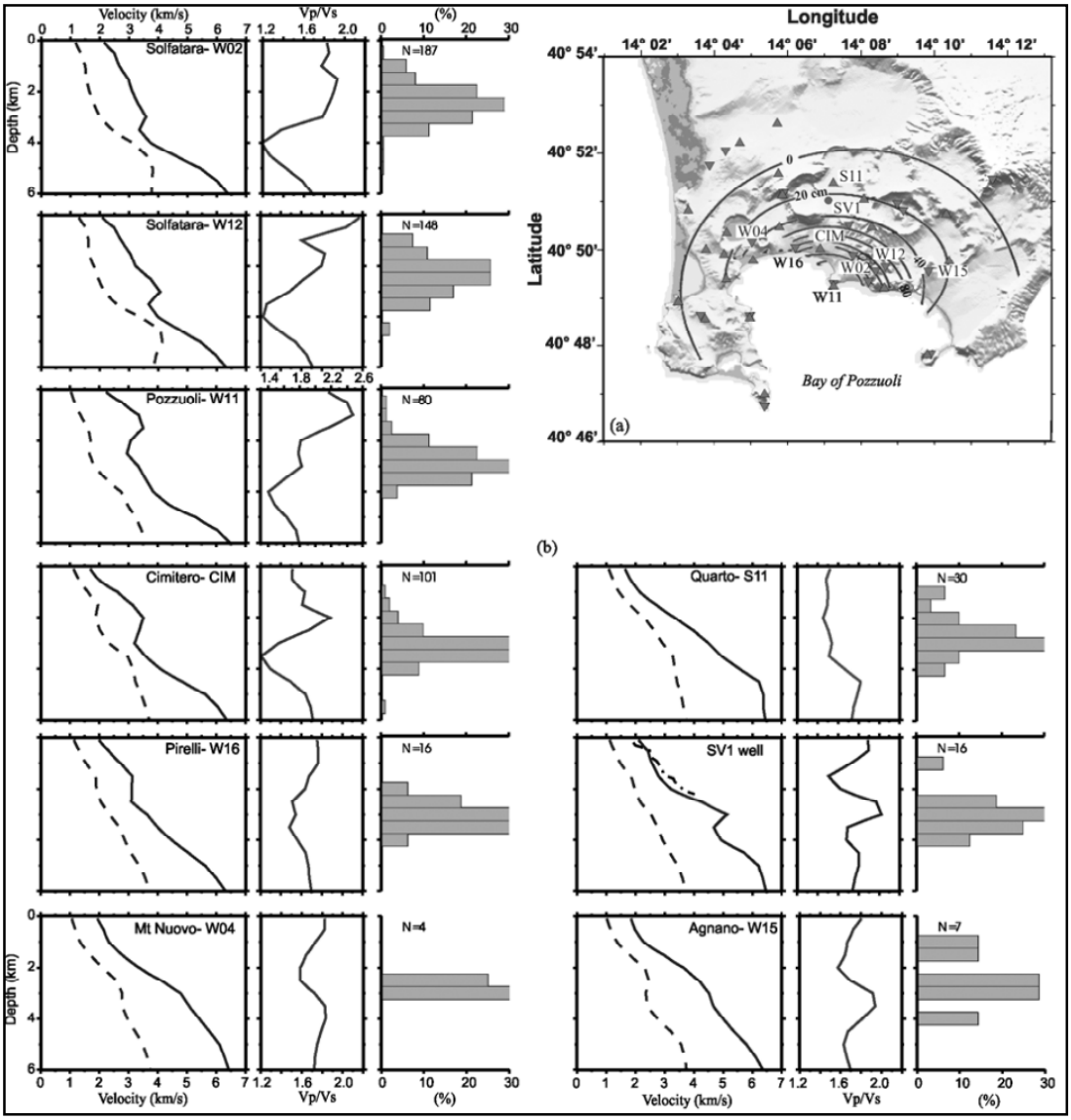

Fig.1.29 *- Map view of site locations of the vertical profiles (a); velocity logs showing V_P (solid line), V_S (dashed line) and the V_P/V_S ratio extracted from the final 3-D velocity models obtained by Vanorio et al. (2005)(b). The distribution of the epicenter of the analysed earthquakes is also shown (from Vanorio et al., 2005).*

More recently Battaglia et al. (2008) reanalysed the active seismic signals used by Judenherc and Zollo (2004), merging them with passive seismic data recorded during the end of the 1982-1984 bradyseismic crisis in Campi Flegrei. A new tomographic map of P-waves has been proposed which confirms the presence of a high P-wave velocity ring in the southern part of the Gulf of Pozzuoli, which is particularly clear around 1.5 km b.s.l. and is recognizable down to 2.5-3.0 km. Its trace extends inland along the western border

of the gulf and is less clear along the eastern border below and north of the island of Nisida.

The joint inversion of active and passive seismic data allowed the authors to obtain both V_P and V_S models and hence they presented the V_P/V_S ratio distribution in Campi Flegrei (Fig.1.30). Two main features are identified: a very high V_P/V_S ratio that reaches the maximum value of 2.7 at a depth of about 1 km below the town of Pozzuoli; a very low V_P/V_S ratio with values down to 1.3-1.4 at 3-4 km depth extending below a large part of the caldera (Fig.1.30).

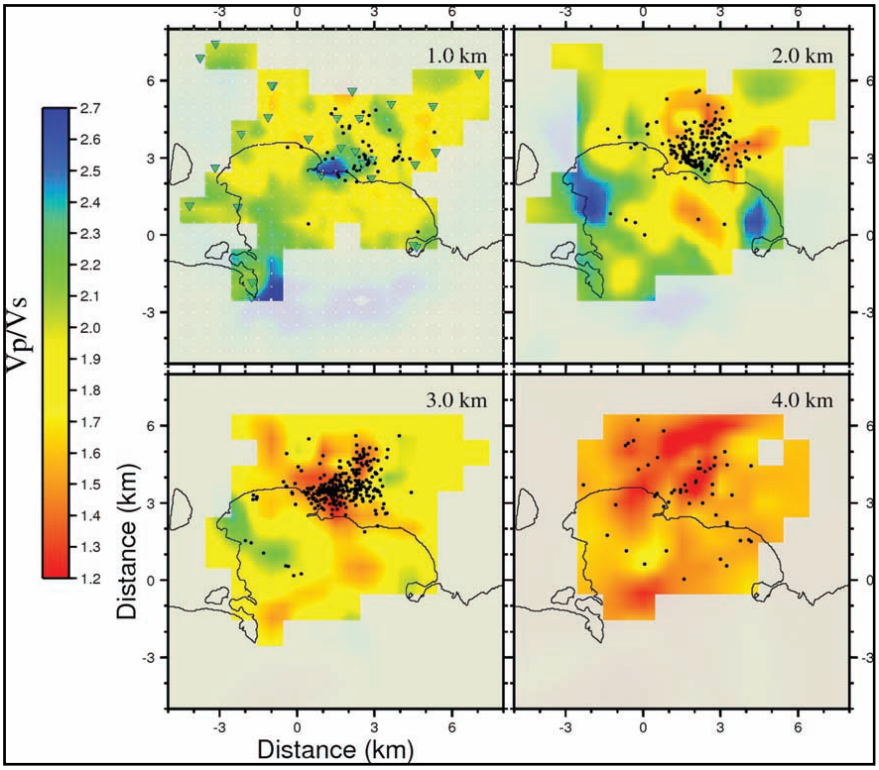

Fig.1.30 *- Horizontal cross-sections of the Vp/Vs ratio distribution in Campi Flegrei (from Battaglia et al., 2008).*

Dello Iacono et al. (2009) defined a more detailed model of the shallow structure of the Campi Flegrei caldera by the joint analysis of seismic reflection sections and tomographic images. 1-D velocity profiles extracted from the 3-D tomographic model show a steep change in the P-wave velocity at about 0.6 km depth in the Gulf of Pozzuoli. Above that depth, V_P values ranging from 1.5 to 2 km/s have been related by the authors to the presence of a thick, low velocity sediment formation filling the shallower part of the caldera, which is characterized by a very high V_P/V_S ratio (3.7±0.9). This value, together with the estimated P-wave velocities, provides S-wave velocities of 0.450-0.515 km/s. According to the authors the high V_P/V_S ratio represents an average estimate of the whole

shallow layer, and thus such a value could be strongly influenced by the saturation conditions of the rocks in the first hundreds of meters. In contrast, from 0.6 km down to 0.9 km depth, the P-wave velocity increases sharply from 2 to 2.6 km/s (Fig.1.31).

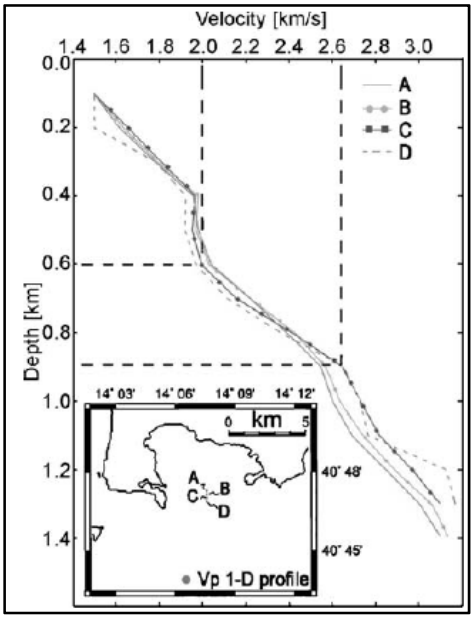

Fig.1.31 *- 1-D V_P profiles located in the Gulf of Pozzuoli extracted from the 3-D tomographic model (from Dello Iacono et al., 2009).*

1.2 The island of Ischia

1.2.1 Geological and structural setting of Ischia

The island of Ischia is the westernmost active volcano of the Campanian Plain (Fig.1.1) and, rising about 1,000 m from the seafloor, it represents the emergent part of a more extensive volcanic area developed mainly to the west of the island (Vezzoli, 1988; Bruno et al., 2002). The volcanic complex is located along NE-SW trending fractures that control the volcanic activity in the Campanian Plain (Vezzoli, 1988).

The Ischia offshore area is characterized by several monogenetic edifices aligned along the NE-SW system of faults that connects the southeastern sector of Ischia to the island of Procida and to the Campi Flegrei volcanic field (Di Girolamo and Stanzione, 1973; de Alteris and Toscano, 2003). These edifices have been mainly formed through subaqueous explosive eruptions of potassic magma (Di Girolamo and Rolandi, 1975), but a few lava domes can also be found (Di Girolamo et al., 1984).

Ischia is composed mainly of volcanic rocks (Fig.1.32) deriving from a number of eruptive centres which have been largely destroyed or covered by subsequent activity and

can now be identified only in part (Carlino et al., 2006). Also marine sediments and landslide deposits occur (Fig.1.32), so the presence of all these products define a complex geological setting resulted from the interplay of tectonism, volcanism, erosion, sedimentation and slope instability (de Vita et al., 2006).

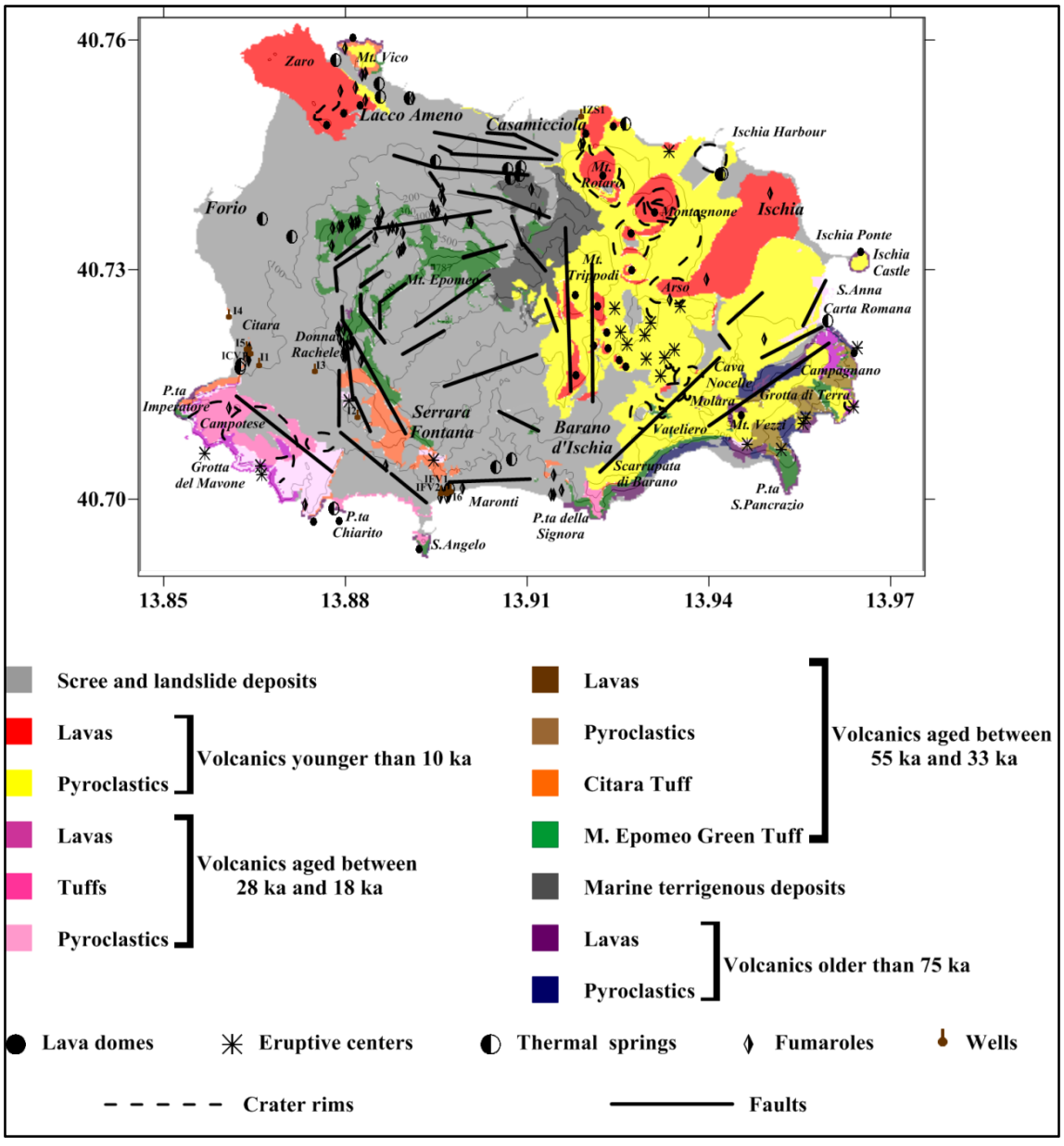

Fig.1.32 *– Simplified geological map of the island of Ischia (modified after Progetto Finalizzato Geodinamica, CNR, 1988 and Vezzoli, 1988); geothermal wells executed by Penta and Conforto (1951) are also shown.*

The oldest known products (>150 ka B.P.) are pyroclastic deposits cropping out at the southeastern corner of Ischia, while lava domes and pyroclastic deposits of the activity between 150 and 75 ka crop out all around the periphery of the island (Gillot et al., 1982; Vezzoli, 1988 and references therein) (Fig.1.32) where the presence of a caldera structure

with an age between 150 ka and 75 ka has been inferred (Poli et al., 1987; Vezzoli, 1988). Several explosive eruptions have been recognized in the period 75-50 ka B.P., many of which produced pyroclastic flow deposits that covered entirely Ischia, and the near island of Procida (Brown et al., 2008).

The greatest volcanic event of the island of Ischia is the eruption of Mt. Epomeo Green Tuff (~55 ka B.P.), an alkali-trachytic ash flow (Vezzoli, 1988), which caused Ischia caldera collapse. In the period 55-33 ka, marine sediments and distal pyroclastic deposits aggraded onto the caldera floor. The Ischia caldera started its resurgent uplift 33-28 ka ago (Gillot et al., 1982; Vezzoli, 1988) resulting in a composite trapdoor structure, with a central, asymmetric, faulted block, ~4×5 km wide, which reaches the maximum height (787 m a.s.l.) at Mt. Epomeo (Rittmann, 1930; Vezzoli, 1988; Acocella and Funiciello, 1999; Tibaldi and Vezzoli, 2000) (Fig.1.32). Coeval with the caldera resurgence, volcanism occurred mainly in two distinct periods, namely from 28 to 18 ka B.P. and from 10 ka B.P. to 1302 A.D. when the last volcanic event, i.e. the Arso lava flow, occurred. In the last 10 ka, alkali-trachytic to trachyandesitic effusive and explosive activity developed mainly in the eastern sector of the caldera (Fig.1.32), along both resurgence-related faults and regional NNW-SSE and NE-SW striking faults (Vezzoli, 1988; Orsi et al., 1996b).

As suggested by Orsi et al. (1991b) and Acocella and Funiciello (1999), the structural setting of the island seems to result from the interplay between the NE-SW and NW-SE regional lineaments and local tectonics mainly represented by four fault systems (Vezzoli, 1988; Molin et al., 2003): a ENE-WSW to E-W striking system in the northern and southern sector of Mt. Epomeo; a NE-SW system cutting the deposits of the eastern sector; a NW-SE striking fault in the southwestern corner of the island; a NNW-SSE to N-S system bordering the eastern and western side of Mt. Epomeo (Fig.1.33).

The morphological setting of Ischia is strongly affected by these structural lineaments, in fact the main features are a central uplifted area in correspondence of the Mt. Epomeo (787 m a.s.l.) and a triangular shaped graben extending in the central-eastern part of the island bordered by NNE trending (from S.Angelo area to the islet of Ischia Castle) and N trending (from Barano to Casamicciola) fracture systems (Capaldi et al., 1976) (Fig.1.32).

Other evidences of the fault systems are recognizable in the southeastern area of the island, where the lava domes of Campagnano, Monte Vezzi and Punta della Signora (dated between 150 ka and 55 ka B.P.) are cut by a NE-SW extending fault. In the southwestern sector of the island the presence of a depressed area extending between S.Angelo and Citara is related to a NW-SE extending fault (Fig.1.32).

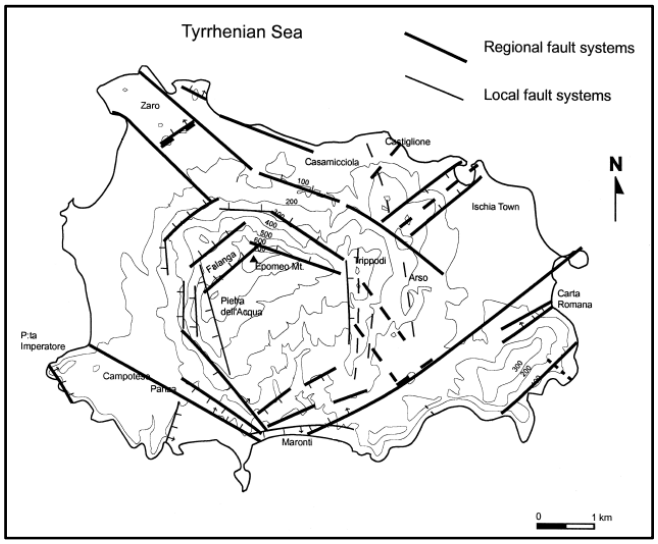

Fig.1.33 *- Structural map of Ischia island: continue lines=faults; dashed lines=volcano-tectonic alignments (modified after Acocella and Funiciello, 1999).*

Ischia is characterized by strong heat flow and hydrothermal manifestations (Penta, 1954). Some drillings have been executed by Penta and Conforto (1951) in the western (Citara area) and in the southern (Maronti area) sectors of the island (Fig.1.32) which allowed to reconstruct the thermal state and to obtain important stratigraphic information of the investigated areas (Fig.1.34B).

The highest temperature (about 230° C) was measured at 1,135 m of depth in a deep well (I6) at Maronti, in the southwestern side of the island (Fig.1.34A-B). Data from shallow wells located on the western side of the island (Penta and Conforto, 1951) suggested that the hydrothermal circulation concentrates in the highly fractured lavas underlying the Green Tuff.

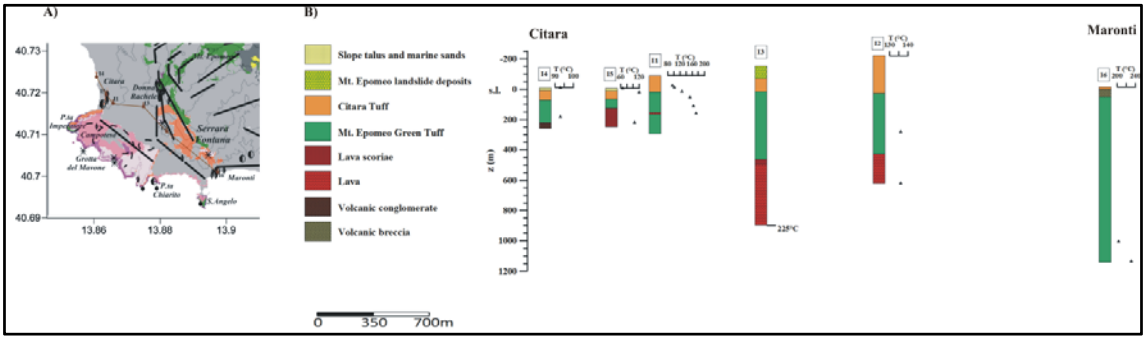

Fig.1.34 *– NW-SE profile from Citara to Maronti areas (soutwestern sector of Ischia) through the geothermal wells carried out by Penta and Conforto (1951) (A); stratigraphic columns and temperature data in the wells (B).*

Geochemical analyses of fumaroles on the western side of Mt. Epomeo (Donna Rachele area) (Fig.1.32) let to hypothesize two distinct hydrothermal aquifers at ~400 m and ~900 m with temperatures of ~250° C and ~300° C (Chiodini et al., 2004). The analysis of

chemical and isotopic composition of 120 groundwater samples suggested that the composition of surface manifestations reflect contributions from meteoric water, sea water and thermal fluids rising from two distinct hydrothermal reservoir, with equilibrium temperatures of respectively ~150° C and ~270° C, and depths of 150-300 m and >300 m (but possibly >1,000 m) (Di Napoli et al., 2009).

Due to the presence of several fractures and faults, which are the major pathways for hot fluids, and to argillification phenomena connected to the hydrothermal alteration of these fluids in presence of volcanic materials, it is very probable that the geothermal structure of the island consists of a number of subsystems (Chiodini et al., 2004; Di Napoli et al., 2009).

The island of Ischia is also affected by seismic hazard mainly concentrated in the northern sector. Historical accounts and scientific documents on Ischia earthquakes are completely lacking before the 17th century with the only exceptions of summary reports on the 1228 A.D. (Buchner, 1986) and 1557 A.D. (Rittmann, 1930) events. Critical catalogues of Ischia seismicity since 1622 A.D. were presented by Mercalli (1884), Rittmann (1930) and Boschi et al. (2000). The effects of an earthquake dated at the second century A.D. were detected in the necropolis of Pithekusa, in the southwestern sector of the island (Buchner, 1986).

Some information about the epicentral area and the maximum intensity relative to the most important earthquakes occurred at Ischia are reported by Karnik (1969) (Tab.1.1). The data show that the epicenters of these events are located in the northern part of the island concentrating in the town of Casamicciola. The most important seismic events occurred in 1881 and 1883. The last one is known as the most destructive event occurred at Ischia since it destroyed the upper part of the town of Casamicciola, caused many damages also at Lacco Ameno and Forio and triggered several landslides in the northwestern slopes of Mt. Epomeo (de Vita et al., 2006). This sector of the island was indeed recognized by Rapolla et al. (2010) as characterized by very high susceptibility to earthquake-induced landslides. The earthquake was characterized by I_0=X–XI MCS and estimated magnitude of 5.78 (Carlino et al., 2010 and references therein).

The restricted area of the maximum damage and the close location of historical epicenters, thermal springs and fumaroles suggest a shallow source for these earthquakes (possibly within the hydrothermal system) (Chiodini et al., 2004), which are generally related to a local stress field (i.e., a pressure increase in the magmatic system at shallow depth) and do not seem to correlate directly to the regional tectonics (Carlino et al., 2006).

Carlino et al. (2010 and references therein) suggested a hypocentral depth of 1 km or slightly more for the 1883 A.D. and individuated two possible fault planes trending E-W and NW-SE. The origin of this earthquake has been attributed to resurgence (Alessio et al., 1996).

Year	Epicentral area	Intensity (MCS) at the epicentral area
1228	Casamicciola	IX-X
1302	Eastern sector of the island	VIII
1557	Campagnano	VII-VIII
1762	Casamicciola	VII
1767	Northern sector of the island	VII-VIII
1796	Casamicciola	VIII
1828	Casamicciola	VIII-IX
1841	Casamicciola	VII
1863	Casamicciola	VII
1867	Casamicciola	VI-VII
1881	Casamicciola	IX
1883	Casamicciola	XI

Tab.1.1 *– List of the most significant earthquakes occurred at Ischia since the 13th century as reported by Karnik (1969).*

1.2.2 Volcanic history of Ischia

The volcanic history of Ischia and the petrology of its magmas have been reconstructed by several authors (e.g. Rittmann, 1930; 1948; Forcella et al., 1981; 1983; Gillot et al., 1982; Chiesa et al., 1985; 1987; Poli et al., 1987; Vezzoli, 1988; Civetta et al., 1991b).
Volcanism began prior to 150 ka B.P. and has continued intermittently, with quiescent periods lasting centuries to millennia, until the last eruption in 1302 A.D. (Vezzoli, 1988; Orsi et al., 1996b; de Vita et al., 2010).
The volcanic and deformation history of Ischia is dominated by the caldera-forming Mt. Epomeo Green Tuff eruption occurred about 55 ka B.P. (Vezzoli, 1988) during a period of activity that generated the most voluminous and devastating eruptions of the island (Brown et al., 2008 and references therein). This significant eruption divides the volcanic history of Ischia in two cycles: the first, called Ancient Cycle (>150-75 ka B.P.), is composed of two eruptive phases; the second, known as the Recent Cycle (55 ka B.P.-1302 A.D.), is composed of three eruptive phases.

Ischia volcanic rocks vary in composition from shoshonite to trachyte (D'Antonio et al., 2007); the most abundant rock type is trachyte. The least evolved magmas were erupted during the 28-18 ka period of activity (Grotta di Terra shoshonitic dyke, 28 ka B.P.) and over the past 3 ka (Molara, Vateliero, Cava Nocelle and Arso shoshonitic-latitic tephras).

The latter ones are characterized by petrographic, geochemical and isotopic features suggesting mingling or mixing among differently evolved, small magma batches, and entrapment of crystals inherited from previously erupted magmas (Civetta et al., 1991b; Piochi et al., 1999; D'Antonio et al., 2007; 2013).

The deep structure of the Ischia caldera is poorly constrained. Modeling of magnetic data (Orsi et al., 1999b) points to a large magma body at ~7 km depth, which is either solidified or partially liquid, as the geothermal flux (Della Vedova et al., 2001) suggests a solidus temperature of ~1,000° C at that depth. However, in the absence of seismic data, the role of petrology in assessing the characteristics of the deep magma storage system and magma crystallization depth is of fundamental importance. Eruption of shoshonitic to latitic magmas at the margin of the caldera and of differentiated magmas within it suggests the ascent of weakly differentiated, CO_2-rich magmas of deep origin along regional faults and the occurrence of a shallow magma storage region beneath the caldera, where the magmas evolve to trachyte and phonolite. This is also supported by phenocryst-hosted melt inclusion studies on trachytes and phonolites (Sbrana et al., 2009) which suggest the occurrence of a relatively shallow magma reservoir (~2 km deep) below the caldera in the last few thousands of years, filled by hot (1,000° C) trachytic magma. Gravity and magnetic data point to the occurrence of an intrusive crystalline body, with few and sparse partially molten portions (Paoletti et al., 2009), below the caldera. These data are consistent with petrological and isotopic data, which suggest that the volcanic activity of the last 5 ka was fed by isotopically distinct small magma batches (Civetta et al., 1991b; Piochi et al., 1999; D'Antonio et al., 2007; 2013), which differentiated and mixed prior to extrusion.

Following Brown et al. (2008), the volcanic products belonging to the Ancient Cycle have phonolitic and trachytic composition and consist in pyroclastic deposits with interbedded lavas. In the period 75-50 ka, the island was significantly more active than previously known. In particular, the authors recognized several explosive eruptions, fed by latite through trachyte and phonolite magmas, many of which produced pyroclastic flow deposits that covered entirely Ischia, and the near island of Procida. The authors suggested that the volcanism between 75 and 50 ka was influenced by the existence and dynamics of one or more, wide reservoirs filled by differentiated magma. After the collapse or partial destruction of these magma chambers, the spatial and temporal distribution of the younger than 55 ka volcanism was instead controlled by resurgence (Orsi et al., 1991b).

The three different eruptive phases belonging to the Recent Cycle have been distinguished on the base of radiometric dating (Civetta et al. 1991b), considering the trend of both Sr isotopic composition and trace elements. Each eruptive period was characterized by magmatic fractioning, allowing for compositional variations of the volcanic products.

The first period (55-33 ka B.P.) started with the Mt. Epomeo Green Tuff eruption (~55 ka B.P.), that caused a caldera collapse demolishing an older caldera whose products are dated 130-75 ka B.P. (Vezzoli, 1988; Orsi et al., 1991b; Tibaldi and Vezzoli, 1998). This eruption, fed by trachytic to phonolitic magma, emplaced an ignimbrite that covers much of the older deposits (Vezzoli, 1988) on the island, and whose finer products were dispersed over a large area in the Mediterranean Sea (Wulf et al., 2004). The ignimbrite deposited both offshore (in an area actually located in the central sector of the island) and now exposed onshore at the Epomeo (Fig.1.32). The subaerial volcanic products of the Epomeo Green Tuffs crop out at Monte Vico, S.Angelo and along the Scarrupata di Barano. The eruption led also to the emplacement of marine terrigenous formations in the central part of the island (Barra et al., 1992a) (Fig.1.32). Vezzoli (1988), Orsi et al. (1991b) and Tibaldi and Vezzoli (1998) hypothesized that the Green Tuff eruption caldera was characterized by an elliptical shape, with an E-W main axis and approximate dimensions of 10 by 7 km. The volcanic activity of this first period proceeded up to 33 ka with several explosive eruptions. The corresponding volcanites crop out both along the coastal cliffs of S.Angelo and Punta Imperatore (southwestern sector) and at Citara (western sector) and Monte Vico (northwestern sector) (Fig.1.32). One of the most important events is the Citara Tuff eruption occurred off the western coast between 44 and 33 ka B.P.

The volcanic activity following the Green Tuff eruption has been influenced by complex geological processes of calderic resurgence that started about 30 ka ago. The uplift, related to this last event, has been evaluated in the order of 800-1,100 m (Barra et al., 1992a, b).

The second period (28-18 ka B.P.) (Civetta et al. 1991b) started with the eruption of the Grotta di Terra volcanic centre (28 ka B.P.), whose products, fed by trachybasaltic magmas, are exposed along the southeastern coasts of the island (Fig.1.32). The volcanic activity persisted up to 18 ka B.P. and the corresponding products crop out at Grotta del Mavone, Monte di Vezzi, Sant'Anna, Carta Romana and between Punta Imperatore and S.Angelo (Vezzoli, 1988) (Fig.1.32).

The third period started about 10 ka B.P. (Civetta et al., 1991b) and concluded with the so-called Arso lava flow (1302 A.D.) (Vezzoli, 1988). The activity was also explosive and included the formation of lava domes, and the generation of tuff rings and pyroclastic fall

deposits. Many eruptive centres were active in the Ischia graben, the depression located in the central-eastern sector of Ischia (Orsi et al., 1994). The Zaro lava flow (in the northwestern sector) and the pyroclastic deposits cropping out at Punta del Chiarito (in the southwestern sector) (Vezzoli, 1988) belong to this period of activity (Fig.1.32).

The last eruption occurred in February 1302, when a crater opened in the central-eastern area: a large lava flow was emplaced (Arso lava flow) reaching the beach between the Ischia harbour and Ischia Ponte and destroying the ancient town of Geronda (Aiello et al., 2012) (Fig.1.32).

1.2.3 Resurgence and dynamics at Ischia

The most recent volcanic activity, as well as the high volcanic, seismic and landslide hazards at Ischia are closely connected with the uplift of Mt. Epomeo block , ~4×5 km wide (de Vita et al., 2006; Vezzoli et al., 2009). The amount of total uplift has been estimated to be between 800 and 1,100 m (Rittman and Gottini, 1980; Gillot et al., 1982; Orsi et al., 1991b; Barra et al., 1992a). The southern sector of the island has been uplifted by 710 m, while the northern sector by 920-970 m (Tibaldi and Vezzoli, 2004). Resurgence started likely not later than 33 ka B.P., as rocks of this age are deformed by the uplift, and proceeded with alternated phases of uplift and subsidence until historical times (Gillot et al., 1982; Orsi et al., 1991b; Barra et al., 1992a; Buchner et al., 1996; Tibaldi and Vezzoli, 1998). Thus, the uplift rate has been estimated to be of 2.3-3.3 cm/y (Tibaldi and Vezzoli, 2004; Carlino et al., 2006; Vezzoli et al., 2009). The resurgence took place inside the younger caldera and was accompanied by seismic activity (Vezzoli et al., 2009). The increase in the Mt. Epomeo slope steepness, related to uplift and seismic activity, is considered the major cause of slope instability on the island (de Vita et al., 2006; Tinti et al., 2011).

At present a subsidence of Mt. Epomeo is observed through the analysis of leveling data collected from 1990 to 2003 (Sepe et al., 2007). The data relative to the vertical deformation component (Manzo et al., 2006) show that the present-day subsidence of Ischia mainly develops in areas characterized by active landsliding and along faults, such as the southern slope of Mt. Epomeo and the northwestern sector of the island. As regards the data relative to the horizontal displacement component (Manzo et al., 2006), they suggest a deflation (contraction) of the island located between the western sector and the N-S striking faults that bound the eastern sector of Mt. Epomeo, along which recent (<30

ka) volcanism developed. This deflation might be related to a de-pressurization of the island hydrothermal system (Manzo et al., 2006).

Many models have been proposed to explain the Mt. Epomeo resurgence at Ischia that can be grouped in: *i)* models involving a simple-shear mechanism or a trapdoor uplift with a hinge in the southeastern area of the island, in which the thrust is an increase in pressure in the upper part of a shallow reservoir due to input of fresh magma (Civetta et al., 1991b; Orsi et al., 1991b; Acocella and Funiciello, 1999; Acocella et al., 2001; Molin et al., 2003). The resurgent block underwent an asymmetrical uplift along high-angle, inland-dipping reverse faults, which was followed by an adjustment along normal faults (Fig.1.35); *ii)* models involving the existence of a resurgent dome, resulting from growth of a laccolith by input of fresh magma, and originating a volcano-tectonic horst, symmetrically uplifted along outward-dipping normal faults and with minor reverse faults (Rittman and Gottini, 1980; Tibaldi and Vezzoli, 1998; Carlino et al., 2006 and references therein; Sbrana et al., 2009; Carlino, 2012) (Fig.1.36).

Both resurgence models assume the arrival of fresh magma at shallow depth, representing the drive for resurgence. Civetta et al. (1991b) suggested that resurgence is associated with the compositionally and isotopically distinct magma that entered the Ischia plumbing system in the period 28 to 18 ka B.P., producing volcanic deposits of less evolved composition with respect to those of previous eruptions. Instead, the differences between resurgent block and dome mainly regard the location of the largest deformation of the block, along its boundaries for resurgent block and at its centre for resurgent dome (Molin et al., 2003).

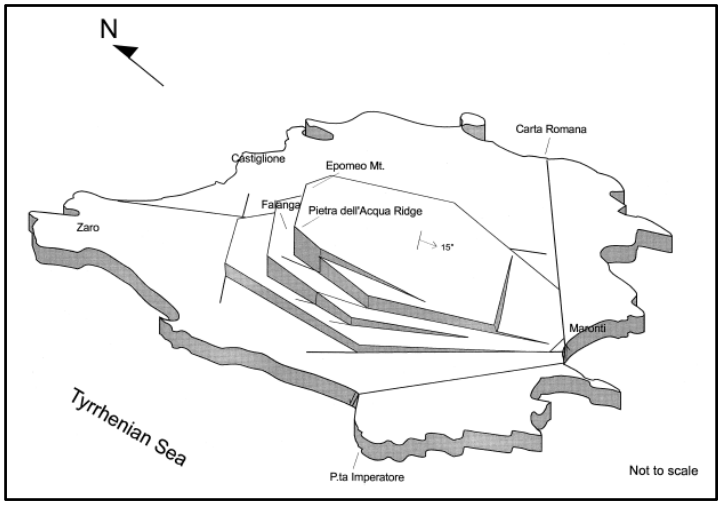

Fig.1.35 *- Sketch models of the resurgent block according to Acocella and Funiciello (1999): the block shows an asymmetrical uplift along reverse faults, with a NE-SW tilt axis (from Acocella and Funiciello, 1999).*

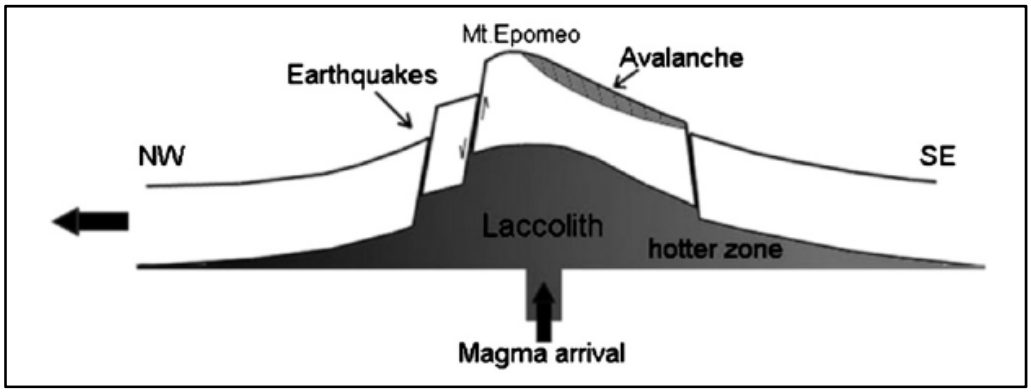

Fig.1.36 *- Sketch model of the resurgent dome (Carlino, 2012): the block is symmetrically bent and uplifted along normal faults and with minor reverse faults (modified after Carlino et al., 2006 and Paoletti et al., 2013).*

According to experiments on analogue models, Acocella et al. (2001) suggested that the ratio *T/D* between the depth *T* of the thrust's source (magma chamber) and the horizontal dimensions *D* of the resurgent block can be used to choose between resurgent block and resurgent dome. When *T/D*≈1, a resurgent block is defined and this block is uniformly tilted and asymmetrically uplifted. The volcanic activity develops along the margins of the block under extension (Fig.1.37a). When *T/D*≈0.4, a resurgent dome is defined and the block is uniformly uplifted and bent. The doming process is usually accompanied by the formation of a depression on the crest of the dome with development of volcanic activity at the dome edges and inside the crestal depression (Fig.1.37b).

The authors favour the resurgent block model and place a spherical magma chamber with a diameter of 5 km, whose top is placed at 4.5 km depth (Acocella and Funiciello, 1999 and references therein).

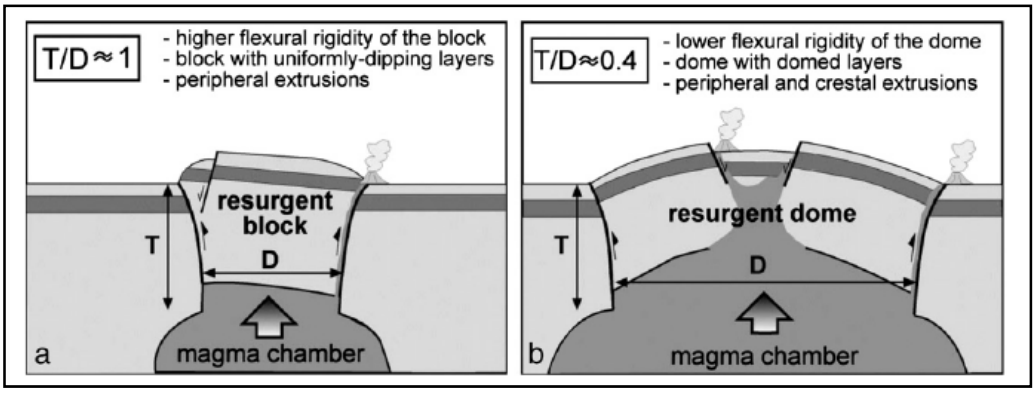

Fig.1.37 *- Possible resurgence mechanisms as function of the ratio (T/D) of the depth T of the thrust source and the width D of the resurgent block (Acocella et al., 2001): a) resurgent block with uniformly-dipping layers and volcanic activity along the borders, when the ratio T/D≈1; b) resurgent dome with domed layers, a crestal depression and volcanic activity at the margins and within the dome, with T/D≈0.4 (from Paoletti et al., 2013).*

A third theory, involving both the dome and block resurgence models, was formulated by Vezzoli et al. (2009). During the 7200-6800 B.C. and 4100-2300 B.C. periods of volcanism, the resurgent dome caused recurrent lateral collapses that removed about 2.5 km^3 of rocks (Tibaldi and Vezzoli, 2004). This sudden removal of material left a non-equilibrium pressure gradient in the uplifted area, causing a hydrostatic rebound of the crustal block and triggering an increase in uplift rate. This mechanism could have possibly changed the resurgence structure from a dome to a fault-bounded block, favoring the intense volcanism of the last 4,000 years.

1.2.4 Structural models of Ischia

Several volcanological, petrological and geophysical studies have been performed in Campi Flegrei, while they are very few regarding Ischia. Deep structures of the island are poorly known as they are restricted to some drilling (Penta and Conforto, 1951) and the interpretation of gravity and magnetic data (Nunziata and Rapolla, 1987; Paoletti et al., 2009). Hence some uncertainties on the main characteristics of the structural setting of Ischia, such as the precise location of the caldera boundaries and the depth of the magma chamber representing the drive for the resurgence, still remain.

The gravity field of Ischia is characterized by very local anomalies which are superimposed on a wider anomaly with positive gradients toward the centre of the island. The most important gravity lows are over the N-S trending Casamicciola-Barano fault, the Campotese and M. di Vezzi formations. A main gravity high exists on the southern flank of the Mt. Epomeo, whereas local gravity highs of small amplitude occur over the Zaro lava flow, Mt. di Vezzi formation, the Castello-Barano fracture line, Cetara formation and the north of the Campotese formation and the Ischia dome (Fig.1.38, see also the localities in Fig.1.32).

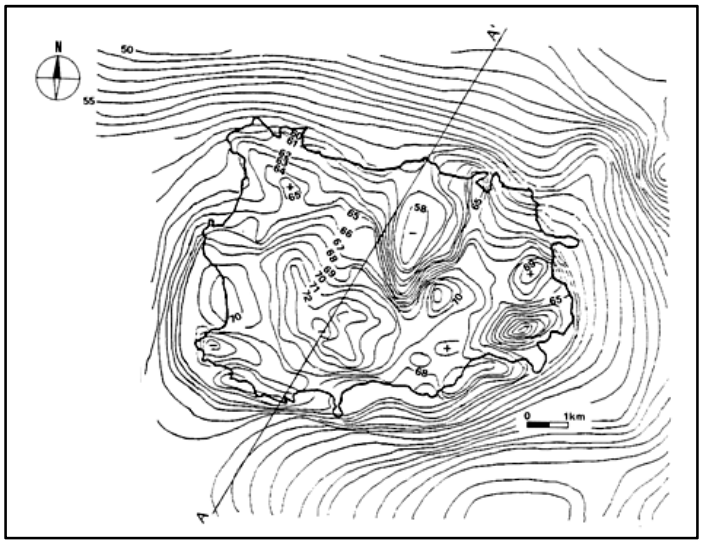

Fig.1.38 *– Map of Bouguer anomalies of Ischia (from Maino and Tribalto, 1971; Barberi et al., 1979). The contour interval is 1 mgal (modified after Nunziata and Rapolla, 1987).*

A 2-D modeling for the interpretation of the gravity anomalies was performed by assigning a density contrast of 0.5 g/cm^3 between the basement material (ρ=2.5 g/cm^3) and the pyroclastic sediments (ρ=2.0 g/cm^3) (Nunziata and Rapolla, 1987). The interpretative model was an elongated ellipsoidal "horst" in the southwestern part of the island at about 1.0 km depth, in the south of the centre of the island and deepening both north and southwards to about 2.0 km, the southern side being steeper (Fig.1.39). By reducing the density contrast to 0.3 g/cm^3 the top of the basement comes up to 0.6 km and viceversa extends down to 1.4 km for a density contrast of 0.7 g/cm^3. The values of 0.3 g/cm^3 and 0.7 g/cm^3 can be considered as the minimum and maximum density contrasts, respectively, that can be assumed on the basis of geo-volcanological available data. This interpretation was in agreement with drilling data which showed trachytic material at a depth of 0.6 km b.s.l. 1 km east of Cetara (I3 well in Fig.1.34) and its disappearance at Maronti, near S. Angelo (I6 well in Fig.1.34). Moreover, the authors concluded that a variable density contrast, in the above mentioned range, should be assumed to take into account also the lateral geological heterogeneities.

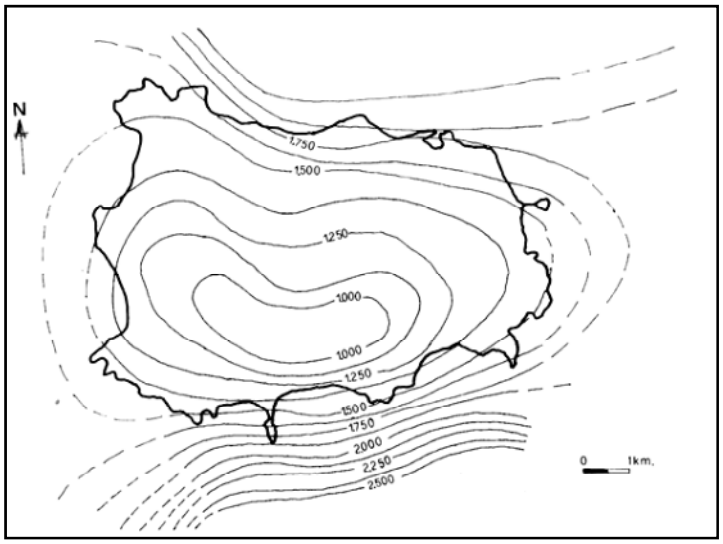

Fig.1.39 *– Basement bathymetry (km) as deduced by the interpretation of gravity data ($\Delta\rho$=0.5 g/cm^3) (from Nunziata and Rapolla, 1987).*

The interpretation of the magnetic map of Ischia was performed by Nunziata and Rapolla (1987) along two approximately N-S profiles, located on the eastern and western parts of the island (Fig.1.40). The magnetic anomaly was fitted by attributing lower susceptibility to the gravity basement in the western side of the island and justified by an anomalous thermal state of the basement.

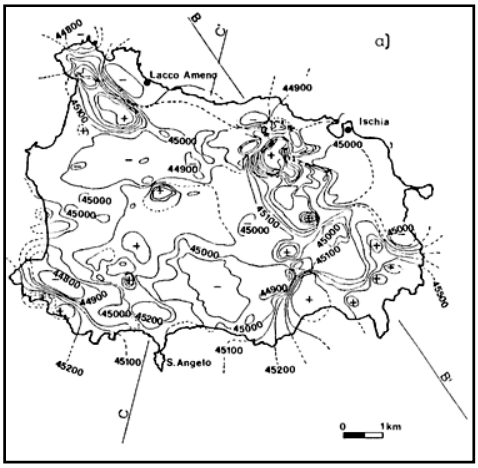

Fig.1.40 *– Magnetic field total intensity map of Ischia (from Nunziata and Rapolla, 1987).*

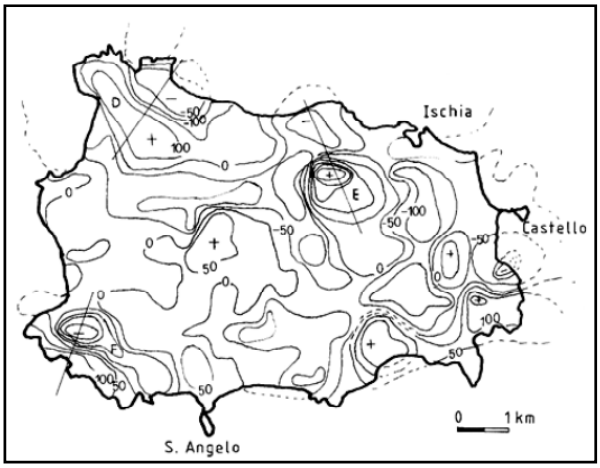

Fig.1.41 *- Short-period component of the magnetic field of Ischia (from Nunziata and Rapolla, 1987).*

The main short-period anomalies (Fig.1.41) are in correspondence of the Zaro lava flow, the Campotese crater and the Mt. Rotaro lava flow (Fig.1.32). These anomalies have been associated to the lava bodies outcropping in these areas (Fig.1.32) characterized by density and susceptibility values higher than those of pyroclastic deposits.

From a joint modeling of gravity and aeromagnetic data, Paoletti et al. (2009) provided a model of Ischia along a SW-NE profile. This model is characterized by an igneous,

probably trachytic, basement with top at about 1,300 m b.s.l., which is demagnetized in the central-western part of the island, below Mt. Epomeo. Such demagnetization was interpreted by the authors as due to hydrothermal alteration phenomena of the igneous materials, related to the high geothermal gradient measured in the wells located in the south-western sector of the island (Penta, 1954; Ippolito and Rapolla, 1982) and/or to the presence of partially molten areas inside the basement.

Chapter 2

METHODOLOGIES

Methodologies used to obtain shear wave velocity models in the studied area are described in this section:

- seismic noise cross-correlation, computed between two receivers, that allowed us to achieve Green's function of the medium between two measurement sites;
- FTAN analysis, by which group velocity dispersion curves of the fundamental mode of Rayleigh surface waves have been extracted;
- Hedgehog non-linear inversion method, by which average group velocity dispersion curves, relative to analysed paths, have been inverted in order to obtain 1-D V_S models vs. depth.

2.1 Seismic noise cross-correlation method

Ambient seismic noise is ground natural and unperceivable oscillation, caused by sea and wind actions and waves scattering generated by medium heterogeneities. Seismic noise is also produced by human activities, but frequencies relative to these sources are too high, so they allow to compute study only at small scale.

Since the beginning of the 20th century, some authors observed a particular noise on seismograms related to microseisms concentrated in 0.1-0.4 Hz frequency range (Peterson, 1993) (Fig.2.1). Lee (1935) and Haubrich et al. (1963) demonstrated that microseisms consist in Rayleigh waves: they analysed particle motion and observed the distinctive retrograde elliptical motion of Rayleigh surface waves.

Frequency content of microseisms show another peak at lower frequencies, i.e. 0.05-0.07 Hz (Fig.2.1): Longuet-Higgins (1950) demonstrated that the interaction of two oceanic waves travelling along opposite directions can generate "double-frequency microseisms": this phenomenon can take place when oceanic waves reflected by coastline collide with those one impacting on the coast (Tanimoto and Artru-Lambin, 2006).

Outwardly signals relative to ambient noise are not coherent, but they could show a residual consistency: if seismic noise is acquired during a time interval long enough to consider the medium scattering a repeatable phenomenon, the recorded signals contain coherent information (Larose et al., 2004).

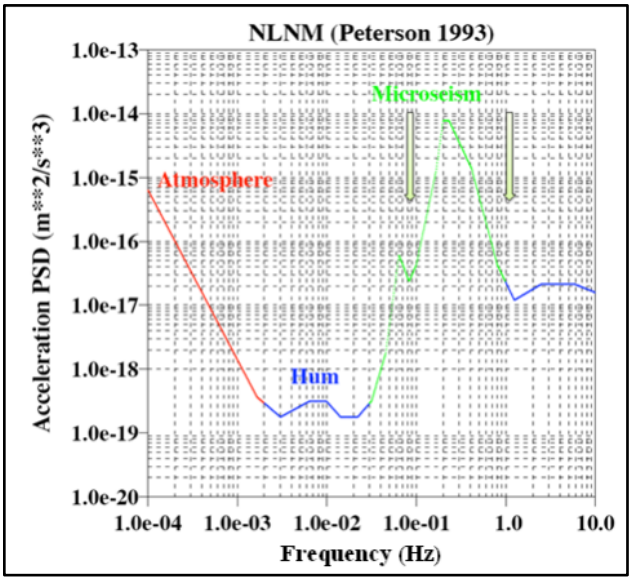

Fig.2.1 *– Power spectral density relative to seismic noise recorded by 75 receivers distributed at global scale (modified after Peterson, 1993). Green arrows indicate frequency range of analysis used in this work.*

So ambient seismic noise can be recorded everywhere by a pair of receivers and it can be cross-correlated in order to enhance coherent information. In presence of a homogeneous distribution of sources around the two receivers (i.e. diffuse wavefield condition), all the possible paths that a seismic ray can travel have been sampled; one of these rays has been recorded by the first receiver and, after a time interval, by the second one (Shapiro and Campillo, 2004). So these two recorded signals can be cross-correlated, in order to obtain Green's function of the medium between the receivers (Fig.2.2).

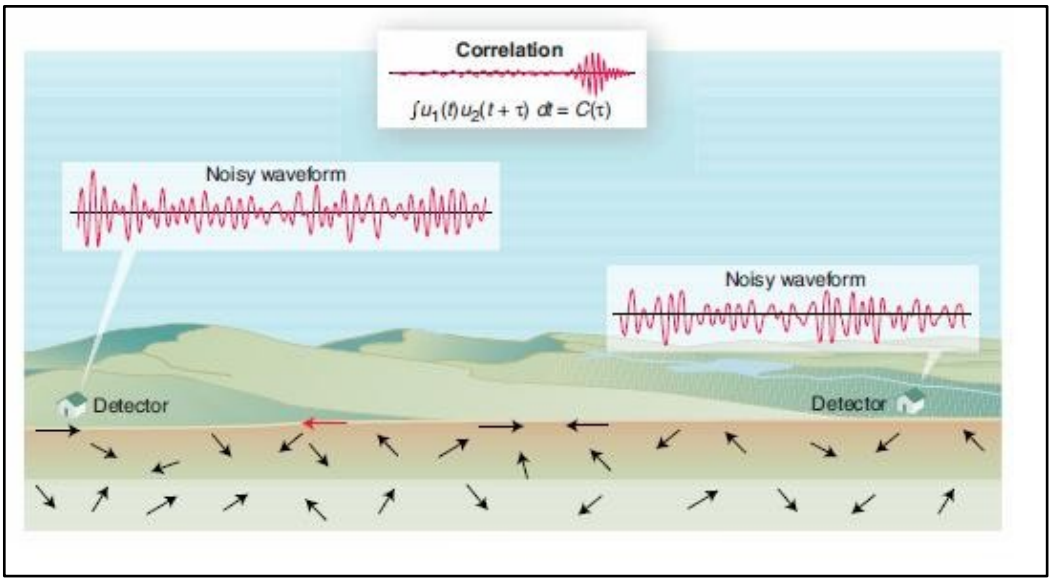

Fig.2.2 *- Representation of a diffuse wavefield and cross-correlation function computed between two stations (from Weaver, 2005).*

The temporal cross-correlation function between the signals received simultaneously in two distinct transducers is shown to be the signal which one transducer would receive when the other is given an impulsive excitation. The correlation displays all travel paths between the two points, including those with multiple reflections (Draeger and Fink, 1995).

Lobkis and Weaver (2001) demonstrated that the cross-correlation function of a diffuse wavefield is related to local transient response.

A diffuse field Φ in a finite body can be expressed in the point x at the time t as:

$$\Phi(x,t) = \Re\sum_{n=1}^{\infty} a_n u_n(x) e^{i\omega_n t}$$

where $\Re$ indicates the real part of a complex quantity, a_n are the complex modal amplitudes, u_n and ω_n are Earth's eigenfunctions and eigenfrequencies. A diffuse field is characterized by modal amplitudes that are uncorrelated random variables:

$$\left\langle a_n a_m^* \right\rangle = \delta_{nm} F(\omega_n)$$

where $F(\omega_n)$ is a function related to spectral energy density.

So cross-correlation of the diffuse field between points x and y is:

$$\left\langle \Phi(x,t)\Phi(y,t+\tau) \right\rangle = \frac{1}{2}\Re\sum_{n=1}^{\infty} F(\omega_n) u_n(x) u_n(y) e^{-i\omega_n \tau}$$

If $F(\omega_n)$ is a constant function, cross-correlation function is similar to time derivative of Green's function (G_{xy}) of the medium:

$$G_{xy}(\tau) = \sum_{n=1}^{\infty} u_n(x) u_n(y) \frac{sen\omega_n \tau}{\omega_n} \qquad \text{(for } \tau>0\text{, otherwise 0)}$$

The cross-correlation function differs from the time derivative of the Green's function by the presence of the factor $F(\omega_n)/2$ which modifies its spectrum and by the presence of a negative part of the function ($\tau<0$).

Ambient seismic noise can be considered as a random and isotropic wavefield both because the distribution of the ambient sources responsible for the noise randomizes when averaged over long times and because of scattering from heterogeneities that occur within the Earth (Nunziata et al., 2009).

By virtue of the time-reversal symmetry of the Green's function (Derode et al., 2003) and in presence of a homogeneous distribution of sources, cross-correlation function should be symmetric. This means that the exact impulse response can be recovered from either the causal ($t>0$) or the anticausal ($t<0$) part of the cross correlation. Instead asymmetry in

amplitude and spectral content is often observed due to a dishomogeneous distribution of sources around receivers (Larose et al., 2004; Bensen et al., 2007). In some case averaging positive and negative parts of noise cross-correlation function results to be a symmetric function. This expedient allows to increase the signal-to-noise ratio and effectively mixes the signals coming from opposite directions, which helps to homogenize the source distribution. If the Green's function is recognized in only one part of the cross-correlation function or if a time shift between positive and negative parts is visible, seismic noise could have a preferential direction. Then it is not possible to design the geometry of the array so that correct wave velocity can be computed. If the possible preferred orientation source is identified and the array is installed parallel to it, the Green's function is obviously seen only in one part of the noise cross-correlation function (Nunziata et al., 2009).

Noise cross-correlation method is very suitable for urban areas, where active seismic experiments are prohibitive. Moreover, it allows to obtain seismic data in those areas where earthquake recordings are rarely available, because of their scarcity and the seismic waves attenuation. Earthquakes registered at local scale let to sample narrow range of period, i.e. maximum 2-3 s; while those registered at regional scale allows to investigate period range that start from 7-10 s. So a gap exists between these two period intervals: noise cross-correlation method could allow to bridge this gap between 4-8 s. This period range is known as ocean microseism: this phenomenon is caused by seawaves pressure variations on the ground, so it's observable at global scale (Romeo and Braun, 2006). Many experiments have been performed both at large and local scale. At global scale we remind, for example the experiments in California and in northwestern Pacific Ocean (Moschetti et al., 2007), in Tibet (Yao et al., 2006), in Europe (Yang et al., 2007) and in New Zealand (Lin et al., 2007). At local scale, experiments have been conducted in the Campanian Plain along a 26 km path. Group velocity dispersion curves extracted from noise cross-correlation successfully matched those ones extracted from earthquake recordings (De Nisco and Nunziata, 2011). Lastly cross-correlation method has been tested at small scale in Napoli, allowing to obtain V_S models as far as 1 km of depth (Nunziata et al., 2012).

Despite this advantage, noise cross-correlation method presents a limit both at global and local scale, as the investigated thickness depends on the receivers distance. In fact, surface waves let to explore at depths equal to about 0.4 maximum sampled wavelength, which is one third of the receiver distance.

In order to compute noise cross-correlation function (NCF) different phases of data processing are recommended (Bensen et al., 2007).

1) The first phase of data processing consists of preparing waveform data from each station individually: removal of the instrument response, de-meaning, de-trending, bandpass filtering the seismogram and time-domain normalization.
2) The second phase consists of NCF computation: daily time-series data relative to the two receivers are cross-correlated using a time window wide enough to sample the Green's function many times. The length of the time-series needed will depend on the group speeds of the waves and the longest interstation distance: in this work time window of 30, 40 and 60 s have been used. So daily cross-correlation functions are stacked in order to increase signal-to-noise ratio.
3) The third phase consists of dispersion measurement: group and/or phase velocity dispersion curve of stacked NCF are extracted.

The most important step in single-station data preparation is the temporal normalization. Time-domain normalization is a procedure for reducing the effect on the cross-correlations of earthquakes, instrumental irregularities and non stationary noise sources near to stations. Bensen et al. (2007) suggest five types of time-domain normalization: the first is the one-bit normalization, which retains only the sign of the raw signal by replacing all positive amplitudes with a 1 and all negative amplitudes with a -1 (Fig.2.3b). The second method involves the application of a clipping threshold equal to the r.m.s. amplitude of the signal for the given day (Fig.2.3c). The third method involves automated event detection and removal in which 30 min of the waveform are set to zero if the amplitude of the waveform is above a critical threshold (Fig.2.3d). The fourth method is running-absolute-mean normalization (Fig.2.3e). Finally, the fifth method is called iterative 'water-level' normalization: any amplitude above a specified multiple of the daily r.m.s. amplitude is down-weighted; the method is run repeatedly until the entire waveform is below the water-level (Fig.2.3f).

Fig.2.4 presents examples of year-long cross-correlations, using each of these methods of time-domain normalization. The raw data (Fig.2.4a), the clipped waveform method (Fig.2.4c), and the automated event detection method (Fig.2.4d) produce noisy cross-correlations. The one-bit normalization (Fig.2.4b), the running-absolute-mean normalization (Fig.2.4e) and the water-level normalization (Fig.2.4f) methods produce relatively high SNR waveforms displaying signals that arrive at nearly the same time. In

this example, the one-bit and the running-absolute-mean normalizations are nearly identical (Bensen et al., 2007).

In this work one-bit normalization has been used.

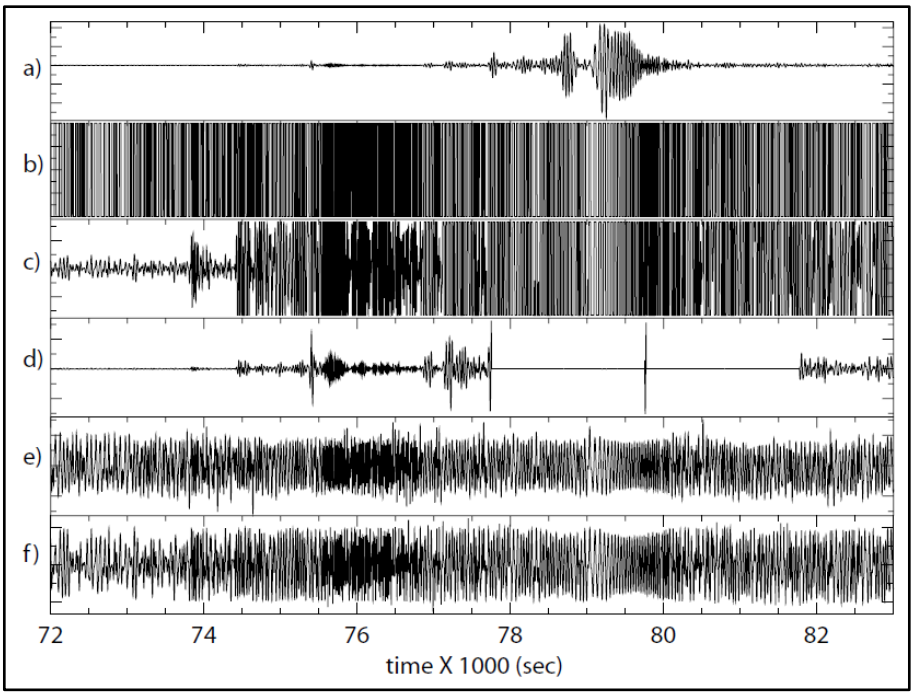

Fig.2.3 *- Waveforms displaying examples of the five types of time-domain normalization (b, c, d, e, f) tested on a signal lasting 3h windowed around a large earthquake (a) (from Bensen et al., 2007).*

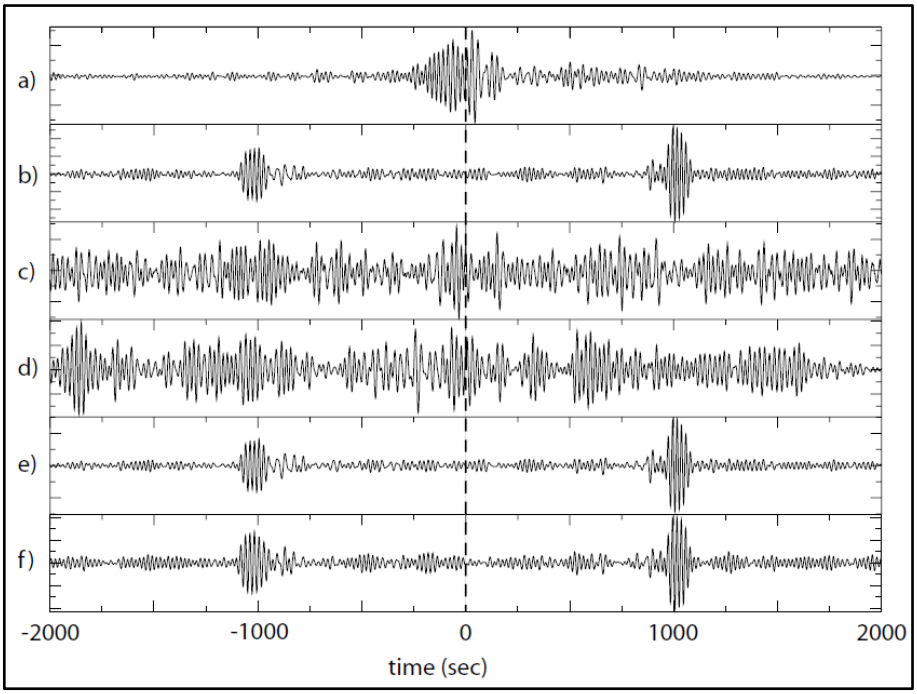

Fig.2.4 *– Cross-correlation functions computed using time-domain normalization methods shown in Fig.2.3 (from Bensen et al., 2007).*

2.2 FTAN method

FTAN (Frequency-Time Analysis) method analyses seismic signals both in frequency and in time domains. It allows to separate different oscillation modes of Rayleigh and Love surface waves, in order to extract group velocity dispersion curves of the fundamental mode. The method represents a significant improvement, due to Levshin et al. (1972; 1992), of the multiple filter analysis originally developed by Dziewonski et al. (1969).

If the source of the event is known, also phase velocity dispersion curves can be extracted. This method can be applied to a single channel as long as the source-receiver distance (r) is greater than source depth (D), that is $r>>D$ (Levshin et al., 1992).

Dispersion is the main peculiarity of surface waves: it means that velocity is dependent on frequency, so in a multi-layered medium the waves that make up the whole signal have different velocity according to medium properties.

The dispersion of surface waves provides an important tool for determining the vertical velocity structure of the crust and upper mantle. Rayleigh waves over a uniform halfspace are non-dispersive. However, horizontal layers with different velocities are usually present or there is a vertical velocity gradient. Rayleigh waves with long wavelengths (low frequencies) penetrate more deeply into the Earth than those with short wavelengths (high frequencies). The speed of Rayleigh surface waves (V_R) is proportional to the shear-wave velocity (V_S) ($V_R=0.92\ V_S$) and in the crust and uppermost mantle V_S generally increases with depth. Thus, the deeper penetrating long wavelengths travel with faster seismic velocities than the short wavelengths. As a result, the Rayleigh waves are dispersive (Fig.2.5). The packet of energy that propagates as surface waves contains a spectrum of wavelengths: the energy in the wave propagates as the envelope of the wave packet at a speed that is called the group velocity; the individual waves that make up the wave packet travel with phase velocity.

The phase velocity $c(\omega)$ and the group velocity $U(\omega)$ are defined as:

$$c(\omega)=\frac{\omega}{k(\omega)} \qquad U(\omega)=\frac{1}{\frac{dk(\omega)}{d\omega}}$$

being $k(\omega)$ wave number. The functions $c(\omega)$ and $U(\omega)$ are named phase and group velocity dispersion curves, respectively, and are related by:

$$\frac{1}{U(\omega)}=\frac{1}{c(\omega)}+\omega\frac{d}{d\omega}\left(\frac{1}{c(\omega)}\right)$$

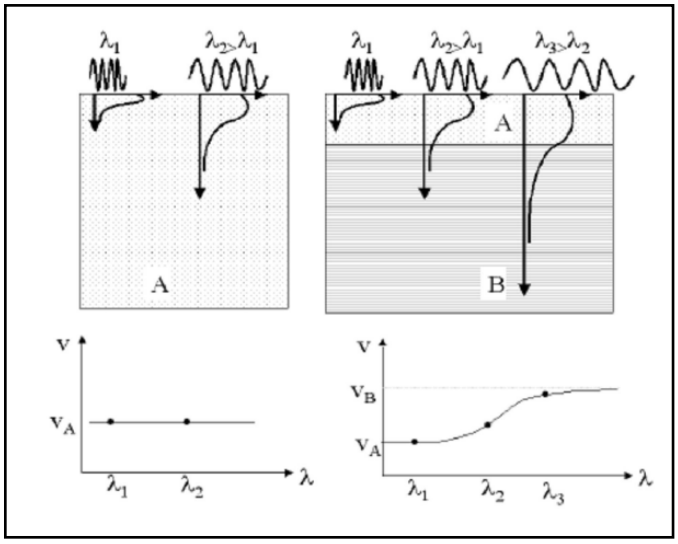

Fig.2.5 *– In a homogeneous medium (on the left) there is no dispersion, so phase velocity is constant; in a layered medium (on the right) phase velocity is dependent on wavelength.*

FTAN analysis is performed on a signal *W(t)* defined as:

$$W(t) = |W(t)|e^{i\Phi(t)}$$

where $|W(t)|$ is the amplitude and $\Phi(t)$ is the phase.

On the seismogram the Rayleigh dispersive waves are identified and Fourier transform, $K(\omega)$, is computed in order to recognize its frequency content:

$$K(\omega) = |K(\omega)|e^{i\psi(\omega)}$$

where $|K(\omega)|$ is the amplitude spectrum and $\psi(\omega)$ is the phase spectrum.

A main characteristic of surface wave signal is the group time $\tau(\omega)$, which is strictly related to the medium properties and it is named spectral dispersion curve of the signal:

$$\tau(\omega) = -\frac{d\psi(\omega)}{d\omega}$$

The phase spectrum of surface waves in a laterally homogeneous medium is:

$$\psi(\omega) = -k(\omega)r + \psi_S(\omega)$$

where $\psi_s(\omega)$ is the source phase.

Then the group time is:

$$\tau(\omega) = -\frac{d\psi(\omega)}{d\omega} = \frac{r}{U(\omega)} - \frac{d\psi_S(\omega)}{d\omega}$$

As the source duration is short relatively to $\tau(\omega)$, the contribution of the source phase can be neglected and the group time equation becomes:

$$\tau(\omega) = \frac{r}{U(\omega)}$$

FTAN analysis consist in passing the dispersed signal through a system of parallel relatively narrow-band filters $H(\omega-\omega^H)$ with varying central frequency ω^H. The choice of the filters $H(\omega-\omega^H)$ for surface waves must satisfy two conditions: no phase distortion (H must be real) and the best resolution. The optimal choice is a Gaussian filter, with central frequency ω^H and width of frequency band β (Fig.2.6):

$$H(\omega)=\frac{1}{\sqrt{2\pi}\beta}e^{-\frac{(\omega-\omega^H)^2}{2\beta^2}}$$

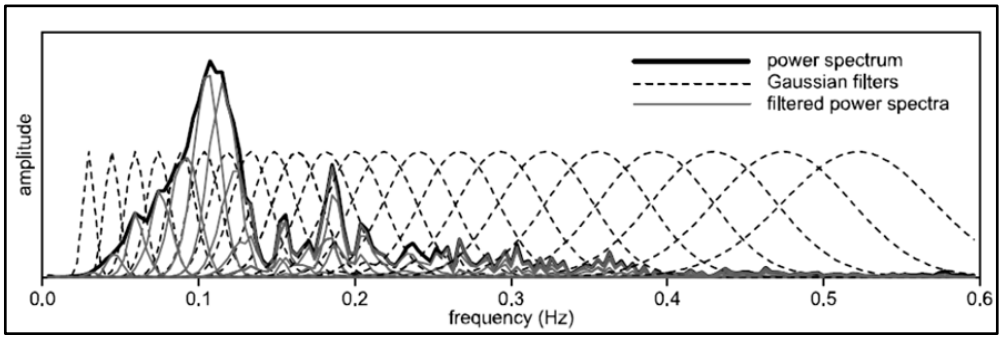

Fig.2.6 *– Representation of Gaussian filters (dashed lines) applied to power spectrum (bold solid line) of a real earthquake; filtered power spectra (gray lines) are also shown. The frequency step is bigger and the filters are broader towards the high frequencies (from Kolinsky, 2004).*

The combination of all so filtered signals is a complex function of two variables, ω^H and t:

$$S(\omega^H,t)=\int_{-\infty}^{+\infty}H(\omega-\omega^H)K(\omega)e^{i\omega t}d\omega$$

The function $S(\omega^H,t)$ is the frequency-time representation of the signal, that is a FTAN map (Levshin et al., 1972; Nunziata, 2005): it represents the signal envelope at the output of the relevant filter. The frequency-time region of a signal is that part of the (ω^H, t) plane occupied by the relevant crest. The mountain ridge in the FTAN map indicates the maximum values of $S(\omega^H,t)$ function at the arrival time $t_m(\omega^H) = \tau(\omega^H)$. Being known the source-receiver distance, the group time $\tau(\omega_i)$ is transformed in group velocity, so the maximum values of $S(\omega^H,t)$ function are shown as function of period (T) and group velocity (U). Following the trend of the mountain ridge, the dispersion curve can be picked (Fig.2.7d). Then the signal is separated from noise: FTAN method uses the linear filtering method, that is a transformation whose parameters are invariant under a time shift (frequency filtering). Such filtering procedure should separate, without distortion as far as possible, the part of the plane in which the signal frequency-time region lies. This operation is called floating point filtering, because the filter band is "floating" along the dispersion curve. As the signal energy is concentrated along the dispersion curve, it is not

significantly distorted, while the noise outside the dispersion curve does not pass through a floating filter. The most important thing in a floating filter is phase equalization. If we approximately know the dispersion curve of a signal from FTAN results, subtracting from the filtered signals the phase makes the signal weakly dispersed and the envelope of the amplitudes is a narrow peak. Such operation has the only effect to alter the initial phase of the resulting signal and shifting it to a convenient instant of time (Fig.2.7c). The recovering of the original signal shape is obtained by applying the inverse procedure of phase equalization, that is by adding the same function to the signal phase spectrum. Lastly, FTAN analysis can be repeated on the resulting signal and, going back to time domain, signal only containing the fundamental mode is obtained (Fig2.7a-e) (Nunziata, 2005).

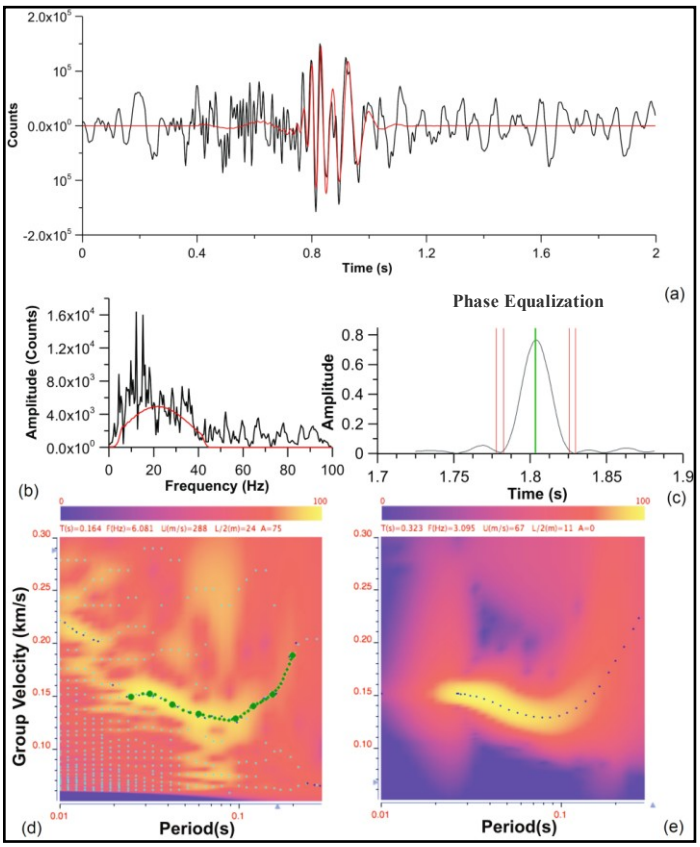

Fig.2.7 *- Example of FTAN analysis on a signal of active experiment at Napoli with 120m offset: (a) the raw waveform (black line); (b) Fourier spectrum amplitude of the signal; (d) a raw group velocity curve (green dots) is chosen by the analyst by picking maxima on the FTAN map. This raw group velocity dispersion curve is back Fourier transformed to get the dispersed signal. Phase-matched (anti-dispersion) filtering is performed on the chosen period-band to remove dispersion. (c) The anti-dispersed signal will collapse into a single narrow spike. Such operation has the only effect to alter the initial phase of the resulting signal, so it can be shifted to a convenient instant of time, for example, to the midpoint of the record. The collapsed waveform is then cut (vertical lines) from the surrounding time-series and re-dispersed to give the clean waveform. (e) The FTAN image of the cleaned waveform is computed and, using the same process applied to the raw waveform, the cleaned group velocity curve (blue dots) and fundamental mode waveform (red line in (a)) are obtained (from Nunziata et al., 2012).*

2.3 Hedgehog non-linear inversion method

Hedgehog non-linear inversion method (Valyus et al., 1968; Panza, 1981) allows to invert group and/or phase velocity dispersion curve of Rayleigh and/or Love surface waves, in order to obtain 1-D models of shear wave velocity vs. depth. This method consists of an optimized Monte Carlo and a trial-and-error methods.

On the basis of geological and geophysical information about the investigated area, a structure is modelled, in the elastic approximation, as a stack of N homogeneous isotropic layers, each one defined by four parameters: shear wave velocity and thickness (independent parameters), compressional wave velocity (dependent parameter) and density (fixed parameter). The value of the fixed parameters is held constant during the inversion according to independent geophysical evidences; the value of the independent parameters is searched during the inversion; the value of the dependent parameter is linked, through a formal relationship, to the independent parameter. The number of independent parameters has to be small in order to interpret more easily the inversion results but not too small because the result, in this case, could be too rough and therefore some interesting features could be missed. Moreover for each independent parameter the region in the model space in which the parameter value is searched have to be specified. The range of variability of the independent parameters is fixed according to the available geophysical information and the parameterization is controlled by the resolving power of the data (Knopoff and Panza, 1977; Panza, 1981; Panza et al., 2007).

Given the error of the experimental group and/or phase velocity data, it is possible to compute the resolution of the parameters, computing partial derivatives of the dispersion curve with respect to the parameters to be inverted (Panza, 1981). The parameterization for the inversion is defined so that the parameter steps are minima, subject to the condition:

$$\sum_j \left(\frac{\partial V(T_i)}{\partial P_i} \right) \partial P_j = \sigma(T_i)$$

where σ is the standard deviation of measurements, V is group or phase velocity, T_i is the ith period and P_j is the jth parameter; in this way, each parameter step represents a satisfactory measure of the uncertainty affecting each parameter (Nunziata, 2010).

The multidimensional region, in the investigated model space, is thus divided into a grid: it is convenient that the knots of the grid are equidistant on the axis of the parameter; the variation step along this axis is related to the resolving power of each parameter. The number of the knots is K^N, where K is the number of the different possible values of each

parameter and N is the number of the parameters. So N hasn't to be too big, otherwise K^N becomes too high.

Monte Carlo method investigates the space of the parameter until a solution $X(P_1, P_2,...,P_j)$ is found; trial-and-error method, instead, analyses neighbouring points $X'=(P_j+ndP_j)$, where $j=1,2,...N$, dP_j is the variation step along the axis of the parameter P_j and is corresponding to the resolving power $\sigma(T_i)$, $n=0,1,2,...,N$ is a positive entire quantity whose upper limit is depending on the range of variability of each parameter. All the neighbouring points at the minimum X are analysed, so Monte Carlo method identifies a new solution $Y(P_1, P_2,...,P_j)$ and trial-and-error method starts again its investigation. The process ends when the whole space of parameters has been explored.

The theoretical group and/or phase velocities, computed during the inversion with normal-mode summation (Panza, 1981) in every knot of the grid, are then compared with the corresponding experimental ones and the models are accepted as solutions if their difference at each period is less than the measurement errors and if the root mean square (r.m.s.) of the differences, at all periods considered, is less than a chosen quantity (usually 60-70% of the average of the measurement errors). All the solutions of the hedgehog inversion differ by no more than ±1 step from each other. A good rule of thumb is that the number of solutions is comparable with the number of the inverted parameters (Nunziata, 2010).

The Hedgehog inversion produces an ensemble of acceptable models consistent with the dispersion data, but, in order to summarize and interpret the results, it is very useful to identify a representative model. There are different approaches: the first one consists in choosing the 'Median Model' of all the solutions (Shapiro and Ritzwoller, 2002) as the representative model; the second approach chooses the model characterized by the minimum r.m.s. The third one considers as a representative solution the one with the r.m.s. closest to the average error computed all over the set of solutions, reducing in this way the projection of possible systematic errors into the structural model (Panza, 1981; Boyadzhiev et al., 2008).

Chapter 3

ANALYSIS OF SEISMIC NOISE CROSS-CORRELATION FUNCTIONS AT CAMPI FLEGREI

3.1 Seismic noise data set

Synchronous recordings of seismic noise at Campi Flegrei have been acquired in order to compute noise cross-correlation functions (NCF) along 52 paths crossing the Phlegraean area (Fig.3.1). Different instruments have been employed during different time periods, so two different data sets can be distinguished:

- seismic noise data acquired during February, March and April 2010 by 11 stations belonging to the seismic network of INGV-OV (Osservatorio Vesuviano) at Campi Flegrei;
- seismic noise data acquired by 2 stations belonging to the Osservatorio Geofisico - sez. Sismologia (www.ogsism.unina.it) of the Dipartimento di Scienze della Terra, dell'Ambiente e delle Risorse (University of Napoli Federico II) located, respectively, on the foundations of the Monumental Complex of SS.Marcellino and Festo (historical centre of Napoli), which is still recording, and in the Archeological Park of Cuma (western sector of Campi Flegrei) operating in January-May 2012.

Seven stations belonging to the seismic network of INGV-OV are equipped with short-period (1Hz) sensors (Mark L4-C or Teledyne Geotech S13): in particular three of them are vertical geophones, while four sensors are three-components geophones. The other four stations are provided with three-components broad-band sensors (Guralp CMG-40T) characterized by a flat frequency response in 0.016-50 Hz range. All the data are digitized with 100 Hz sampling frequency by Kinemetrics K2 stations.

The broad-band stations belonging to the Osservatorio Geofisico are equipped with three-components accelerometers Episensor ES-T FBA (Force Balanced Accelerometer) characterized by a bandwidth DC-200 Hz. Data are digitized with different sampling frequencies (1, 20 and 100 Hz) by Kinemetrics Q330 stations.

Characteristics of each station are listed in Tab.3.1 and their location is shown in Fig.3.1.

Station location	Station name	Latitude	Longitude	Sensor type
INGV-OV stations				
Arco Felice	ARCO	40.84383	14.09333	BB-3C
Astroni crater	ASE	40.8410	14.1592	SP-1C
Bacoli	BAC	40.8097	14.0827	SP-1C
Monte S.Angelo	CMSA	40.8382	14.1818	BB-3C
Solfatara	CSOB	40.8275	14.1443	BB-3C
Pozzuoli	DMP	40.8350	14.1142	SP-3C
Nisida	NIS	40.7968	14.1633	SP-3C
Pozzuoli harbour	POZ	40.8203	14.1205	SP-1C
Quarto	QUAR	40.88565	14.15383	BB-3C
Solfatara	SFT	40.8291	14.1396	SP-3C
Pisciarelli	STH	40.8297	14.1500	SP-3C
OGSISM stations				
Cuma	CUMA	40.84351	14.05718	BB-3C
Napoli	SMN	40.84717	14.25812	BB-3C

Tab.3.1 - *Stations of INGV-OV seismic network and of OGSISM network located in Campi Flegrei. Geographical coordinates and sensor types are given for each station: SP=short period, BB=broad-band; 1C=vertical component, 3C=three components.*

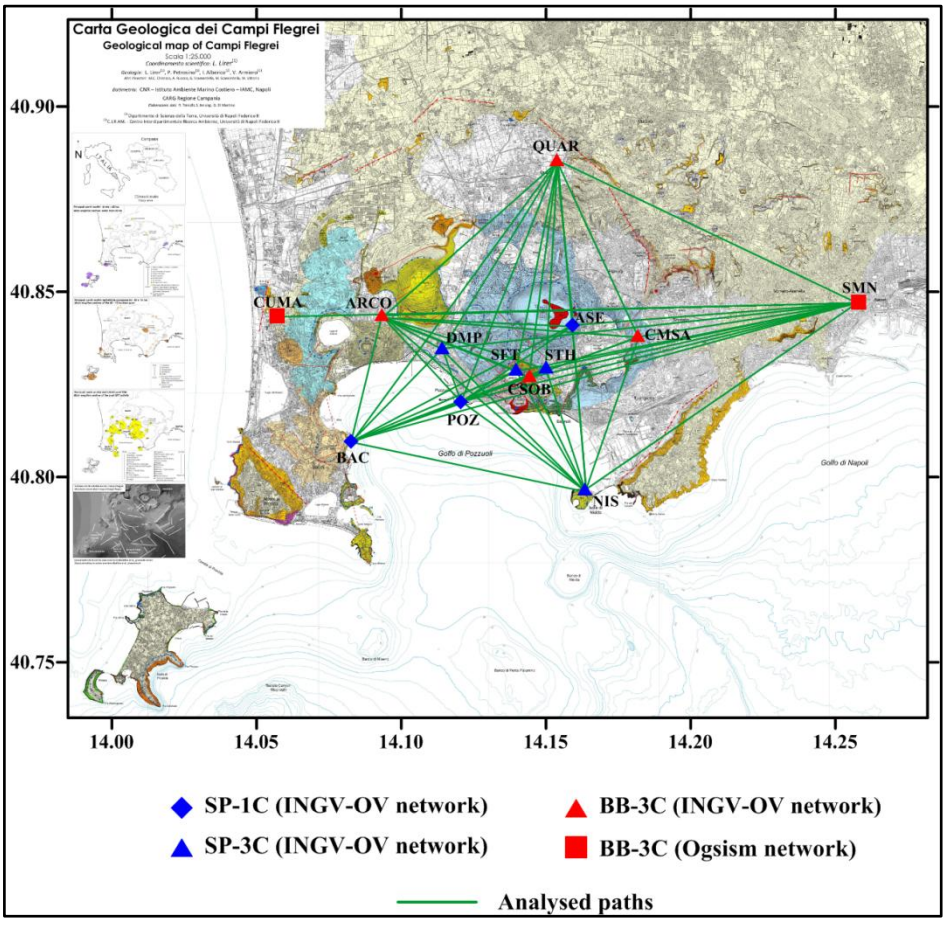

Fig.3.1 – *INGV-OV and OGSISM stations used to compute NCF along the 52 analysed paths crossing Campi Flegrei are located on the geological map of Campi Flegrei (1:25000) (Lirer et al., 2010).*

3.2 Cross-correlation analysis

3.2.1 Preliminary considerations on cross-correlation analysis

Seismic noise cross-correlation analysis is strictly dependent on the knowledge of geological and geophysical setting of the investigated area. In fact stratigraphic and geophysical data can offer important constrains on velocity values expected along the analysed paths. Fundamental considerations must be done before computing noise cross-correlation functions and regard the maximum investigated depth and period. By assuming that the maximum sampled wavelength (λ_{max}) is one third of the receiver distance (Δ) (Bensen et al., 2007; De Nisco and Nunziata, 2011) and that the maximum investigated thickness is equal to about 0.4 maximum wavelength (as explained before in 2.1 section), the maximum investigated depth is 2 km at best. Geological and geophysical models of the upper crust (about 2 km) of Campi Flegrei (see 1.1.1 and 1.1.5 sections) suggest the presence of pyroclastic materials, tuffs (from highly fractured and altered facies to compact facies), tuffites and hydrotermalized lavas. Moreover, measurements of shear wave velocities in the urban area of Napoli (Fig.3.2) allow to attribute average V_S of 0.45 km/s to incoherent pyroclastic materials, of 0.6 km/s to fractured tuffs, of 0.8 km/s to compact tuff (Nunziata et al., 2004). As regards depths greater than 0.5 km average V_S of 1.5 km/s can be attributed to tuffs and tuffites up to depths of 1.3 km and of 2.5 km/s to tuffs, tuffites and lavas (Nunziata et al., 2012). If an average phase velocity (c) varying from 0.4 to 2.2 km/s is assumed, a minimum sampled frequency (v) of ~0.2 Hz ($c=\lambda v$) can be estimated. So cross-correlation analysis has been focused in frequency ranges that start from 0.2 Hz, since lower frequencies haven't been sampled and are not consistent with this study scale. Obviously this value could represent the minimum frequency competent to the longest paths crossing the investigated area, while higher frequencies have been sampled along the shorter paths (Tab.3.2).

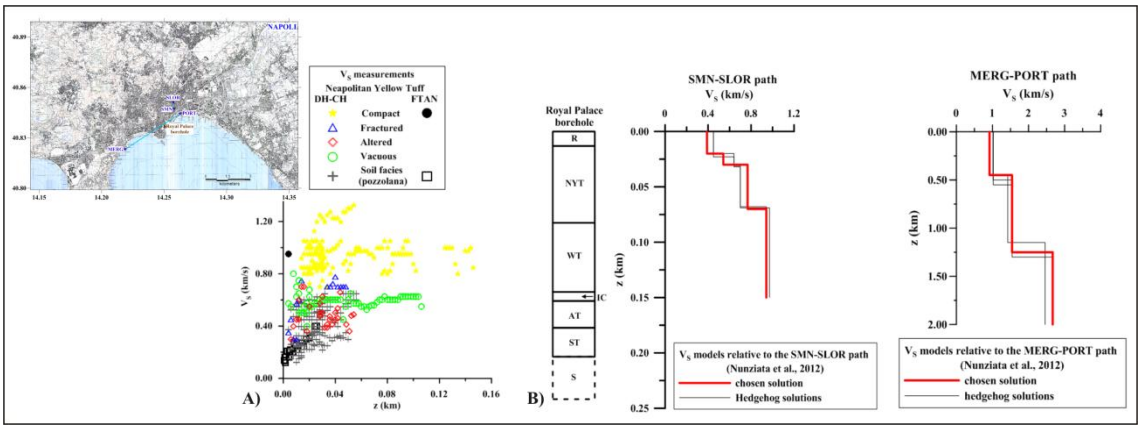

Fig.3.2 *- V_S velocities of Neapolitan Yellow Tuff, both soil and lithoid facies (A) (modified after Nunziata et al., 2004); V_S models (red lines) chosen for the SMN-SLOR and MERG-PORT paths (located in the map) compared with the stratigraphy of the deep Royal Palace borehole (Perrotta et al., 2006) (located in the map) (B) (modified after Nunziata et al., 2012).*
Legend: R=man made ground material and recent pyroclastic deposits; NYT=Neapolitan Yellow Tuff; WT=Whitish tuff; IC= Campanian Ignimbrite; AT= Ancient Tuffs; ST= tuffs and sedimentary rocks; S= sedimentary rocks.

3.2.2 Pre-processing of single-station data

Noise seismic data have been analysed by SAC (Seismic Analysis Code) (Goldstein et al., 2003) software. Seismic data recorded by INGV-OV stations consist of 24 hours signals. These data have been decimated from 100 to 20 Hz, mean removed, high-pass filtered with a Butterworth filter with 0.05 Hz corner frequency and, finally, tapered with a Hanning window. Moreover the instrument response has been removed from signals acquired by short-period (1 Hz) sensors.

Unfortunately signals recorded by INGV-OV stations were contaminated by low frequency spikes, probably due to data transmission. Such contamination mostly affected recordings by short-period sensors. In order to overcome this problem, signals have been furtherly high-pass filtered with corner frequency ≥0.3 Hz. This operation obviously affected the frequency ranges of analysis and, consequently, of the computed cross-correlations (Tab.3.2).

Data acquired by OGSISM stations, digitized with 20 Hz sampling frequency, are archived as a continuous signal in mseed format, so I had to divide the recording in daily portions and convert them from mseed to sac format. De-meaning, de-trending and 0.05 Hz high-pass filtering have been applied (as for signals acquired by INGV-OV stations). Data have been integrated in order to convert acceleration data in velocity data, and high-pass filtered (> 0.05 Hz).

Signals relative to N-S and E-W components have been rotated in order to obtain the radial (R) and the transverse (T) components of ground motion along each path. In particular one of the components is aligned with the back-azimuth of the source-receiver vector (radial component) while the other component is orthogonal to this direction (transverse component).

Then, a one-bit normalization has been applied to all the signals in order to increase the signal-to-noise ratio.

3.2.3 Cross-correlation functions

Noise cross-correlation functions are computed between the synchronous seismic signals acquired by two stations of which one is the master, i.e. it is considered as coincident with the source of the sampled wavefield, while the other one is considered as the slave, that is the receiver station.

At Campi Flegrei, NCFs have been computed using ARCO, BAC, NIS, POZ and QUAR stations as masters. Moreover each of the 11 stations has been used as master with respect to SMN station. Seismic noise data recorded from February to April 2010 have been used, but for the path CUMA-SMN noise recordings were performed from January to May 2012. In this way 52 paths have been defined (Tab.3.2 and Fig.3.1), of which the CMSA-SMN and QUAR-SMN paths have been previously analysed by Costanzo (2011).

ARCO, BAC, NIS, and QUAR stations are located on the edges of the NYT caldera, while their correlations with SMN station allow to investigate greater depths. For this reason a station was installed at Cuma, being the CUMA-SMN distance the greatest possible to study Campi Flegrei area in E-W direction (Tab.3.2 and Fig.3.1).

Daily stacked noise cross-correlation functions have been computed by using time windows of 30, 40 and 60 s depending on the receiver distance (Tab.3.2). The NCF is composed of the causal ($t>0$) and the anticausal ($t<0$) part: the former represents the wavefield propagating from master to slave station, the latter is relative to the wavefield propagating in the opposite direction (see section 2.1 for more details).

In order to identify the frequency content, Fourier spectra of the NCF have been computed after applying a Butterworth high-pass filter with corner frequency of 0.3 Hz (for signals acquired by short-period sensors) and 0.05 Hz (for signals acquired by broad-band sensors). The energy of the NCFs is mainly concentrated in the 0.3-1.5 Hz frequency

range, with minor content till 2 Hz. Hence the analysis has generally been focused in the frequency band 0.3-2 Hz: the used frequency ranges for each path are listed in Tab.3.2.

Daily cross-correlation functions have been stacked to obtain a monthly average NCF. Cross-correlation functions relative to recordings shorter than 24 hours, because of a loss of GPS signal, have been removed from stacking.

In some cases averaging positive and negative parts of NCFs has been very useful to increase signal-to-noise ratio, as symmetric functions resulted (see section 2.1 for more details).

Path	***Receiver distance (km)***	***Acquiring period***	***Frequency range (Hz)***
ARCO-ASE (*)	5.6	February-April 2010	0.4-1 (Z)
ARCO-CMSA (*)	7.5	February-April 2010	0.5-1 (Z, R, T)
ARCO-CSOB (*)	4.7	February-April 2010	0.6-1.5 (Z); 0.5-1 (R,T)
ARCO-DMP (+)	2	February-April 2010	0.7-1.2 (Z, R); 0.9-1.2 (T)
ARCO-QUAR (*)	6.9	February-April 2010	0.4-1 (Z); 0.6-1 (R,T)
ARCO-SFT (+)	4.2	February-April 2010	0.5-1 (Z, R, T)
ARCO-SMN (*)	14	February-April 2010	0.4-1 (Z, R, T)
ARCO-STH (+)	5	February-April 2010	0.4-1 (Z, R, T)
ASE-SMN (*)	8.4	February-April 2010	0.3-1 (Z)
BAC-ARCO (*)	3.9	February-April 2010	February 0.4-1.5 (Z) March 0.5-1.5 (Z) April 0.6-1.5 (Z)
BAC-ASE (*)	7.3	February-April 2010	0.6-2 (Z)
BAC-CMSA (+)	8.9	February-April 2010	February 0.4-1.2 (Z) March 0.5-1.2 (Z) April 0.6-1.2 (Z)
BAC-CSOB (+)	5.6	February-April 2010	February 0.4-1.5 (Z) March 0.5-1.5 (Z) April 0.6-1.5 (Z)
BAC-DMP (+)	3.9	February-April 2010	February, April 0.6-2 (Z) March 0.7-2 (Z)
BAC-NIS (*)	6.9	February-April 2010	February, March 0.5-1.5 (Z) April 0.6-1.5 (Z)
BAC-POZ (*)	3.4	February-April 2010	0.6-1.5 (Z)
BAC-QUAR (-)	10.3	February-April 2010	February 0.4-1.5 (Z) March 0.5-1.5 (Z) April 0.6-1.5 (Z)
BAC-SFT (+)	5.3	February-April 2010	February 0.5-1.5 (Z) March, April 0.8-1.5 (Z)
BAC-SMN (-)	15.4	February-April 2010	0.4-1 (Z)
BAC-STH (+)	6.1	February-April 2010	February, April 0.7-1.5 (Z) March 0.8-1.5 (Z)
CMSA-SMN (*)	6.5	February-April 2010	0.5-1.5 (Z); 0.4-1.5 (R,T)
CSOB-SMN (*)	9.8	February-April 2010	0.5-1 (Z, R, T)
CUMA-SMN (-)	17	January-May 2012	January, March 0.5-1 (Z, R, T) February 0.5-0.9 (Z); 0.5-1 (R,T) April 0.6-1 (Z, R, T) May 0.6-1 (Z, T); 0.5-1 (R)
DMP-SMN (+)	12.2	February-April 2010	0.4-1 (Z, R, T)
NIS-ARCO (*)	7.9	February-April 2010	February 0.5-1.5 (Z); 0.4-1.5 (R, T) March 0.5-1.5 (Z, R, T) April 0.5-1.5 (Z, R, T)
NIS-ASE (*)	4.9	February-April 2010	0.6-1.5 (Z)

NIS-CMSA (*)	4.8	February-April 2010	February 0.5-1.5 (Z); 0.4-1.2 (R, T) March 0.5-1.5 (Z); 0.5-1.2 (R, T) April 0.6-1.5 (Z); 0.5-1.2 (R, T)
NIS-CSOB (+)	3.8	February-April 2010	February 0.5-1.5 (Z); 0.4-1.5 (R, T) March 0.5-1.5 (Z, R, T) April 0.6-1.5 (Z); 0.5-1.5 (R, T)
NIS-DMP (-)	5.9	February-April 2010	February 0.6-1.4 (Z); 0.6-1.2 (R); 0.5-1.2 (T) March 0.7-1.2 (Z, R); 0.6-1.3 (T) April 0.6-1.2 (Z); 0.7-1.2 (R); 0.6-1.5 (T)
NIS-QUAR (*)	9.9	February-April 2010	February 0.5-1.5 (Z); 0.4-1 (R); 0.4-1.5 (T) March 0.5-1.5 (Z, T); 0.5-1 (R) April 0.6-1.5 (Z); 0.5-1 (R); 0.5-1.5 (T)
NIS-SFT (+)	4.1	February-April 2010	0.8-2 (Z, R, T)
NIS-SMN (*)	9.8	February-April 2010	0.5-1 (Z, R, T)
NIS-STH (*)	3.8	February-April 2010	February 0.7-2 (Z); 0.7-1.5 (R, T) March 0.8-2 (Z); 0.8-1.5 (R, T) April 0.7-2 (Z); 0.8-1.5 (R, T)
POZ-ARCO (*)	3.5	February-April 2010	0.6-1.5 (Z)
POZ-ASE (*)	4	February-April 2010	0.6-1.5 (Z)
POZ-CMSA (*)	5.5	February-April 2010	February 0.6-1.5 (Z) March, April 0.7-1.5 (Z)
POZ-CSOB (*)	2.2	February-April 2010	February 0.6-1.5 (Z) March, April 0.7-1.5 (Z)
POZ-DMP (+)	1.7	February-April 2010	2-3 (Z)
POZ-NIS (*)	4.4	February-April 2010	February 0.6-2 (Z) March, April 0.7-2 (Z)
POZ-QUAR (*)	7.8	February-April 2010	February 0.6-1.5 (Z) March, April 0.7-1.5 (Z)
POZ-SFT (+)	1.9	February-April 2010	February 0.6-1.5 (Z) March, April 0.8-1.5 (Z)
POZ-SMN (+)	12	February-April 2010	February 0.3-1 (Z) March, April 0.4-0.9 (Z)
POZ-STH (*)	2.7	February-April 2010	February 0.7-1.5 (Z) March, April 0.8-1.5 (Z)
QUAR-ASE (*)	5	February-April 2010	0.5-1.2 (Z)
QUAR-CMSA (*)	5.8	February-April 2010	February 0.4-1 (Z, R); 0.6-1 (T) March, April 0.4-1 (Z, R,T)
QUAR-CSOB (*)	6.5	February-April 2010	0.4-1 (Z); 0.5-1 (R); 0.6-1 (T)
QUAR-DMP (+)	6.5	February-April 2010	0.5-1 (Z, R, T)
QUAR-SFT (*)	6.4	February-April 2010	February, March 0.4-1 (Z); 0.5-1 (R); 0.6-1 (T) April 0.4-1 (Z); 0.6-1 (R, T)
QUAR-SMN (*)	9.8	February-April 2010	0.5-1.5 (Z, R, T)
QUAR-STH (*)	6.2	February-April 2010	0.5-1 (Z, R, T)
SFT-SMN (*)	10.2	February-April 2010	February, March:0.4-1 (Z, R, T); April:0.5-1(Z, R, T)
STH-SMN (+)	9.3	February-April 2010	0.5-1 (Z, R, T)

Tab.3.2 *– List of the NCF paths at Campi Flegrei, receiver distances and the time recordings (Z=vertical component, R=radial component, T=transverse component). Frequency range of analysis is specified for each month; where month is not specified, the frequency range is the same for all the months.*
(*) indicates that average group velocity dispersion curve has been computed and V_S model has been obtained; (+) indicates that average group velocity dispersion curve has been computed, but it hasn't been inverted because of high error bar; (-) indicates that average group velocity dispersion curve couldn't be computed for lacking of enough dispersion curves (at least 3 dispersion curves) or for a bad signal-to-noise ratio affecting the NCFs.

3.3 Examples of NCFs computed in Campi Flegrei area

Given the high number of investigated paths in Campi Flegrei area, in this section I present and comment some examples of NCFs as representative of the analysis on all the paths. The monthly stacked NCFs computed for the remaining paths and the relative average dispersion curves are shown without discussion.

3.3.1 No reliability of the transverse component of the ground motion

Cross-correlation analysis has been performed on signals relative to vertical, radial and transverse components for those paths identified by pair of stations equipped with three-dimensional sensors (Tab.3.1).

As an example the QUAR-CMSA path, long 5.8 km (Fig.3.1) is presented here. The cross-correlation functions have been computed by considering 40 s time windows, and filtered in 0.4-1 Hz frequency band, but the transverse component of February which has been analysed in 0.6-1 Hz frequency range (Tab.3.2).

Monthly NCFs computed for the three components present different waveforms. All the three monthly vertical and radial NCFs are characterized by the presence of a stable surface wave train arriving at about 5 s on the anticausal part of the functions (Fig.3.3B).

In the hypothesis that the sea action is the main source of the seismic noise acting in the considered frequency range, the vertical and radial NCFs demonstrate that the wavefield has actually a preferential direction from CMSA to QUAR station (Fig.3.1). On the contrary the NCFs of the transverse component are in disagreement with this trend, since they don’t show a stable surface wave train on the anticausal part of the function as expected along this path on the basis of the previous considerations. In fact February NCF shows two distinct wave trains on the negative part of the function, while March and April NCFs present a wave train with higher amplitude on the positive part of the functions (Fig.3.3B).

This behaviour of the transverse component has been often observed: in most cases, NCFs computed for the transverse component presented a low stability and a lower signal-to-noise ratio, and often in disagreement with the radial and vertical components as in the shown best example.

Hence the cross-correlation analysis has been focused only on Rayleigh surface waves.

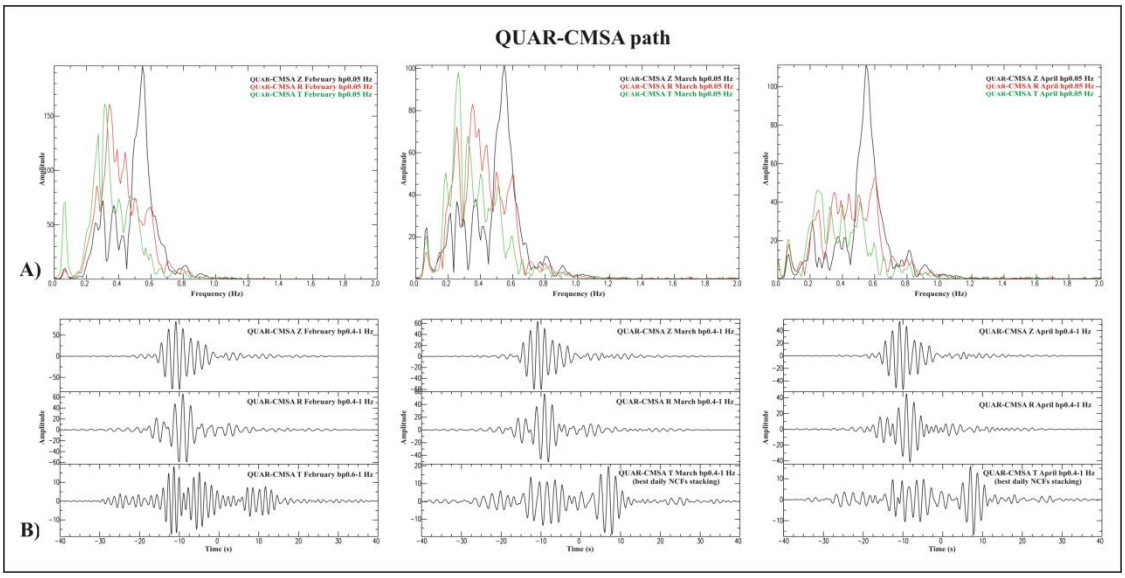

Fig.3.3 *– Fourier spectra (A) of the monthly NCFs (B) (vertical, radial and transverse components) of February, March and April computed for QUAR-CMSA path.*

3.3.2 Stability of NCF

The acquisition of seismic noise for a long time allows to verify the stability and the repeatability of the cross-correlation function. In other words, it's possible to define a minimum time interval necessary to identify a surface wave train stable in waveform and in frequency content according to the receiver distance.

Some monthly stacked cross-correlation functions show daily stability: as an example I show the NCFs relative to POZ-ASE path (4 km), crossing the Solfatara crater (Fig.3.1).

NCFs relative to the vertical component are illustrated since both POZ and ASE stations are equipped with vertical geophone (Tab.3.1). All the daily NCFs, computed in 0.6-1.5 Hz frequency band using 30 s time windows, show a stable evident surface wave train with an arrival time of 4 s on the causal part (Fig.3.4).

Monthly stack of daily NCFs obviously shows the same features for the three months (Fig.3.5). Based on this result, it can be argued that 24 hours are enough for the emergence of a surface wave train along the POZ-ASE path (4 km long).

The presence of a clear and stable surface wave train on the causal part of the NCF functions means that the wavefield has a preferential direction along this path, that is from POZ station (located on the coastline) to ASE station (Fig.3.1). This strengthens the hypothesis that the sea is the main source of seismic noise acting in the frequency range of this experiment (see 2.1 section).

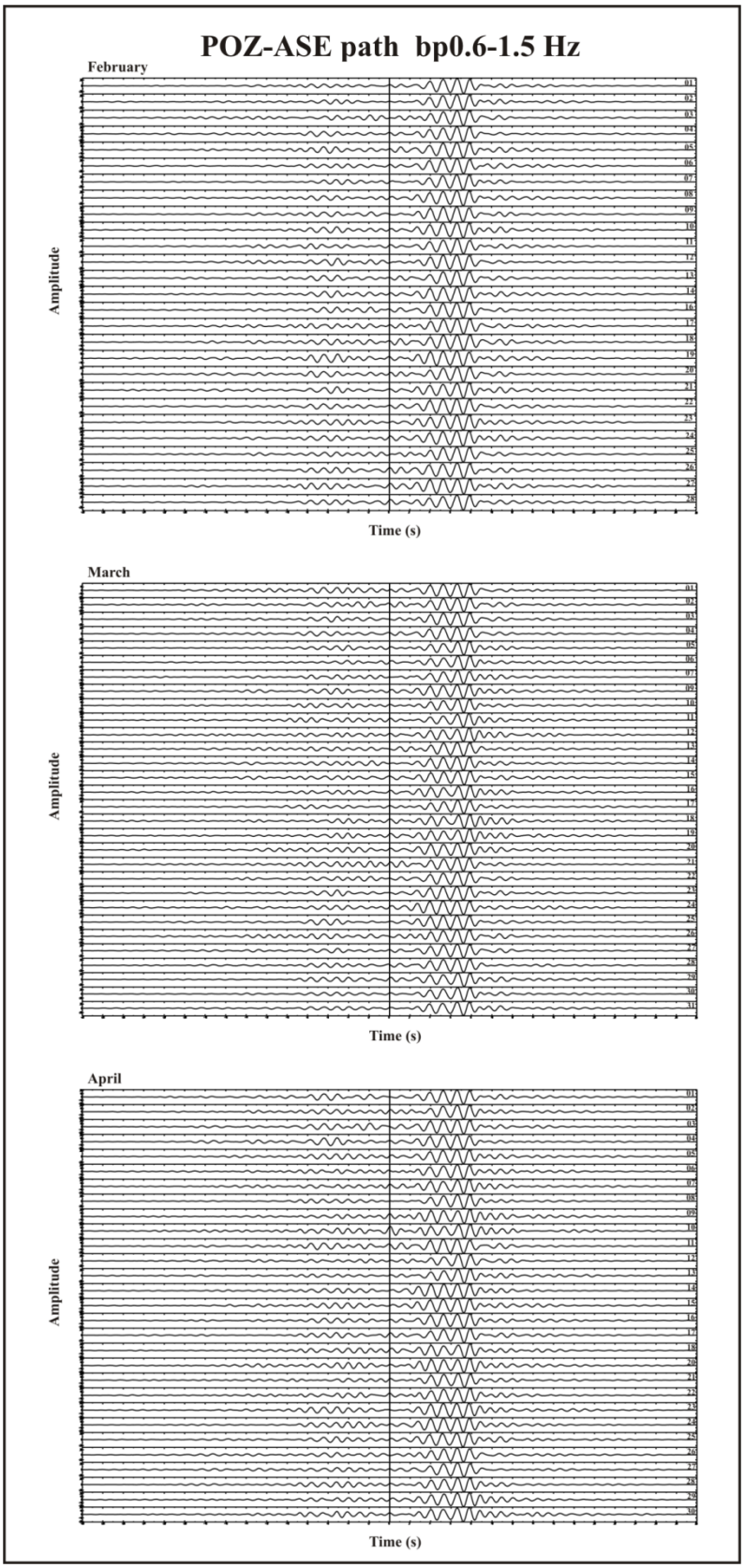

Fig.3.4 *– Daily NCFs (vertical component) of February, March and April computed for POZ-ASE path in 0.6-1.5 Hz frequency range.*

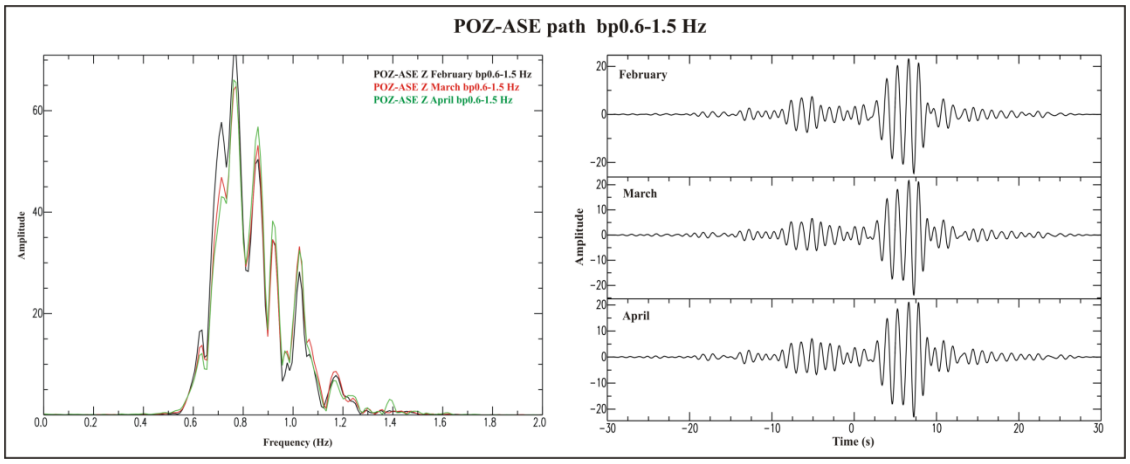

Fig.3.5 *– Fourier spectra (on the left) of the monthly NCFs (on the right) (vertical component) of February, March and April computed for POZ-ASE path in 0.6-1.5 Hz frequency range.*

Then the monthly stacked NCFs have been analysed by FTAN method: maps relative to the three monthly stacked NCFs show clear mountain ridges in 0.8-1.7 s period range and in 0.5-1.2 km/s group velocity range (Fig.3.6A-F-M). The picking of the dispersion curves (Fig.3.6B-G-N) and the maps resulting from the floating point filtering are also shown (Fig.3.6C-H-O) (see 2.2 section for more details). The extracted fundamental mode is superimposed to the original signal: the fitting is very good both in time (Fig.3.6D-I-P) and in frequency domain (Fig.3.6E-L-Q).

Finally the average group velocity dispersion curve, with error bar, has been computed from the February, March and April dispersion curves in 0.85-1.71 s period range and in ~0.46-1 km/s group velocity range (Fig.3.7).

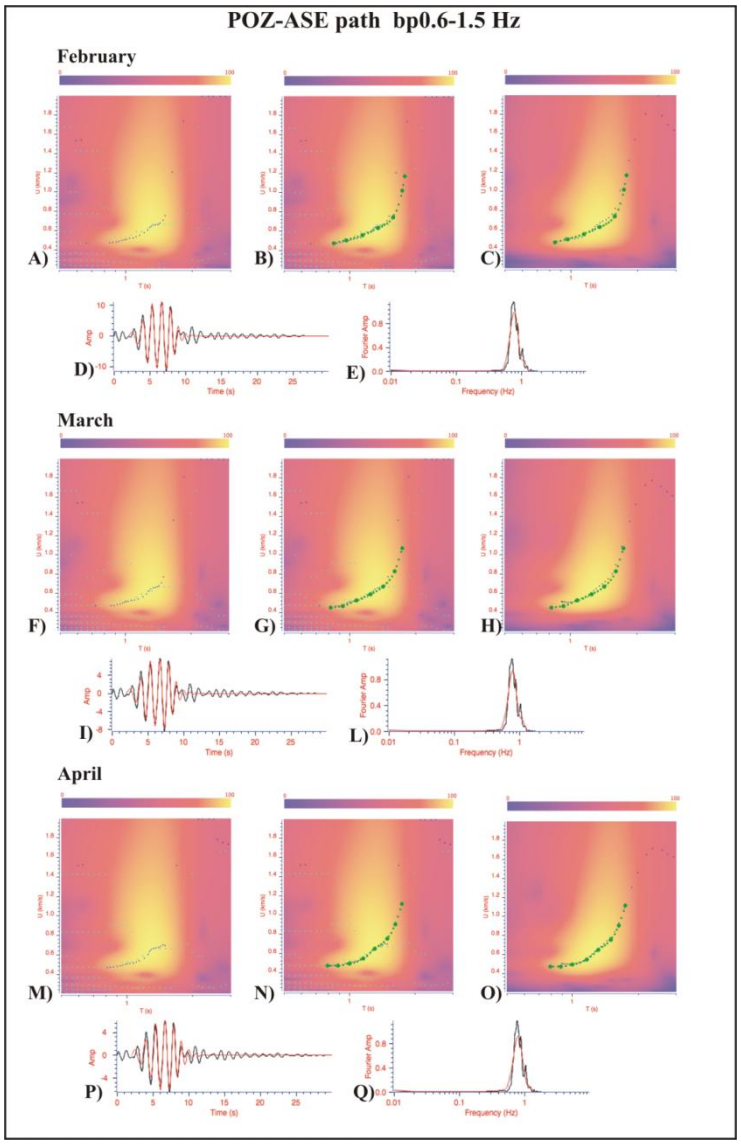

Fig.3.6 *– Steps of the FTAN analysis on the February, March and April monthly stacked NCFs (vertical component) computed for POZ-ASE path in 0.6-1.5 Hz frequency range.*

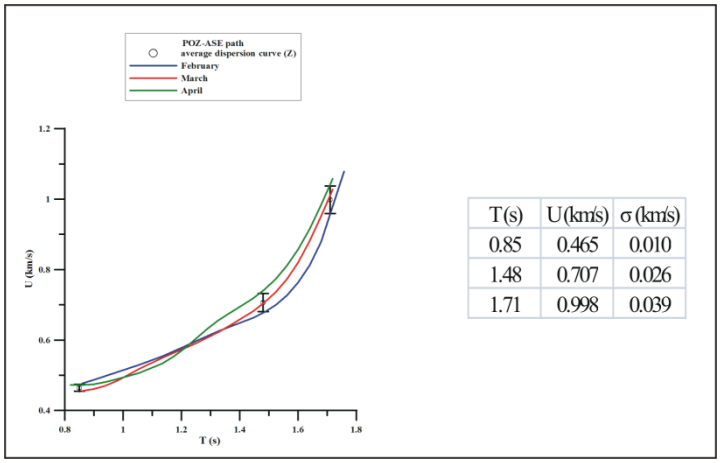

T(s)	U(km/s)	σ (km/s)
0.85	0.465	0.010
1.48	0.707	0.026
1.71	0.998	0.039

Fig.3.7 *– Average group velocity dispersion curve with error bar computed for POZ-ASE path.*

Some other paths did not show the NCF stability observed for the POZ-ASE path. An example is given by the QUAR-STH path (6.2 km) crossing the Astroni vent (Fig.3.1).
The analysis has been conducted in 0.5-1 Hz frequency range using 40 s time windows for the three components. Here NCFs computed for vertical component are shown. The three monthly stacked NCFs are characterized by a quite low signal-to-noise ratio with a wave packet with higher amplitude arriving around 6 s on the anticausal part, but disturbed by a contribution on the zero time and by a wave packet between -20 and -10 s (Fig.3.8). Daily NCFs have been accurately observed: most of them are characterized by a low signal-to-noise ratio, but for few days (5 in February, 3 in March and 3 in April). These few daily NCFs with a high signal-to-noise ratio are predominant in the monthly stacking (Fig.3.8).

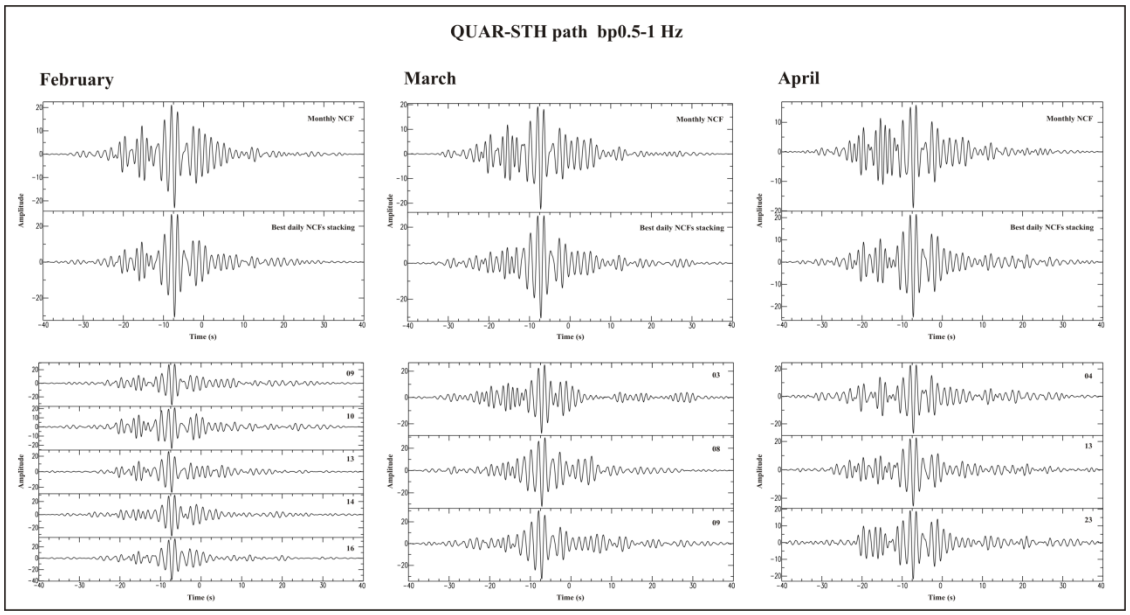

Fig.3.8 *– Monthly NCFs, best daily NCFs stacking and best single-day NCFs (vertical component) of February, March and April computed for QUAR-STH path in 0.5-1 Hz frequency range.*

Extreme cases are represented by those paths along which the wavefield didn't result stable like the BAC-SMN path (15.4 km) (Fig.3.1).
Monthly NCFs of the vertical component (as BAC station is equipped with a vertical geophone) presented a very low signal-to-noise ratio that prevented to distinguish a surface wave train, particularly evident in April (Fig.3.9). The results did not improve by selecting few daily NCFs with a good signal-to-noise ratio. A wave train arriving at ~20 s is visible on February and March stacked NCFs.

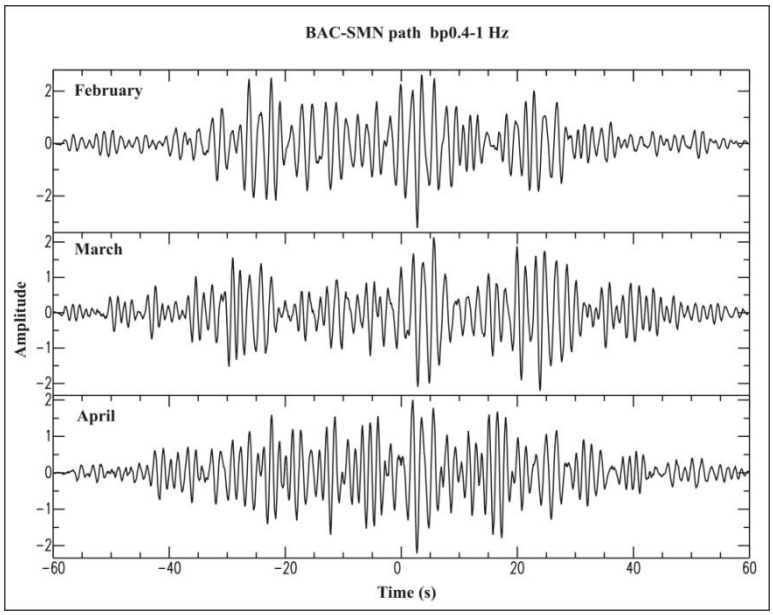

Fig.3.9 *– Monthly NCFs (vertical component) of February, March and April computed for BAC-SMN path in 0.4-1 Hz frequency range.*

FTAN maps of the monthly stacked NCFs have shown different and confused alignment of mountain ridges (Fig.3.10), which didn't allow to extract the fundamental mode.

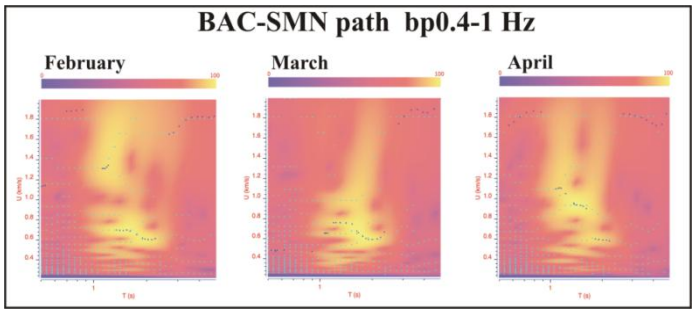

Fig.3.10 *– FTAN maps of February, March and April stacked NCFs (vertical component) computed for BAC-SMN path in 0.4-1 Hz frequency range.*

An explanation of the unsuccessful NCFs along the BAC-SMN path may be the transverse orientation with respect to the coastline or the presence of several, conflicting sources with a resulting destroying interference. Moreover, the BAC-SMN path crosses both offshore and onshore areas, with strong lateral variation in geological setting (see 1.1.1 and 1.1.5 sections).

3.3.3 Symmetric cross-correlation functions

Monthly cross-correlation functions relative to ARCO-ASE path (5.6 km) (Fig.3.1) are shown as an example of symmetric NCF. Being ASE station provided with a vertical

geophone, NCF analysis has been performed only for the vertical component, in the frequency band 0.4-1 Hz using 40 s time windows.

All the three monthly stacked NCFs present an evident surface wave train both on the causal and the anticausal part of NCFs, but surface wave train arrival times are slightly different: ~5 s on the causal part and ~3 s on the anticausal part (Fig.3.11).

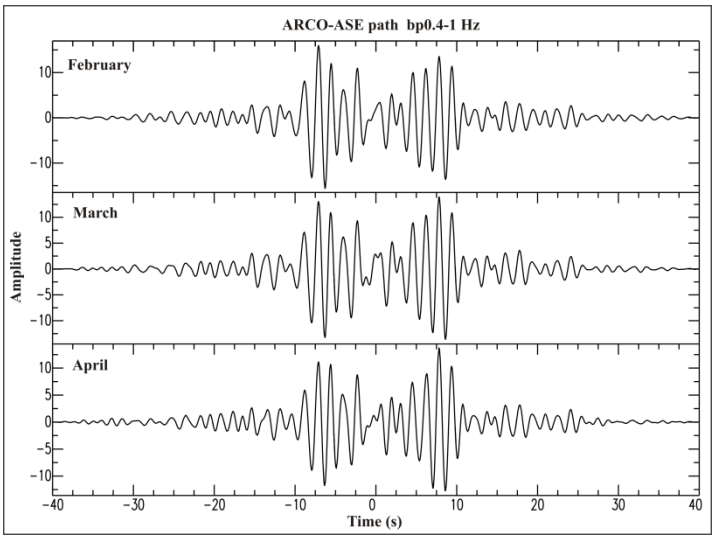

Fig.3.11 *- Monthly NCFs (vertical component) of February, March and April computed for ARCO-ASE path in 0.4-1 Hz frequency range.*

FTAN maps of both the positive and the negative part of all the three NCFs have been considered. They show very different trends, so this is a case of "apparent symmetry of NCFs": maps of the NCFs causal part present a clear trend of mountain ridge in the group velocity range expected for this distance (i.e. ~0.5-1.1 km/s estimated for the wave packet arriving at about 5 s), while maps of the NCFs anticausal part show a descending-trend curve with higher group velocity values (Fig.3.12).

So the monthly group velocity dispersion curves along the ARCO-ASE path have been extracted from the causal portion of the three monthly stacked NCFs.

In Fig.3.13 the steps of the FTAN analysis on the February stacked NCF are shown, being representative of the other two monthly stacked NCFs.

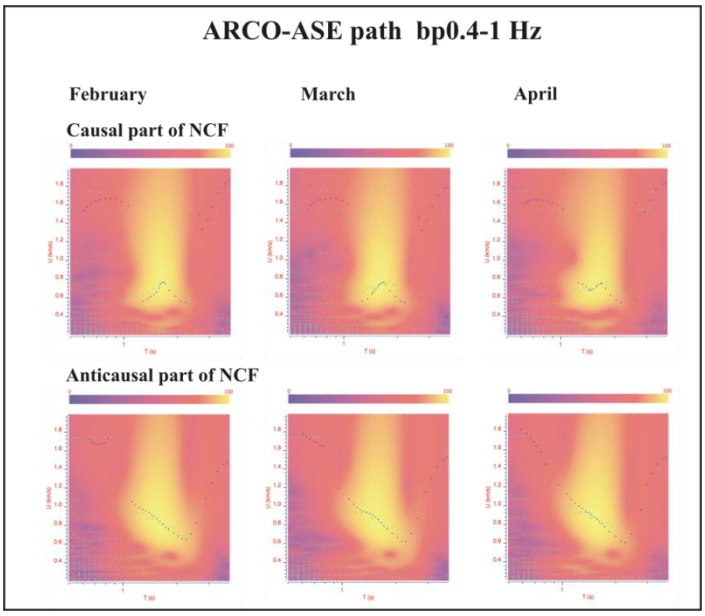

Fig.3.12 *– FTAN maps of causal and anticausal parts of February, March and April monthly stacked NCFs (vertical component) computed for ARCO-ASE path in 0.4-1 Hz frequency range.*

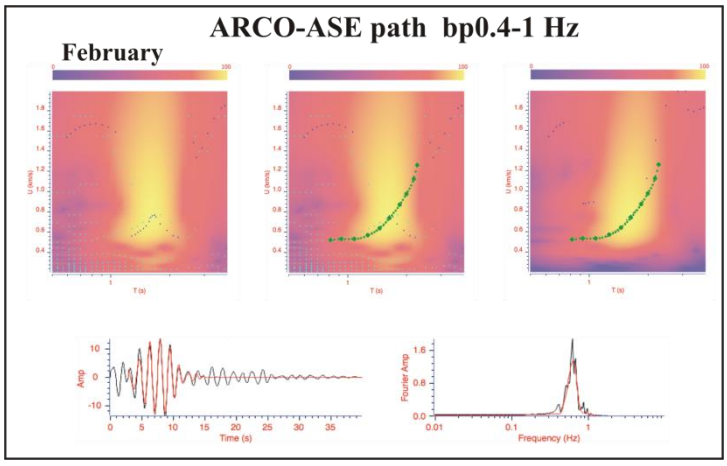

Fig.3.13 *– Steps of FTAN analysis on February stacked NCF (vertical component) relative to ARCO-ASE path (0.4-1 Hz).*

A different example of symmetric function is represented by monthly NCFs computed for NIS-ASE path (4.9 km) (Fig.3.1) in 0.6-1.5 Hz frequency range with 30 s time windows.

The NCFs relative to the vertical component are characterized by the presence of two surface wave trains both on the causal (at 6 s) and on the anticausal part (at 7 s). They present comparable amplitude and waveforms, and, averaging the positive and the negative part of the three functions, symmetric NCFs have been obtained with a better signal-to-noise ratio (Fig.3.14).

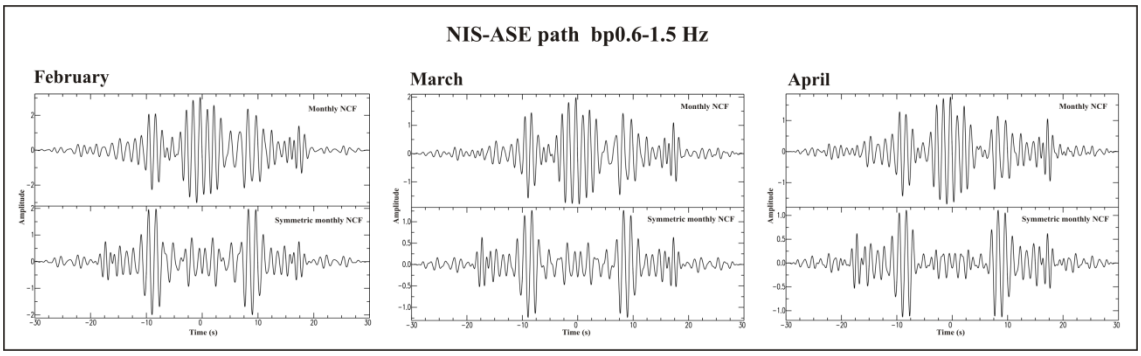

Fig.3.14 *- Monthly and symmetric monthly NCFs (vertical component) of February, March and April computed for NIS-ASE path in 0.6-1.5 Hz frequency range.*

The improvement of signal-to-noise ratio is also evident on FTAN maps (Fig.3.15). Hence the FTAN analysis has been performed on the symmetric NCFs. As an example, the FTAN analysis on the February monthly stacked NCF is shown in Fig.3.16.

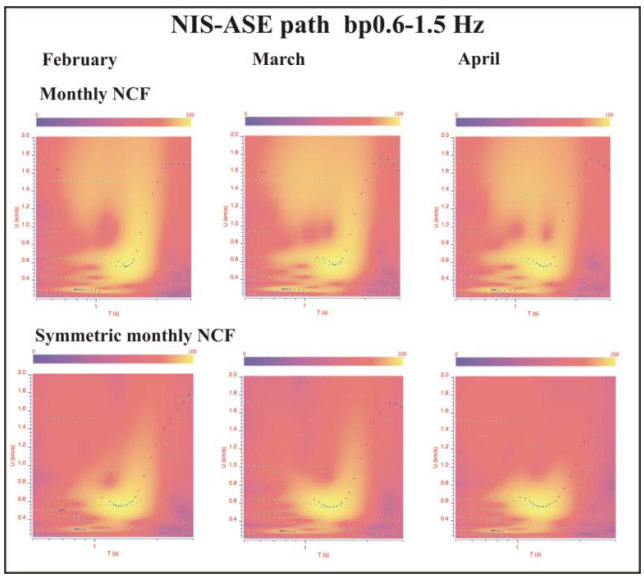

Fig.3.15 *– FTAN maps of monthly and symmetric monthly NCFs (vertical component) of February, March and April computed for NIS-ASE path in 0.6-1.5 Hz frequency range.*

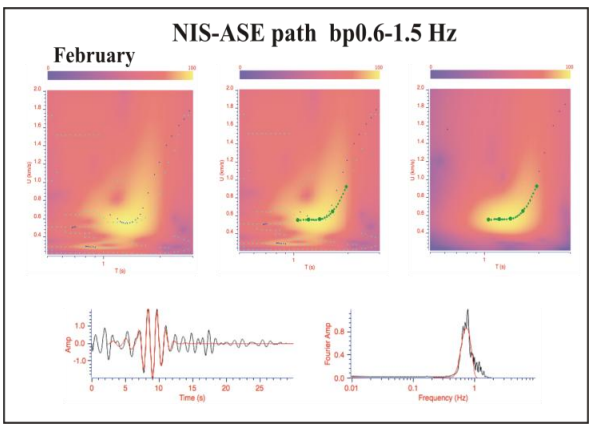

Fig.3.16 *– FTAN analysis of February symmetric NCF (vertical component) relative to NIS-ASE path (0.6-1.5 Hz).*

The average group velocity dispersion curve along the NIS-ASE path has been computed by taking into account the three symmetric monthly stacked NCFs which show a great stability in 1.05-1.91 s period range and 0.55-0.8 km/s group velocity range (Fig.3.17).

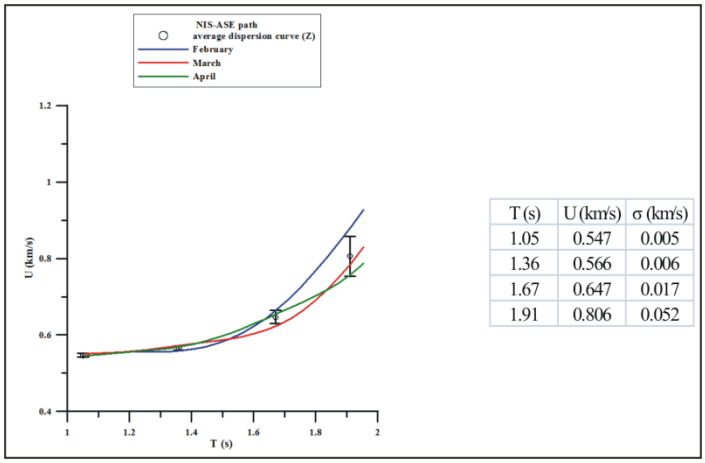

T (s)	U (km/s)	σ (km/s)
1.05	0.547	0.005
1.36	0.566	0.006
1.67	0.647	0.017
1.91	0.806	0.052

Fig.3.17 *– Average group velocity dispersion curve with error bar computed for NIS-ASE path.*

3.3.4 "Flat" group velocity dispersion curve

BAC-POZ path (3.4 km) (Fig.3.1) represents a particular example of clear and stable cross-correlation function with a very high signal-to-noise ratio: a very evident surface wave train with an arrival time of ~7 s is present on the causal part (Fig.3.18), but the relative FTAN maps put in evidence a "flat" trend of mountain ridges (Fig.3.19).

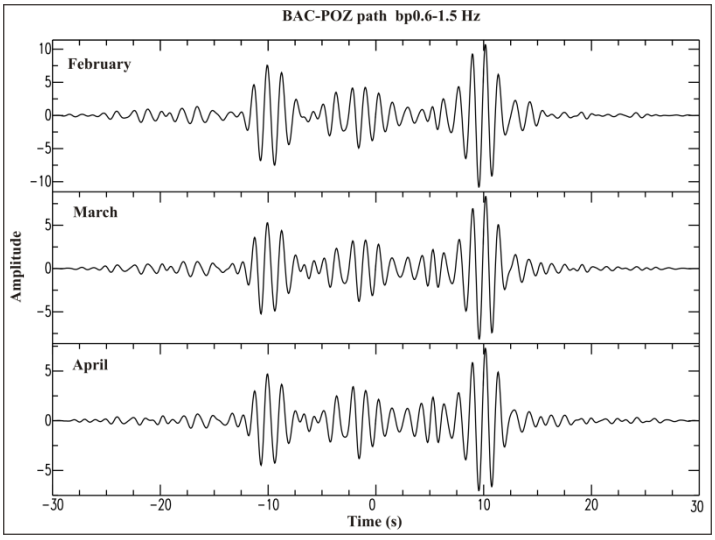

Fig.3.18 *- Monthly NCFs (vertical component) of February, March and April computed for BAC-POZ path in 0.6-1.5 Hz frequency range.*

The analysis has been done in the 0.6-1.5 Hz frequency range only on the vertical component, since both BAC and POZ stations are equipped with vertical geophones.

Maps relative to monthly NCFs show a very similar trend: the energy of the signals is located in ~0.9-1.7 s period range and in ~0.3-0.4 km/s group velocity range (Fig.3.19A-F-M). The extracted fundamental mode fits the surface wave train both in time (Fig.3.19D-I-P) and in frequency (Fig.3.19E-L-Q) domain, but it is not so much dispersed (Fig.3.19B-G-N).

This path crosses the Gulf of Pozzuoli (Fig.3.1), where the maximum thickness of pyroclastic deposits (~2 km, see 1.1.5 section) filling the Campi Flegrei caldera is inferred. According to the receiver distance, the extracted curves sampled about 0.5 km thickness of these pyroclastic materials that would be homogeneous.

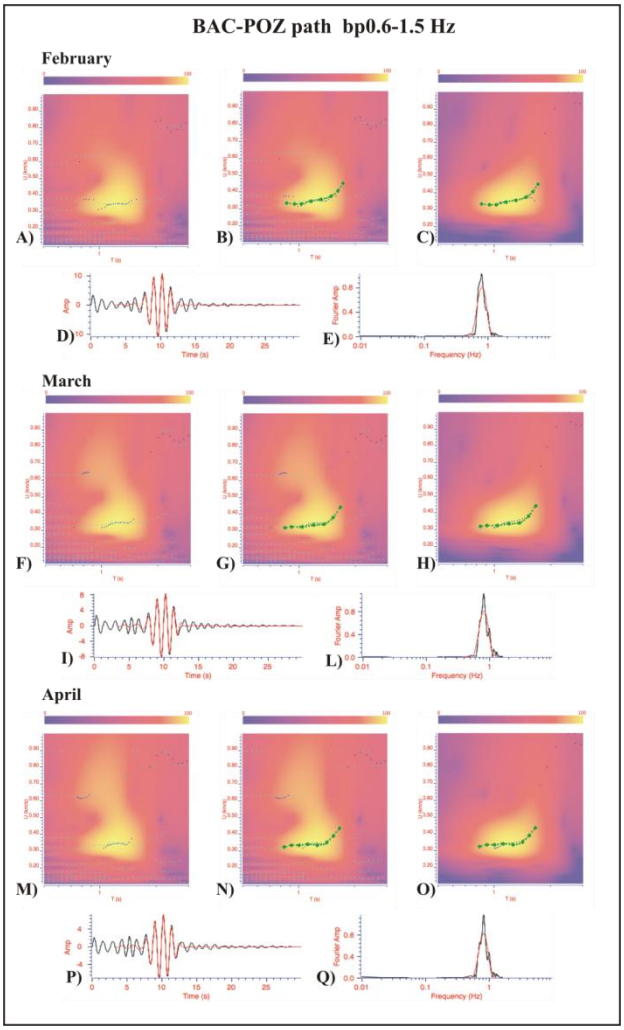

Fig.3.19 *– FTAN analysis of monthly stacked NCFs (vertical component) computed for BAC-POZ path in 0.6-1.5 Hz frequency range.*

The average group velocity dispersion curve, with error bar, has been computed from the February, March and April dispersion curves in 0.89-1.64 s period range and ~0.33-0.42 km/s group velocity range (Fig.3.20).

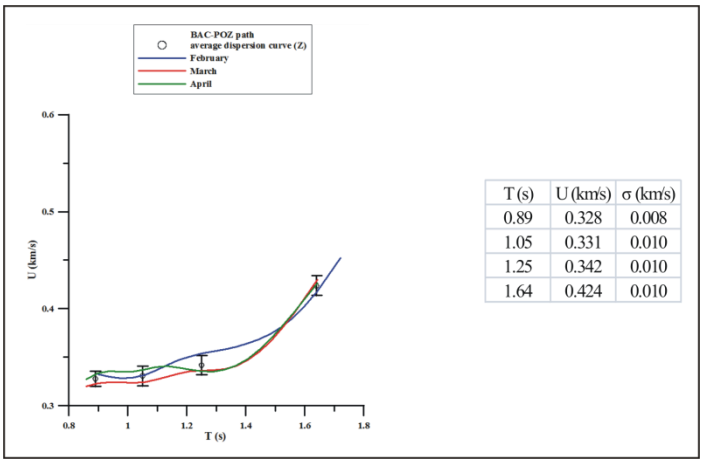

T (s)	U (km/s)	σ (km/s)
0.89	0.328	0.008
1.05	0.331	0.010
1.25	0.342	0.010
1.64	0.424	0.010

Fig.3.20 *– Average group velocity dispersion curve with error bar computed for BAC-POZ path.*

3.3.5 NCFs characterized by more than one wave train

Cross-correlation functions computed for some paths show an ambiguity, as NCFs present more than one surface wave train: an example is given by QUAR-ASE path, 5 km long, crossing the northern part of Campi Flegrei area (Fig.3.1).

The NCFs have been computed in 0.5-1.2 Hz frequency range with 40 s time windows and they are restricted to the vertical component as ASE station has a vertical geophone. Monthly NCFs relative to February, March and April present a good stability and a high signal-to-noise ratio, but all of the three functions are characterized by the presence of two distinct wave trains on the anticausal part with arrival times of about 4 s and 10 s respectively (Fig.3.21).

The knowledge of the geological and geophysical setting of the studied area is fundamental to solve the ambiguity (see 3.2.1 section). A group velocity of 1.25 km/s, relative to the surface wave train arriving at 4 s, seems too high with respect to the expected values on the basis of the available geological models (see 1.1.5 and 3.2.1 sections). Hence the analysis has been focused on the surface wave train arriving at 10 s: it has a greater amplitude than the faster surface wave train and its estimated group velocity value (0.5 km/s) seems more realistic in this context. FTAN analysis has been performed in 0.2-1 km/s group velocity range in order to isolate and enhance the energy relative to this portion of the signal. The fitting between the extracted fundamental mode and the original signal is very satisfactory both in time and in frequency domain (Fig.3.22).

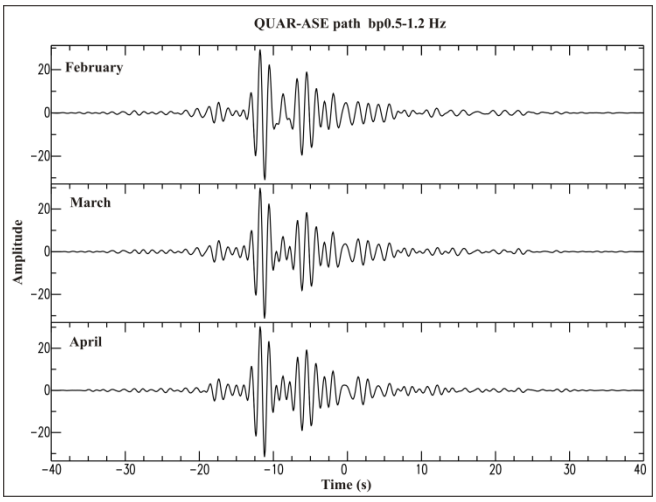

Fig.3.21 *- Monthly NCFs (vertical component) relative to February, March and April computed for QUAR-ASE path in 0.5-1.2 Hz frequency range.*

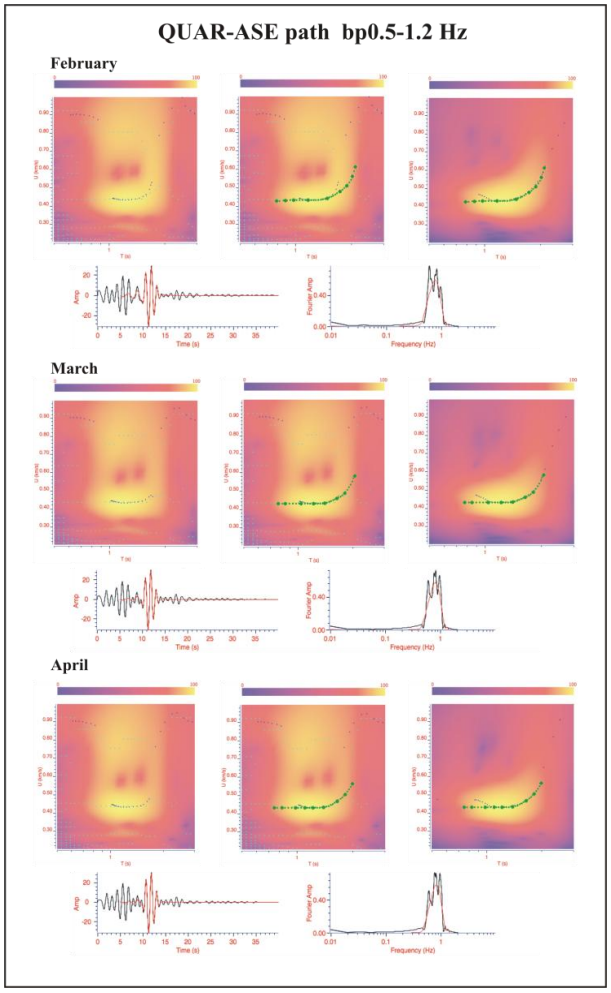

Fig.3.22 *– FTAN analysis on monthly stacked NCFs (vertical component) relative to February, March and April computed for QUAR-ASE path in 0.5-1.2 Hz frequency range.*

The average group velocity dispersion curve, characterized by a very small error bar, has been computed from the February, March and April dispersion curves in ~0.82-2 s period range and ~0.43-0.57 km/s group velocity range (Fig.3.23).

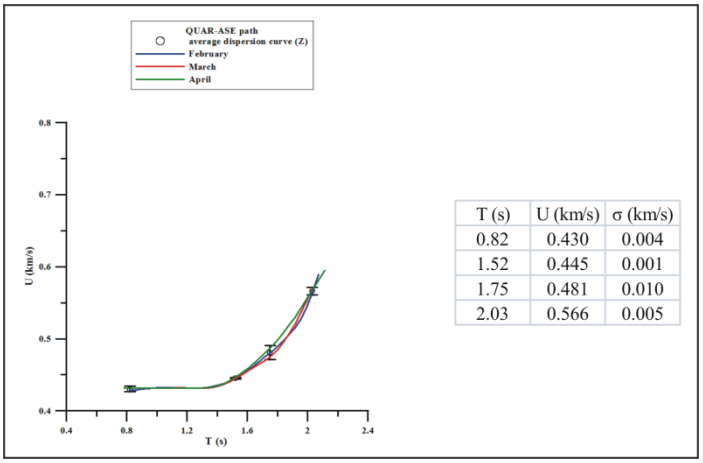

T (s)	U (km/s)	σ (km/s)
0.82	0.430	0.004
1.52	0.445	0.001
1.75	0.481	0.010
2.03	0.566	0.005

Fig.3.23 *– Average group velocity dispersion curve with error bar computed for QUAR-ASE path.*

3.3.6 Coherence between vertical and radial components of ground motion

Few paths have shown stability and coherence between vertical and radial components both in terms of NCFs and FTAN maps. ARCO-DMP path (2 km) (Fig.3.1) is shown here as an example: it has been analysed in 0.7-1.2 Hz frequency range for vertical and radial components, using 40 s time windows.

Fourier spectra of the monthly stacked NCFs relative to the two components show that the energy is mainly concentrated at low frequencies, i.e. in 0.2-0.8 Hz range, corresponding to wavelengths much longer than the path distance (see 3.2.1 section) (Fig.3.24A).

Monthly stacked NCFs are stable: a surface wave train arrives at about 3 s on the anticausal part of the vertical and radial components of NCFs (Fig.3.24B).

This coherence between NCFs relative to vertical and radial components is also found in the FTAN maps: even if maps of the vertical component are disturbed by a descending trend, the energy of the signals is concentrated in the same windows of period (0.9-1.6 s) and group velocity (0.4-0.7 km/s), for all the 3 months (Fig.3.25).

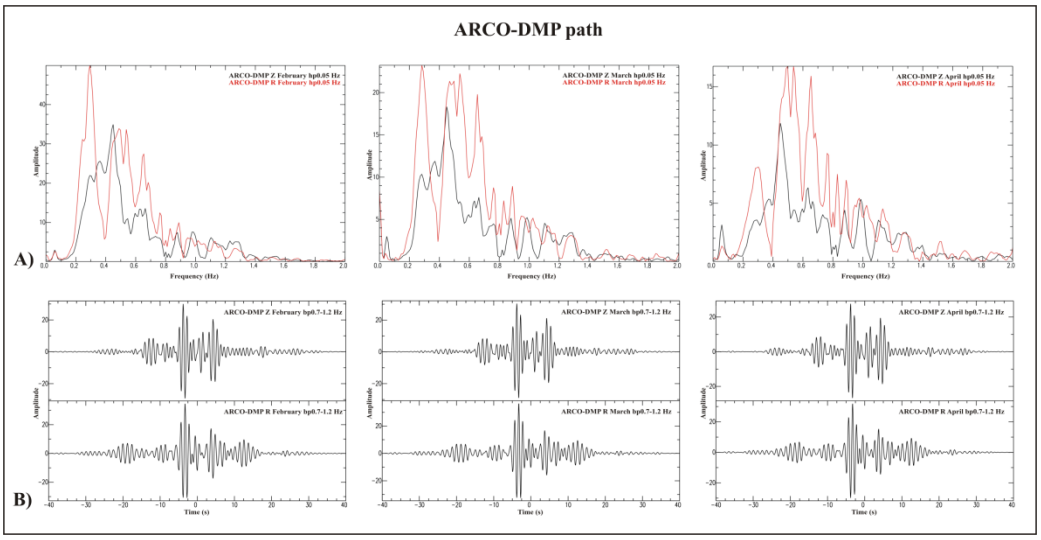

Fig.3.24 *– Fourier spectra (A) of the monthly stacked NCFs (B) (vertical and radial components) relative to February, March and April computed for ARCO-DMP path.*

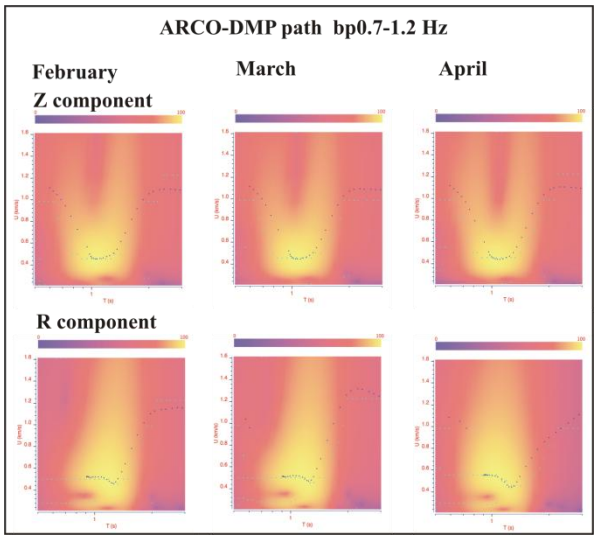

Fig.3.25 *- FTAN maps of monthly NCFs (vertical and radial components) of February, March and April computed for ARCO-DMP path in 0.7-1.2 Hz frequency range.*

FTAN analysis of the February NCFs, vertical (Fig.3.26A) and radial (Fig.3.26B) components, are shown as representative examples of the three months. It is evident the agreement between the dispersion curves of the fundamental mode for vertical and radial components.

Then, the average dispersion curve, with error bar, has been computed using all dispersion curves: group velocities range from 0.46 to 0.78 km/s at periods from 0.97 to 1.64 s (Fig.3.27).

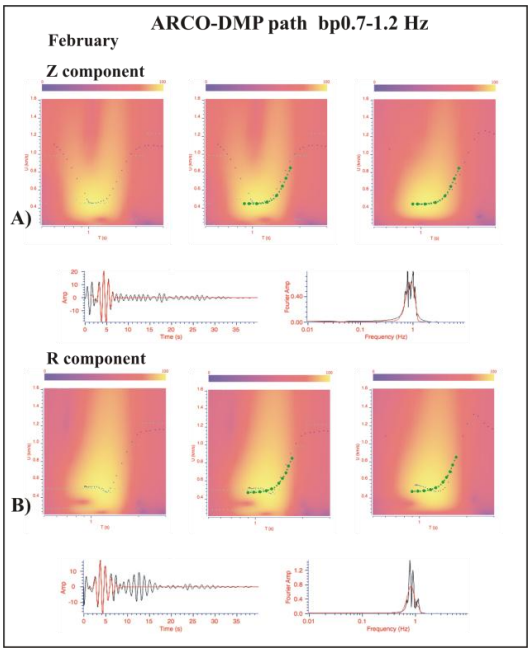

Fig.3.26 *– FTAN analysis on monthly NCFs of vertical (A) and radial (B) components relative to February computed for ARCO-DMP path in 0.7-1.2 Hz frequency range.*

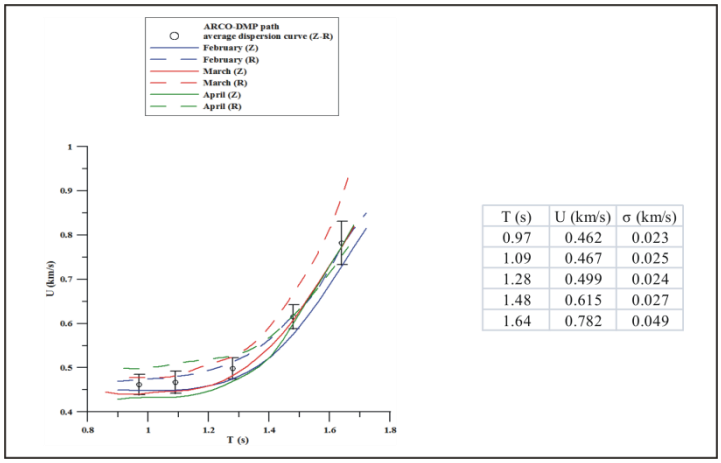

T (s)	U (km/s)	σ (km/s)
0.97	0.462	0.023
1.09	0.467	0.025
1.28	0.499	0.024
1.48	0.615	0.027
1.64	0.782	0.049

Fig.3.27 *– Average group velocity dispersion curve with error bar computed for ARCO-DMP path.*

3.3.7 Resemblances and differences between NCF of close paths

A special attention has been devoted to the close paths as average physical properties of the buried geological structures shouldn't have strong discrepancies.

As an example I show the NCF analysis along the QUAR-CSOB (6.5 km), QUAR-SFT (6.4 km) and QUAR-STH (6.2 km) paths (Fig.3.1) which cross the Astroni crater and are quite orthogonal to the coastline of the central part of the Gulf of Pozzuoli.

Frequency ranges used in the analysis of the vertical and radial components of each path are listed in Tab.3.2; 40 s time windows have been used.

Stacked cross-correlation functions show resemblances for these three paths both on vertical and radial components.

NCFs of the vertical component present a good signal-to-noise ratio: a clear surface wave train is evident on the anticausal part for all the three months. Arrival time (about 5 s) and amplitude of the wave trains are comparable, while the waveforms are quite different. In particular surface wave train identified on NCFs of QUAR-SFT path seems to consist of two different envelopes, while some coda phases seem to enrich the surface wave train identified on NCFs of QUAR-CSOB path (Fig.3.28A).

NCFs of the radial components also show discrete signal-to-noise ratio and a surface wave train recognizable on the anticausal part with arrival time of 6-7 s. As for the vertical component, some differences emerge. The surface wave train recognizable on NCFs relative to QUAR-CSOB path is disturbed by a contribution on the zero time, especially for February. As regards the QUAR-SFT path, the April stacked NCF shows different waveform with respect to the previous monthly functions, since three distinct wave trains are visible. The QUAR-STH path presents the most stable functions in terms of amplitude and arrival time (Fig.3.28B).

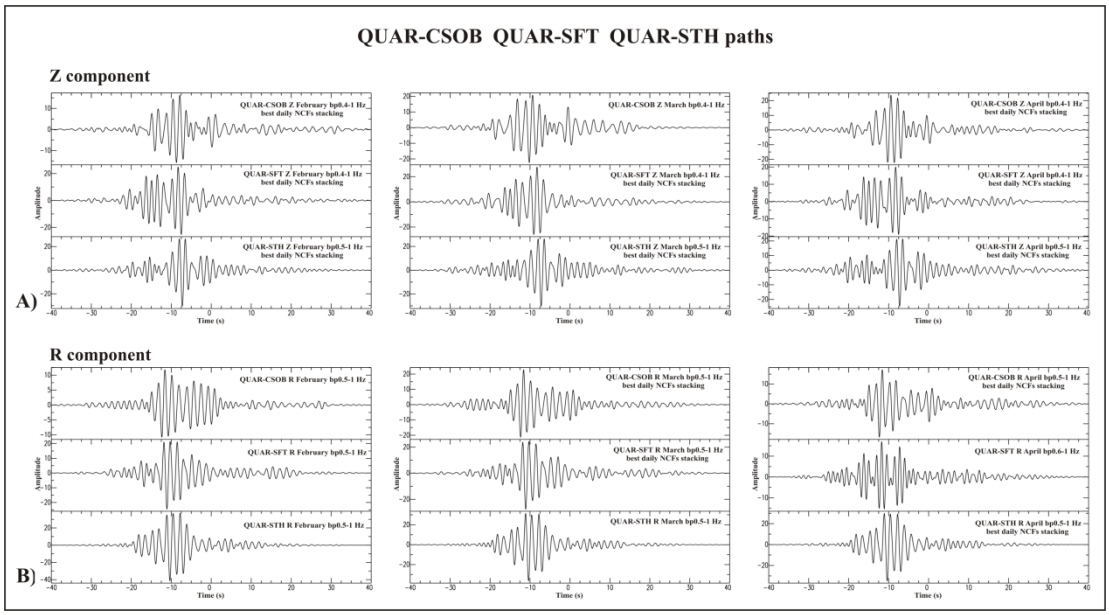

Fig.3.28 *- Stacked vertical (A) and radial (B) NCFs of February, March and April computed for QUAR-CSOB, QUAR-SFT and QUAR-STH paths.*

As regards FTAN analysis, a descending trend of mountain ridge in ~1-2.5 s period range characterizes the maps of the NCFs vertical component relative to QUAR-CSOB path (Fig.3.29A). Two separate trends of mountain ridges are recognizable at about 0.4 km/s and 0.8 km/s on maps of the NCFs vertical component relative to QUAR-SFT path

(Fig.3.29B), referable to the two distinct wave packets identified on NCFs (Fig.3.28A). This trend characterizes also maps relative to QUAR-STH path, even if the energy of the signals is mostly centred at higher group velocities (Fig.3.29C).

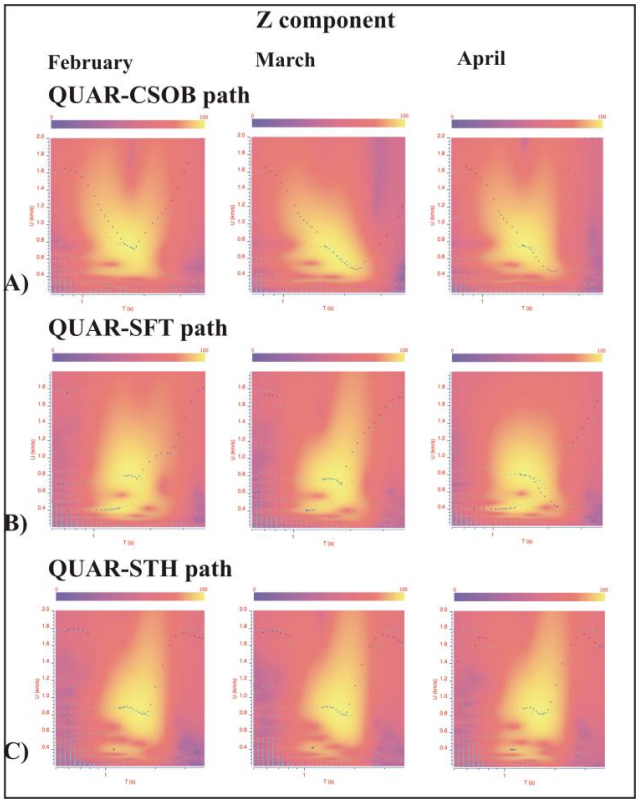

Fig.3.29 *- FTAN maps of monthly stacked NCFs (vertical component) of February, March and April relative to QUAR-CSOB (A), QUAR-SFT (B) and QUAR-STH (C) paths.*

Instead FTAN maps of the NCF radial components show evident similarities among the three paths as the energy is centred in 0.9-2.5 s period range and in 0.5-1.2 km/s group velocity range, defining a very clear trend of mountain ridge (Fig.3.30).

As an example, the steps of the FTAN analysis are shown in Fig.3.31 relatively to March NCF (radial component) for the QUAR-SFT path.

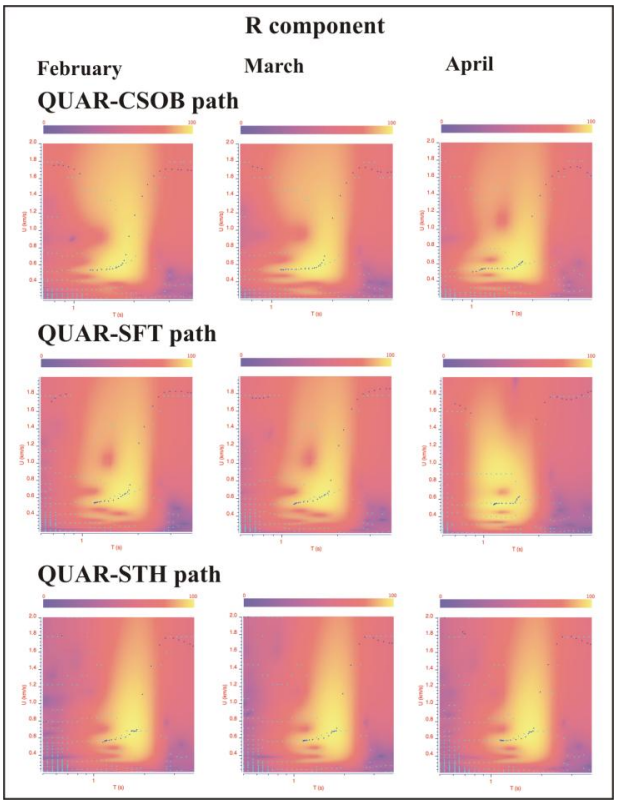

Fig.3.30 *- FTAN maps of monthly stacked NCFs (radial component) of February, March and April relative to QUAR-CSOB, QUAR-SFT and QUAR-STH paths.*

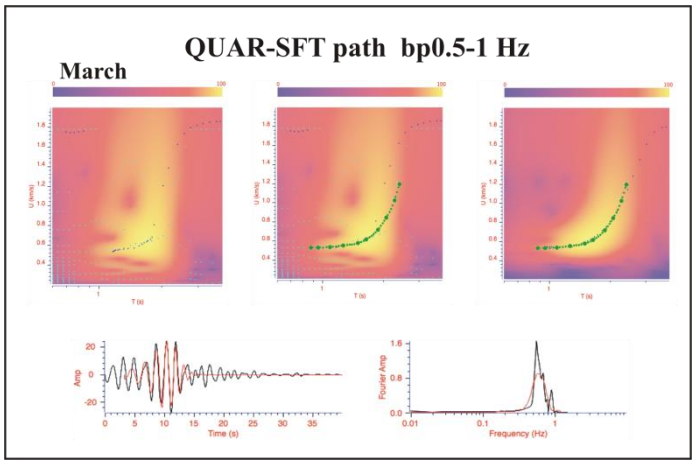

Fig.3.31 *- FTAN analysis on March NCF (radial component) relative to QUAR-SFT path (0.5-1 Hz).*

In the light of these analyses, radial components have been taken into account and an average dispersion curve has been computed for the QUAR-CSOB, QUAR-SFT and QUAR-STH paths (Fig.3.32B): group velocities vary from about 0.54 to 0.91 km/s at periods ranging from 0.97 to 2.1 s. Dispersion curve of QUAR-SFT path relatively to April (Fig.3.32A) has not been included in the computation of the average in order to have a smaller error bar.

Being CSOB, SFT and STH stations located near the Solfatara crater (Fig.3.1), for the sake of brevity, hereafter QUAR-CSOB, QUAR-SFT and QUAR-STH paths will be identified as one path, the QUAR-SOLF path.

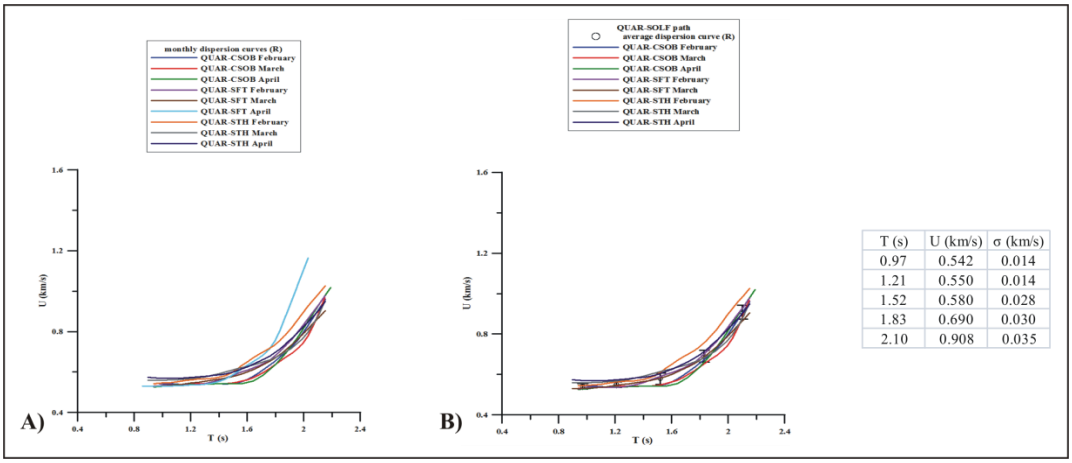

T (s)	U (km/s)	σ (km/s)
0.97	0.542	0.014
1.21	0.550	0.014
1.52	0.580	0.028
1.83	0.690	0.030
2.10	0.908	0.035

Fig.3.32 *– Group velocity dispersion curves extracted from monthly radial NCFs relative to QUAR-CSOB, QUAR-SFT and QUAR-STH paths (A); average group velocity dispersion curve with error bar computed for the average QUAR-SOLF path (B).*

3.4 NCFs and average group velocity dispersion curves computed in Campi Flegrei area

In this section I show the computed vertical and radial cross-correlation functions relative to all the analysed paths crossing the Campi Flegrei area. The computed average group velocity dispersion curves with error bar are also shown for each path (from Fig.3.33 to Fig.3.68).

Results obtained by the analysis of the ARCO-ASE, ARCO-DMP, BAC-SMN, BAC-POZ, NIS-ASE, POZ-ASE, QUAR-ASE, QUAR-CSOB, QUAR-SFT and QUAR-STH paths have already been presented and commented in the previous paragraphs (from 3.3.2 to 3.3.7), so the relative NCFs and average dispersion curves will not be repeated in this section.

Monthly dispersion curves of the Rayleigh wave fundamental mode couldn't be extracted for the BAC-QUAR, BAC-SMN, CUMA-SMN and NIS-DMP paths (Tab.3.2), so only the computed NCFs are illustrated for these four paths (Figs.3.46-3.9-3.50-3.55 respectively).

NCFs computed for the CSOB-SMN, SFT-SMN and STH-SMN paths are shown in one figure (Fig.3.49A-B-C) as their monthly dispersion curves have been averaged in one average dispersion curve (Fig.3.49E). The same has been done for the NCFs relative to the

POZ-CSOB, POZ-SFT and POZ-STH paths (Fig.3.62). In this way the so called SOLF-SMN and POZ-SOLF paths have been respectively identified.

Dispersion curves extracted from monthly vertical NCFs relative to ARCO-ASE (Fig.3.11) and ARCO-CMSA paths (Fig.3.33A) show a similar trend in the same period and group velocity ranges, so they have been averaged obtaining one dispersion curve representative of the two paths (Fig.3.33B).

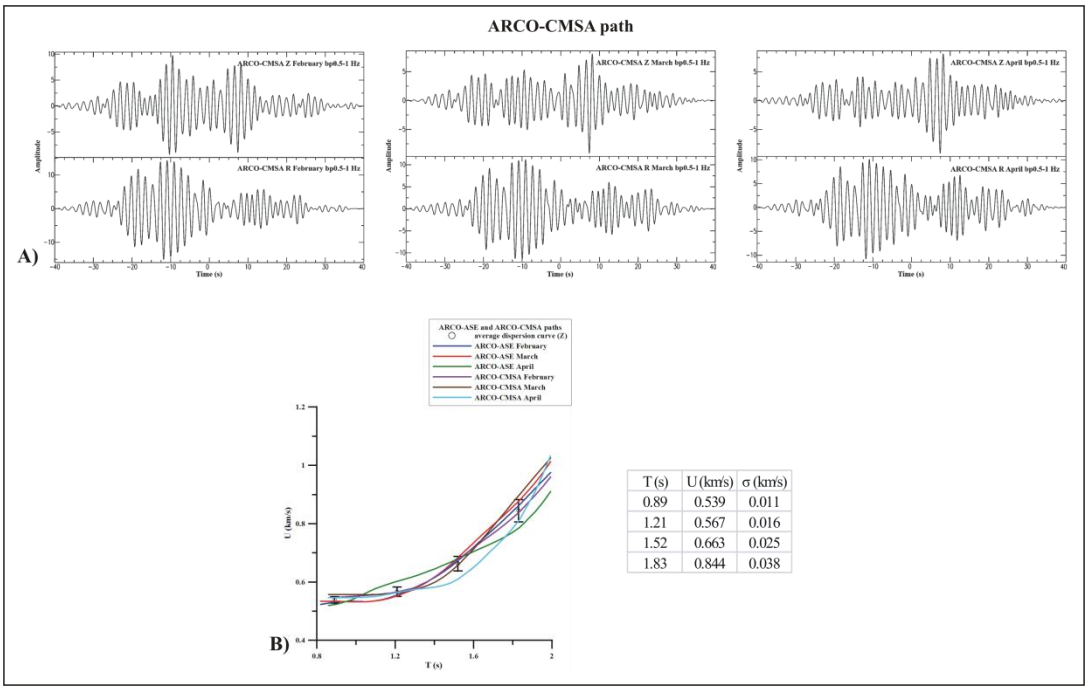

Fig.3.33 *– Monthly stacked NCFs (vertical and radial components) of February, March and April computed for ARCO-CMSA path (A) and average group velocity dispersion curve with error bar relative to NCFs vertical component computed for ARCO-ASE and ARCO-CMSA paths (B).*

Although the NCFs of vertical and radial components computed for the ARCO-CSOB path (Fig.3.1) present similar waveforms (Fig.3.34A), FTAN maps relative to the radial components show a descending-trend of mountain ridges. So only the three monthly vertical dispersion curves have been used to compute the average group velocity dispersion curve in 0.85-1.71 s period range and ~0.52-0.86 km/s group velocity range (Fig.3.34B).

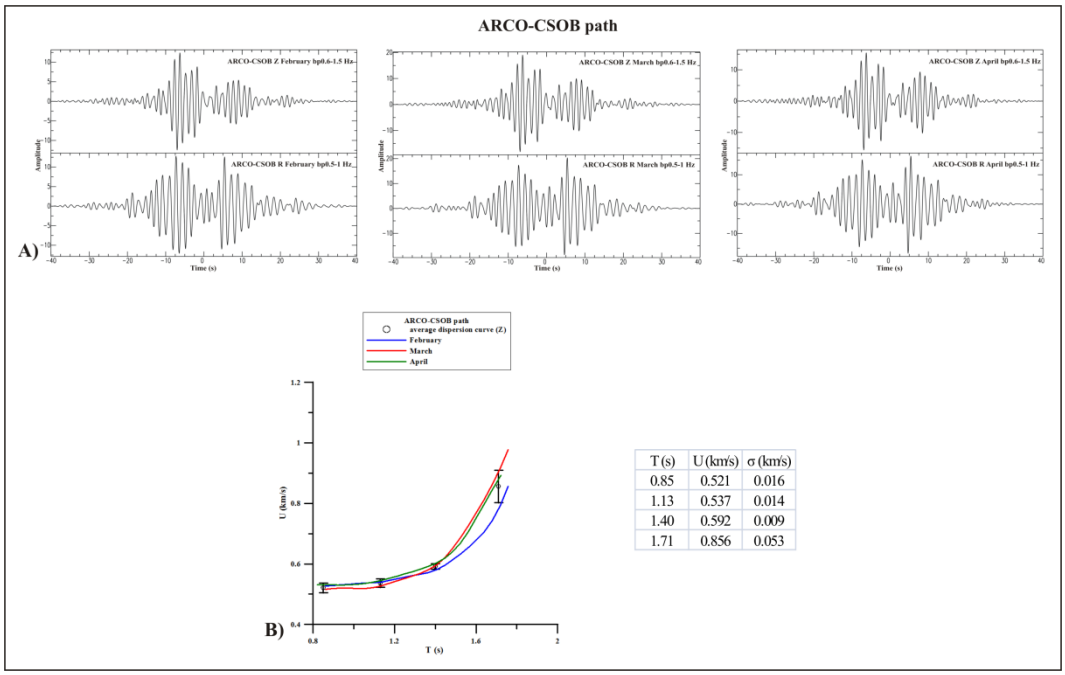

T (s)	U (km/s)	σ (km/s)
0.85	0.521	0.016
1.13	0.537	0.014
1.40	0.592	0.009
1.71	0.856	0.053

Fig.3.34 *– Monthly stacked NCFs (vertical and radial components) of February, March and April computed for ARCO-CSOB path (A) and average group velocity dispersion curve with error bar relative to NCFs vertical component (B).*

Since radial NCFs computed for the ARCO-QUAR path (Fig.3.1) show lower signal-to-noise ratio and stability than the vertical ones (Fig.3.35A), the average group velocity dispersion curve has been computed among the three monthly vertical dispersion curves in 1-2.65 s period range and ~0.47-1 km/s group velocity range (Fig.3.35B).

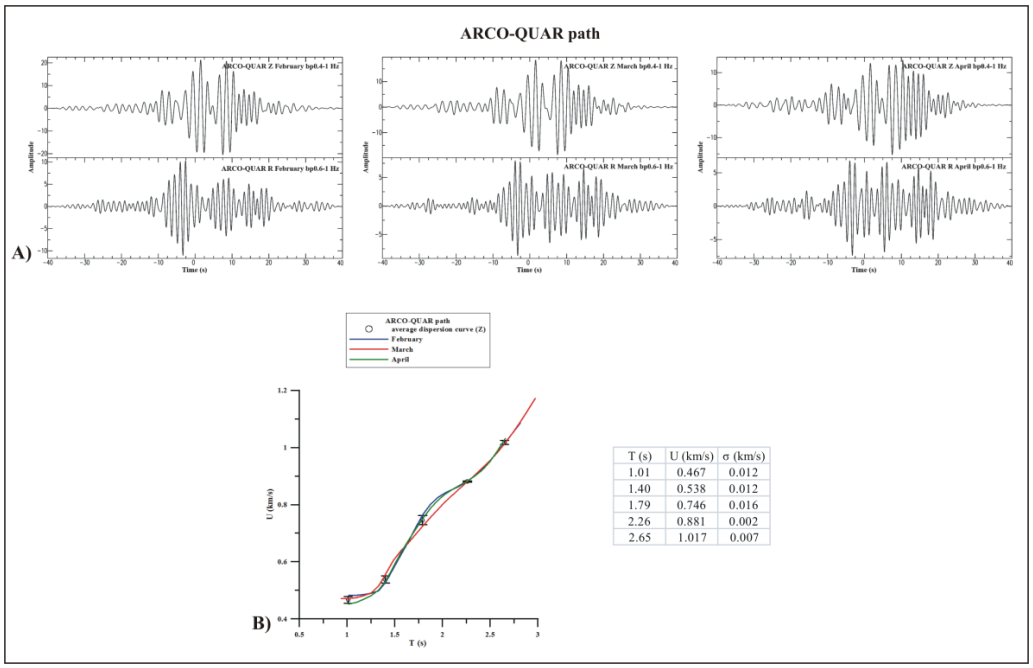

T (s)	U (km/s)	σ (km/s)
1.01	0.467	0.012
1.40	0.538	0.012
1.79	0.746	0.016
2.26	0.881	0.002
2.65	1.017	0.007

Fig.3.35 *– Monthly stacked NCFs (vertical and radial components) of February, March and April computed for ARCO-QUAR path (A) and average group velocity dispersion curve with error bar relative to NCFs vertical component (B).*

Although the symmetric vertical NCFs computed for the ARCO-SFT path (Fig.3.1) show good signal-to-noise ratio and stability (Fig.3.36A), relative FTAN maps present a not very clear trend, so the extracted monthly dispersion curves and the computed average dispersion curve (Fig.3.36B) haven't been considered so reliable to perform the Hedgehog inversion.

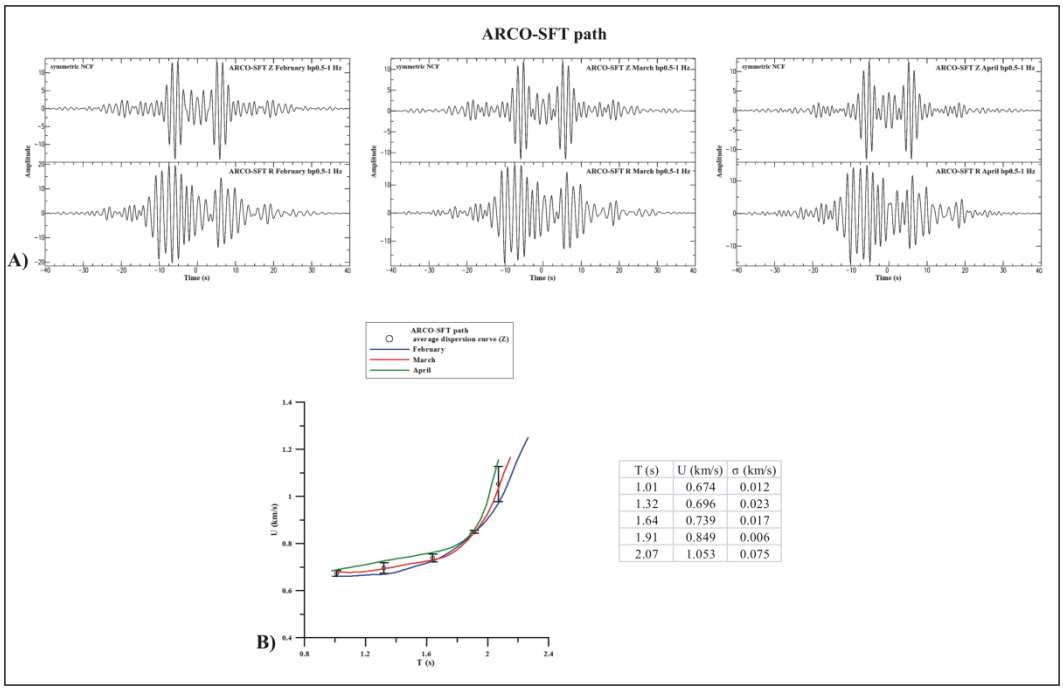

Fig.3.36 *– Monthly stacked NCFs (vertical and radial components) of February, March and April computed for ARCO-SFT path (A) and average group velocity dispersion curve with error bar relative to NCFs vertical component (B).*

Even if the vertical NCFs computed for the ARCO-SMN path (Fig.3.1) don't show a very high signal-to-noise ratio (on the contrary radial functions are very chaotic) (Fig.3.37A), the average group velocity dispersion curve has a very little error bar: periods range from 1.32 to 2.65 s and group velocities range from ~0.6 to 0.86 km/s (Fig.3.37B).

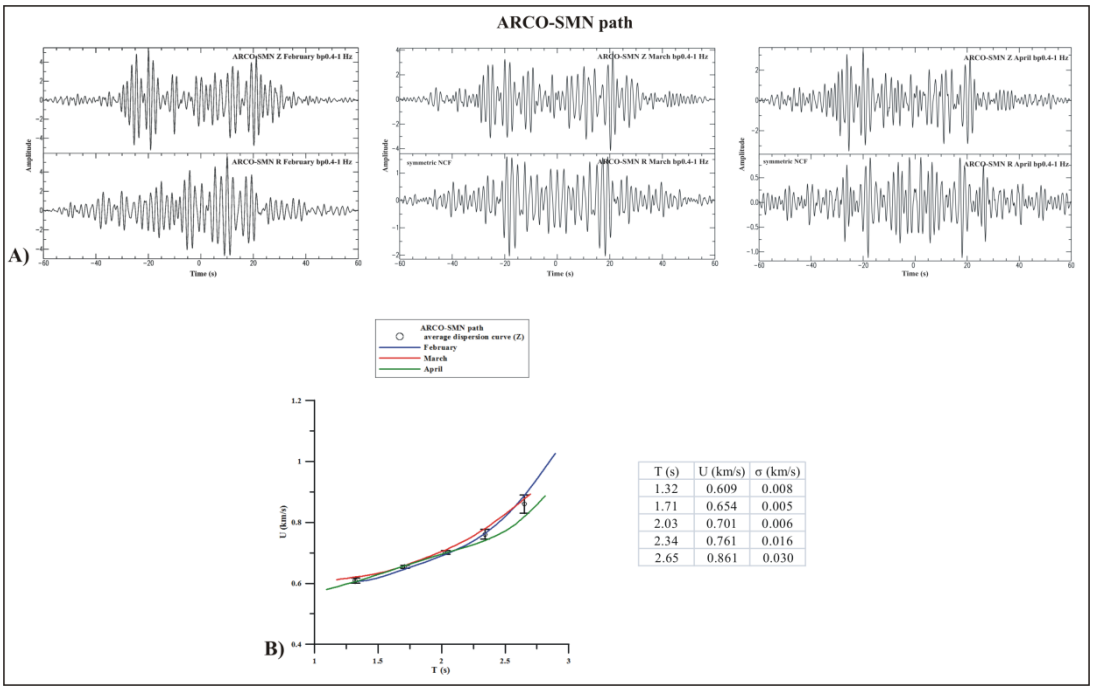

T (s)	U (km/s)	σ (km/s)
1.32	0.609	0.008
1.71	0.654	0.005
2.03	0.701	0.006
2.34	0.761	0.016
2.65	0.861	0.030

Fig.3.37 *– Monthly stacked NCFs (vertical and radial components) of February, March and April computed for ARCO-SMN path (A) and average group velocity dispersion curve with error bar relative to NCFs vertical component (B).*

NCFs computed for the ARCO-STH path (Fig.3.1) don't present a stable surface wave train (Fig.3.38A). Average group velocity dispersion curve has been computed between only February and March dispersion curves (Fig.3.38B), because the dispersion curve relative to April scatters respect to the other ones. Hence the average dispersion curve hasn't been considered reliable enough to perform the Hedgehog inversion, even if it's characterized by a very little error bar.

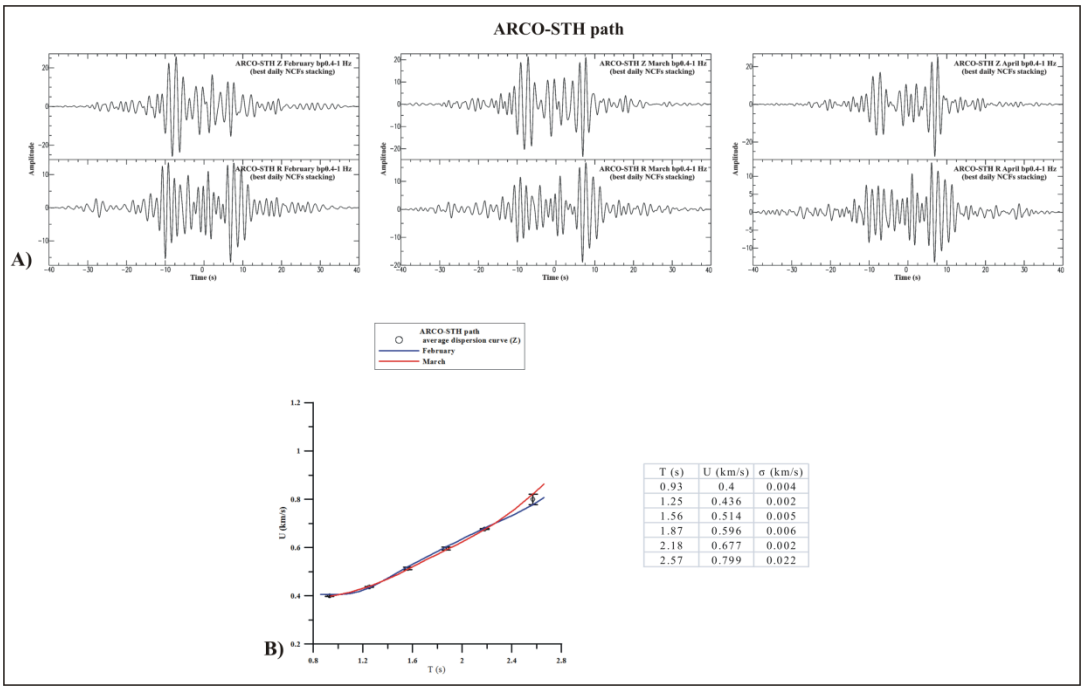

T (s)	U (km/s)	σ (km/s)
0.93	0.4	0.004
1.25	0.436	0.002
1.56	0.514	0.005
1.87	0.596	0.006
2.18	0.677	0.002
2.57	0.799	0.022

Fig.3.38 *–Stacked NCFs (vertical and radial components) of February, March and April computed for ARCO-STH path (A) and average group velocity dispersion curve with error bar relative to NCFs vertical component (B).*

The three monthly dispersion curves extracted from the vertical stacked NCFs (Fig.3.39A) computed for the ASE-SMN path (Fig.3.1) have been averaged in 1-2 s period range and ~0.49-0.88 km/s group velocity range (Fig.3.39B).

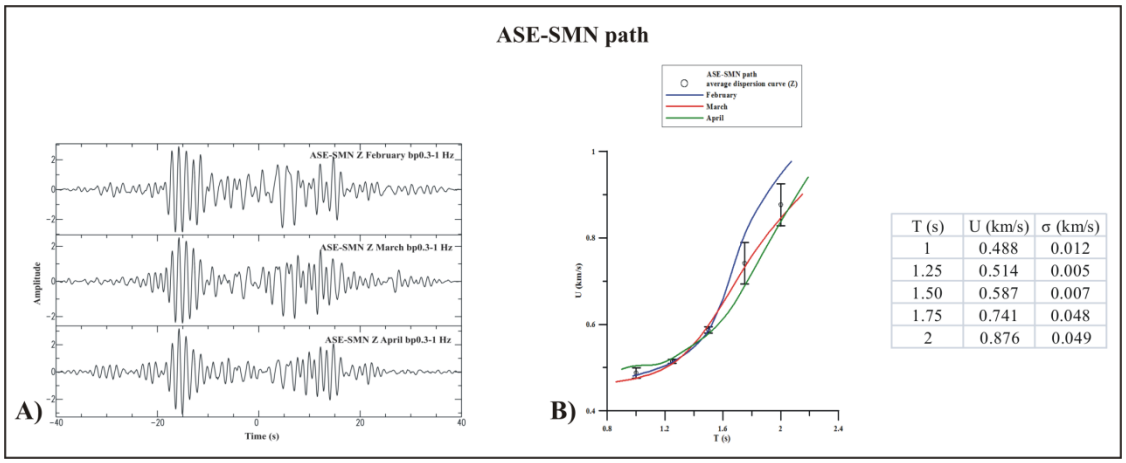

T (s)	U (km/s)	σ (km/s)
1	0.488	0.012
1.25	0.514	0.005
1.50	0.587	0.007
1.75	0.741	0.048
2	0.876	0.049

Fig.3.39 *– Monthly stacked NCFs (vertical component) of February, March and April computed for ASE-SMN path (A) and average group velocity dispersion curve with error bar (B).*

The three monthly dispersion curves extracted from the vertical stacked NCFs (Fig.3.40A) computed for the BAC-ARCO path (Fig.3.1) have been averaged in 0.94-1.95 s period range and 0.43-0.62 km/s group velocity range (Fig.3.40B).

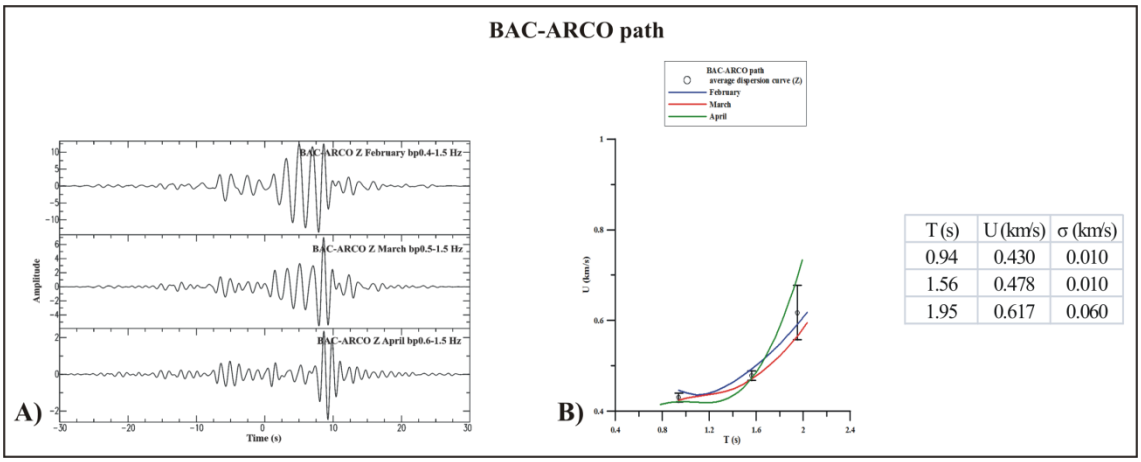

T (s)	U (km/s)	σ (km/s)
0.94	0.430	0.010
1.56	0.478	0.010
1.95	0.617	0.060

Fig.3.40 *– Monthly stacked NCFs (vertical component) of February, March and April computed for BAC-ARCO path (A) and average group velocity dispersion curve with error bar(B).*

The three monthly dispersion curves extracted from the vertical stacked NCFs (Fig.3.41A) computed for the BAC-ASE path (Fig.3.1) have been averaged in 0.78-1.99 s period range and ~0.4-0.65 km/s group velocity range (Fig.3.41B).

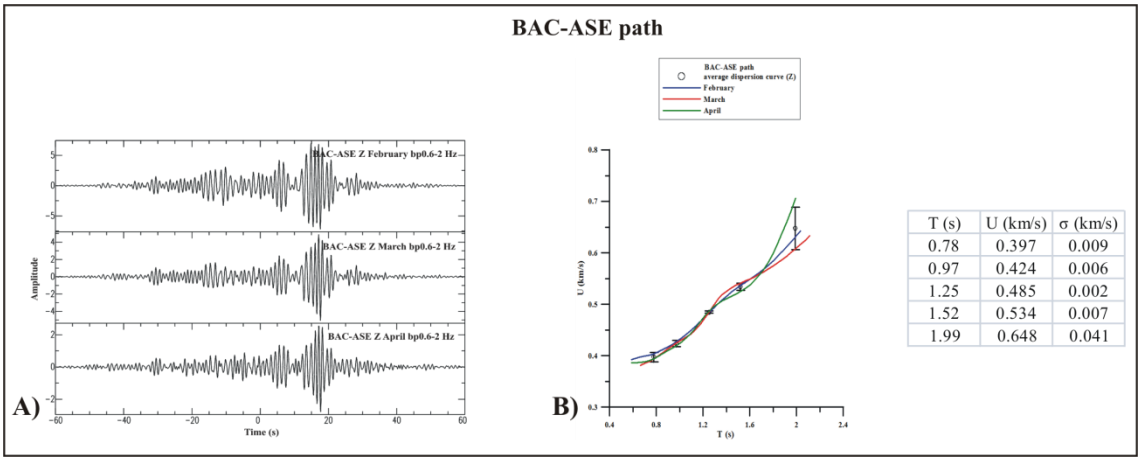

T (s)	U (km/s)	σ (km/s)
0.78	0.397	0.009
0.97	0.424	0.006
1.25	0.485	0.002
1.52	0.534	0.007
1.99	0.648	0.041

Fig.3.41 *– Monthly stacked NCFs (vertical component) of February, March and April computed for BAC-ASE path (A) and average group velocity dispersion curve with error bar (B).*

The average group velocity dispersion curve relative to the BAC-CMSA path (Fig.3.1) has been computed only between dispersion curves relative to February and March (Fig.3.42B), as April NCF presents a very bad signal-to-noise ratio (Fig.3.42A). Hence it hasn't been considered reliable enough to perform the Hedgehog inversion.

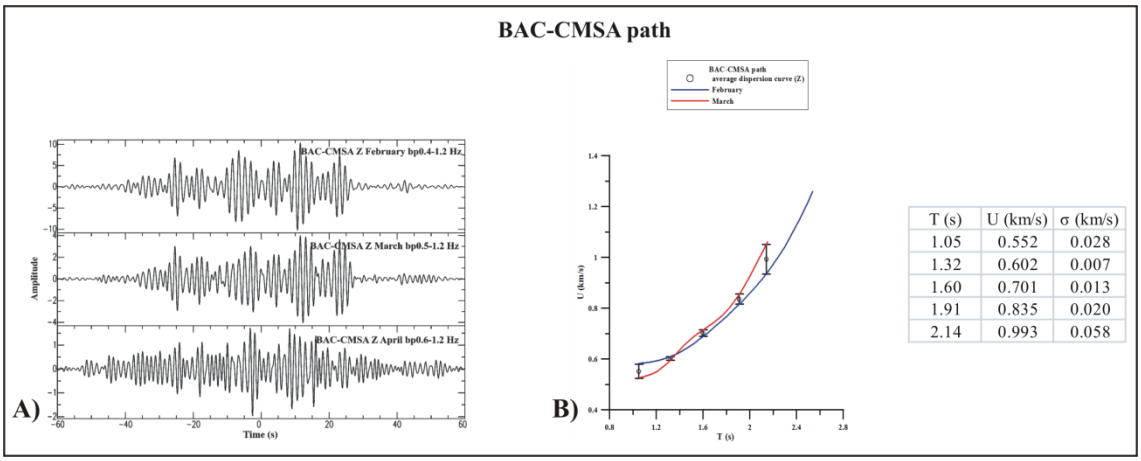

T (s)	U (km/s)	σ (km/s)
1.05	0.552	0.028
1.32	0.602	0.007
1.60	0.701	0.013
1.91	0.835	0.020
2.14	0.993	0.058

Fig.3.42 *– Monthly stacked NCFs (vertical component) of February, March and April computed for BAC-CMSA path (A) and average group velocity dispersion curve with error bar (B).*

The same consideration has been done for the average group velocity dispersion curve (Fig.3.43) computed for the BAC-CSOB path (Fig.3.1).

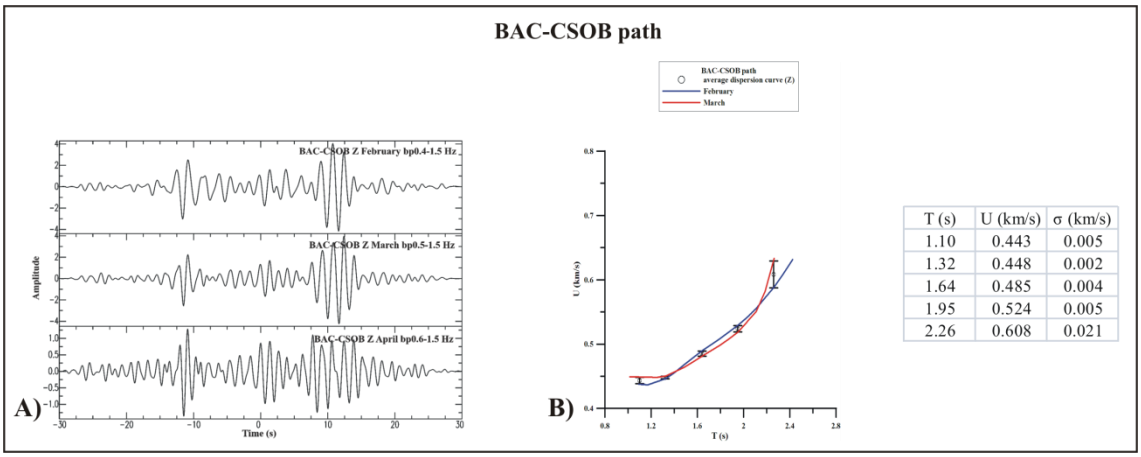

T (s)	U (km/s)	σ (km/s)
1.10	0.443	0.005
1.32	0.448	0.002
1.64	0.485	0.004
1.95	0.524	0.005
2.26	0.608	0.021

Fig.3.43 *– Monthly stacked NCFs (vertical component) of February, March and April computed for BAC-CSOB path (A) and average group velocity dispersion curve with error bar (B).*

Although NCFs computed for the BAC-DMP path (Fig.3.1) present good signal-to-noise ratio and stability (Fig.3.44A), the average group velocity dispersion curve hasn't been inverted because if we exclude the data at the greatest period (being characterized by a very big error bar), the average dispersion curve covers a very short range of period (Fig.3.44B).

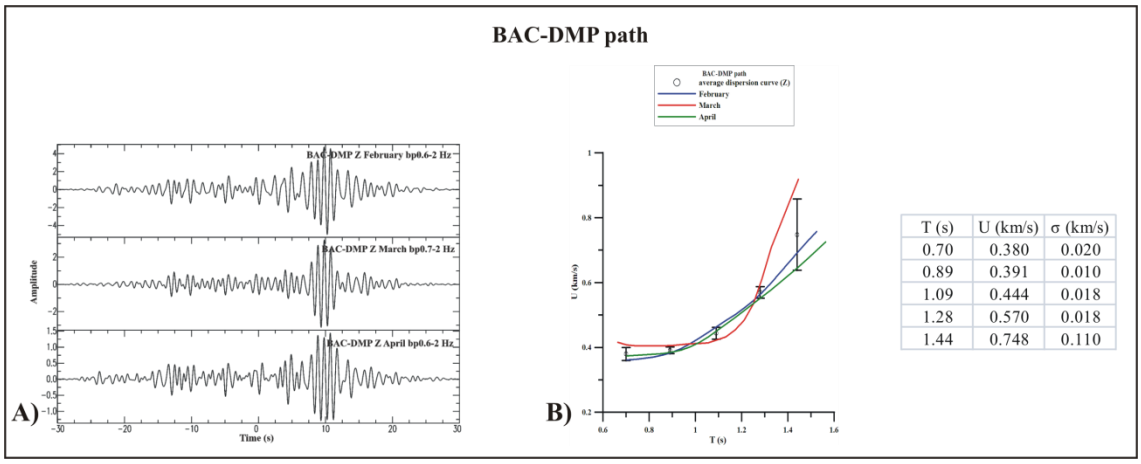

T (s)	U (km/s)	σ (km/s)
0.70	0.380	0.020
0.89	0.391	0.010
1.09	0.444	0.018
1.28	0.570	0.018
1.44	0.748	0.110

Fig.3.44 *– Monthly stacked NCFs (vertical component) of February, March and April computed for BAC-DMP path (A) and average group velocity dispersion curve with error bar (B).*

April stacked NCF computed for the BAC-NIS path (Fig.3.1) hasn't allowed to recognize a surface wave train coherent with that one identified on February and March NCFs (Fig.3.45A). Stacking 14 daily NCFs for February and 15 daily NCFs for March, that corresponds to divide monthly NCFs of February and March in two portions, it has been noted that NCFs relative to February 1-13 and 14-28 and March 17-31 present similar waveforms, while the NCF of March 1-16 is a very different function (Fig.3.45A). Thus the average group velocity dispersion curve relative to the BAC-NIS path has been computed among the three vertical curves extracted from NCFs computed on the two halves of February and the second half of March (Fig.3.45B).

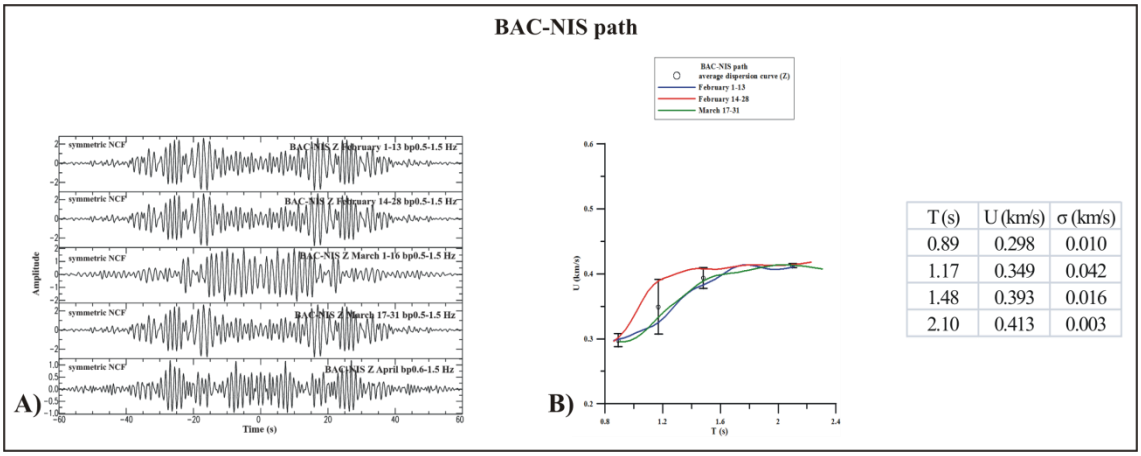

T (s)	U (km/s)	σ (km/s)
0.89	0.298	0.010
1.17	0.349	0.042
1.48	0.393	0.016
2.10	0.413	0.003

Fig.3.45 *– Symmetric stacked NCFs (vertical component) of February, March and April computed for BAC-NIS path (A) and average group velocity dispersion curve with error bar (B).*

NCFs computed for the BAC-QUAR path (Fig.3.1) present very different and not stable waveforms (Fig.3.46), this feature prevented to compute an average group velocity dispersion curve.

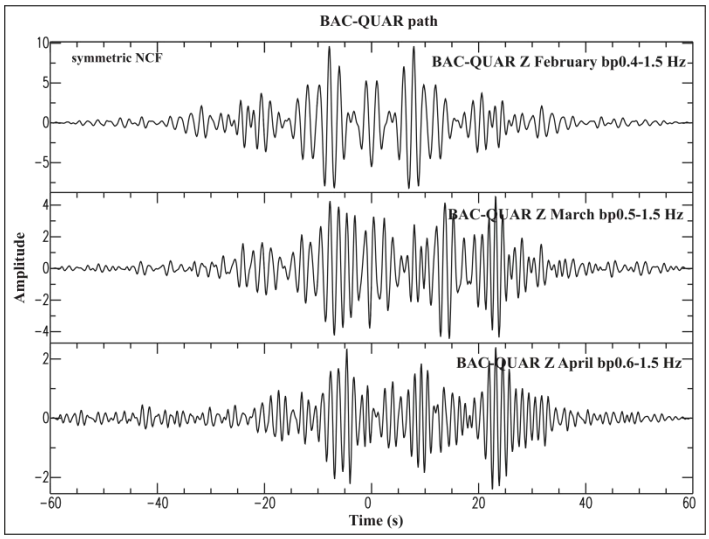

Fig.3.46 *– Monthly stacked NCFs (vertical component) of February, March and April computed for BAC-QUAR path.*

Although NCFs computed for the BAC-SFT path (Fig.3.1) present good signal-to-noise ratio and stability (Fig.3.47A), the obtained average group velocity dispersion curve is characterized by a very big error bar (Fig.3.47B), which prevented to proceed in the inversion.

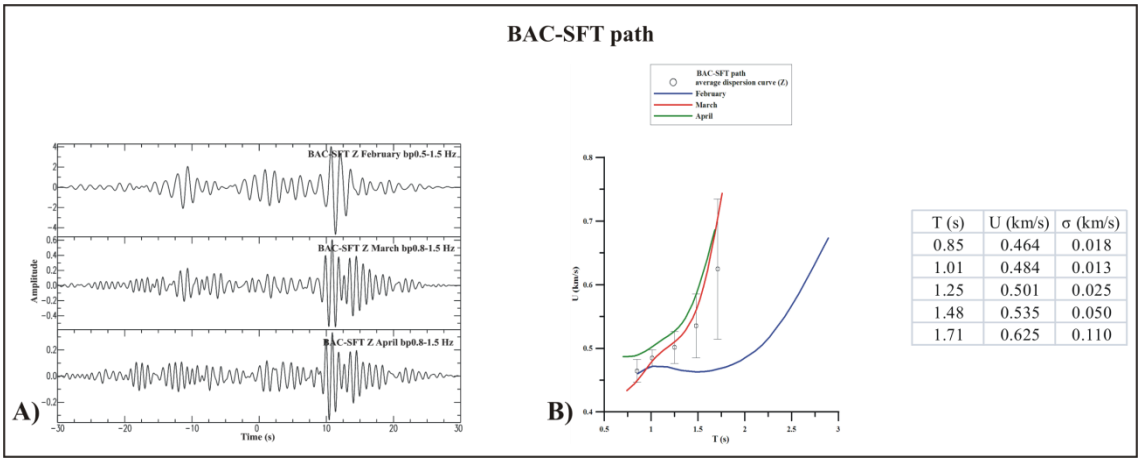

Fig.3.47 *– Monthly stacked NCFs (vertical component) of February, March and April computed for BAC-SFT path (A) and average group velocity dispersion curve with error bar (B).*

NCFs computed for the BAC-STH path (Fig.3.1) don't present a good signal-to-noise ratio (Fig.3.48A), in fact the extracted monthly dispersion curves have very different trend (Fig.3.48B). Moreover the obtained average dispersion curve covers a very short period range: for these reasons it hasn't been considered for later inversion.

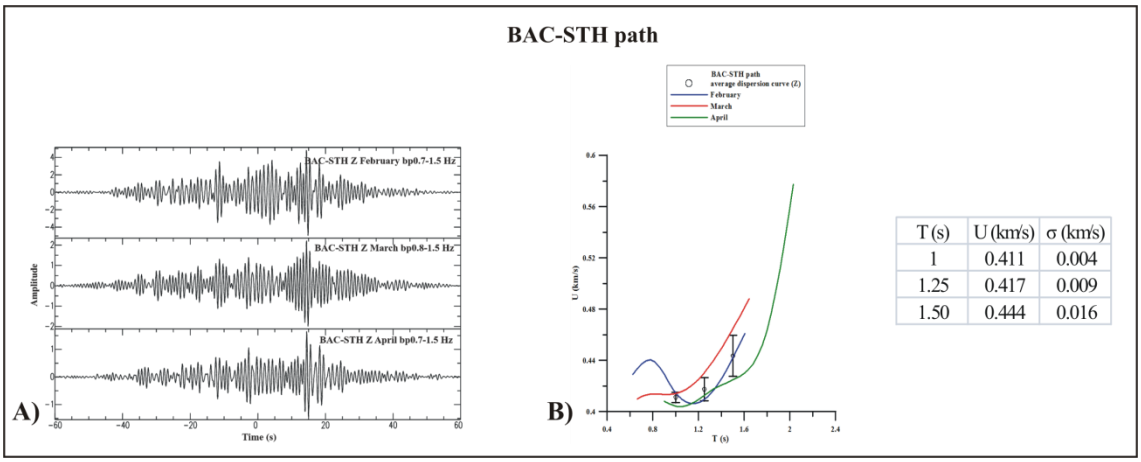

T (s)	U (km/s)	σ (km/s)
1	0.411	0.004
1.25	0.417	0.009
1.50	0.444	0.016

Fig.3.48 *– Monthly stacked NCFs (vertical component) of February, March and April computed for BAC-STH path (A) and average group velocity dispersion curve with error bar (B).*

Monthly dispersion curves relative to the CSOB-SMN and SFT-SMN paths (Fig.3.1) define a common trend in the same period and group velocity ranges, while those ones relative to the STH-SMN path (Fig.3.1) are strongly different from the previous ones. Moreover monthly dispersion curves extracted from NCFs having a lower signal-to-noise ratio (i.e. February of CSOB-SMN and April of SFT-SMN) (Fig.3.49A-B) have been excluded, as also the curve relative to February of SFT-SMN. The average group velocity dispersion curve representative of the SOLF-SMN path is characterized by periods ranging from 0.97 to 2.22 s and group velocities from ~0.58 to ~0.89 km/s (Fig.3.49D).

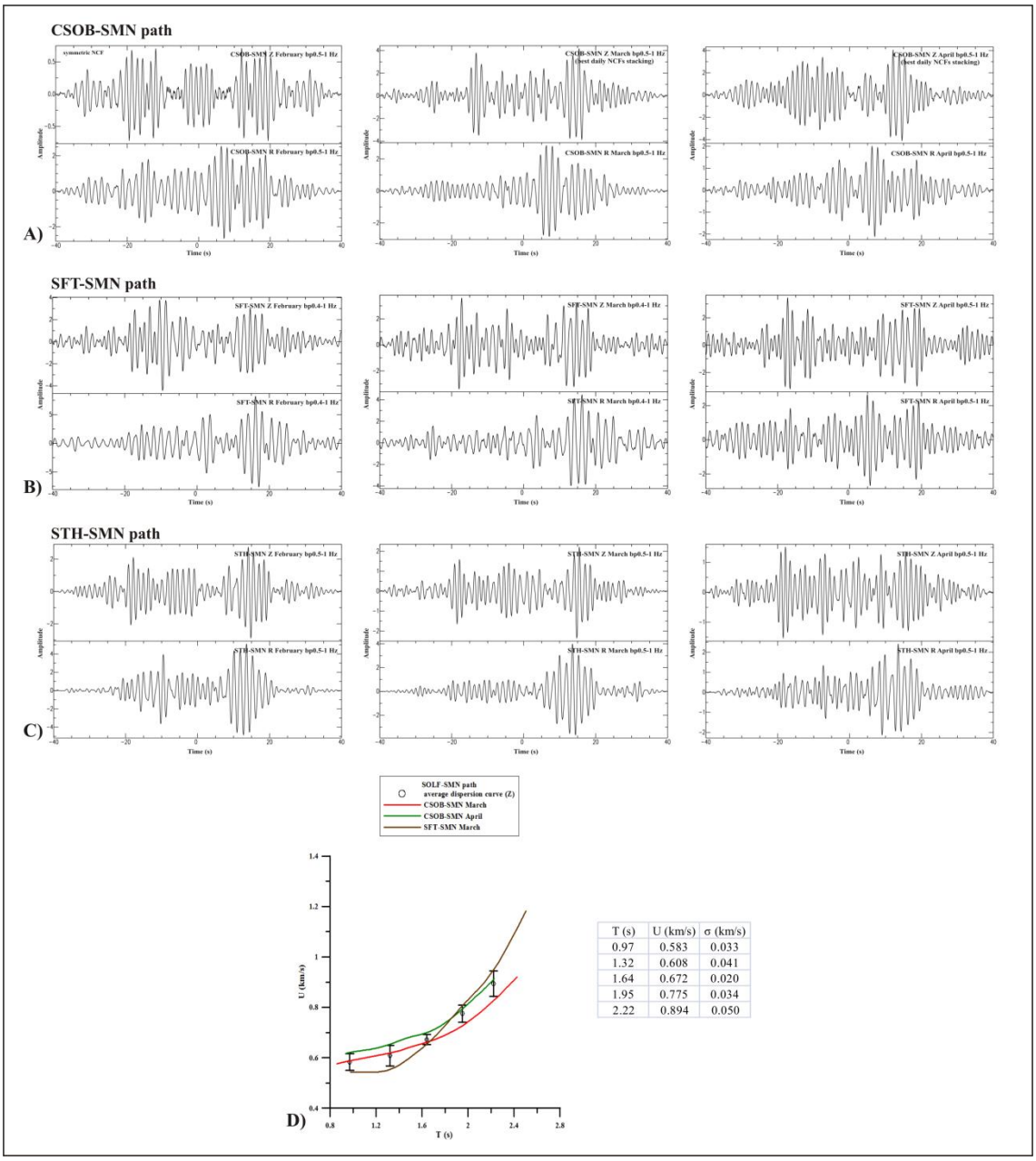

T (s)	U (km/s)	σ (km/s)
0.97	0.583	0.033
1.32	0.608	0.041
1.64	0.672	0.020
1.95	0.775	0.034
2.22	0.894	0.050

Fig.3.49 *– Stacked NCFs (vertical and radial components) of February, March and April computed for CSOB-SMN (A), SFT-SMN (B) and STH-SMN (C) paths and average group velocity dispersion curve with error bar relative to NCFs vertical component computed for SOLF-SMN path (D).*

Unfortunately NCFs were not stable along the CUMA-SMN path (Fig.3.50), the longest path (17 km) (Fig.3.1). The NCF analysis has been performed in narrower and narrower frequency ranges trying to increase the signal-to-noise ratio, but without success.

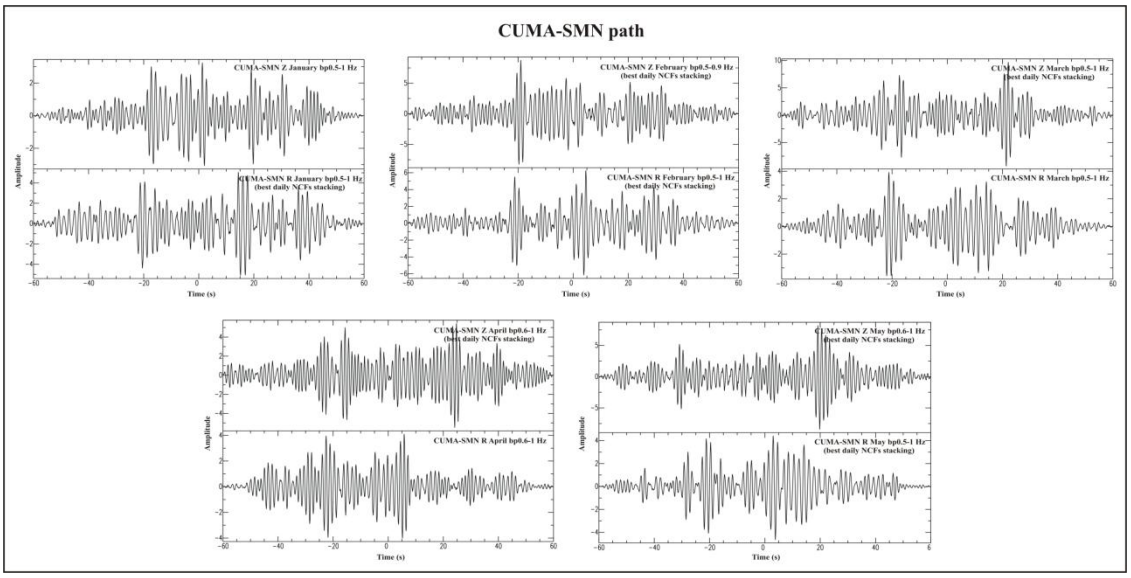

Fig.3.50 *– Stacked NCFs (vertical and radial components) of January, February, March, April and May computed for CUMA-SMN path.*

The computed NCFs for the DMP-SMN path (Fig.3.1) present a low signal-to-noise ratio (Fig.3.51A). Despite the average group velocity dispersion curve with a little error bar (Fig.3.51B), the data haven't been considered reliable to be inverted.

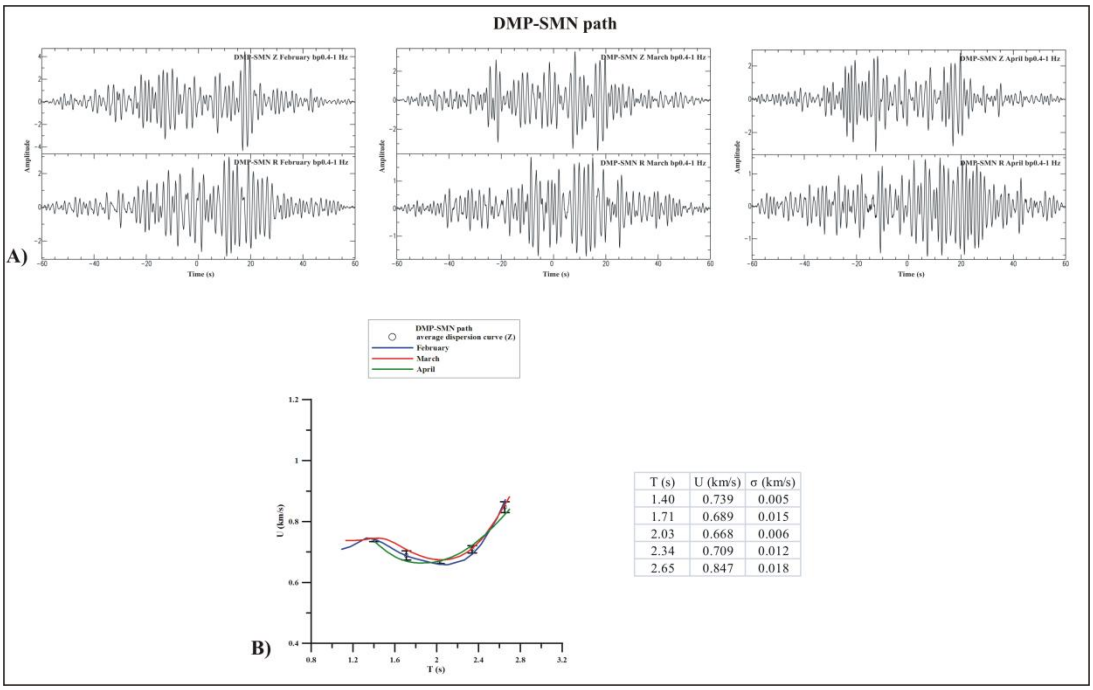

Fig.3.51 *– Monthly stacked NCFs (vertical and radial components) of February, March and April computed for DMP-SMN path (A) and average group velocity dispersion curve with error bar relative to NCFs vertical component (B).*

The three monthly dispersion curves extracted from the vertical stacked NCFs (Fig.3.52A) computed for the NIS-ARCO path (Fig.3.1) have been averaged in 1.25-2.1 s period range and ~0.71-1 km/s group velocity range (Fig.3.52B).

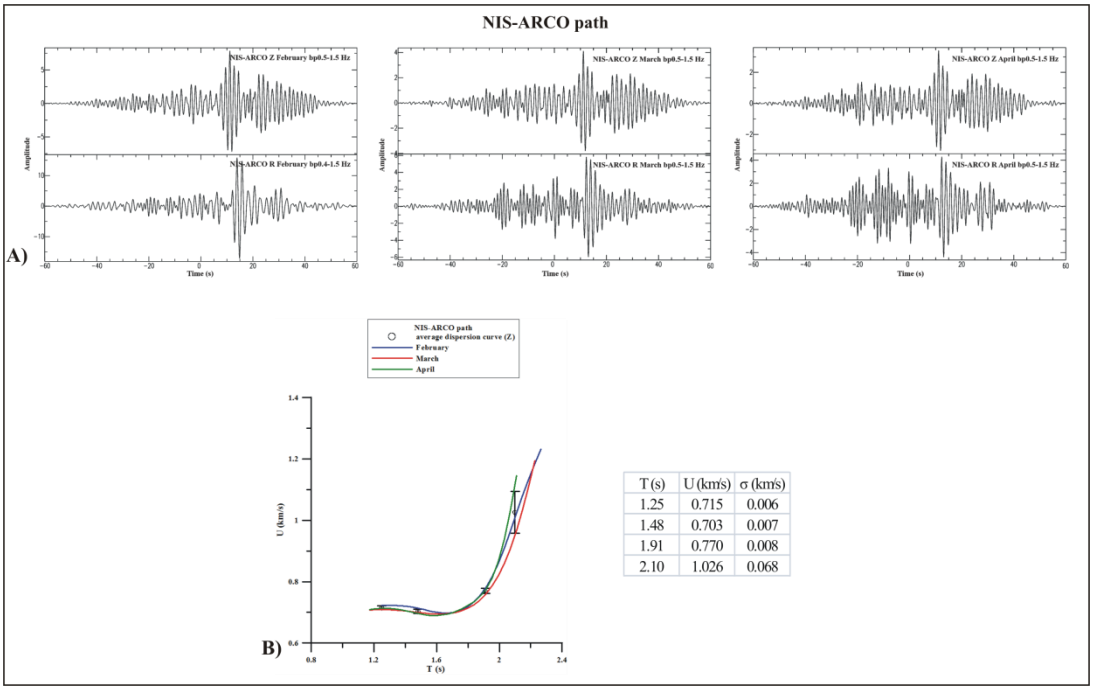

Fig.3.52 *– Monthly stacked NCFs (vertical and radial components) of February, March and April computed for NIS-ARCO path (A) and average group velocity dispersion curve with error bar relative to NCFs vertical component (B).*

The three monthly dispersion curves extracted from the vertical stacked NCFs (Fig.3.53A) computed for the NIS-CMSA path (Fig.3.1) have been averaged in ~1-2 s period range and ~0.6-0.89 km/s group velocity range (Fig.3.53B).

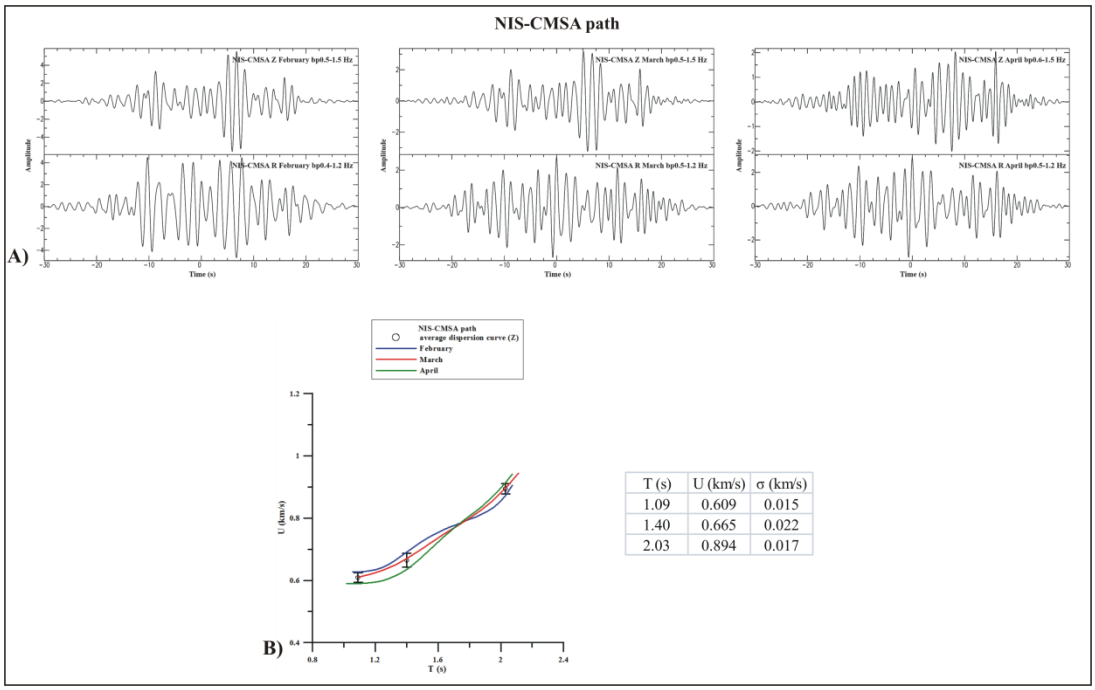

T (s)	U (km/s)	σ (km/s)
1.09	0.609	0.015
1.40	0.665	0.022
2.03	0.894	0.017

Fig.3.53 *– Monthly stacked NCFs (vertical and radial components) of February, March and April computed for NIS-CMSA path (A) and average group velocity dispersion curve with error bar relative to NCFs vertical component (B).*

NCFs computed for the NIS-CSOB path (Fig.3.1) are not stable and characterized by different waveforms (Fig.3.54A). Dispersion curves were not considered for the later inversion (Fig.3.54B).

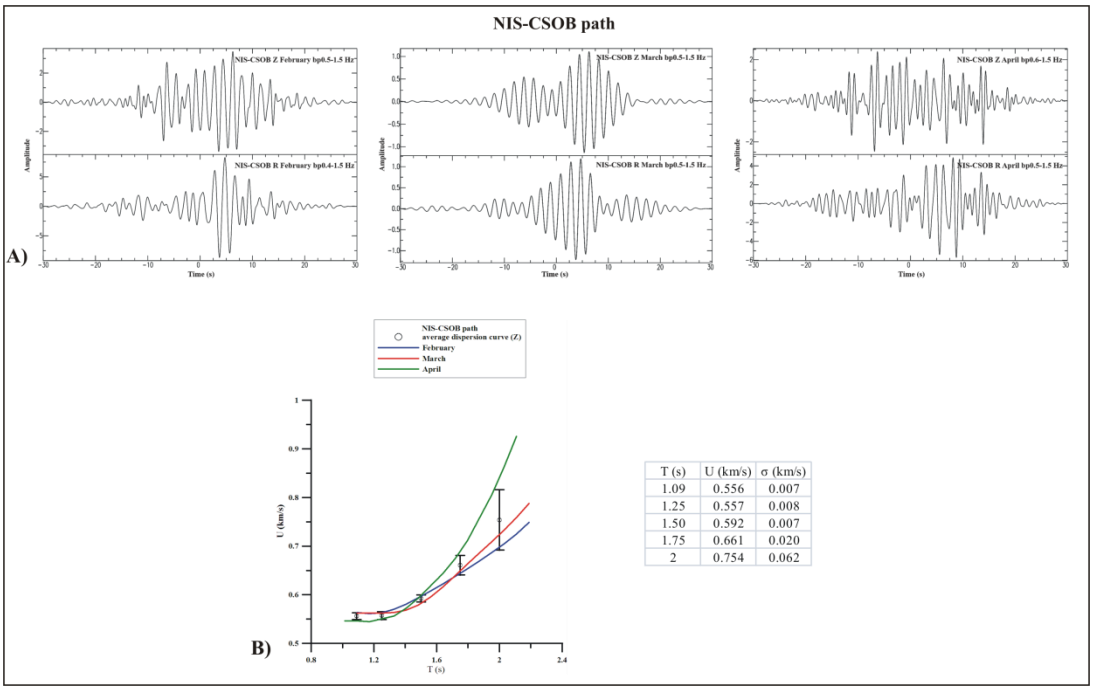

T (s)	U (km/s)	σ (km/s)
1.09	0.556	0.007
1.25	0.557	0.008
1.50	0.592	0.007
1.75	0.661	0.020
2	0.754	0.062

Fig.3.54 *– Monthly stacked NCFs (vertical and radial components) of February, March and April computed for NIS-CSOB path (A) and average group velocity dispersion curve with error bar relative to NCFs vertical component (B).*

NCFs computed for the NIS-DMP path (Fig.3.1) present very different and not stable waveforms (Fig.3.55).

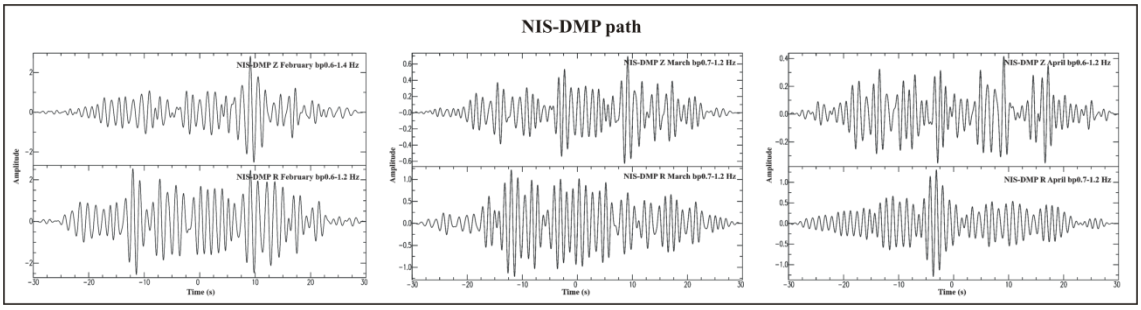

Fig.3.55 *– Monthly stacked NCFs (vertical and radial components) of February, March and April computed for NIS-DMP path.*

Although the NCFs computed for the NIS-QUAR path (Fig.3.1) present a quite low signal-to-noise ratio (Fig.3.56A), FTAN maps of the vertical component showed a clear region of energy maxima, which allowed to extract three coherent dispersion curves. The average group velocity dispersion curve has been computed in ~1-2 s period range and ~0.7-0.92 km/s group velocity range (Fig.3.56B).

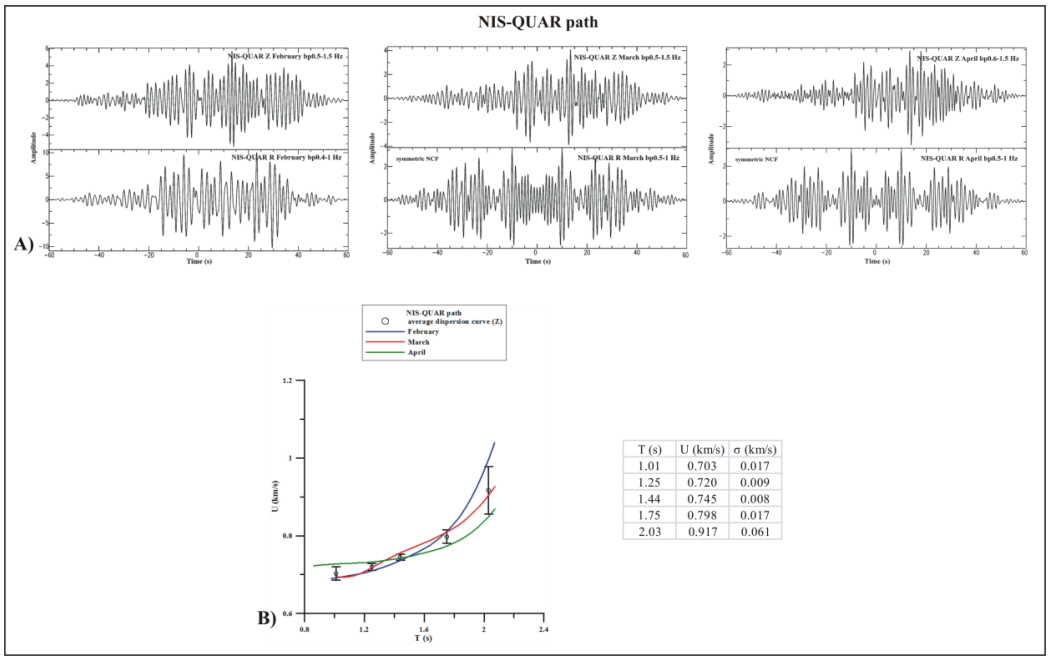

T (s)	U (km/s)	σ (km/s)
1.01	0.703	0.017
1.25	0.720	0.009
1.44	0.745	0.008
1.75	0.798	0.017
2.03	0.917	0.061

Fig.3.56 *– Monthly stacked NCFs (vertical and radial components) of February, March and April computed for NIS-QUAR path (A) and average group velocity dispersion curve with error bar relative to NCFs vertical component (B).*

The average group velocity dispersion curve obtained for the NIS-SFT path (Fig.3.1) has been computed among two vertical and two radial monthly dispersion curves (Fig.3.57B). But, excluding the point at the greatest period (being characterized by a big error bar), the curve covers a very short period range, so it hasn't been inverted by the Hedgehog method.

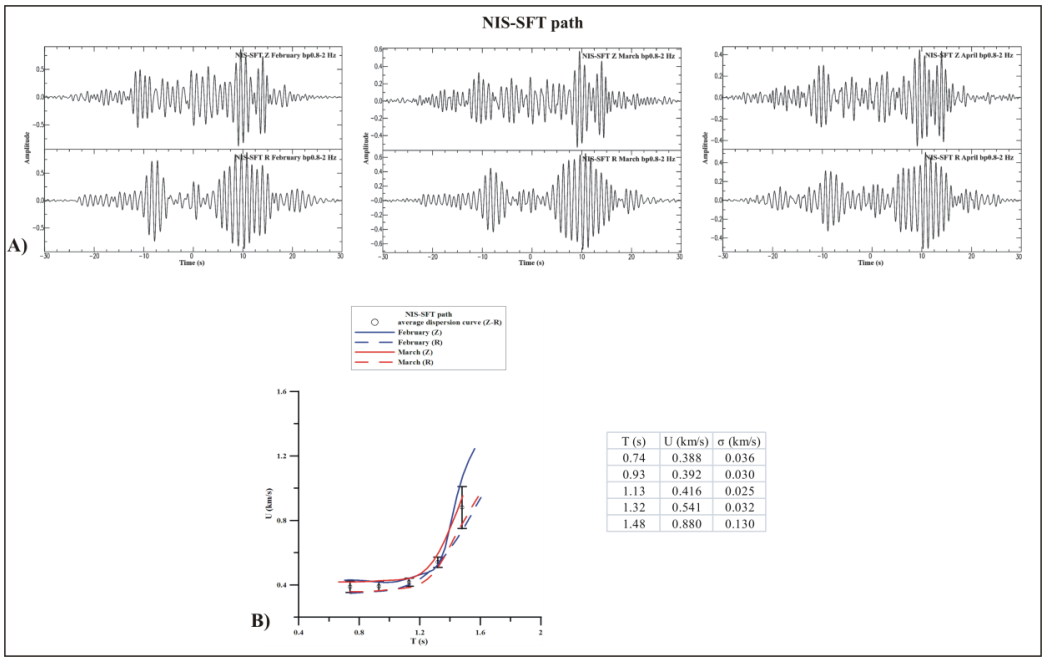

T (s)	U (km/s)	σ (km/s)
0.74	0.388	0.036
0.93	0.392	0.030
1.13	0.416	0.025
1.32	0.541	0.032
1.48	0.880	0.130

Fig.3.57 *– Monthly stacked NCFs (vertical and radial components) of February, March and April computed for NIS-SFT path (A) and average group velocity dispersion curve with error bar (B).*

As explained before, also in the case of the NIS-SMN path (Fig.3.1) NCFs are not characterized by a great signal-to-noise ratio (Fig.3.58A), but clear FTAN maps allowed to extract similar monthly dispersion curves which have been averaged in 0.93-2.1 s period range and ~0.58-0.91 km/s group velocity range (Fig.3.58B).

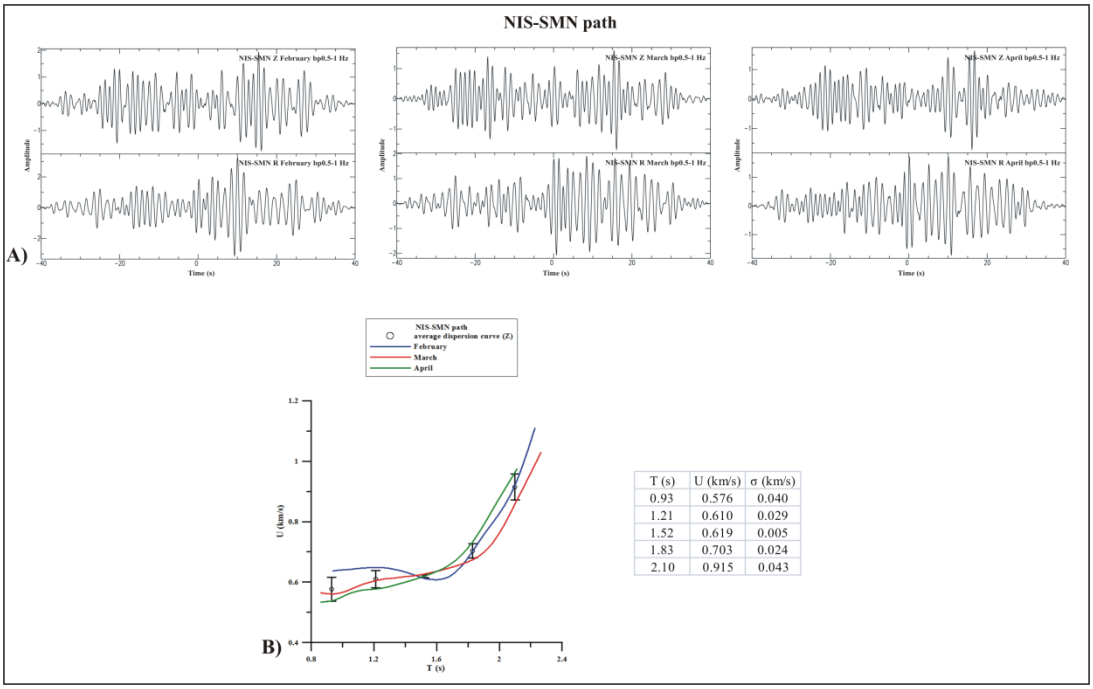

T (s)	U (km/s)	σ (km/s)
0.93	0.576	0.040
1.21	0.610	0.029
1.52	0.619	0.005
1.83	0.703	0.024
2.10	0.915	0.043

Fig.3.58 *– Monthly stacked NCFs (vertical and radial components) of February, March and April computed for NIS-SMN path (A) and average group velocity dispersion curve with error bar relative to NCFs vertical component (B).*

Although the average group velocity dispersion curve relative to the NIS-STH path (Fig.3.1) covers a narrow period range, it has been preferred to the average dispersion curves relative to NIS-CSOB and NIS-SFT paths (Figs.3.54B-3.57B respectively). Monthly dispersion curves relative to the NIS-STH path have been extracted from more stable NCFs (Fig.3.59A) and clear FTAN maps. So the average dispersion curve computed for the NIS-STH path in 1-1.5 s period range and 0.41-0.52 km/s group velocity range (Fig.3.59B) has been inverted by Hedgehog non-linear inversion method.

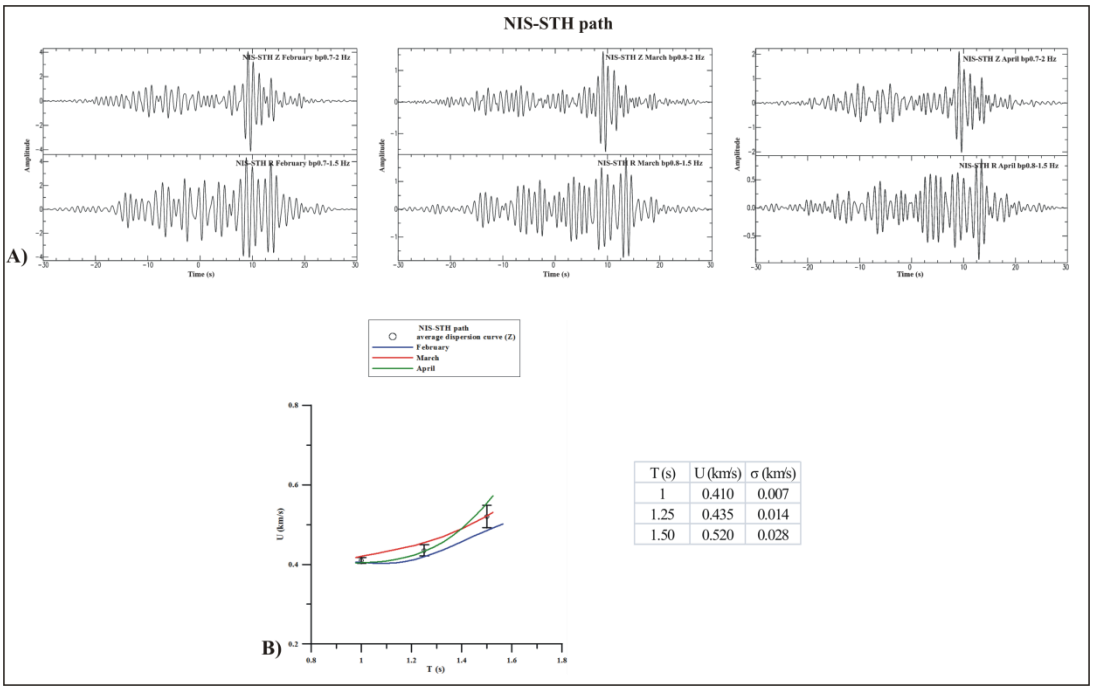

T (s)	U (km/s)	σ (km/s)
1	0.410	0.007
1.25	0.435	0.014
1.50	0.520	0.028

Fig.3.59 *– Monthly stacked NCFs (vertical and radial components) of February, March and April computed for NIS-STH path (A) and average group velocity dispersion curve with error bar relative to NCFs vertical component (B).*

The three monthly dispersion curves extracted from the vertical stacked NCFs (Fig.3.60A) computed for the POZ-ARCO path (Fig.3.1) have been averaged in 0.89-1.6 s period range and ~0.65-0.89 km/s group velocity range (Fig.3.60B).

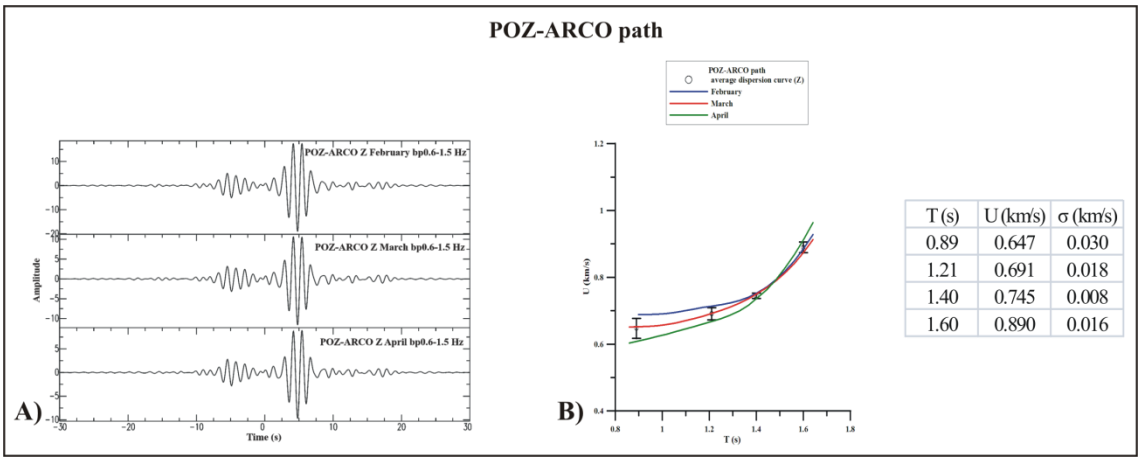

T (s)	U (km/s)	σ (km/s)
0.89	0.647	0.030
1.21	0.691	0.018
1.40	0.745	0.008
1.60	0.890	0.016

Fig.3.60 *– Monthly stacked NCFs (vertical component) of February, March and April computed for POZ-ARCO path (A) and average group velocity dispersion curve with error bar (B).*

The three monthly dispersion curves extracted from the vertical stacked NCFs (Fig.3.61A) computed for the POZ-CMSA path (Fig.3.1) have been averaged in 1-1.75 s period range and ~0.62-0.92 km/s group velocity range (Fig.3.61B).

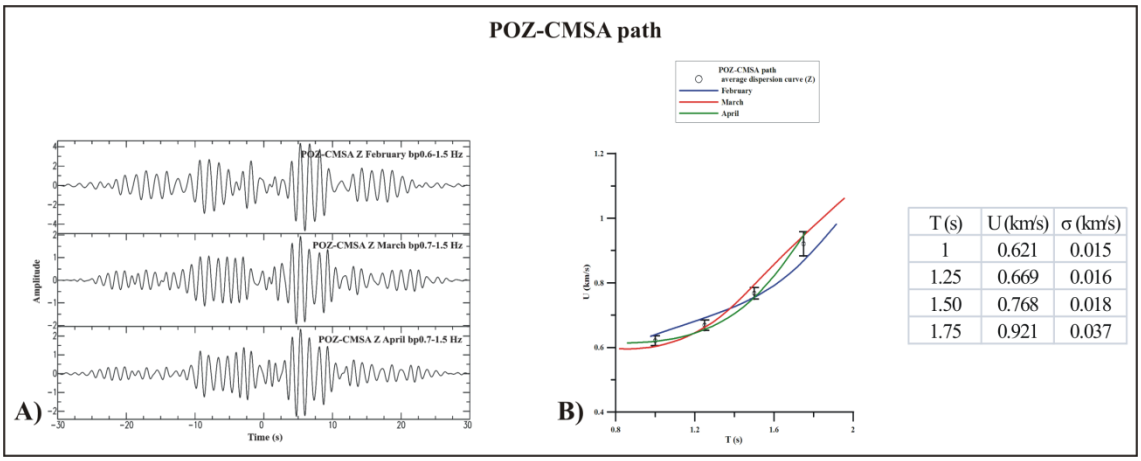

T (s)	U (km/s)	σ (km/s)
1	0.621	0.015
1.25	0.669	0.016
1.50	0.768	0.018
1.75	0.921	0.037

Fig.3.61 *– Monthly stacked NCFs (vertical component) of February, March and April computed for POZ-CMSA path (A) and average group velocity dispersion curve with error bar (B).*

NCFs relative to the POZ-CSOB, POZ-SFT and POZ-STH paths (Fig.3.1) are characterized by a very high signal-to-noise ratio (Fig.3.62A-B-C). Comparing the nine extracted dispersion curves, those relative to the POZ-CSOB and POZ-STH paths show the same trend, different from that of the POZ-SFT path (Fig.3.62D). Hence the average group velocity dispersion curve relative to the POZ-SOLF path has been computed among POZ-CSOB and POZ-STH monthly dispersion curves: its periods range from 0.89 to 1.4 s and group velocities from 0.68 to 0.8 km/s (Fig.3.62E).

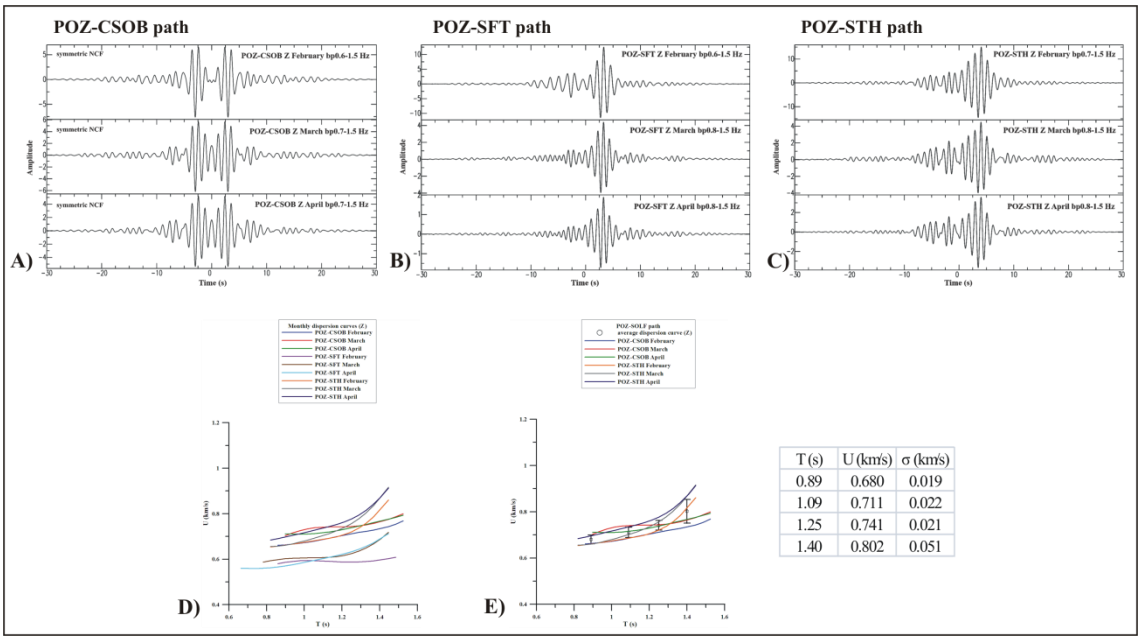

T (s)	U (km/s)	σ (km/s)
0.89	0.680	0.019
1.09	0.711	0.022
1.25	0.741	0.021
1.40	0.802	0.051

Fig.3.62 *– Monthly stacked NCFs (vertical component) of February, March and April computed for POZ-CSOB (A), POZ-SFT (B) and POZ-STH (C) paths and average group velocity dispersion curve with error bar computed for POZ-SOLF path (E).*

The average group velocity dispersion curve computed for the POZ-DMP path (Fig.3.1) hasn't been inverted, because it covers a very narrow period range (Fig.3.63B).

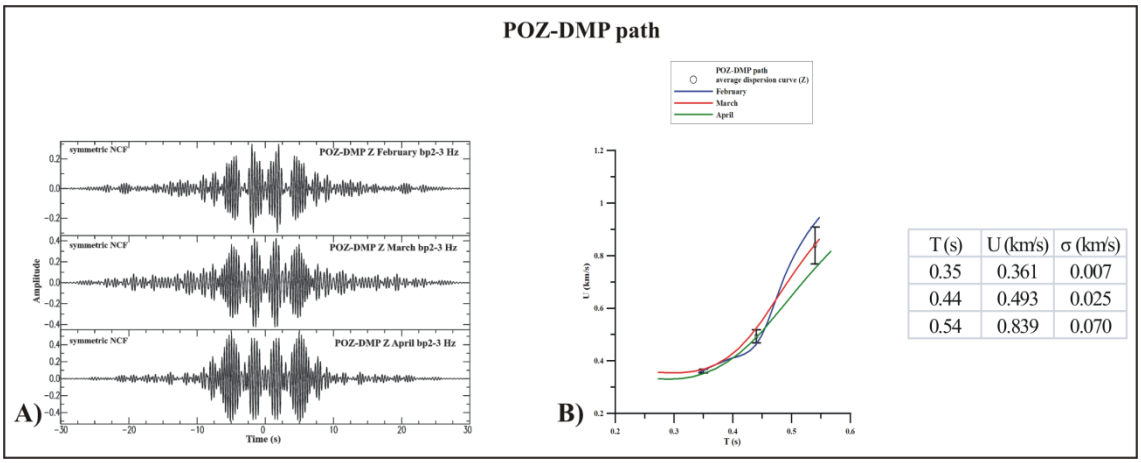

T (s)	U (km/s)	σ (km/s)
0.35	0.361	0.007
0.44	0.493	0.025
0.54	0.839	0.070

Fig.3.63 *– Monthly symmetric stacked NCFs (vertical component) of February, March and April computed for POZ-DMP path (A) and average group velocity dispersion curve with error bar (B).*

The three monthly dispersion curves extracted from the vertical stacked NCFs (Fig.3.64A) computed for the POZ-NIS path (Fig.3.1) have been averaged in 0.82-1.75 s period range and ~0.31-0.41 km/s group velocity range (Fig.3.64B).

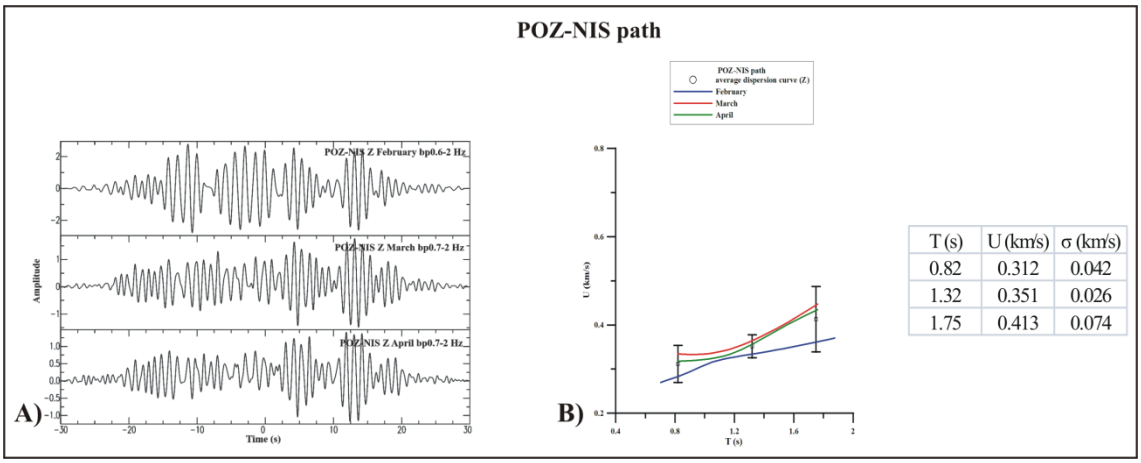

T (s)	U (km/s)	σ (km/s)
0.82	0.312	0.042
1.32	0.351	0.026
1.75	0.413	0.074

Fig.3.64 *– Monthly stacked NCFs (vertical component) of February, March and April computed for POZ-NIS path (A) and average group velocity dispersion curve with error bar (B).*

The vertical stacked NCFs computed for the POZ-QUAR path (Fig.3.1) show stability and a good signal-to-noise ratio (Fig.3.65A). The average group velocity dispersion curve has been computed in 1.17-1.79 s period range and ~0.43-0.55 km/s group velocity range (Fig.3.65B).

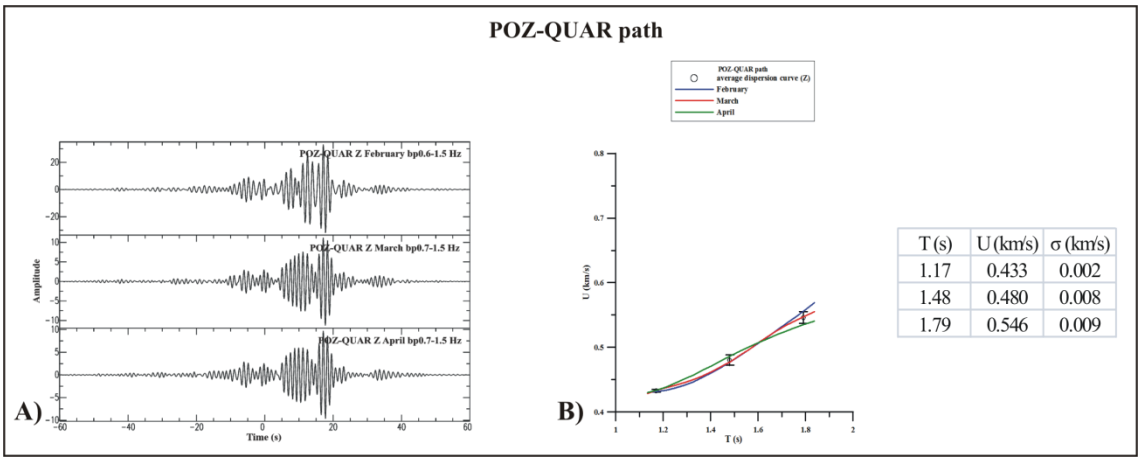

T (s)	U (km/s)	σ (km/s)
1.17	0.433	0.002
1.48	0.480	0.008
1.79	0.546	0.009

Fig.3.65 *– Monthly stacked NCFs (vertical component) of February, March and April computed for POZ-QUAR path (A) and average group velocity dispersion curve with error bar (B).*

Despite the stability of the stacked NCFs (Fig.3.66A) computed for the POZ-SMN path (Fig.3.1), the dispersion curves present very different trends. Hence the average group velocity dispersion curve is characterized by a very big error bar (Fig.3.66B) and hasn't been later inverted.

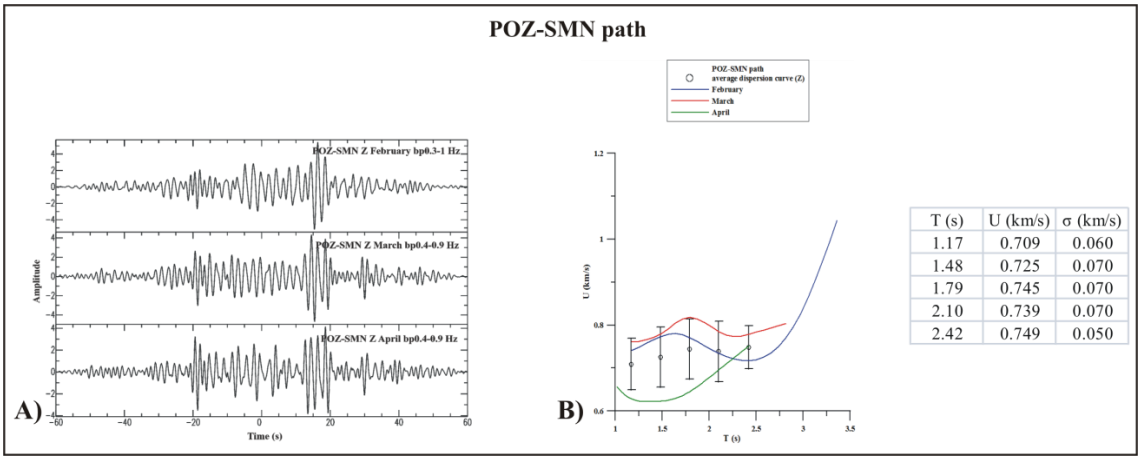

T (s)	U (km/s)	σ (km/s)
1.17	0.709	0.060
1.48	0.725	0.070
1.79	0.745	0.070
2.10	0.739	0.070
2.42	0.749	0.050

Fig.3.66 *– Monthly stacked NCFs (vertical component) of February, March and April computed for POZ-SMN path (A) and average group velocity dispersion curve with error bar (B).*

The average group velocity dispersion curve relative to the QUAR-CMSA path (Fig.3.1) has been computed among vertical and radial monthly dispersion curves: its periods range from 1.09 to 2.26 s and group velocities from ~0.49 to ~0.75 km/s (Fig.3.67B).

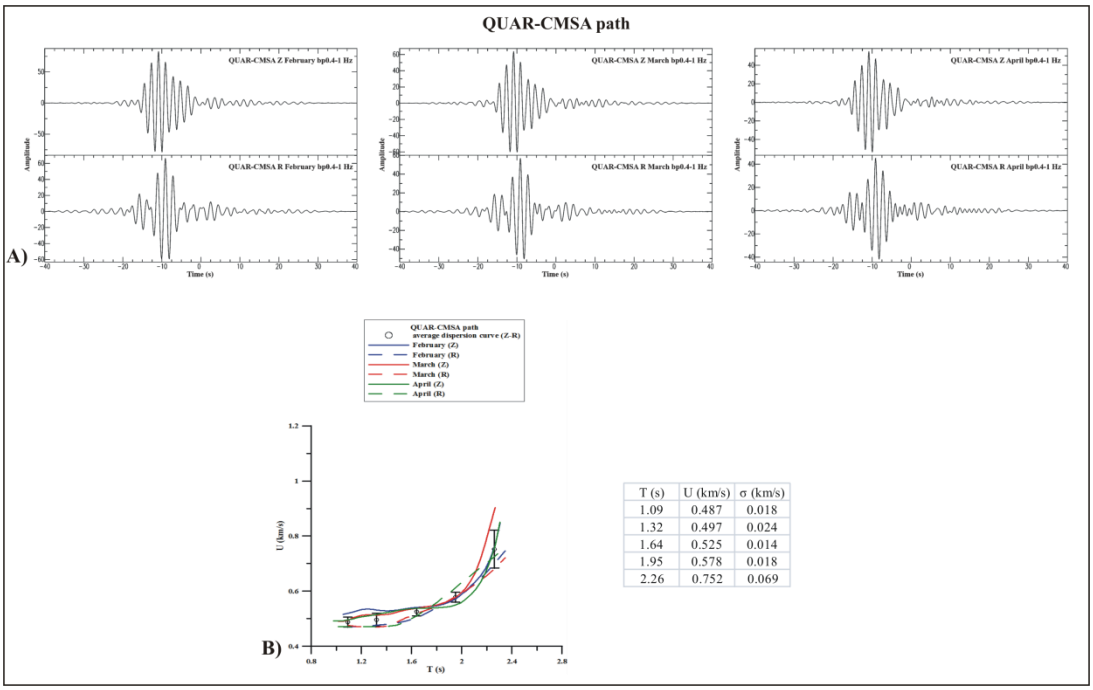

T (s)	U (km/s)	σ (km/s)
1.09	0.487	0.018
1.32	0.497	0.024
1.64	0.525	0.014
1.95	0.578	0.018
2.26	0.752	0.069

Fig.3.67*– Monthly stacked NCFs (vertical and radial components) of February, March and April computed for QUAR-CMSA path (A) and average group velocity dispersion curve with error bar (B).*

The average group velocity dispersion curve relative to the QUAR-DMP path (Fig.3.1) has been computed among monthly dispersion curve extracted from NCFs showing similar waveforms (Fig.3.68A), but from very confused FTAN maps. So the average dispersion curve (Fig.3.68B) hasn't been considered so much reliable to perform the Hedgehog non-linear inversion.

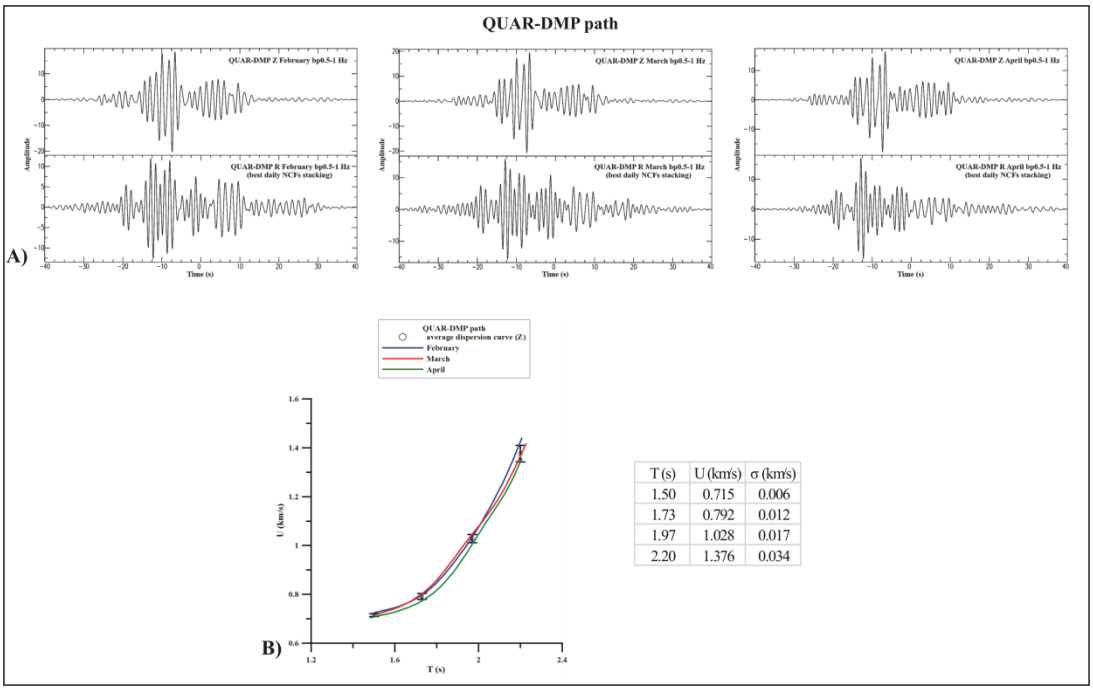

Fig.3.68 *– Stacked NCFs (vertical and radial components) of February, March and April computed for QUAR-DMP path (A) and average group velocity dispersion curve with error bar relative to NCFs vertical component (B).*

3.5 Summary of group velocity dispersion curves

Although some difficulties encountered during the analysis phases, results obtained by the application of cross-correlation method in Campi Flegrei can be considered satisfactory. For most of the paths, in fact, monthly NCFs (Green functions of the medium), computed in February-April 2010, are stable in terms of frequency content and waveforms. Consequently average group velocity dispersion curves computed for such paths are characterized by small error bars.

For most of the paths only vertical components have been reliable. Three paths (i.e. QUAR-CSOB, QUAR-SFT and QUAR-STH) presented better results on radial components. Three paths (i.e. ARCO-DMP, NIS-SFT and QUAR-CMSA) have given good results for vertical and radial components.

In the light of the results obtained by the cross-correlation and the FTAN analyses (summarized in the previous section), average group velocity dispersion curves relative to 25 paths (marked by (*) in Tab.3.2) are resulted reliable to perform the Hedgehog non-linear inversion and obtain V_S profiles vs. depth. In Fig.3.69 these average group velocity dispersion curves of Rayleigh wave fundamental modes with the relative error bars are shown by grouping paths having common station as master. Average group velocity

dispersion curves obtained and inverted by Costanzo (2011) for the CMSA-SMN and QUAR-SMN paths are also included for a total of 27 investigated paths.

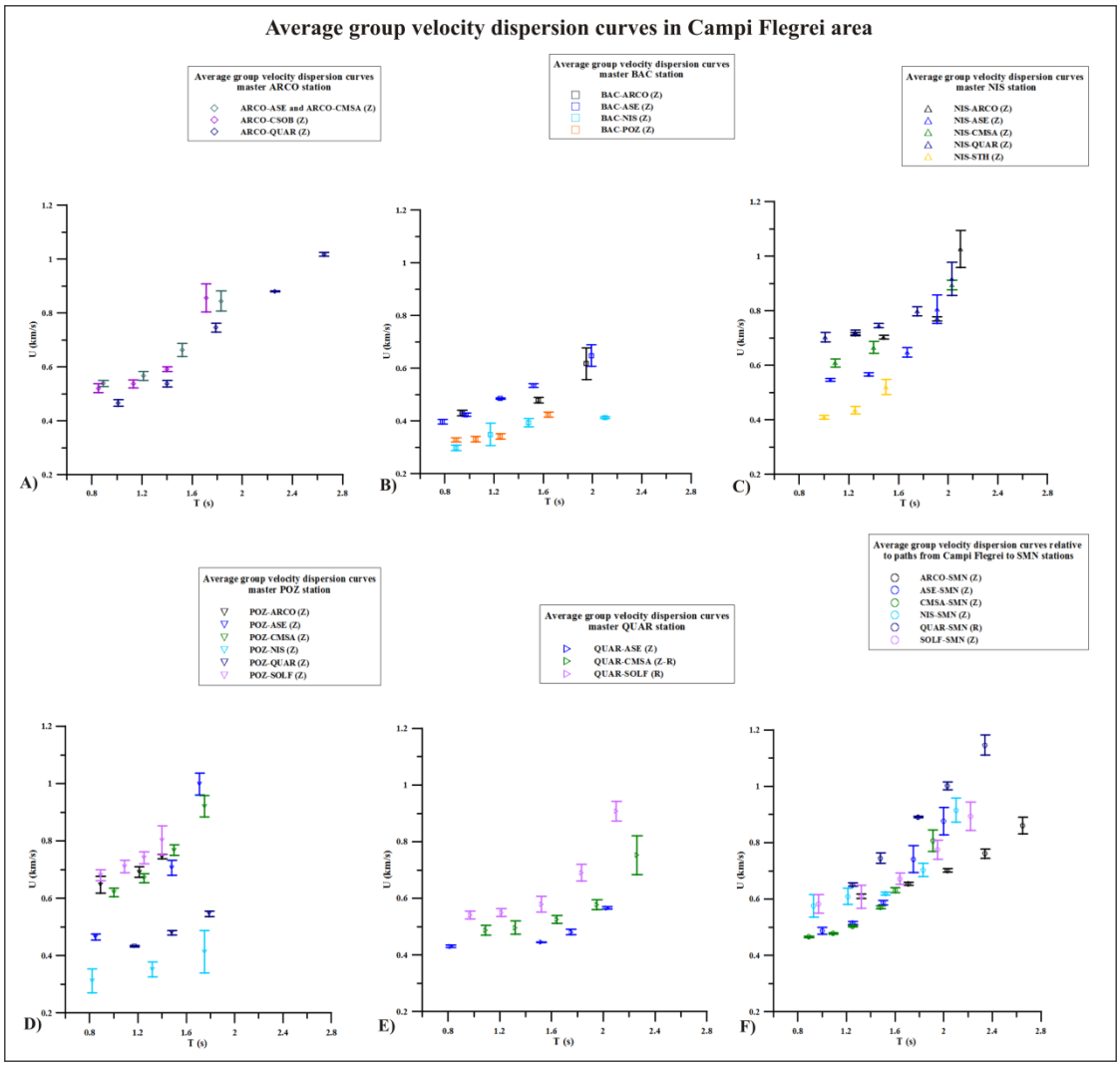

Fig.3.69 *– Average group velocity dispersion curves of Rayleigh wave fundamental mode with the relative error bars along 27 paths (located in Fig.3.70) crossing Campi Flegrei area. Average dispersion curves are presented in six different graphs, being grouped according to the stations used as master for computing NCFs.*

It can be observed that the lowest group velocities characterize the paths crossing the Gulf of Pozzuoli, i.e. paths having BAC station as master (Fig.3.69B) and POZ-NIS path (Fig3.69D). Paths with POZ station as master (Fig3.69D) show wide variation of average dispersion curves. In particular an evident difference exists between POZ-NIS curve and the other ones: this may be due to the different geological setting of the Gulf of Pozzuoli area and the onshore sector of the caldera.

The 27 paths cross different sectors of Campi Flegrei area (Fig.3.70) and a correlation can be performed to evidence differences or common features existing among the Gulf of Pozzuoli, the onshore portion and the marginal areas of the Campi Flegrei caldera.

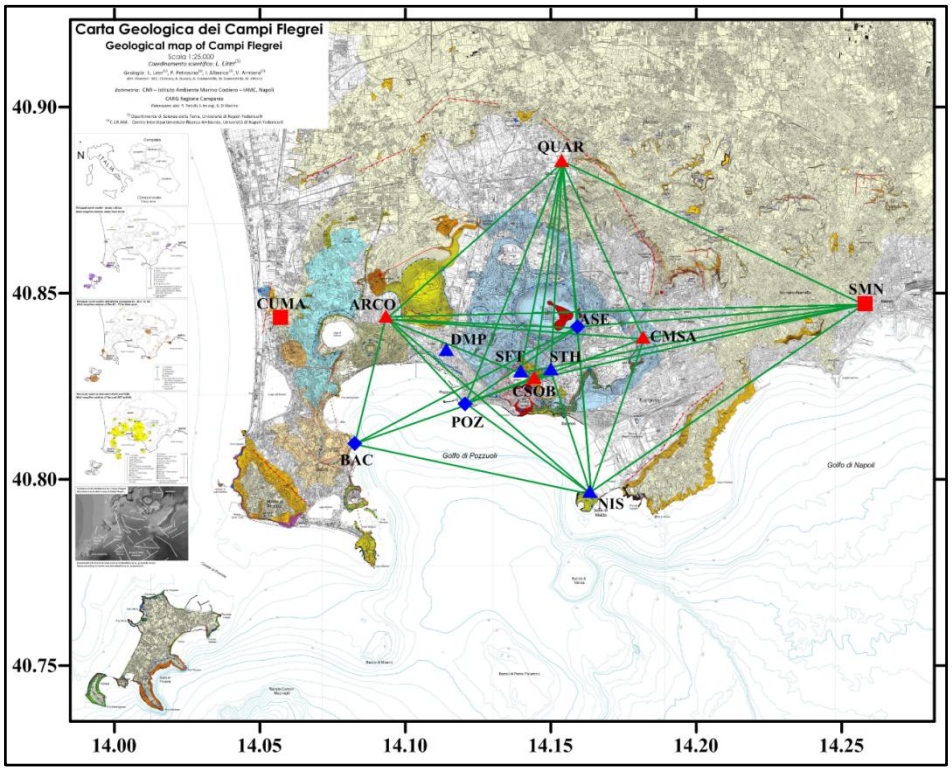

Fig.3.70 *– Paths crossing Campi Flegrei area (green lines) for which the average group velocity dispersion curves of Rayleigh wave fundamental mode has been computed (shown in Fig.3.69).*

Chapter 4

ANALYSIS OF SEISMIC NOISE CROSS-CORRELATION FUNCTIONS AT ISCHIA

4.1 Seismic noise data set

Seismic noise data have been acquired at Ischia by using 2 seismographs Tromino Micromed and a broad-band station (at ISC site in the town of Ischia) (Tab.4.1) belonging to the Osservatorio Geofisico (see 3.1 section) in order to perform cross-correlation between synchronous recordings at two stations. A total of 14 paths have been investigated (Fig.4.1) during two different field surveys: 5 paths along the edges of the island in June 2011, and 9 paths crossing the central part of Ischia in September-October 2012 (Tab.4.2).

Ischia measurement sites				
Station location	**Station name**	**Latitude**	**Longitude**	**Sensor type**
East Testaccio	ETES	40.7063	13.9283	Tromino Micromed
Ischia town	ISC	40.7296	13.9383	BB-3C
Ischia Harbour	ISCH	40.7425	13.9431	Tromino Micromed
Mortella	MOR	40.7549	13.8717	Tromino Micromed
Negombo	NEG	40.7568	13.8790	Tromino Micromed
North Forio	NFOR	40.7380	13.8569	Tromino Micromed
North Piano Liguori	NPL	40.7215	13.9490	Tromino Micromed
Perrone	PER	40.7485	13.9149	Tromino Micromed
Sant'Angelo	SAN	40.7022	13.8901	Tromino Micromed
South Forio	SFOR	40.7163	13.8640	Tromino Micromed
South Piano Liguori	SPL	40.7188	13.9507	Tromino Micromed
Succhivo	SUC	40.7015	13.8838	Tromino Micromed
West Testaccio	WTES	40.7062	13.9193	Tromino Micromed

Tab.4.1 *- Measurement sites at Ischia island. Geographical coordinates and sensor types are given for each station.*

In the first field survey, noise was simultaneously recorded for some hour, depending on the two receiver distance. The analysis of the cross-correlation functions suggested to increase the time duration of the recordings so that, in the second field survey, recordings of 20 hours were acquired (Tab.4.2).

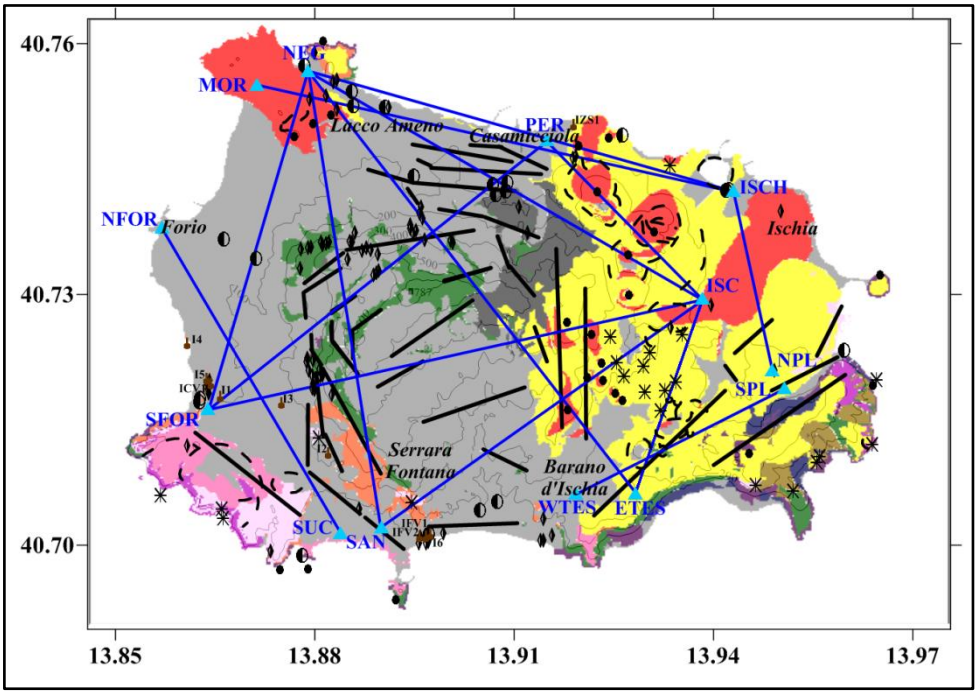

Fig.4.1 *- Measurement sites (light blue triangles) used to compute NCF along 14 analysed paths (blue lines) crossing Ischia island (see the legend of the simplified geological map of Ischia in Fig.1.32).*

Path	*Receiver distance (km)*	*Recording length*	*Frequency range (Hz)*
First set of measurement (June 2011)			
ISCH –MOR	6.2	3 h	0.5 – 1.5
ISCH –NEG	5.6	4 h	0.4 – 1
ISCH –NPL	2.4	9 h	0.5 – 1.5
SPL –WTES	3	2 h	0.7 – 2
SUC –NFOR	4.6	2 h	0.4 – 1.2
Second set of measurement (September-October 2012)			
ISC –ETES	2.7	20 h	0.6 – 1.5
ISC –NEG	5.8	20 h	0.6 – 1.2
ISC –PER	2.9	20 h	0.5 – 1.5
ISC –SAN	5.1	20 h	0.6 – 1.5
NEG –ETES	7	20 h	0.6 – 1.5
NEG –SAN	6.1	20 h	0.5 – 1.5
NEG –SFOR	4.7	20 h	0.7 – 1.5
PER –SFOR	5.6	20 h	0.7 – 1.5
SFOR –ISC	6.4	20 h	0.5 – 1.5

Tab.4.2 *- Paths, receiver distance, recording length and used frequency range in the computation of the noise cross-correlation functions at Ischia.*

4.2 Cross-correlation and FTAN analysis

4.2.1 Preliminary considerations and pre-processing of single-station data

Signals acquired by Trominos at 128 Hz sampling rate have been converted from ascii to sac format, and interpolated to 20 Hz (Q330 sampling rate); then average has been

removed, high-pass filtered (> 0.05 Hz) with a Butterworth filter and tapered in order to remove the low frequency trend.

Accelerometer data acquired at ISC site have been extracted from the continuous signal archived by the Kinemetrics Q330 station, according to data recorded by Tromino for the cross-correlation analysis. Then processing steps as explained in 3.2.2 section have been applied.

Synchronous recordings of vertical and radial components at two receivers have been cross-correlated. First of all NCFs have been computed and Fourier transformed in order to recognize the main energy content in the frequency domain (Tab.4.2). Moreover NCFs have been computed by using 20 and 30 s time windows, in order to improve the signal-to-noise ratio. For all the paths, except ISCH-NEG path, time windows of 20 s gave better results.

For all paths, the energy of the NCFs is mainly concentrated at very low frequencies, i.e. in 0.1-0.2 Hz range, with minor content at 2 Hz, but these frequencies are not of interest for this study as, if we take into account the geological setting and the relation between the maximum sampled wavelength and the maximum investigated thickness (see 3.2.1 section for more details), it turns out that 1 km depth at best has been realistically reached in this study. In fact, geological data available in literature (see 1.2.1 section) suggest the presence of tuffs (in facies from highly fractured to compact) and lavas in the shallower 1 km of subsoil. Average V_S values of 0.6 km/s can be reasonably attributed to fractured tuffs, of 0.8 km/s to compact tuff and of 2.5 km/s to lavas (like measured in the Neapolitan urban area by Nunziata et al. (2004; 2012) (see 3.2.1 section)), with average phase velocities (c) varying from 0.5 to 2.2 km/s, so a minimum sampled frequency (ν) of ~0.3 Hz ($c=\lambda\nu$) can be estimated for the path distances. Hence the cross-correlation analysis has been focused in the frequency band 0.3-2 Hz. Frequency ranges of cross-correlation analysis are reported for each path in Tab.4.2.

For each path several cross-correlation functions have been computed in narrower and narrower frequency ranges to emphasize surface wave train. Then FTAN analysis has been performed to measure the group velocities dispersion curve of Rayleigh wave fundamental mode.

Steps used in the analysis of NEG-ETES path (Fig.4.1) are shown as an example, while the final results are presented for the other paths in the following sections.

4.2.2 NEG-ETES path

NEG-ETES path (7 km) crosses the eastern flank of Mt. Epomeo in NW-SE direction (Fig.4.1). The Fourier amplitude spectrum of the NCFs shows that the energy is concentrated in the 0.4-1.5 Hz frequency range (Fig.4.2A). By filtering NCFs, both vertical and radial components in a narrower band, a surface wave train arriving at about 8 s can be discerned, which is more evident in 0.6-1.5 Hz frequency range (Fig.4.2B-C), as also supported by the elliptical particle motion (Fig.4.3).

The wave train arriving at about 2 s on the NCF vertical component is not consistent with the geological setting of the area having a very high velocity (Fig.4.2B). Despite many trials to emphasize the surface wave train, a strong contribution appeared on the zero time. This feature has been observed for most of the paths and it has represented a very strong limit to the application of cross-correlation method at Ischia island. As a result, the NCFs with a reasonable signal-to-noise ratio are not so many, as shown in the following figures, and the analysis has been focused on the slower wave trains, even if they are less evident or hidden by the stronger contribution at zero delay.

FTAN maps of NCFs' vertical and radial components relative to NEG-ETES path show a very clear trend of mountain ridges in the 0.5-3 s period range and 0.3-2 km/s group velocity range (Fig.4.4A-C). Group velocity dispersion curves of vertical and radial components have been picked, the fundamental mode has been extracted and its fitting with the original signal is good both in time and frequency domain (Fig.4.4B-D). The average group velocity dispersion curve, with error bar, is characterized by velocities from 0.69 to 1.21 km/s at periods varying from 0.74 to 1.79 s (Fig.4.4E).

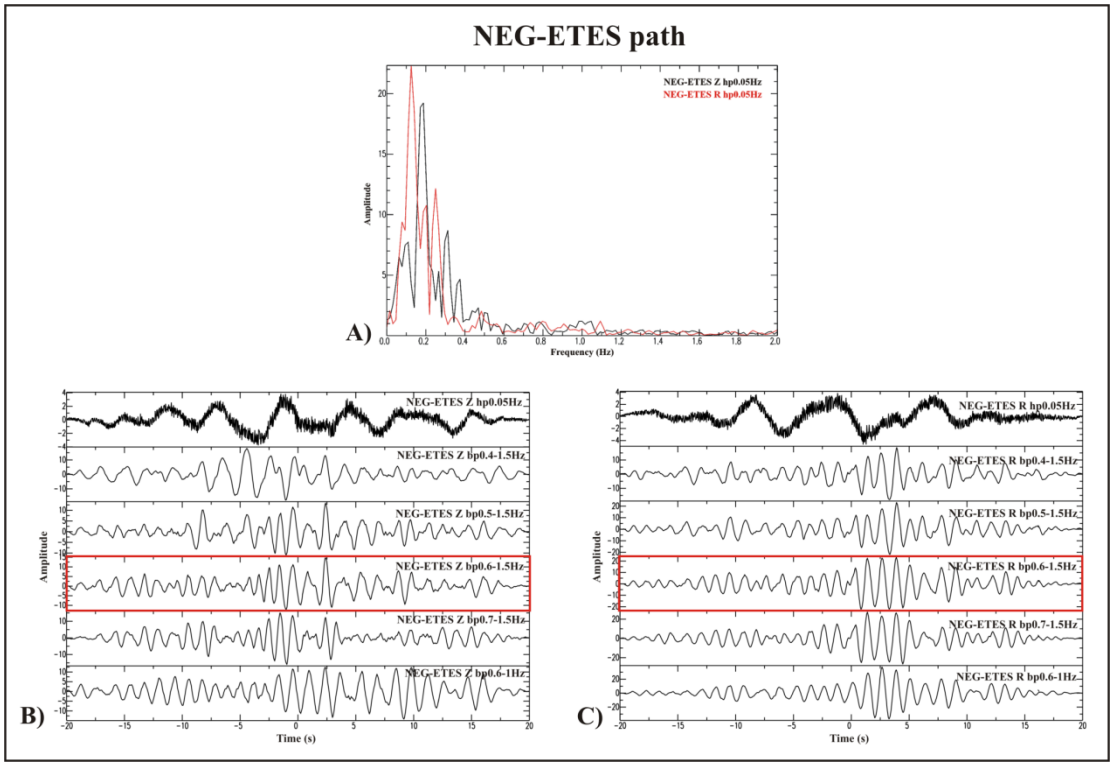

Fig.4.2 *– Fourier spectrum of NCFs (0.05 Hz high-passed) computed for the NEG-ETES path (A); NCF of vertical (B) and radial (C) components computed in different frequency ranges. The chosen frequency band is evidenced by red rectangles.*

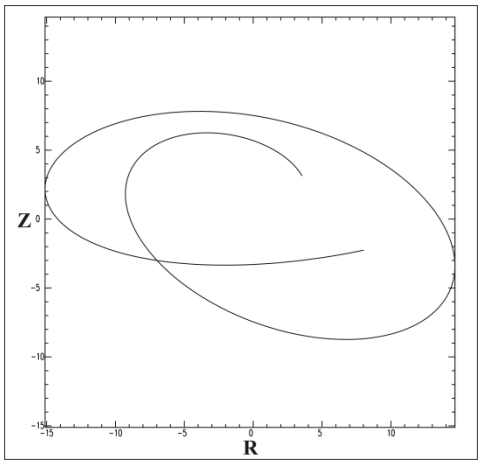

Fig.4.3 *– Particle motion of Rayleigh waves in 8-10 s time range and 0.6-1.5 Hz frequency range relative to NEG-ETES path.*

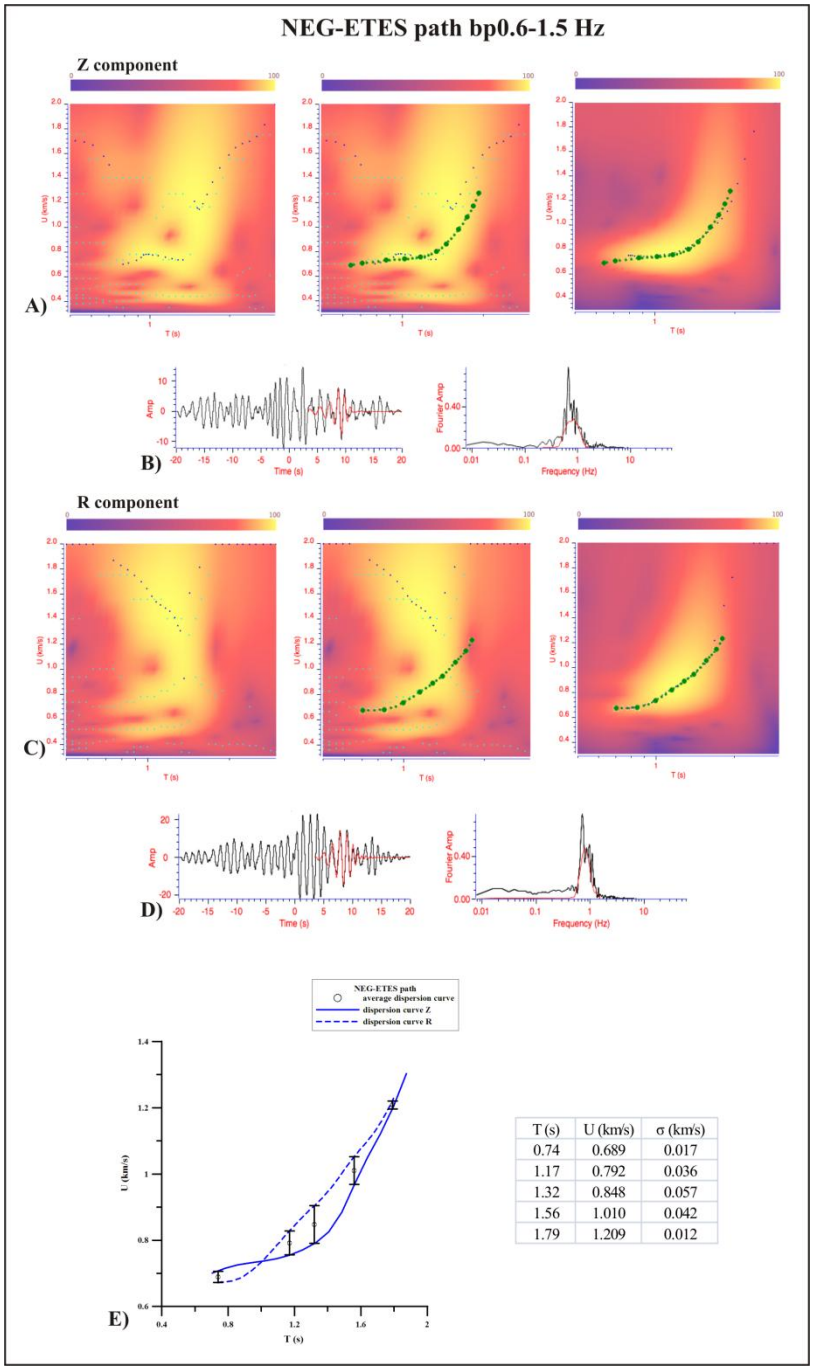

T (s)	U (km/s)	σ (km/s)
0.74	0.689	0.017
1.17	0.792	0.036
1.32	0.848	0.057
1.56	1.010	0.042
1.79	1.209	0.012

Fig.4.4 *– Steps of FTAN analysis computed on NCFs' vertical and radial components relative to NEG-ETES path (from A to D); average group velocity dispersion curve with error bar (E).*

4.2.3 ISCH-NEG and ISCH-MOR paths

The analysis of seismic noise data acquired along ISCH-NEG (5.6 km) and ISCH-MOR (6.2 km) paths (that cross the northern part of the island) (Fig.4.1) has been particularly complex as NCFs relative to vertical components are affected by ambiguity and a Rayleigh wave train doesn't emerge on radial components.

Computed functions of vertical component in 0.5-1.5 Hz frequency range for ISCH-MOR path and 0.4-1 Hz frequency range for ISCH-NEG path show two wave trains on the causal part of NCF: at 2 s and 7 s for the former, at 3 s and 8 s for the latter (Fig.4.5B).

This ambiguity is also evident on the relative FTAN maps showing two different trends of mountain ridges (Fig.4.5C-D), one of which is characterized by group velocities higher than those shown by the dispersion curve of the PER-SFOR path crossing the Mt. Epomeo (see 4.2.13 section). Since in the northern area structures are deepened by a ENE-WSW to E-W fault system (Vezzoli, 1988; Molin et al., 2003) and the basement is inferred at greater depth (~2 km) (Nunziata and Rapolla, 1987) (see 1.2.1 and 1.2.4 sections), lower velocities are expected than in the central area. So the lower group velocity "crest" has been picked.

Moreover, the similarity of the ISCH-MOR and ISCH-NEG paths, both as NCF and FTAN maps, evidently related to the geological homogeneity because of their very short distance, has suggested to compute one average group velocity dispersion curve between them. Hereafter this average path is called the ISCH-NEG path.

Average dispersion curve shows group velocities varying from 0.54 to 1 km/s at periods varying from 0.97 to 2.22 s (Fig.4.5E).

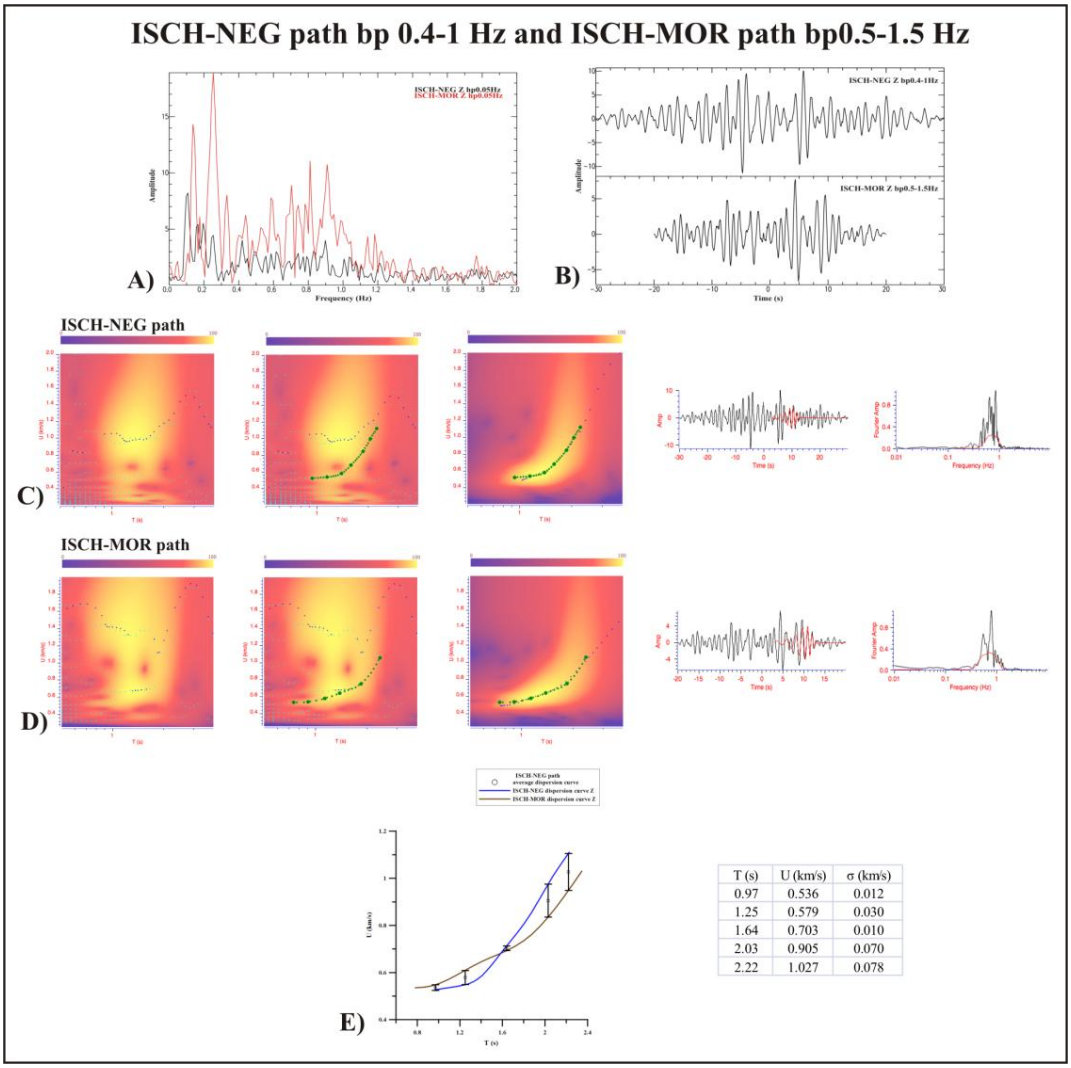

Fig.4.5 *– Fourier spectrum (A) and NCFs (B) relative to ISCH-NEG and ISCH-MOR paths; steps of FTAN analysis (C-D); average group velocity dispersion curve computed between the two paths (E).*

4.2.4 ISCH-NPL path

As regards the ISCH-NPL path (2.4 km) (eastern part of Ischia) (Fig.4.1), the cross-correlation computed for the radial component had a very bad signal-noise ratio. NCF relative to vertical component has been computed in 0.5-1.5 Hz frequency range: this function shows a surface wave train arriving at 7 s, even if the function is masked by low frequency contribution (Fig.4.6A).

In order to compute an average dispersion curve, the 9 hour recording has been split in 3 hours intervals. NCFs relative to the three time intervals are very similar to the NCF computed on the whole signal (Fig.4.6C), but only NCFs relative to the first (Z1) and the third (Z3) time interval show FTAN maps slightly clearer than the second one (Z2) (Fig.4.6D-E). Hence the average dispersion curve for ISCH-NPL path has been computed using the dispersion curves measured for the NCFs relative to the Z1 and Z3 portions.

Average group velocities vary from 0.29 to 0.43 km/s at periods varying from 0.78 to 1.64 s (Fig.4.6F).

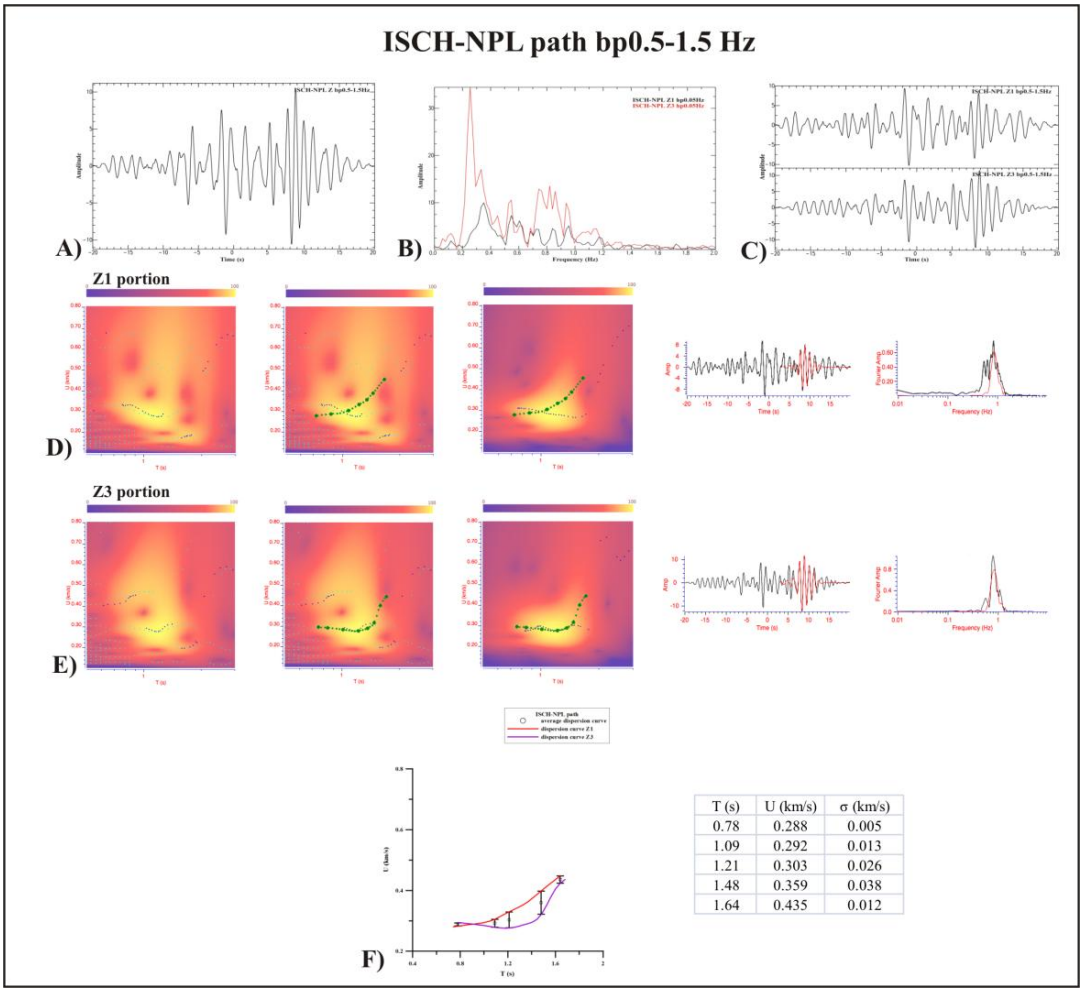

Fig.4.6 *– ISCH-NPL path: Fourier spectrum (B) and NCFs of the whole signal (9 hours recording) (A) and of two portions (3 hours) of the original signal split in three parts (C); steps of FTAN analysis (D-E); average group velocity dispersion curve with error bar (F).*

4.2.5 SPL-WTES path

As regards SPL-WTES path (3 km long and crossing the south-eastern part of Ischia) (Fig.4.1), NCFs computed in the 0.7-2 Hz frequency range, both vertical and radial components, show a strongly predominant contribution on the zero time (Fig.4.7B).

FTAN map of the NCF vertical component is very clear (Fig.4.7C), allowing to extract the fundamental mode and identifying the Rayleigh surface wave train arriving at 2 s, and helping to recognize the dispersion curve of the fundamental mode also on the FTAN map of the NCF radial component (Fig.4.7D).

The average group velocity dispersion curve has been computed at periods from 0.74 to 1.60 s and characterized by velocities between 0.57 and 1.13 km/s (Fig.4.7E).

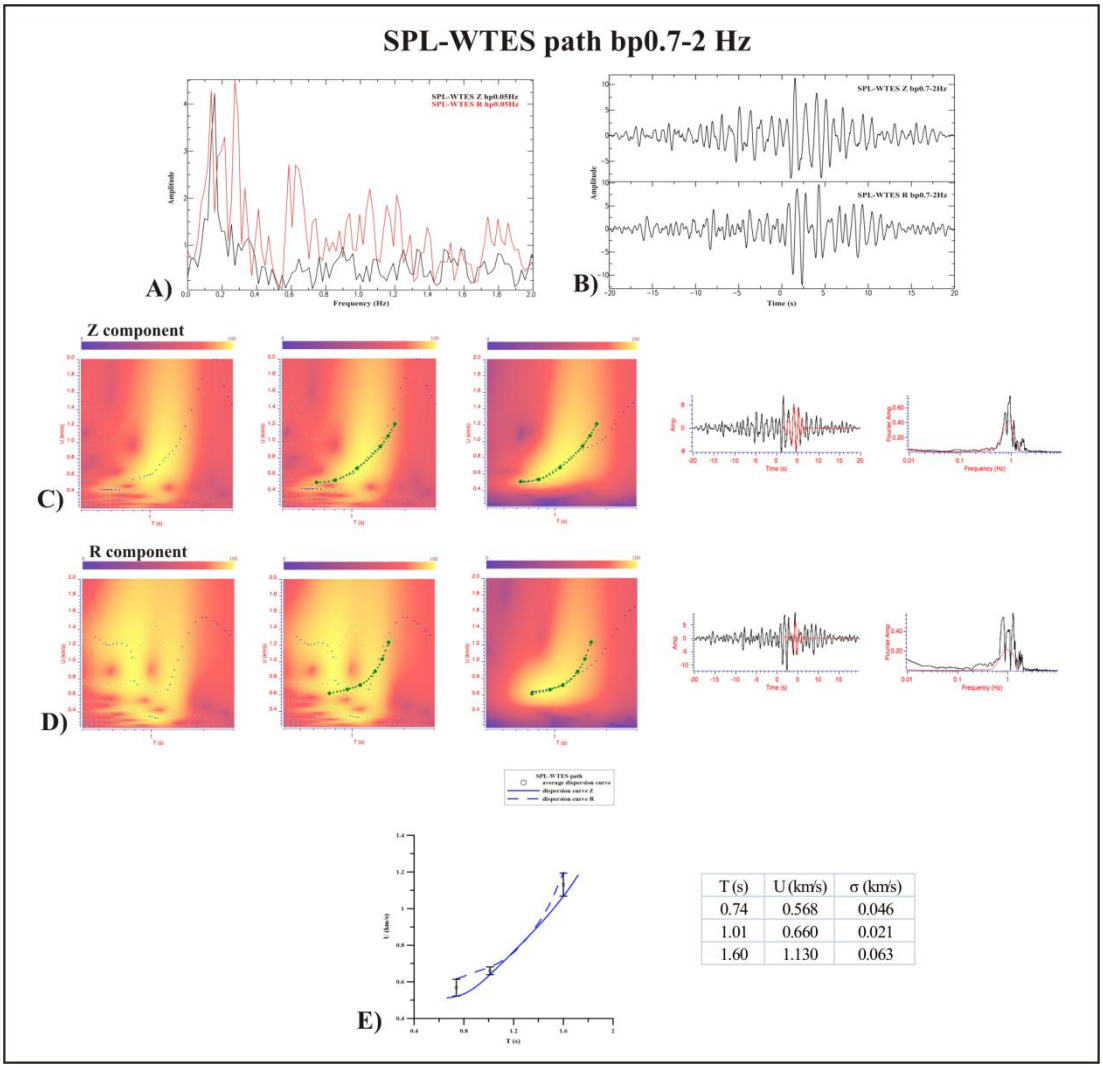

Fig.4.7 *– Fourier spectrum (A) and NCFs (B) relative to SPL-WTES path; steps of FTAN analysis (C-D); average group velocity dispersion curve computed for this path (E).*

4.2.6 SUC-NFOR path

NCF computed in the 0.4-1.2 Hz frequency range for vertical component relative to SUC-NFOR path (4.6 km long and crossing the south-western side of the island in NW-SE direction) (Fig.4.1) shows an evident wave train on the causal part arriving at 8 s (Fig.4.8B).

The FTAN map shows a clear mountain ridge (Fig.4.8C), which has been used as guide to pick the dispersion curve of the fundamental mode also on the NCF radial component (Fig.4.8D). Then, an average group velocity dispersion curve has been computed in the 1.01-1.75 s period range with velocities in the 0.38-0.52 km/s range (Fig.4.8E).

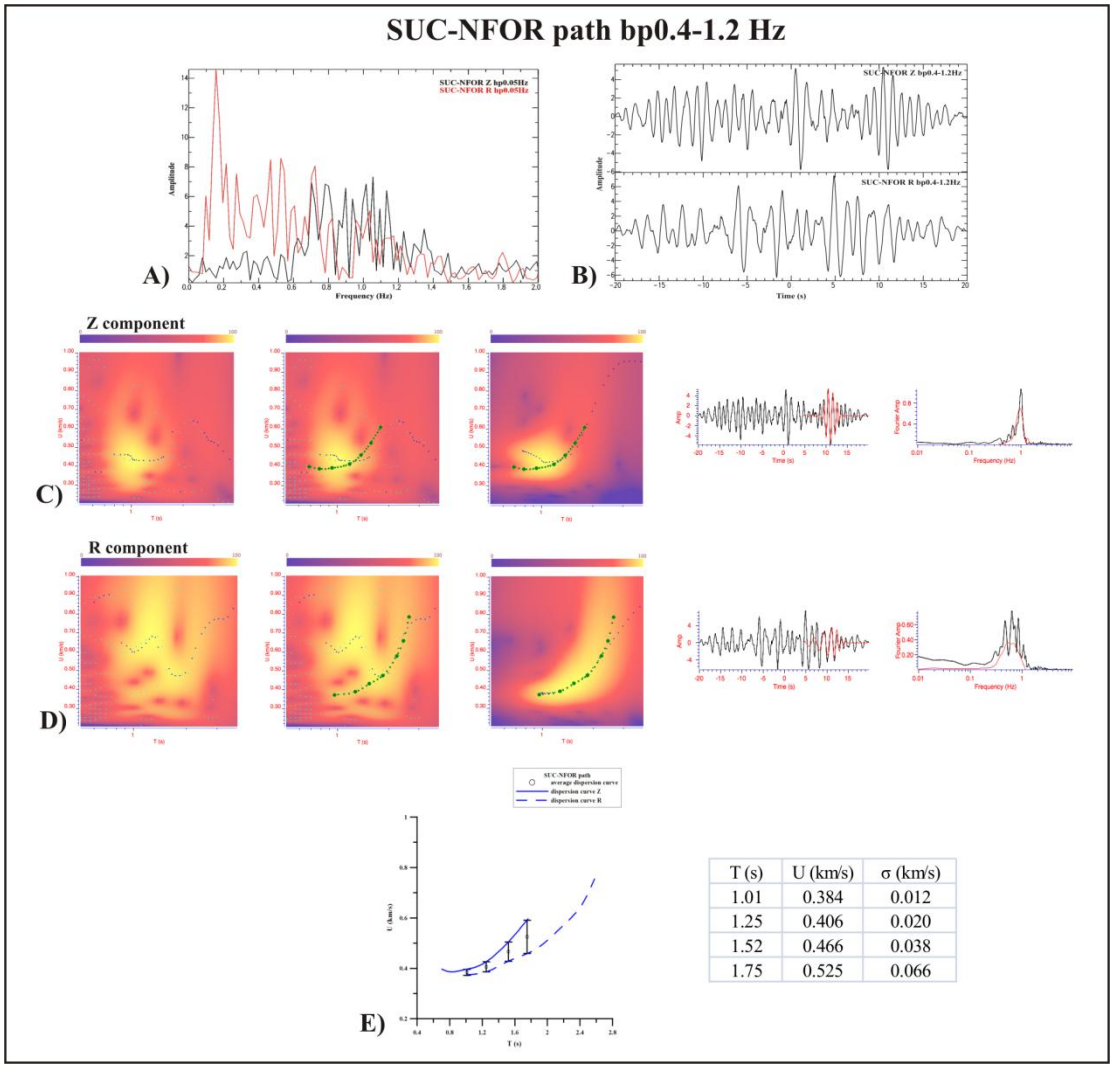

Fig.4.8 *– Fourier spectrum (A) and NCFs (B) relative to SUC-NFOR path; steps of FTAN analysis (C-D); average group velocity dispersion curve computed for this path (E).*

4.2.7 ISC-ETES path

NCFs computed in 0.6-1.5 Hz frequency range on vertical and radial components relative to ISC-ETES path (eastern side of the island) (Fig.4.1) provided good results, as both functions show an evident wave train on the causal part, but there is no consistency in the arrival time between the two components (Fig.4.9A).

If I consider the arrival time of wave train recognizable on NCF of radial component, the estimated group velocity is too high, hence the analysis has been focused only on the vertical component. The whole recording has been split in three portions of about 7 hours. The NCFs computed for these three portions (Fig.4.9C) show a quite similar behaviour than that relative to the whole signal, even if some differences can be noted. In fact NCF relative to the first portion shows an evident wave train arriving at 3 s, while on the NCFs relative to the second and third portions the arrival of this wave train is masked by a great

contribution on the zero time (Fig.4.9C). Fortunately, FTAN maps of all NCFs show a clear trend in the same period-group velocity window that allowed to extract three group velocity dispersion curves (Fig.4.9D-E-F). These curves have been averaged and the resulting average dispersion curve is characterized by velocities from 0.50 to 0.86 km/s at periods from 0.78 to 1.42 s (Fig.4.9G).

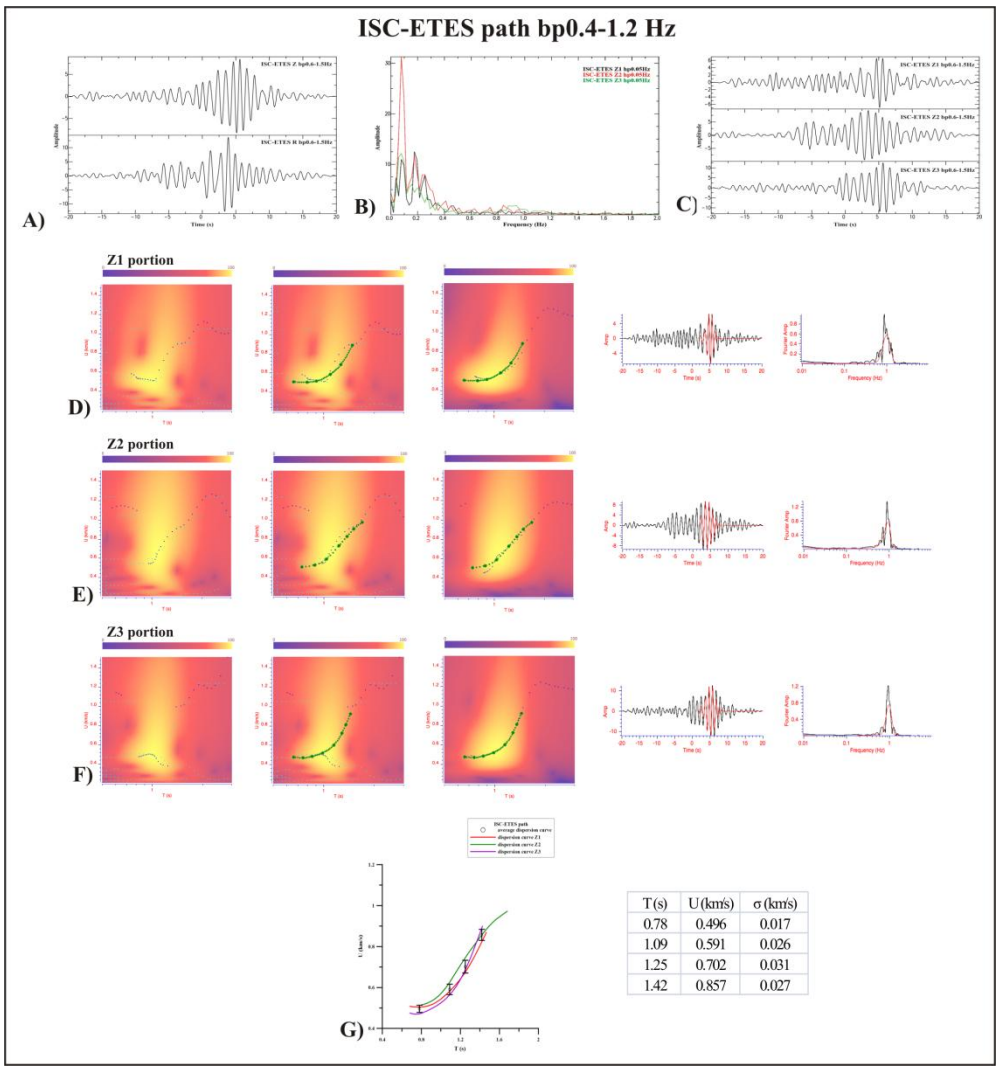

Fig.4.9 - *Fourier spectrum (B) and NCFs of the whole signal (A) and of the three split portions (C) relative to ISC-ETES path; steps of FTAN analysis (D-E-F); average group velocity dispersion curve computed for this path (G).*

4.2.8 ISC-NEG path

Average group velocity dispersion curve relative to ISC-NEG path (5.8 km long and crossing the northern part of Ischia in NW-SE direction) (Fig.4.1) has been evaluated between dispersion curves extracted from NCFs computed in the 0.6-1.2 Hz frequency range for vertical and radial components. Despite a very bad signal-to-noise ratio (surface

wave train arrival, at about 5 s, is hidden by other great contributions) (Fig.4.10B), their FTAN maps show a clear trend of mountain ridges covering the same period and group velocity ranges (Fig.4.10C-D). The obtained average dispersion curve shows velocities from 0.65 to 0.99 km/s at periods from 0.85 to 1.58 s (Fig.4.10E).

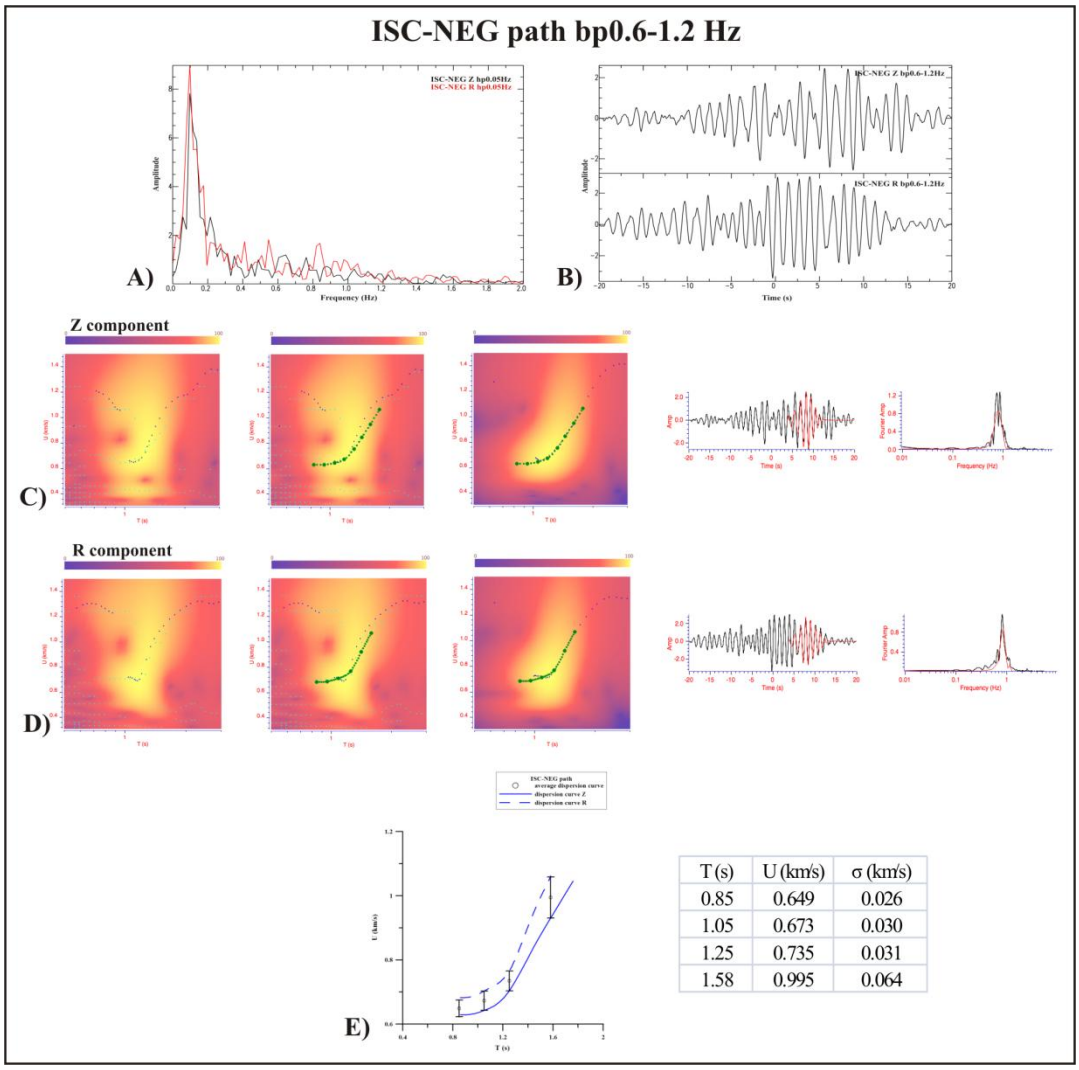

Fig.4.10 *– Fourier spectrum (A) and NCFs (B) relative to ISC-NEG path; steps of FTAN analysis (C-D); average group velocity dispersion curve computed for this path (E).*

4.2.9 ISC-PER path

NCFs of vertical and radial components (computed in the 0.5-1.5 Hz frequency range) relative to ISC-PER path (2.9 km long and crossing the north-eastern part of the island in NW-SE direction) (Fig.4.1) are strongly different: the former presents two symmetrical wave trains, the latter doesn't show any relevant contribution (Fig.4.11A). Signals relative to both vertical and radial components have been split in three portions. Only three functions, i.e. second and third portion (Z2 and Z3 portions) of vertical component and

second portion (R2 portion) of radial component, show similar waveforms (Fig.4.11C) and their FTAN maps allowed to extract dispersion curves having similar trend in the same period and group velocity ranges (Fig.4.11D-E-F). In particular, NCFs relative to the second and third portion of the vertical component show symmetry like the NCF computed for the whole signal (Fig.4.11A-C). So these three extracted dispersion curves have been averaged and the obtained curve shows velocities from 0.53 to 0.80 km/s at periods from 0.97 to 2.14 s (Fig.4.11G).

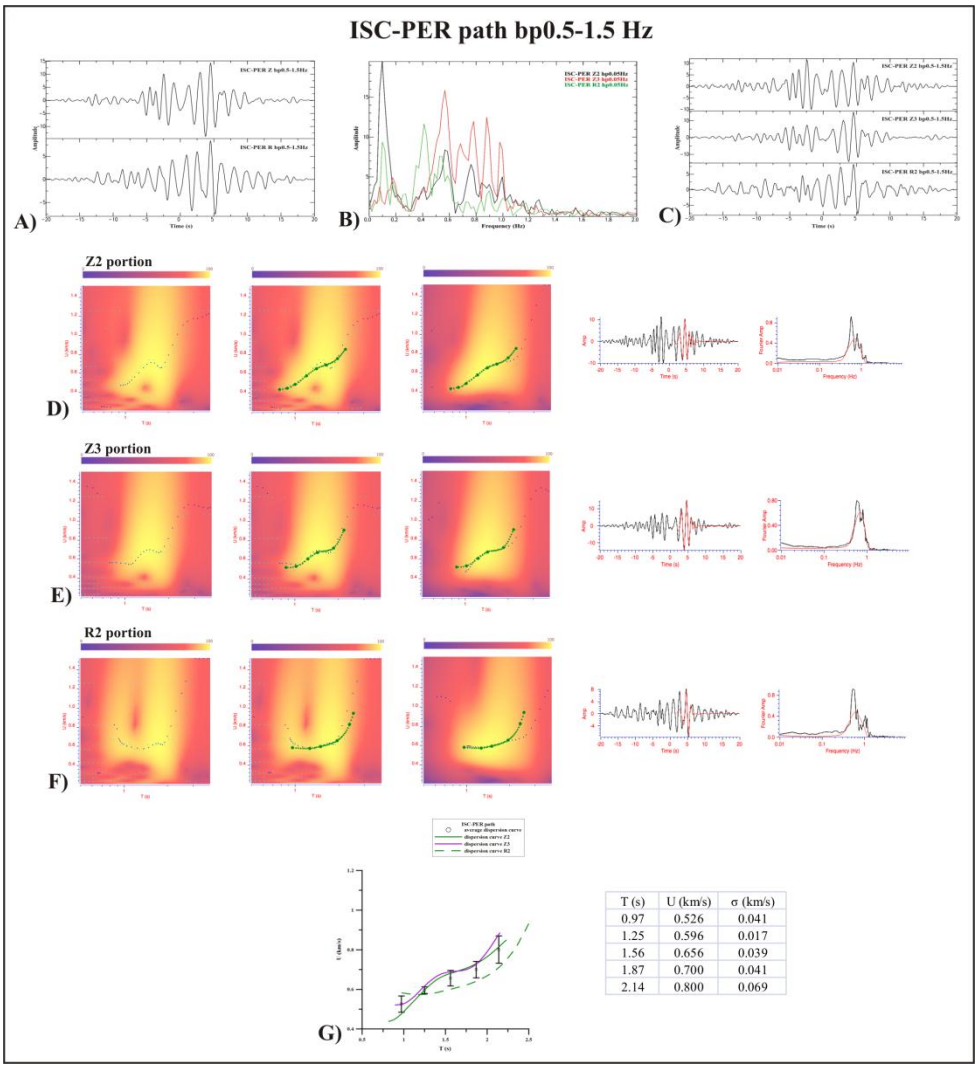

Fig.4.11 *– Fourier spectrum (B) and NCFs of the whole signal (A) and three portions (C) relative to ISC-PER path; steps of FTAN analysis (D-E-F); average group velocity dispersion curve computed for this path (G).*

4.2.10 ISC-SAN path

NCFs computed in the 0.6-1.5 Hz frequency range on vertical and radial components relative to ISC-SAN path (5.1 km long and crossing the south-central part of the island in NE-SW direction) (Fig.4.1) show different waveforms and FTAN maps.

A clear wave train arriving at 4 s is evident on the NCF radial component (Fig.4.12A), but its FTAN map is confusing and shows energy in a very narrow period range. As regards the NCF vertical component, a wave train arriving at 6 s is hidden by a strong contribution on the zero time (Fig.4.12A), but its FTAN map shows a clear trend of mountain ridges in a wider period range. These two curves cannot be averaged. Hence, the NCF vertical component has been split in three portions. The NCFs computed for the first and the second portions present a waveform similar to that computed for the whole signal, while the NCF computed for the third portion shows too many contributions (Fig.4.12C). FTAN maps relative to NCF of the first and the second portion show a very clear trend of mountain ridges (this feature is analogous to FTAN map of the NCF relative to the whole signal) that helped to extract surface waves fundamental mode completely hidden in the time domain (Fig.4.12D-E). As regards the third portion, the picking of the dispersion curve on the FTAN map has been guided by those extracted from the analysis of the other two portions (Fig.4.12F), having the map many maxima. An average dispersion curve has been computed with three curves, characterized by velocities from 0.51 to 0.96 km/s at periods from 0.85 to 1.75 s (Fig.4.12G).

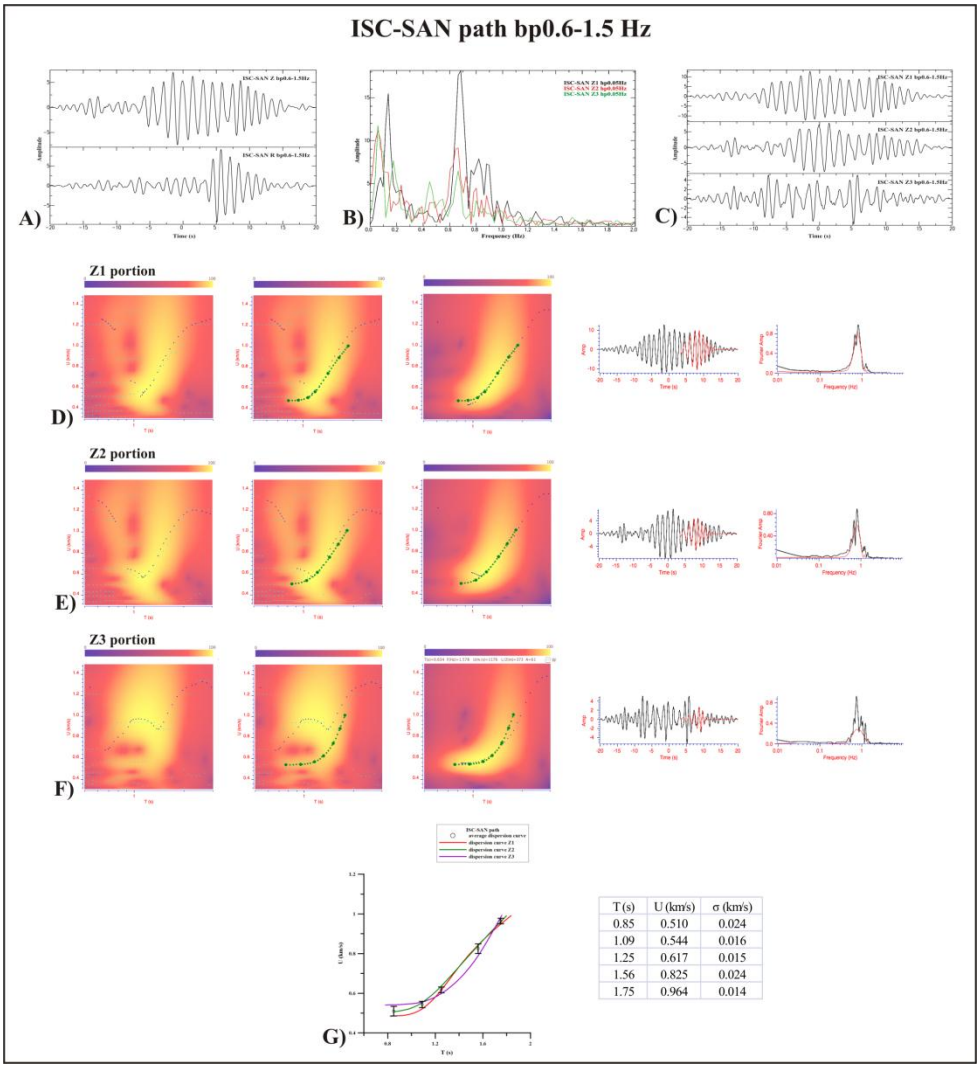

Fig.4.12 *– Fourier spectrum (B) and NCFs vertical component of the whole signal (A) and three portions (C) relative to ISC-SAN path; steps of FTAN analysis (D-E-F); average group velocity dispersion curve computed for this path (G).*

4.2.11 NEG-SAN path

NCFs (computed in the 0.5-1.5 Hz frequency range) of vertical and radial components relative to NEG-SAN path (6.1 km long and crossing the western flank of Mt. Epomeo in N-S direction) (Fig.4.1) are symmetric (Fig.4.13B), despite a strong contribution at low frequencies (Fig.4.13A). Rayleigh wave trains can be recognized arriving at about 5-6 s (Fig.4.13B).

FTAN maps relative to both positive and negative part of NCFs of vertical and radial components have been analysed, but the former show a clear, well defined trend (Fig.4.13C-D). Hence the causal part of NCF has been chosen for the analysis. An average dispersion curve has been computed by using the two curves extracted from vertical and

radial components. It is defined at periods between 1.01 and 1.95 s with velocities between 0.67 and 1.03 km/s (Fig.4.13E).

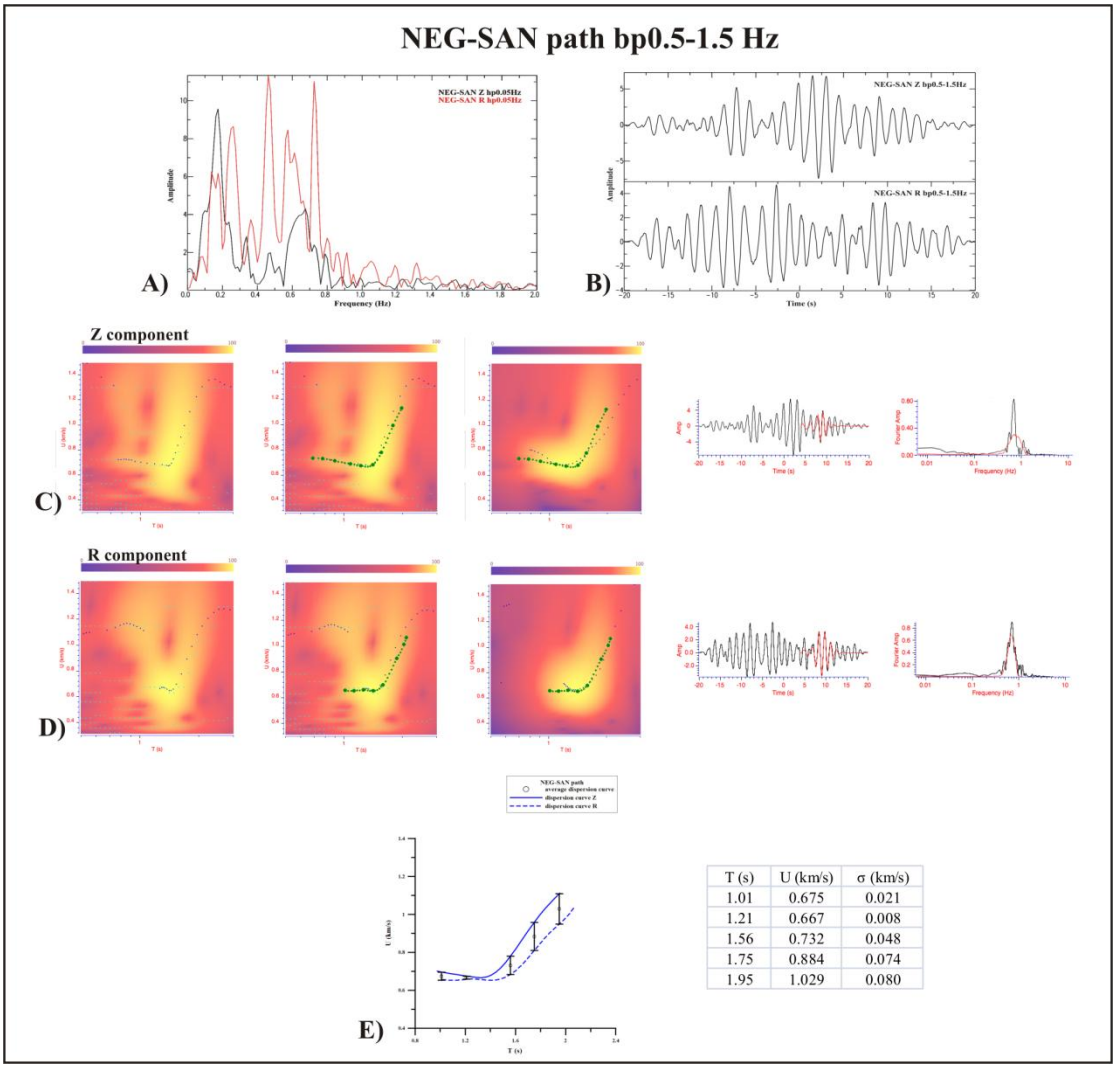

Fig.4.13 *– Fourier spectrum (A) and NCFs (B) relative to NEG-SAN path; steps of FTAN analysis (C-D); average group velocity dispersion curve computed for this path (E).*

4.2.12 NEG-SFOR path

As for many other paths, also NCFs computed in the 0.7-1.5 Hz frequency range for vertical and radial components relative to NEG-SFOR path (4.7 km long and crossing the north-western part of Ischia) (Fig.4.1) show a very bad signal-to-noise ratio, because of both a strong contribution on the zero time and the presence of many wave trains having similar amplitude (Fig.4.14B). Their FTAN maps reflect the existence of these different contributions (Fig.4.14C-D), being that relative to the NCF vertical component more ambiguous. Starting from the radial component, the dispersion curve has been also picked

for the vertical component. The average curve shows group velocities from 0.64 to 0.89 km/s, at periods ranging from 0.66 to 1.21 s (Fig.4.14E).

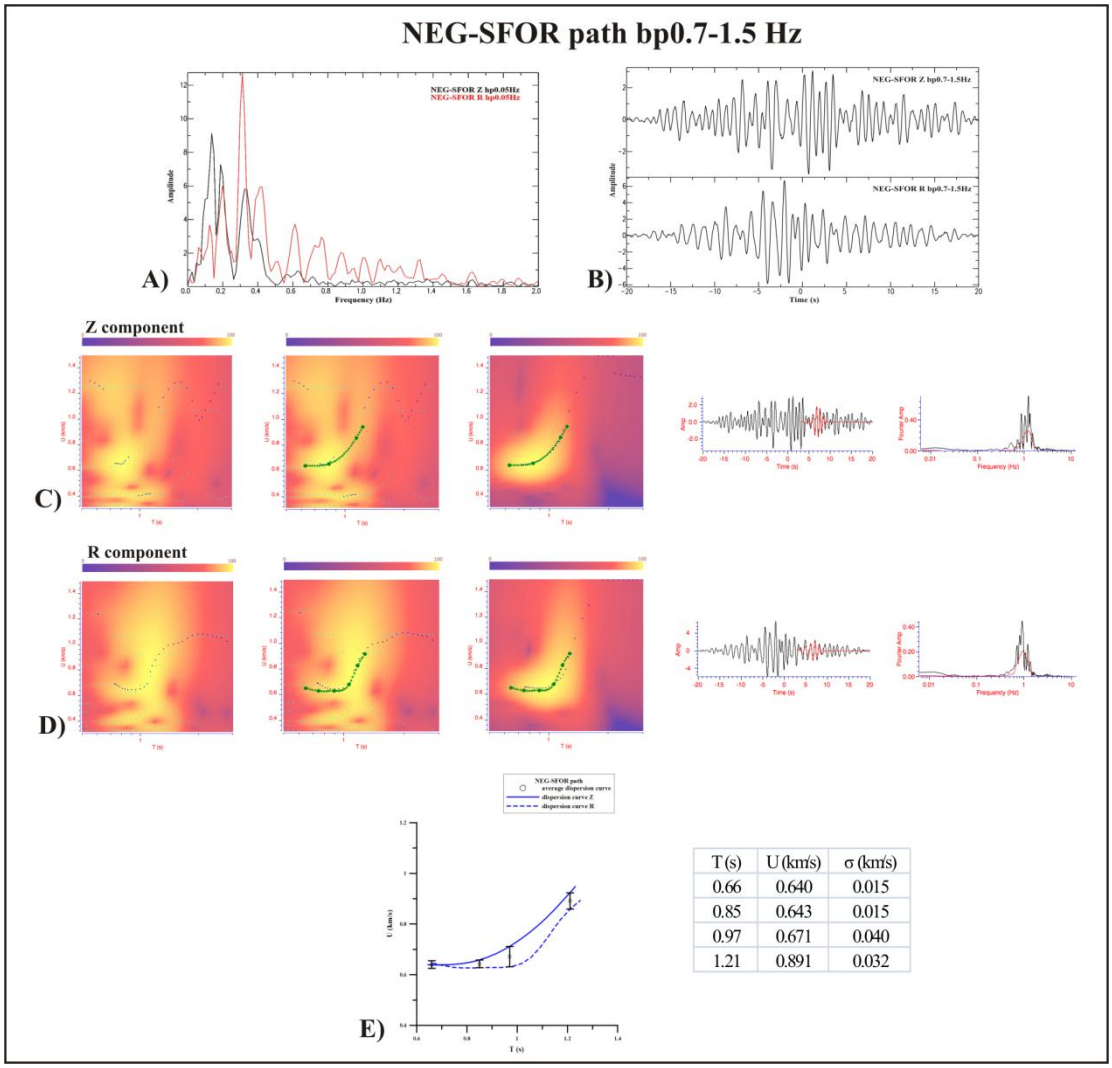

T (s)	U (km/s)	σ (km/s)
0.66	0.640	0.015
0.85	0.643	0.015
0.97	0.671	0.040
1.21	0.891	0.032

Fig.4.14 *– Fourier spectrum (A) and NCFs (B) relative to NEG-SFOR path; steps of FTAN analysis (C-D); average group velocity dispersion curve computed for this path (E).*

4.2.13 PER-SFOR path

As regards PER-SFOR path (5.6 km long and crossing the central area of Ischia with Mt. Epomeo) (Fig.4.1), the NCFs computed in the 0.7-1.5 Hz frequency range, both vertical and radial components, show the relevant contribution of wave trains centered on the zero time (Fig.4.15B). Fortunately, FTAN map of the NCF vertical component presents a clear crest trend (Fig.4.15C), which allows to discriminate the dispersion curve of the Rayleigh wave fundamental mode also on that relative to the NCF radial component (Fig.4.15D). The average dispersion curve has been computed between these two curves:

its period values vary from 0.78 to 1.48 s and its group velocity values vary from 0.93 to 1.22 km/s (Fig.4.15E).

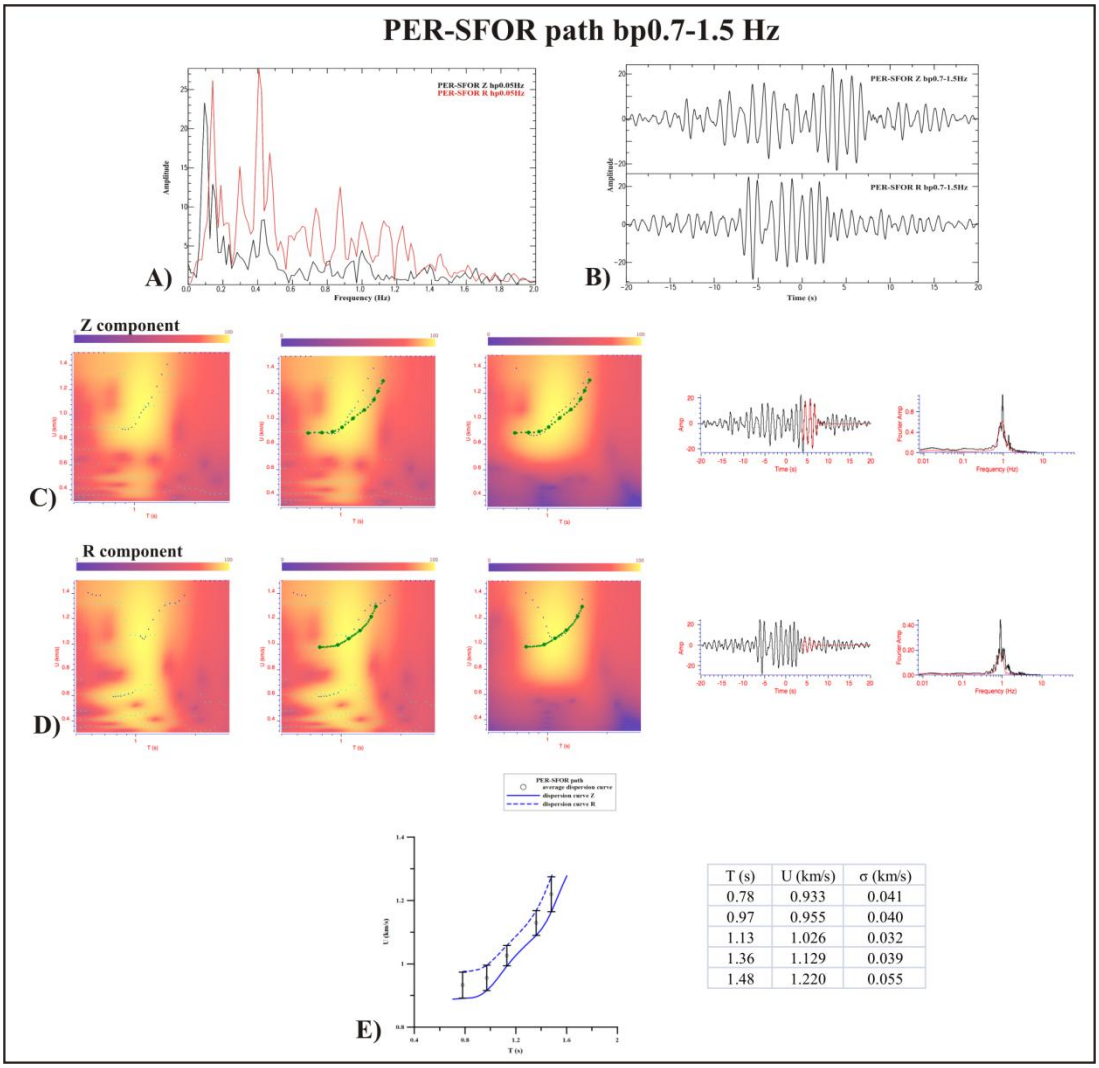

Fig.4.15 *– Fourier spectrum (A) and NCFs (B) relative to PER-SFOR path; steps of FTAN analysis (C-D); average group velocity dispersion curve computed for this path (E).*

4.2.14 SFOR-ISC path

NCFs computed for the SFOR-ISC path (6.4 km long and crossing the central area of Ischia island) (Fig.4.1) (in the 0.5-1.5 Hz frequency range) have given good results only for the vertical component (Fig.4.16A). The whole signal has been split in 3 portions (Fig.4.16C). Only the NCF of the second portion shows a sufficient signal-to-noise ratio, that has allowed to recognize a Rayleigh wave train arriving at about 7 s (Fig.4.16C), even if two symmetric wave trains starting on the zero time are present. Being its FTAN map very clear, group velocity dispersion curve has been picked easily (Fig.4.16E). The NCF relative to the other portions are quite different as the surface wave train is almost hidden,

mostly for the first portion (Fig.4.16C). Their FTAN maps are much less clear, but a similar trend is observable in the same period and group velocity ranges (Fig.4.16D-F). So average group velocity dispersion curve has been computed among three dispersion curves, showing group velocities from 0.54 to 0.94 km/s at periods varying from 0.89 to 1.99 s (Fig.4.16G).

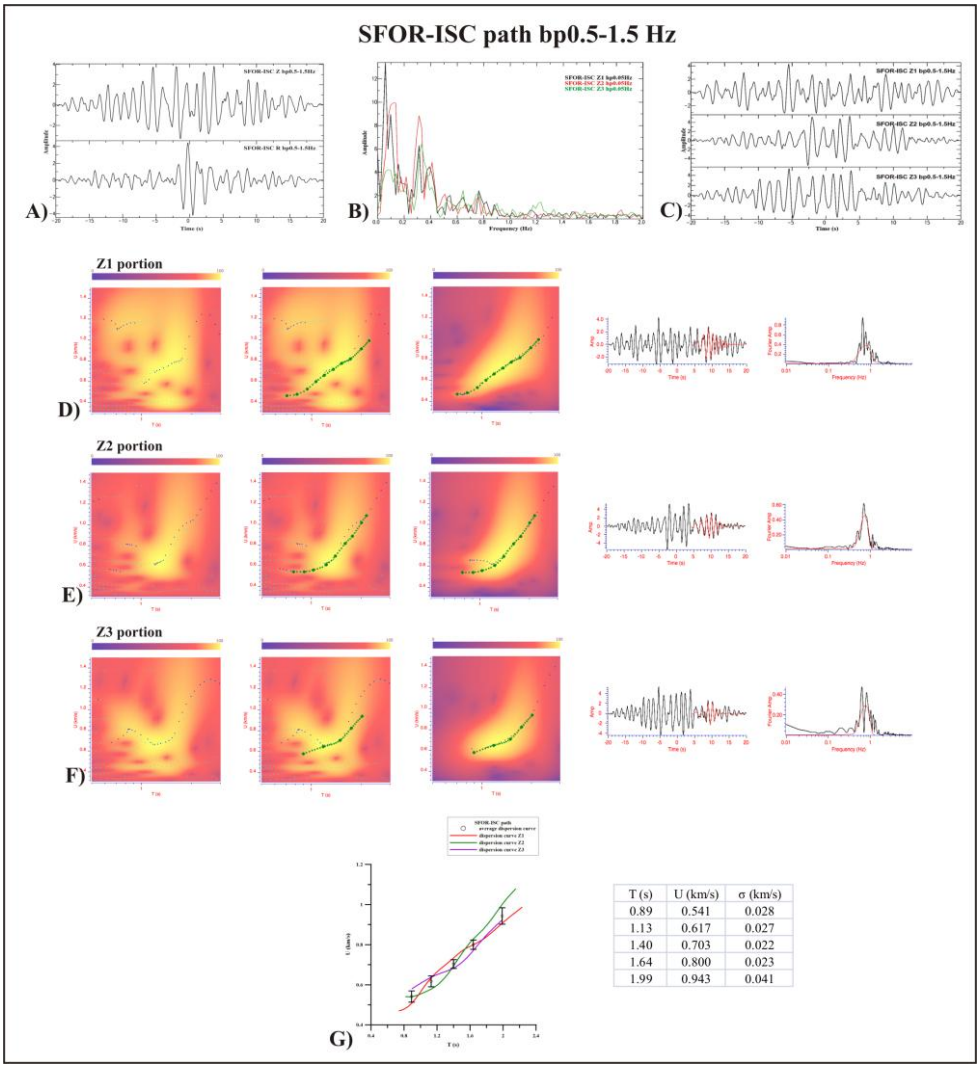

Fig.4.16 *– Fourier spectrum (B) and NCFs of the whole signal (A) and three split portions (C) relative to SFOR-ISC path; steps of FTAN analysis (D-E-F); average group velocity dispersion curve computed for this path (G).*

4.3 Summary of group velocity dispersion curves

The application of cross-correlation method at Ischia has not given satisfactory results as most of the computed NCFs present a low signal-to-noise ratio. This failure may be attributed to the presence at the island of Ischia of many sources acting in different frequency range and at different scales. The contribution at very low frequency is very

strong and difficult to reduce (in fact an evident wave train is often observed on the zero time of NCFs). These features have been observed along most of the paths crossing the island, regardless their azimuth, and longer noise recordings (20 hours). It may be that noise recording for much more long time (month or year) might provide better results.

Despite the difficulty of easy recognition of Rayleigh wave trains, FTAN analysis has been decisive to extract the fundamental mode from noisy NCFs. Average dispersion curves have been computed for all paths (Fig.4.17), sometimes giving up the radial components and splitting the vertical component recording. The average dispersion curves, with velocities from 0.22 to 1.22 km/s, are defined at periods varying from 0.64 to 2.22 s. Moreover, the preliminary estimate of 0.3 Hz as minimum sampled frequency (Tab.4.2) has not been confirmed by our analysis (>0.4 Hz).

The average dispersion curves relative to most of the paths show similar group velocity values, but that relative to PER-SFOR path showing the highest velocities and those relative to the bordering ISCH-NPL and SUC-NFOR paths characterized by lower values (Fig.4.17). This feature puts in evidence the existence of different geological settings between the centre of Ischia and its bordering areas.

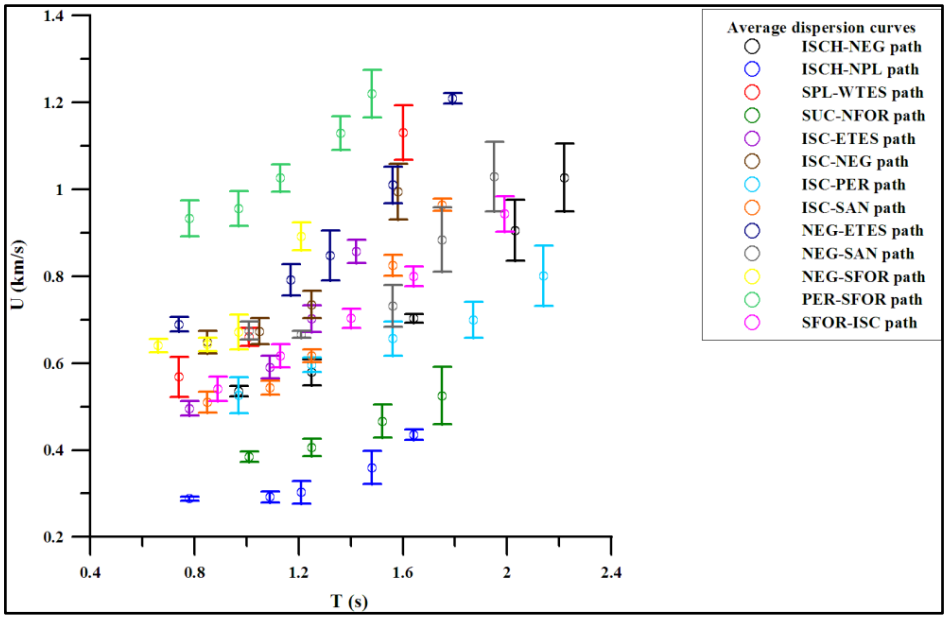

Fig.4.17 *- Average group velocity dispersion curves with the relative error bars extracted from NCFs computed along 13 paths (located in Fig.4.1) crossing the island of Ischia.*

Chapter 5

V_S MODELS AT CAMPI FLEGREI

The average group velocity dispersion curves, with error bar, measured along the 25 paths crossing Campi Flegrei (see 3.5 section) (Figs.3.69-3.70), have been inverted with the Hedgehog non-linear inversion method in order to obtain 1-D shear wave velocity profiles vs. depth.

The inversion has been performed with a starting model based on the available geological and geophysical data. In particular each starting model consists of a number of parameters variable according to the maximum investigated depth by each dispersion curve. The computation of partial derivatives with respect to the parameters to be inverted has allowed to estimate the maximum depth explored by the higher period and the resolution of the parameters (Panza, 1981) (see 2.3 section for more details).

The Hedgehog inversion of the average group velocity dispersion curves has produced an ensemble of accepted models which differ by no more than ±1 step from each other. Each set of solutions is constituted by a number of equivalent models comparable with the number of the inverted parameters. Finally the representative model for each path has been chosen among the obtained solutions: in this thesis the solutions characterized by the minimum r.m.s. have been chosen as the representative models along each analysed path. Really, the solutions with the minimum r.m.s. are very similar to those with the r.m.s. closest to the average error computed for all the solutions. Moreover in some cases the minimum and the average solutions are coincident.

5.1 Hedgehog non-linear inversion of average dispersion curves

The group velocity dispersion curves measured at Campi Flegrei (Fig.3.69) are characterized by periods ranging from 0.78 to 2.65 s (see 3.5 section) allowing to explore a maximum depth of 3 km.

Starting models have been parameterized considering the tomographic studies performed by Aster and Meyer (1988), Judenherc and Zollo (2004) and Battaglia et al. (2008), the gravimetric data (Nunziata and Rapolla, 1981; AGIP, 1987) and the Nafe-Drake empirical relation (Fowler, 1995) for density values.

As regards V_P/V_S ratio values, data include models presented by Aster and Meyer (1988), Vanorio et al. (2005) and Battaglia et al. (2008). These models define a very complex

distribution of V_P/V_S ratio inside the Campi Flegrei caldera, especially in the Gulf of Pozzuoli and in the central sector of the depressed area. Many trials have been performed in order to define the optimal V_P/V_S ratio values for such areas. In particular, V_P/V_S ratio has been considered as an independent parameter varying in 1.8-3 range, with 0.1 step, for paths crossing the Gulf of Pozzuoli and 1.8-2.5 range, with 0.1 step, for paths crossing the central inland sector of the caldera, according to Battaglia et al. (2008). Afterwards, the reasonable V_P/V_S ratio values have been identified among those maximizing the number of solutions, keeping fixed the other parameters. Then, these V_P/V_S ratio values have been fixed in the later inversion.

The starting model is defined by V_S and thickness values (independent parameters), V_P value (dependent parameter linked to V_S through the V_P/V_S ratio value), density and V_P/V_S ratio values (fixed parameters) (see 2.3 section for more details). The shallowest layer has fixed thickness and V_S as the highest sampled frequencies along the analysed paths has not sampled the shallower portions of the crust (i.e. from some tens to few hundreds of meters).

At last, a layer corresponding to the water column (Lirer et al., 2010) has been included in the starting models below the paths crossing the Gulf of Pozzuoli (BAC-ARCO, BAC-NIS, BAC-POZ, NIS-STH and POZ-NIS) (Fig.3.70).

In the following sections I show the starting models for each of the 25 paths, together with the solution sets. The chosen solutions, characterized by the minimum r.m.s., are also shown with the average solutions, i.e. the solution with the r.m.s. closest to the average error computed all over the set of solutions.

5.1.1 ARCO-ASE and ARCO-CMSA paths

The starting model (Tab.5.1) used in the inversion of the average group velocity dispersion curve relative to the ARCO-ASE and ARCO-CMSA paths (Fig.3.33B) is defined by 7 independent parameters (3 thickness and 4 V_S values) and by two different values of V_P/V_S ratio: 2 assigned to the fixed, the first and second inverted layers, and 1.8 to the third and fourth inverted layers. The explored thickness is 1.6 km.

The obtained solution set consists of 5 solutions (Fig.5.1): the model characterized by the minimum r.m.s. presents V_S values increasing from 0.9 to 1.97 km/s, at a depth of 0.965 km.

ARCO-ASE and ARCO-CMSA paths			
Parameters		**Step**	**Range of variability**
h (km)	0.100		
	0.220	0.030	0.109-0.339
	0.200	0.050	0.059-0.349
	0.365	0.065	0.139-0.599
V_S (km/s)	0.450		
	0.900	0.030	0.539-1.039
	1.150	0.045	1.019-1.369
	1.420	0.085	1.009-1.699
	1.885	0.085	1.599-2.049
V_P/V_S	2	for fixed, 1st and 2nd inverted layers	
	1.8	for 3rd and 4th inverted layer	

Tab.5.1 *– Starting model for the inversion of the average group velocity dispersion curve relative to ARCO-ASE and ARCO-CMSA paths (inverted parameters are in black, fixed parameters are in blue).*

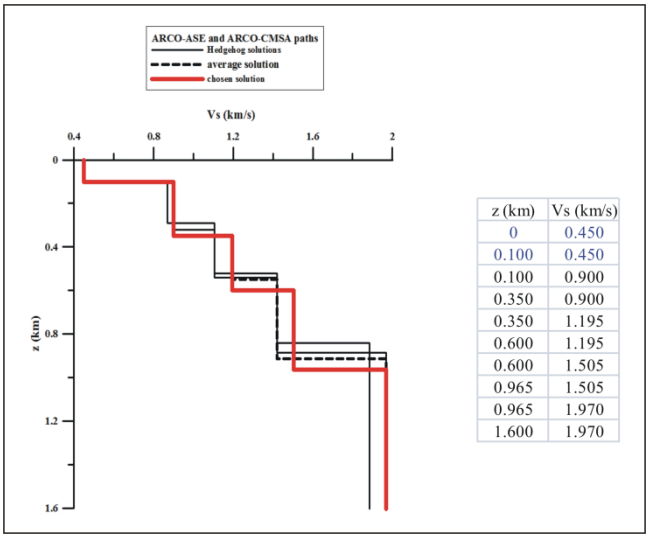

Fig.5.1 *– Set of solutions obtained from the inversion of the average group velocity dispersion curve relative to ARCO-ASE and ARCO-CMSA paths. The chosen solution is evidenced by the red line: this model, characterized by the minimum r.m.s., is presented in the table on the right. The black dotted line indicates the average solution.*

5.1.2 ARCO-CSOB path

The starting model (Tab.5.2) for the inversion of the average group velocity dispersion curve relative to the ARCO-CSOB path (Fig.3.34B) is defined by 5 independent

parameters (2 thickness and 3 V_S values) and by a V_P/V_S ratio value of 2.2 for the fixed and the inverted layers. The explored thickness is 1 km.

ARCO-CSOB path			
Parameters		**Step**	**Range of variability**
h (km)	0.120		
	0.180	0.030	0.029-0.299
	0.250	0.035	0.159-0.601
V_S (km/s)	0.530		
	0.770	0.020	0.499-1.099
	0.895	0.035	0.499-1.099
	1.215	0.035	0.799-1.299
V_P/V_S	2.2	for all the layers	

Tab.5.2 *– Starting model for the inversion of the average group velocity dispersion curve relative to ARCO-CSOB path (inverted parameters are in black, fixed parameters are in blue).*

The obtained solution set consists of 2 solutions (Fig.5.2): the model characterized by the minimum r.m.s. (which is coincident with the average solution) presents V_S values increasing from 0.79 to 1.215 km/s, at a depth of 0.545 km.

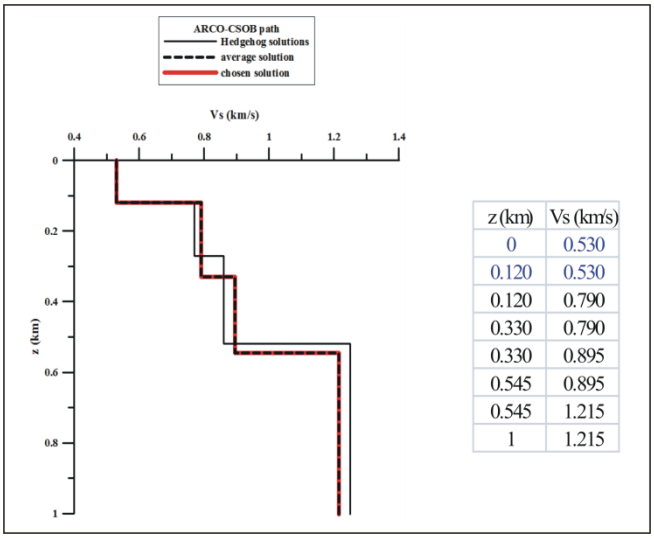

z (km)	Vs (km/s)
0	0.530
0.120	0.530
0.120	0.790
0.330	0.790
0.330	0.895
0.545	0.895
0.545	1.215
1	1.215

Fig.5.2 *– Set of solutions obtained from the inversion of the average group velocity dispersion curve relative to ARCO-CSOB path. The chosen solution is evidenced by the red line: this model, characterized by the minimum r.m.s. and coincident with the average solution (black dotted line), is presented in the table on the right.*

5.1.3 ARCO-QUAR path

The starting model (Tab.5.3) for the inversion of the average group velocity dispersion curve relative to the ARCO-QUAR path (Fig.3.35B) is defined by 7 independent parameters (3 thickness and 4 V_S values) and by two different values of V_P/V_S ratio: 1.9 assigned to the fixed, first, second and third inverted layers, and 1.8 to the fourth inverted layer. The explored thickness is 1.3 km.

ARCO-QUAR path			
Parameters		**Step**	**Range of variability**
h (km)	0.080		
	0.130	0.025	0.019-0.399
	0.210	0.025	0.039-0.499
	0.250	0.035	0.069-0.599
V_S (km/s)	0.600		
	0.665	0.030	0.499-0.799
	0.800	0.040	0.599-1.099
	1.305	0.060	1.019-1.599
	1.620	0.015	1.109-2.299
V_P/V_S	1.9	for fixed, 1st, 2nd and 3rd inverted layers	
	1.8	for 4th inverted layer	

Tab.5.3 *– Starting model of the inversion of the average group velocity dispersion curve relative to ARCO-QUAR path (inverted parameters are in black, fixed parameters are in blue).*

The obtained solution set consists of 3 solutions (Fig.5.3): the model characterized by the minimum r.m.s. presents V_S values increasing from 0.665 to 1.62 km/s, at a depth of 0.67 km.

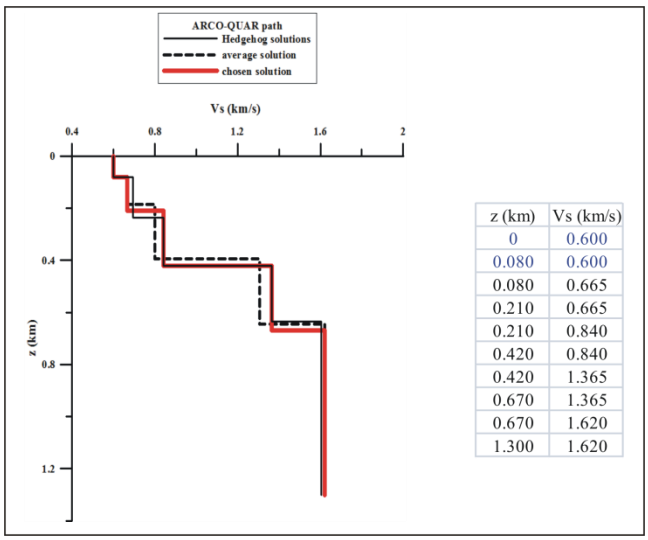

z (km)	Vs (km/s)
0	0.600
0.080	0.600
0.080	0.665
0.210	0.665
0.210	0.840
0.420	0.840
0.420	1.365
0.670	1.365
0.670	1.620
1.300	1.620

Fig.5.3 *– Set of solutions obtained from the inversion of the average group velocity dispersion curve relative to ARCO-QUAR path. The chosen solution is evidenced by the red line: this model, characterized by the minimum r.m.s., is presented in the table on the right. The black dotted line indicates the average solution.*

5.1.4 ARCO-SMN path

The starting model (Tab.5.4) used in the inversion of the average group velocity dispersion curve relative to the ARCO-SMN path (Fig.3.37B) is defined by 7 independent parameters (3 thickness and 4 V_S values) and by two different values of V_P/V_S ratio: 2 assigned to the fixed, first, second and third inverted layers, and 1.8 to the fourth inverted layer. The explored thickness is 2.4 km.

ARCO-SMN path			
Parameters		**Step**	**Range of variability**
h (km)	0.210		
	0.310	0.030	0.209-0.499
	0.400	0.050	0.209-0.599
	0.350	0.050	0.209-0.599
V_S (km/s)	0.720		
	0.890	0.015	0.539-0.999
	1.240	0.045	0.999-1.399
	1.330	0.085	1.009-1.499
	1.955	0.085	1.599-2.299
V_P/V_S	2	for fixed, 1st, 2nd and 3rd inverted layers	
	1.8	for 4th inverted layer	

Tab.5.4*– Starting model used in the inversion of the average group velocity dispersion curve relative to ARCO- SMN path (inverted parameters are in black, fixed parameters are in blue).*

The obtained solution set consists of 4 solutions (Fig.5.4): the model characterized by the minimum r.m.s. presents V_S values increasing from 0.875 to 1.87 km/s, at a depth of 1.19 km.

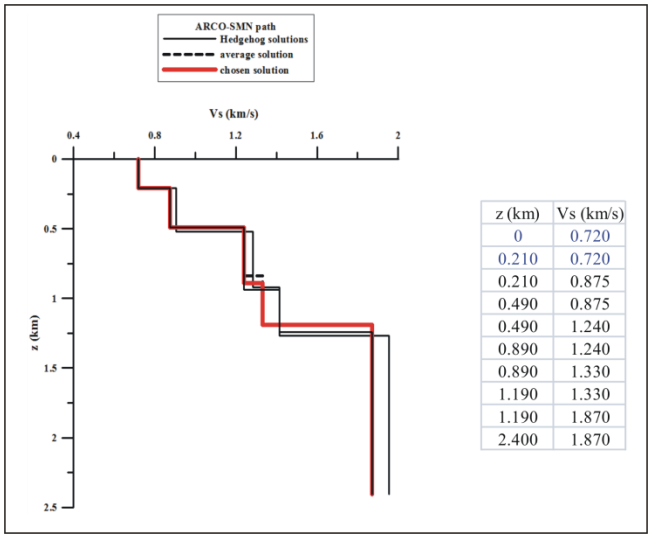

z (km)	Vs (km/s)
0	0.720
0.210	0.720
0.210	0.875
0.490	0.875
0.490	1.240
0.890	1.240
0.890	1.330
1.190	1.330
1.190	1.870
2.400	1.870

Fig.5.4 *– Set of solutions obtained from the inversion of the average group velocity dispersion curve relative to ARCO-SMN path. The chosen solution is evidenced by the red line: this model, characterized by the minimum r.m.s., is presented in the table on the right. The black dotted line indicates the average solution.*

5.1.5 ASE-SMN path

The starting model (Tab.5.5) used in the inversion of the average group velocity dispersion curve relative to the ASE-SMN path (Fig.3.39B) is defined by 7 independent parameters (3 thickness and 4 V_S values) and by a V_P/V_S ratio value of 1.8 for the fixed and the inverted layers. The explored thickness is 1.6 km.

The obtained solution set consists of 4 solutions (Fig.5.5): the model characterized by the minimum r.m.s. presents V_S values increasing from 0.77 to 1.86 km/s, at a depth of 0.685 km.

ASE-SMN path			
Parameters		**Step**	**Range of variability**
h (km)	0.120		
	0.120	0.030	0.029-0.301
	0.195	0.035	0.059-0.399
	0.250	0.055	0.099-0.801
V_S (km/s)	0.500		
	0.770	0.040	0.499-0.999
	1.000	0.055	0.599-1.299
	1.260	0.065	0.799-1.599
	1.780	0.080	1.209-1.999
V_P/V_S	1.8	for all the layers	

Tab.5.5– *Starting model used in the inversion of the average group velocity dispersion curve relative to ASE-SMN path (inverted parameters are in black, fixed parameters are in blue).*

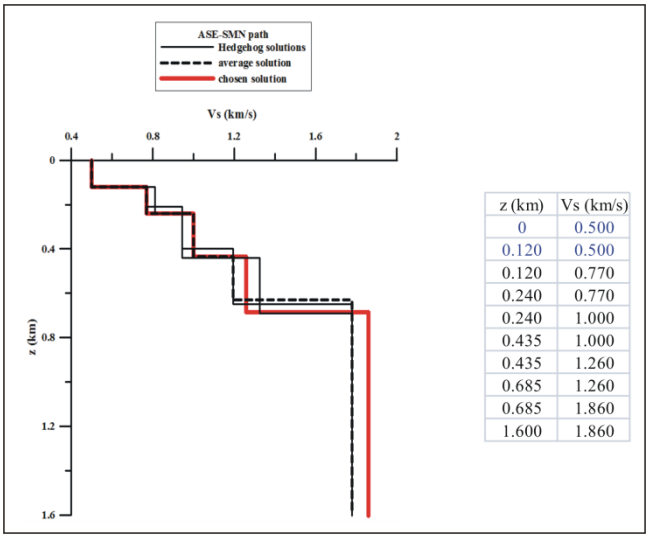

Fig.5.5 *– Set of solutions obtained from the inversion of the average group velocity dispersion curve relative to ASE-SMN path. The chosen solution is evidenced by the red line: this model, characterized by the minimum r.m.s., is presented in the table on the right. The black dotted line indicates the average solution.*

5.1.6 BAC-ARCO path

The starting model (Tab.5.6) used in the inversion of the average group velocity dispersion curve relative to the BAC-ARCO path (Fig.3.40B) is defined by 5 independent parameters (2 thickness and 3 V_S values) and by a V_P/V_S ratio value of 2.9 for the inverted layers, while a V_P/V_S ratio value of 5 has resulted the optimal value for the fixed layer below the water column. The explored thickness is 1.3 km.

The obtained solution set consists of 3 solutions (Fig.5.6): the model characterized by the minimum r.m.s. presents a low velocity layer at depths of 0.44-0.50 km (~17% reduction).

BAC-ARCO path			
Parameters		**Step**	**Range of variability**
h (km)	0.010		
	0.070		
	0.355	0.030	0.109-0.481
	0.110	0.032	0.029-0.319
V_S (km/s)	0		
	0.250		
	0.600	0.020	0.499-1.001
	0.550	0.055	0.419-1.101
	0.730	0.020	0.499-1.501
V_P/V_S	5	for the fixed layer	
	2.9	for all the inverted layers	

Tab.5.6– *Starting model used in the inversion of the average group velocity dispersion curve relative to BAC-ARCO path (inverted parameters are in black, fixed parameters are in blue).*

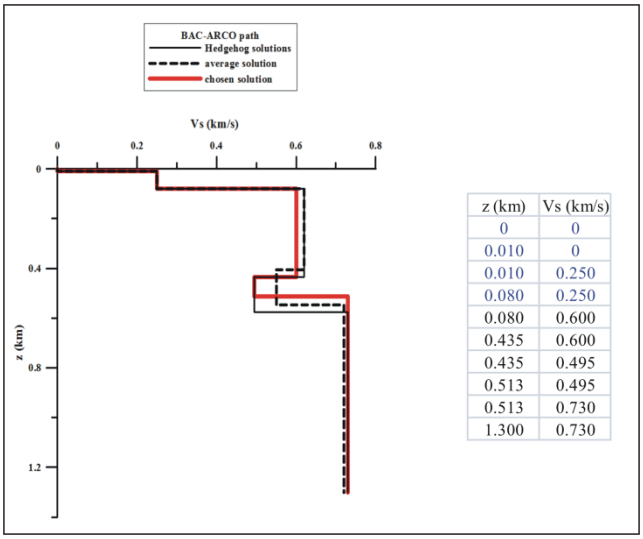

Fig.5.6 *– Set of solutions obtained from the inversion of the average group velocity dispersion curve relative to BAC-ARCO path. The chosen solution is evidenced by the red line: this model, characterized by the minimum r.m.s., is presented in the table on the right. The black dotted line indicates the average solution.*

5.1.7 BAC-ASE path

The starting model (Tab.5.7) used in the inversion of the average group velocity dispersion curve relative to the BAC-ASE path (Fig.3.41B) is defined by 7 independent parameters (3 thickness and 4 V_S values) and by three different values of V_P/V_S ratio: 2.6

associated to the fixed, first and second inverted layers, 2.2 to the third inverted layer, and 1.8 to the fourth inverted layer. The explored thickness is 3 km.

BAC-ASE path			
Parameters		**Step**	**Range of variability**
h (km)	0.100		
	0.180	0.010	0.029-0.401
	0.315	0.020	0.199-0.599
	0.490	0.060	0.299-0.699
V_S (km/s)	0.430		
	0.655	0.010	0.399-0.999
	0.910	0.010	0.499-1.199
	1.260	0.050	0.799-1.599
	1.700	0.050	1.299-2.199
V_P/V_S	2.6	for fixed, 1st and 2nd inverted layers	
	2.2	for 3rd inverted layers	
	1.8	for 4th inverted layers	

Tab.5.7*– Starting model used in the inversion of the average group velocity dispersion curve relative to BAC-ASE path (inverted parameters are in black, fixed parameters are in blue).*

The obtained solution set consists of 4 solutions (Fig.5.7): the model characterized by the minimum r.m.s. presents V_S values increasing from 0.665 to 1.65 km/s, at a depth of 1.035 km.

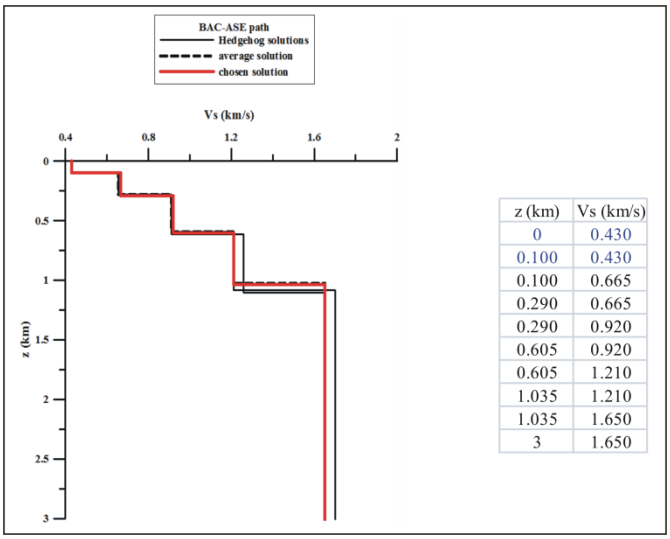

Fig.5.7 *– Set of solutions obtained from the inversion of the average group velocity dispersion curve relative to BAC-ASE path. The chosen solution is evidenced by the red line: this model, characterized by the minimum r.m.s., is presented in the table on the right. The black dotted line indicates the average solution.*

5.1.8 BAC-NIS path

The starting model (Tab.5.8) used in the inversion of the average group velocity dispersion curve relative to the BAC-NIS path (Fig.3.45B) is defined by 7 independent parameters (3 thickness and 4 V_S values) and by three different values of V_P/V_S ratio: 10 associated to the fixed layer, 3 to first, second and third inverted layers, and 2.5 to the fourth inverted layer. The explored thickness is 2 km.

BAC-NIS path			
Parameters		**Step**	**Range of variability**
h (km)	0.060		
	0.110		
	0.375	0.015	0.099-0.599
	0.505	0.015	0.099-0.699
	0.210	0.020	0.059-0.699
V_S (km/s)	0		
	0.140		
	0.390	0.010	0.099-0.699
	0.435	0.015	0.299-0.899
	0.590	0.045	0.299-1.699
	1.150	0.040	0.499-2.799
V_P/V_S	10	for the fixed layer	
	3.0	for 1st, 2nd and 3rd inverted layers	
	2.5	for 4th inverted layers	

Tab.5.8*– Starting model used in the inversion of the average group velocity dispersion curve relative to BAC-NIS path (inverted parameters are in black, fixed parameters are in blue).*

The obtained solution set consists of 3 solutions (Fig.5.8): the model characterized by the minimum r.m.s. (which is coincident with the average solution) presents V_S values increasing from 0.4 to 1.19 km/s, at a depth of 1.26 km.

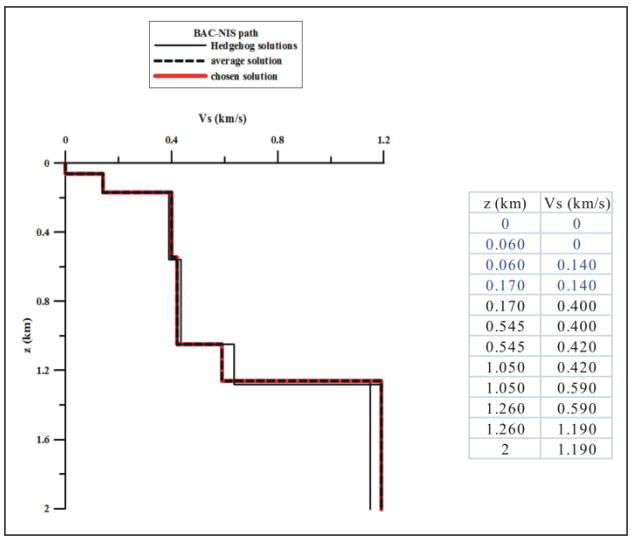

z (km)	Vs (km/s)
0	0
0.060	0
0.060	0.140
0.170	0.140
0.170	0.400
0.545	0.400
0.545	0.420
1.050	0.420
1.050	0.590
1.260	0.590
1.260	1.190
2	1.190

Fig.5.8 *– Set of solutions obtained from the inversion of the average group velocity dispersion curve relative to BAC-NIS path. The chosen solution is evidenced by the red line: this model, characterized by the minimum r.m.s. and coincident with the average solution (black dotted line), is presented in the table on the right.*

5.1.9 BAC-POZ path

The starting model (Tab.5.9) used in the inversion of the average group velocity dispersion curve relative to the BAC-POZ path (Fig.3.20) is defined by 7 independent parameters (3 thickness and 4 V_S values) and by two different values of V_P/V_S ratio: 9 associated to the fixed layer, 2.9 to the inverted layers. The explored thickness is 1.3 km.
The obtained solution set consists of 4 solutions (Fig.5.9): the model characterized by the minimum r.m.s. (which is coincident with the average solution) presents a low velocity layer at depths of 0.38-0.83 km (~17% V_S reduction).

BAC-POZ path			
Parameters		**Step**	**Range of variability**
h (km)	0.040		
	0.100		
	0.250	0.010	0.099-0.599
	0.430	0.020	0.099-0.699
	0.180	0.020	0.059-0.699
V_S (km/s)	0		
	0.150		
	0.385	0.015	0.249-0.699
	0.330	0.015	0.249-0.799
	0.480	0.030	0.299-0.799
	0.800	0.040	0.499-1.199
V_P/V_S	9	for the fixed layer	
	2.9	for all the inverted layers	

Tab.5.9– *Starting model used in the inversion of the average group velocity dispersion curve relative to BAC-POZ path (inverted parameters are in black, fixed parameters are in blue).*

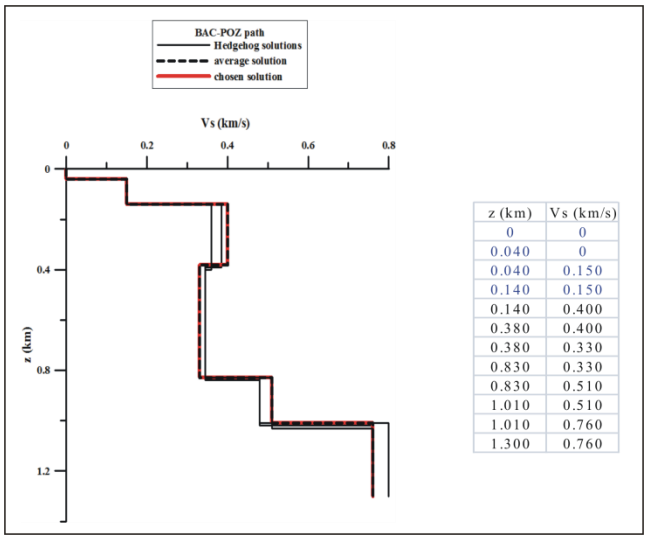

Fig.5.9 *– Set of solutions obtained from the inversion of the average group velocity dispersion curve relative to BAC-POZ path. The chosen solution is evidenced by the red line: this model, characterized by the minimum r.m.s. and coincident with the average solution (black dotted line), is presented in the table on the right.*

5.1.10 NIS-ARCO path

The starting model (Tab.5.10) used in the inversion of the average group velocity dispersion curve relative to the NIS-ARCO path (Fig.3.52B) is defined by 7 independent parameters (3 thickness and 4 V_S values) and by two different values of V_P/V_S ratio: 2.2

associated to the fixed, first, second and third inverted layers, and 1.8 to the fourth inverted layer. The explored thickness is 3 km.

NIS-ARCO path			
Parameters		**Step**	**Range of variability**
h (km)	0.130		
	0.230	0.020	0.159-0.299
	0.220	0.055	0.099-0.499
	0.510	0.050	0.299-0.799
V_S (km/s)	0.750		
	0.900	0.040	0.599-1.199
	1.200	0.030	0.899-1.499
	1.360	0.040	0.899-1.499
	2.380	0.080	0.899-2.799
V_P/V_S	2.2	for fixed, 1st, 2nd and 3rd inverted layers	
	1.8	for 4th inverted layer	

Tab.5.10– *Starting model used in the inversion of the average group velocity dispersion curve relative to NIS-ARCO path (inverted parameters are in black, fixed parameters are in blue).*

The obtained solution set consists of 3 solutions (Fig.5.10): the model characterized by the minimum r.m.s. presents V_S values increasing from 0.9 to 2.38 km/s, at a depth of about 1 km.

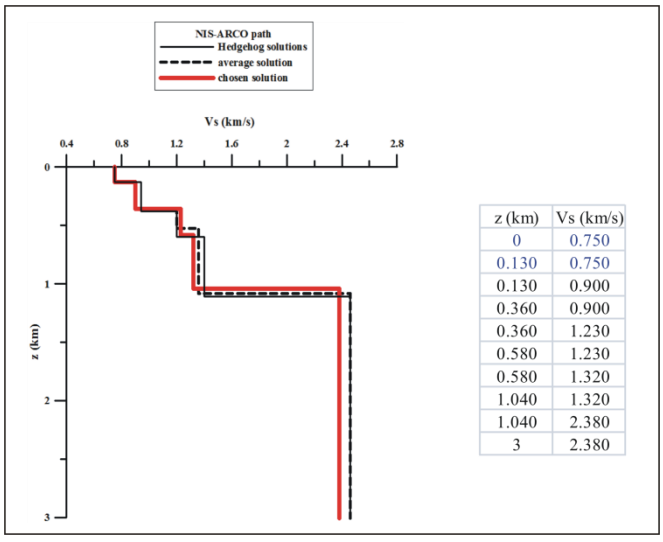

Fig.5.10 *– Set of solutions obtained from the inversion of the average group velocity dispersion curve relative to NIS-ARCO path. The chosen solution is evidenced by the red line: this model, characterized by the minimum r.m.s., is presented in the table on the right. The black dotted line indicates the average solution.*

5.1.11 NIS-ASE path

The starting model (Tab.5.11) used in the inversion of the average group velocity dispersion curve relative to the NIS-ASE path (Fig.3.17) is defined by 7 independent parameters (3 thickness and 4 V_S values) and by two different values of V_P/V_S ratio: 2.3 associated to the fixed, first, second and third inverted layers, and 2 to the fourth inverted layer. The explored thickness is 1.3 km.

NIS-ASE path			
Parameters		**Step**	**Range of variability**
h (km)	0.100		
	0.090	0.030	0.029-0.301
	0.230	0.030	0.149-0.409
	0.380	0.060	0.109-0.559
V_S (km/s)	0.550		
	0.760	0.040	0.589-1.059
	0.840	0.035	0.629-1.401
	1.255	0.045	1.099-1.899
	1.730	0.075	1.399-2.149
V_P/V_S	2.3	for fixed, 1st, 2nd and 3rd inverted layers	
	2	for 4th inverted layer	

Tab.5.11*– Starting model used in the inversion of the average group velocity dispersion curve relative to NIS-ASE path (inverted parameters are in black, fixed parameters are in blue).*

The obtained solution set consists of 4 solutions (Fig.5.11): the model characterized by the minimum r.m.s. presents V_S values increasing from 0.72 to 1.73 km/s, at a depth of 0.8 km.

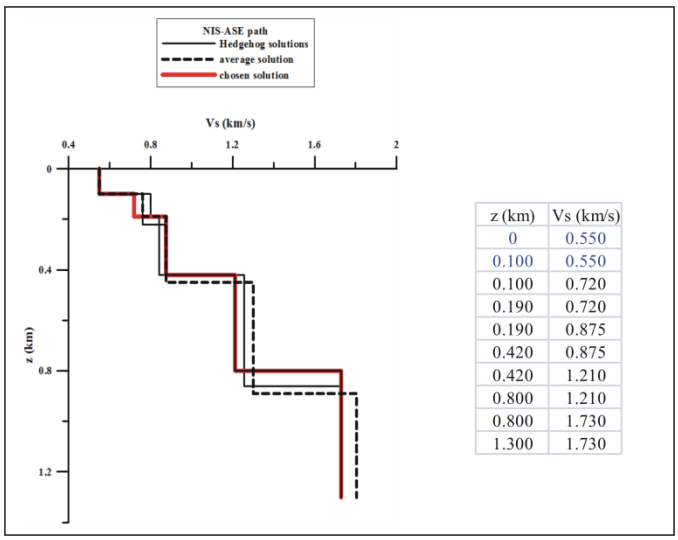

z (km)	Vs (km/s)
0	0.550
0.100	0.550
0.100	0.720
0.190	0.720
0.190	0.875
0.420	0.875
0.420	1.210
0.800	1.210
0.800	1.730
1.300	1.730

Fig.5.11 *– Set of solutions obtained from the inversion of the average group velocity dispersion curve relative to NIS-ASE path. The chosen solution is evidenced by the red line: this model, characterized by the minimum r.m.s., is presented in the table on the right. The black dotted line indicates the average solution.*

5.1.12 NIS-CMSA path

The starting model (Tab.5.12) used in the inversion of the average group velocity dispersion curve relative to the NIS-CMSA path (Fig.3.53B) is defined by 7 independent parameters (3 thickness and 4 V_S values) and by a V_P/V_S ratio value of 2.3 for the fixed and the inverted layers. The explored thickness is 1.2 km.

NIS-CMSA path			
Parameters		**Step**	**Range of variability**
h (km)	0.130		
	0.090	0.045	0.009-0.229
	0.205	0.065	0.029-0.399
	0.450	0.065	0.259-0.699
V_S (km/s)	0.560		
	0.745	0.045	0.569-0.829
	0.890	0.040	0.719-0.969
	1.255	0.055	0.999-1.519
	1.595	0.090	0.709-1.969
V_P/V_S	2.3	for all the layers	

Tab.5.12*– Starting model used in the inversion of the average group velocity dispersion curve relative to NIS-CMSA path (inverted parameters are in black, fixed parameters are in blue).*

The obtained solution set consists of 5 solutions (Fig.5.12): the model characterized by the minimum r.m.s. presents V_S values increasing from 0.79 to 1.595 km/s, at a depth of about 0.9 km.

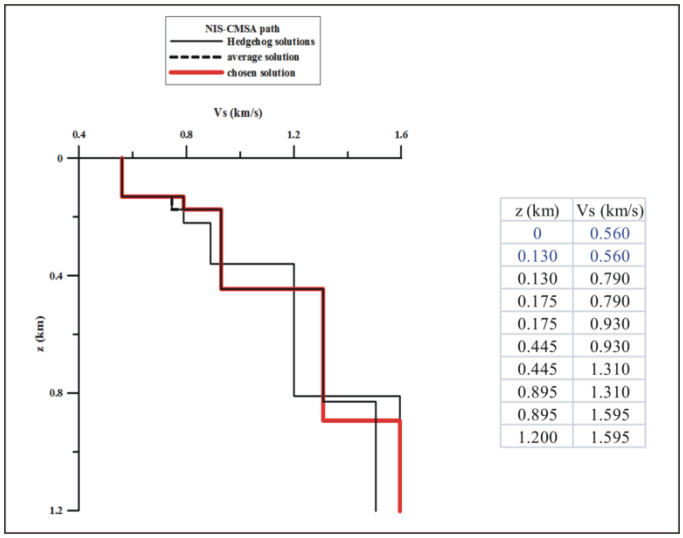

z (km)	Vs (km/s)
0	0.560
0.130	0.560
0.130	0.790
0.175	0.790
0.175	0.930
0.445	0.930
0.445	1.310
0.895	1.310
0.895	1.595
1.200	1.595

Fig.5.12 *– Set of solutions obtained from the inversion of the average group velocity dispersion curve relative to NIS-CMSA path. The chosen solution is evidenced by the red line: this model, characterized by the minimum r.m.s., is presented in the table on the right. The black dotted line indicates the average solution.*

5.1.13 NIS-QUAR path

The starting model (Tab.5.13) used in the inversion of the average group velocity dispersion curve relative to the NIS-QUAR path (Fig.3.56B) is defined by 7 independent parameters (3 thickness and 4 V_S values) and by two different values of V_P/V_S ratio: 2.2 associated to the fixed, first, second and third inverted layers, 2 to the fourth inverted layer. The explored thickness is 2 km.

The obtained solution set consists of 4 solutions (Fig.5.13): the model characterized by the minimum r.m.s. presents V_S values increasing from 0.775 to 1.85 km/s, at a depth of 0.94 km.

NIS-QUAR path			
Parameters		**Step**	**Range of variability**
h (km)	0.090		
	0.085	0.020	0.039-0.169
	0.295	0.030	0.109-0.379
	0.490	0.045	0.109-0.599
V_S (km/s)	0.600		
	0.775	0.045	0.589-1.019
	1.045	0.030	0.909-1.201
	1.345	0.045	1.099-1.899
	1.775	0.075	1.399-1.921
V_P/V_S	2.2	for fixed, 1st, 2nd and 3rd inverted layers	
	2	for 4th inverted layer	

Tab.5.13– *Starting model used in the inversion of the average group velocity dispersion curve relative to NIS-QUAR path (inverted parameters are in black, fixed parameters are in blue).*

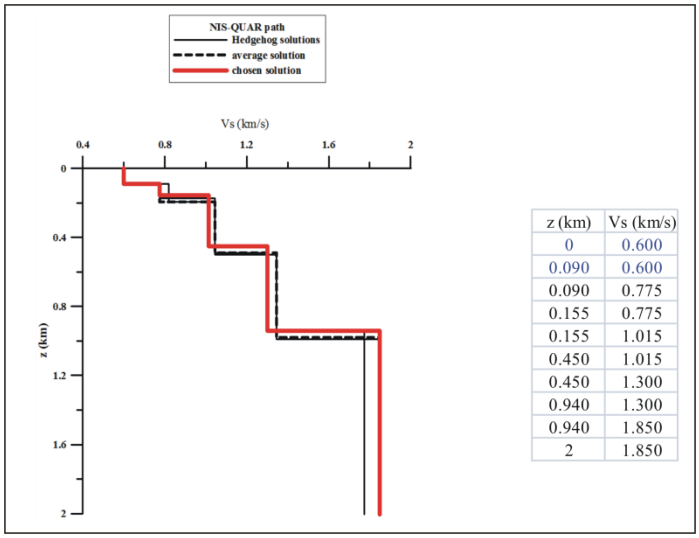

Fig.5.13 *– Set of solutions obtained from the inversion of the average group velocity dispersion curve relative to NIS-QUAR path. The chosen solution is evidenced by the red line: this model, characterized by the minimum r.m.s., is presented in the table on the right. The black dotted line indicates the average solution.*

5.1.14 NIS-SMN path

The starting model (Tab.5.14) used in the inversion of the average group velocity dispersion curve relative to the NIS-SMN path (Fig.3.58B) is defined by 7 independent parameters (3 thickness and 4 V_S values) and by a V_P/V_S ratio value of 1.8 for the fixed and the inverted layers. The explored thickness is 1.5 km.

NIS-SMN path			
Parameters		**Step**	**Range of variability**
h (km)	0.040		
	0.170	0.045	0.029-0.401
	0.200	0.045	0.089-0.319
	0.490	0.045	0.199-0.801
V_S (km/s)	0.530		
	0.810	0.050	0.399-1.001
	0.945	0.055	0.599-1.159
	1.300	0.085	0.909-1.569
	2.300	0.115	1.209-2.639
V_P/V_S	1.8	for all the layers	

Tab.5.14– *Starting model used in the inversion of the average group velocity dispersion curve relative to NIS-SMN path (inverted parameters are in black, fixed parameters are in blue).*

The obtained solution set consists of 5 solutions (Fig.5.14): the model characterized by the minimum r.m.s. presents V_S values increasing from 0.76 to 2.415 km/s, at a depth of 0.9 km.

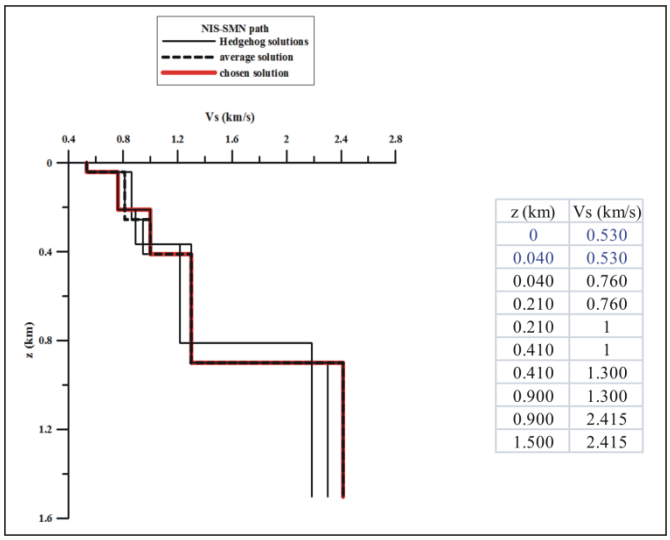

Fig.5.14 *– Set of solutions obtained from the inversion of the average group velocity dispersion curve relative to NIS-SMN path. The chosen solution is evidenced by the red line: this model, characterized by the minimum r.m.s., is presented in the table on the right. The black dotted line indicates the average solution.*

5.1.15 NIS-STH path

The starting model (Tab.5.15) used in the inversion of the average group velocity dispersion curve relative to the NIS-STH path (Fig.3.59B) is defined by 5 independent parameters (2 thickness and 3 V_S values) and by a V_P/V_S ratio value of 2.9 for the inverted

layers, while a V_P/V_S ratio value of 5 has resulted the optimal value for the fixed layer below the water column. The explored thickness is 1.4 km.

NIS-STH path			
Parameters		**Step**	**Range of variability**
h (km)	0.010		
	0.060		
	0.320	0.025	0.109-0.441
	0.150	0.040	0.009-0.289
V_S (km/s)	0		
	0.280		
	0.525	0.025	0.399-1.001
	0.700	0.060	0.499-0.861
	0.700	0.030	0.399-1.501
V_P/V_S	5	for the fixed layer	
	2.9	for all the inverted layers	

Tab.5.15– *Starting model used in the inversion of the average group velocity dispersion curve relative to NIS-STH path (inverted parameters are in black, fixed parameters are in blue).*

The obtained solution set consists of 4 solutions (Fig.5.15): the model characterized by the minimum r.m.s. presents V_S values increasing from 0.525 to 0.7 km/s, at a depth of about 0.4 km. A ~4% reduction in V_S values (from 0.7 to 0.67 km/s) is present at about 0.6 km depth till the bottom of the investigated structure (1.4 km).

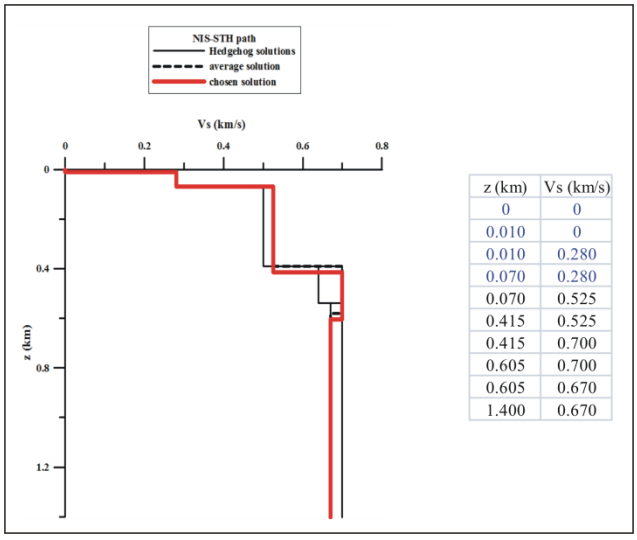

Fig.5.15 *– Set of solutions obtained from the inversion of the average group velocity dispersion curve relative to NIS-STH path. The chosen solution is evidenced by the red line: this model, characterized by the minimum r.m.s., is presented in the table on the right. The black dotted line indicates the average solution.*

5.1.16 POZ-ARCO path

The starting model (Tab.5.16) used in the inversion of the average group velocity dispersion curve relative to the POZ-ARCO path (Fig.3.60B) is defined by 5 independent parameters (2 thickness and 3 V_S values) and by a V_P/V_S ratio value of 2.3 for the fixed and the inverted layers. The explored thickness is 1 km.

POZ-ARCO path			
Parameters		**Step**	**Range of variability**
h (km)	0.100		
	0.200	0.025	0.049-0.401
	0.380	0.030	0.049-0.501
V_S (km/s)	0.750		
	0.850	0.025	0.599-1.501
	1.180	0.060	0.799-1.601
	1.655	0.065	0.999-1.901
V_P/V_S	2.3	for all the layers	

Tab.5.16– *Starting model used in the inversion of average group velocity dispersion curve relative to POZ-ARCO path (inverted parameters are in black, fixed parameters are in blue).*

The obtained solution set consists of 4 solutions (Fig.5.16): the model characterized by the minimum r.m.s. presents V_S values increasing from 0.825 to 1.655 km/s, at a depth of 0.655 km.

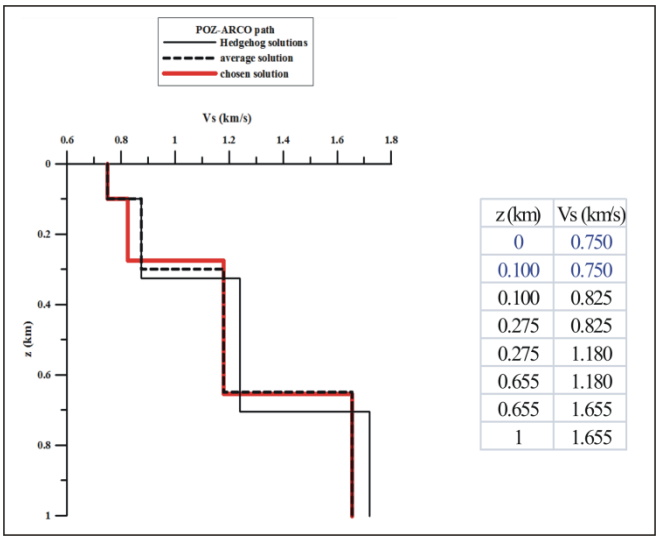

z (km)	Vs (km/s)
0	0.750
0.100	0.750
0.100	0.825
0.275	0.825
0.275	1.180
0.655	1.180
0.655	1.655
1	1.655

Fig.5.16 *– Set of solutions obtained from the inversion of the average group velocity dispersion curve relative to POZ-ARCO path. The chosen solution is evidenced by the red line: this model, characterized by the minimum r.m.s., is presented in the table on the right. The black dotted line indicates the average solution.*

5.1.17 POZ-ASE path

The starting model (Tab.5.17) used in the inversion of the average group velocity dispersion curve relative to the POZ-ASE path (Fig.3.7) is defined by 7 independent parameters (3 thickness and 4 V_S values) and by two different values of V_P/V_S ratio: 2.5 associated to the fixed, first, second and third inverted layers, and 2 to the fourth inverted layer. The explored thickness is 1.4 km.

POZ-ASE path			
Parameters		**Step**	**Range of variability**
h (km)	0.120		
	0.060	0.030	0.009-0.149
	0.265	0.045	0.059-0.449
	0.335	0.045	0.139-0.489
V_S (km/s)	0.360		
	0.675	0.060	0.509-0.789
	0.990	0.060	0.659-1.169
	0.615	0.050	0.409-0.759
	1.380	0.090	0.809-1.649
V_P/V_S	2.5	for fixed, 1st, 2nd and 3rd inverted layers	
	2	for 4th inverted layer	

Tab.5.17*– Starting model used in the inversion of the average group velocity dispersion curve relative to POZ-ASE path (inverted parameters are in black, fixed parameters are in blue).*

The obtained solution set consists of 6 solutions (Fig.5.17): the model characterized by the minimum r.m.s. presents V_S values increasing from 0.675 to 0.93 km/s, at a depth of 0.15 km. At 0.46 km depth a ~40% reduction in V_S values (from 0.93 to 0.565 km/s) is present defining a low velocity layer of about 0.33 km thickness. Below this layer V_S increases again to 1.29 km/s till the bottom of the investigated structure (1.4 km).

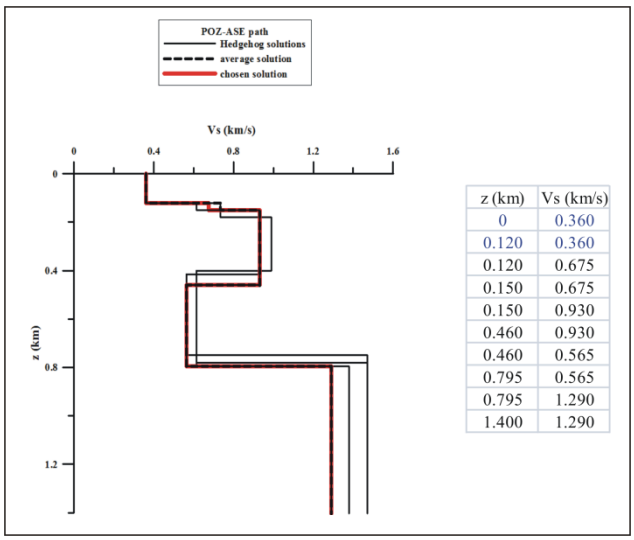

Fig.5.17 *– Set of solutions obtained from the inversion of the average group velocity dispersion curve relative to POZ-ASE path. The chosen solution is evidenced by the red line: this model, characterized by the minimum r.m.s., is presented in the table on the right. The black dotted line indicates the average solution.*

5.1.18 POZ-CMSA path

The starting model (Tab.5.18) used in the inversion of the average group velocity dispersion curve relative to the POZ-CMSA path (Fig.3.61B) is defined by 7 independent parameters (3 thickness and 4 V_S values) and by two different values of V_P/V_S ratio: 2.3 associated to the fixed, first, second and third inverted layers, and 2 to the fourth inverted layer. The explored thickness is 1.4 km.

POZ-CMSA path			
Parameters		**Step**	**Range of variability**
h (km)	0.200		
	0.075	0.020	0.009-0.129
	0.320	0.035	0.209-0.499
	0.555	0.030	0.139-0.989
V_S (km/s)	0.470		
	0.695	0.040	0.599-0.851
	1.045	0.020	0.659-1.169
	0.540	0.025	0.309-1.559
	1.300	0.065	0.809-1.649
V_P/V_S	2.3	for fixed, 1st, 2nd and 3rd inverted layers	
	2	for 4th inverted layer	

Tab.5.18*– Starting model used in the inversion of the average group velocity dispersion curve relative to POZ-CMSA path (inverted parameters are in black, fixed parameters are in blue).*

The obtained solution set consists of 5 solutions (Fig.5.18): the model characterized by the minimum r.m.s. (which is coincident with the average solution) presents V_S values increasing from 0.655 to 1.025 km/s, at a depth of 0.275 km. At about 0.6 km depth a ~47% reduction in V_S values (from 1.025 to 0.54 km/s) is present defining a low velocity layer of about 0.55 km thickness. Below this layer V_S increases again to 1.3 km/s till the bottom of the investigated structure (1.4 km).

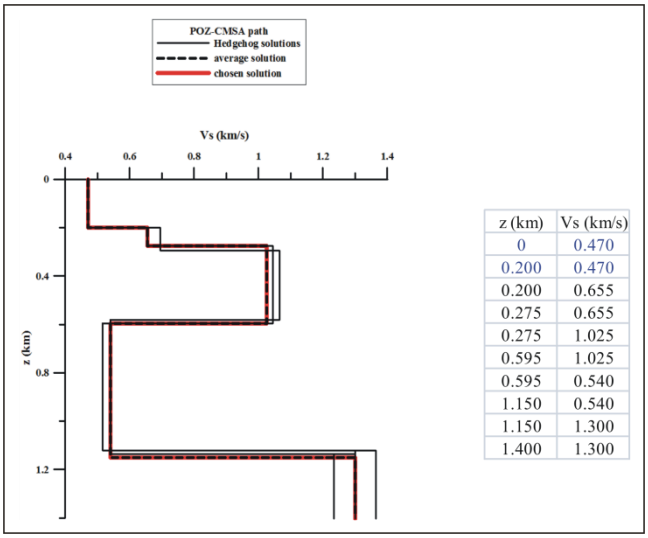

z (km)	Vs (km/s)
0	0.470
0.200	0.470
0.200	0.655
0.275	0.655
0.275	1.025
0.595	1.025
0.595	0.540
1.150	0.540
1.150	1.300
1.400	1.300

Fig.5.18 *– Set of solutions obtained from the inversion of the average group velocity dispersion curve relative to POZ-CMSA path. The chosen solution is evidenced by the red line: this model, characterized by the minimum r.m.s. and coincident with the average solution (black dotted line), is presented in the table on the right.*

5.1.19 POZ-NIS path

The starting model (Tab.5.19) used in the inversion of the average group velocity dispersion curve relative to the POZ-NIS path (Fig.3.64B) is defined by 5 independent parameters (2 thickness and 3 V_S values) and by two V_P/V_S ratio values: ~8 associated to the fixed layer below the water column, and 2.8 to all the inverted layers. The explored thickness is 1.1 km.

The obtained solution set consists of 5 solutions (Fig.5.19): the model characterized by the minimum r.m.s. presents a low velocity layer at a depth of 0.48 km where a ~30% reduction in V_S values (from 0.43 to 0.3 km/s) is present and persists to about 0.73 km depth where the Vs increases to 0.88 km/s.

POZ-NIS path			
Parameters		**Step**	**Range of variability**
h (km)	0.040		
	0.110		
	0.305	0.025	0.209-0.469
	0.255	0.025	0.059-0.389
V_S (km/s)	0		
	0.180		
	0.430	0.035	0.339-0.551
	0.300	0.025	0.189-0.729
	0.880	0.055	0.559-1.099
V_P/V_S	~8	for the fixed layer	
	2.8	for all the inverted layers	

Tab.5.19– *Starting model used in the inversion of the average group velocity dispersion curve relative to POZ-NIS path (inverted parameters are in black, fixed parameters are in blue).*

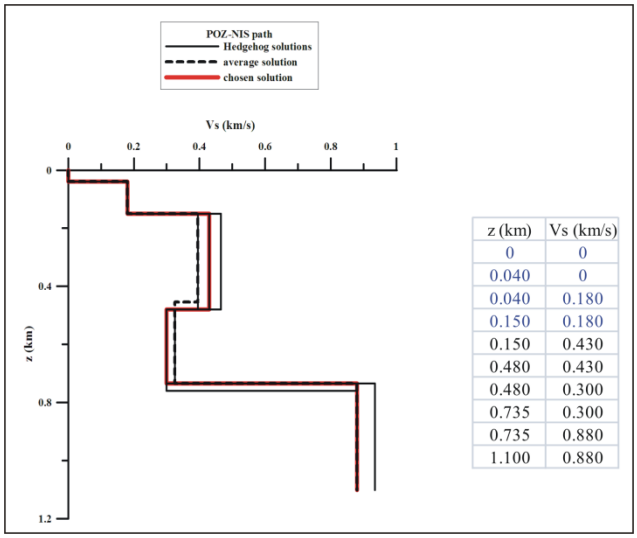

Fig.5.19 *– Set of solutions obtained from the inversion of the average group velocity dispersion curve relative to POZ-NIS path. The chosen solution is evidenced by the red line: this model, characterized by the minimum r.m.s., is presented in the table on the right. The black dotted line indicates the average solution.*

5.1.20 POZ-QUAR path

The starting model (Tab.5.20) used in the inversion of the average group velocity dispersion curve relative to the POZ-QUAR path (Fig.3.65B) is defined by 7 independent parameters (3 thickness and 4 V_S values) and by two different values of V_P/V_S ratio: 2 associated to the fixed, first, second and third inverted layers, and 1.8 to the fourth inverted layer. The explored thickness is 2 km.

POZ-QUAR path			
Parameters		**Step**	**Range of variability**
h (km)	0.120		
	0.190	0.050	0.029-0.399
	0.160	0.055	0.029-0.399
	0.420	0.055	0.199-0.699
V_S (km/s)	0.450		
	0.720	0.020	0.499-0.899
	0.975	0.060	0.599-1.199
	1.135	0.065	0.899-1.399
	1.830	0.085	1.599-2.099
V_P/V_S	2	for fixed, 1st, 2nd and 3rd inverted layers	
	1.8	for 4th inverted layer	

Tab.5.20– *Starting model used in the inversion of the average group velocity dispersion curve relative to POZ-QUAR path (inverted parameters are in black, fixed parameters are in blue).*

The obtained solution set consists of 3 solutions (Fig.5.20): the model characterized by the minimum r.m.s. presents V_S values increasing from 0.7 to 1.83 km/s, at a depth of 0.945 km.

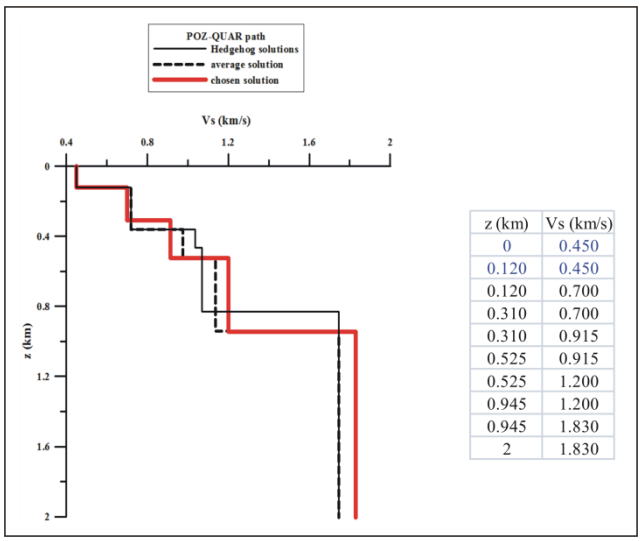

Fig.5.20 *– Set of solutions obtained from the inversion of the average group velocity dispersion curve relative to POZ-QUAR path. The chosen solution is evidenced by the red line: this model, characterized by the minimum r.m.s., is presented in the table on the right. The black dotted line indicates the average solution.*

5.1.21 POZ-SOLF path

The starting model (Tab.5.21) used in the inversion of the average group velocity dispersion curve relative to the POZ-SOLF path (Fig.3.62E) is defined by 5 independent parameters (2 thickness and 3 V_S values) and by a V_P/V_S ratio value of 2.3 for the fixed and the inverted layers. The explored thickness is 0.9 km.

POZ-SOLF path			
Parameters		**Step**	**Range of variability**
h (km)	0.070		
	0.130	0.045	0.029-0.299
	0.310	0.065	0.099-0.499
V_S (km/s)	0.600		
	0.770	0.055	0.599-0.999
	1.000	0.075	0.599-1.201
	1.390	0.085	1.099-1.599
V_P/V_S	2.3	for all the layers	

Tab.5.21– *Starting model used in the inversion of the average group velocity dispersion curve relative to POZ-SOLF path (inverted parameters are in black, fixed parameters are in blue).*

The obtained solution set consists of 4 solutions (Fig.5.21): the model characterized by the minimum r.m.s. presents V_S values increasing from 0.77 to 1.475 km/s, at a depth of 0.575 km.

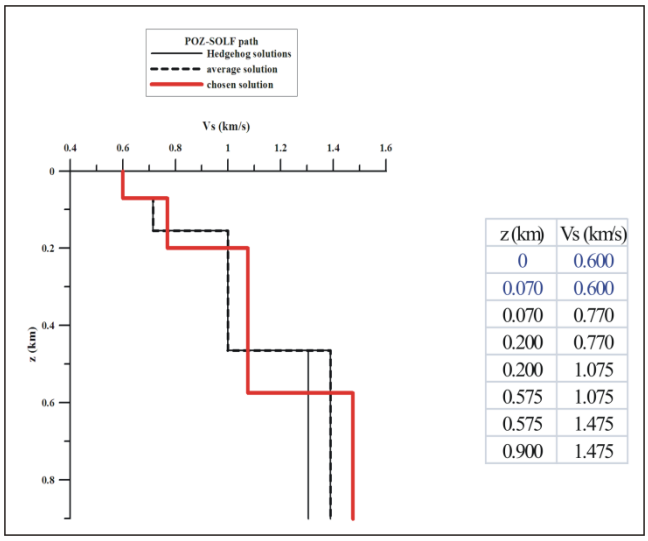

Fig.5.21 *– Set of solutions obtained from the inversion of the average group velocity dispersion curve relative to POZ-SOLF path. The chosen solution is evidenced by the red line: this model, characterized by the minimum r.m.s., is presented in the table on the right. The black dotted line indicates the average solution.*

5.1.22 QUAR-ASE path

The starting model (Tab.5.22) used in the inversion of the average group velocity dispersion curve relative to the QUAR-ASE path (Fig.3.23) is defined by 7 independent parameters (3 thickness and 4 V_S values) and by a V_P/V_S ratio value of 1.9 for the fixed and the inverted layers. The explored thickness is 1 km.

QUAR-ASE path			
Parameters		**Step**	**Range of variability**
h (km)	0.110		
	0.155	0.010	0.049-0.299
	0.120	0.020	0.049-0.399
	0.280	0.040	0.169-0.499
V_S (km/s)	0.520		
	0.600	0.010	0.499-0.899
	0.760	0.030	0.599-0.899
	0.975	0.020	0.799-1.199
	1.280	0.040	1.009-1.499
V_P/V_S	1.9	for all the layers	

***Tab.5.22**– Starting model used in the inversion of the average group velocity dispersion curve relative to QUAR-ASE path (inverted parameters are in black, fixed parameters are in blue).*

The obtained solution set consists of 3 solutions (Fig.5.22): the model characterized by the minimum r.m.s. presents V_S values increasing from 0.59 to 1.32 km/s, at a depth of 0.715 km.

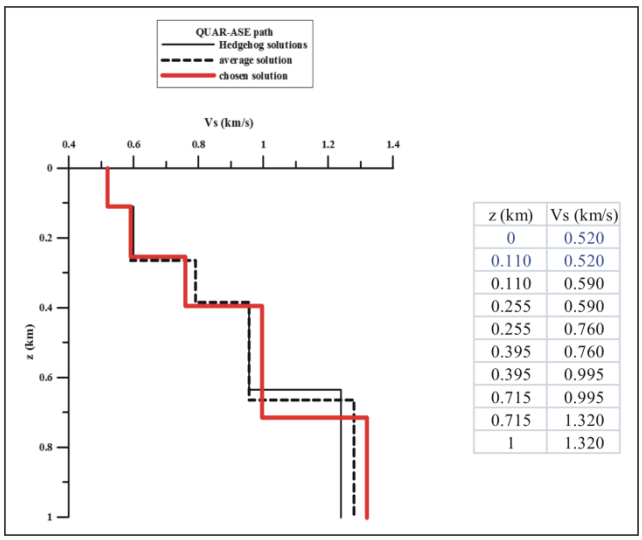

z (km)	Vs (km/s)
0	0.520
0.110	0.520
0.110	0.590
0.255	0.590
0.255	0.760
0.395	0.760
0.395	0.995
0.715	0.995
0.715	1.320
1	1.320

Fig.5.22 *– Set of solutions obtained from the inversion of the average group velocity dispersion curve relative to QUAR-ASE path. The chosen solution is evidenced by the red line: this model, characterized by the minimum r.m.s., is presented in the table on the right. The black dotted line indicates the average solution.*

5.1.23 QUAR-CMSA path

The starting model (Tab.5.23) used in the inversion of the average group velocity dispersion curve relative to the QUAR-CMSA path (Fig.3.67B) is defined by 7 independent parameters (3 thickness and 4 V_S values) and by a V_P/V_S ratio value of 1.9 for the fixed and the inverted layers. The explored thickness is 1 km.

QUAR-CMSA path			
Parameters		**Step**	**Range of variability**
h (km)	0.110		
	0.115	0.030	0.049-0.259
	0.165	0.045	0.049-0.339
	0.225	0.060	0.069-0.399
V_S (km/s)	0.580		
	0.600	0.020	0.499-0.799
	0.800	0.040	0.599-0.999
	0.915	0.060	0.699-1.199
	1.280	0.065	1.009-1.499
V_P/V_S	1.9	for all the layers	

Tab.5.23*– Starting model used in the inversion of the average group velocity dispersion curve relative to QUAR-CMSA path (inverted parameters are in black, fixed parameters are in blue).*

The obtained solution set consists of 5 solutions (Fig.5.23): the model characterized by the minimum r.m.s. presents V_S values increasing from 0.62 to 1.28 km/s , at a depth of 0.66 km.

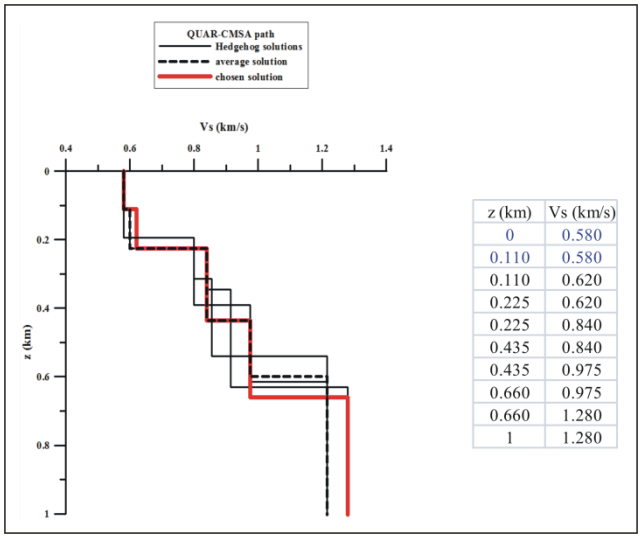

z (km)	Vs (km/s)
0	0.580
0.110	0.580
0.110	0.620
0.225	0.620
0.225	0.840
0.435	0.840
0.435	0.975
0.660	0.975
0.660	1.280
1	1.280

Fig.5.23 *– Set of solutions obtained from the inversion of the average group velocity dispersion curve relative to QUAR-CMSA path. The chosen solution is evidenced by the red line: this model, characterized by the minimum r.m.s., is presented in the table on the right. The black dotted line indicates the average solution.*

5.1.24 QUAR-SOLF path

The starting model (Tab.5.24) used in the inversion of the average group velocity dispersion curve relative to the QUAR-SOLF path (Fig.3.32B) is defined by 7 independent parameters (3 thickness and 4 V_S values) and by two different values of V_P/V_S ratio: 1.9 associated to the fixed, first, second and third inverted layers, and 1.8 to the fourth inverted layer. The explored thickness is 1.3 km.

The obtained solution set consists of 6 solutions (Fig.5.24): the model characterized by the minimum r.m.s. presents V_S values increasing from 0.775 to 1.89 km/s, at a depth of 0.81 km.

QUAR-SOLF path			
Parameters		**Step**	**Range of variability**
h (km)	0.110		
	0.170	0.030	0.049-0.299
	0.230	0.040	0.119-0.699
	0.340	0.055	0.119-0.599
V_S (km/s)	0.590		
	0.775	0.035	0.599-0.999
	0.975	0.035	0.799-1.199
	1.265	0.060	1.009-1.599
	1.950	0.060	1.609-2.099
V_P/V_S	1.9	for fixed, 1st, 2nd and 3rd inverted layers	
	1.8	for 4th inverted layer	

Tab.5.24– *Starting model used in the inversion of the average group velocity dispersion curve relative to QUAR-SOLF path (inverted parameters are in black, fixed parameters are in blue).*

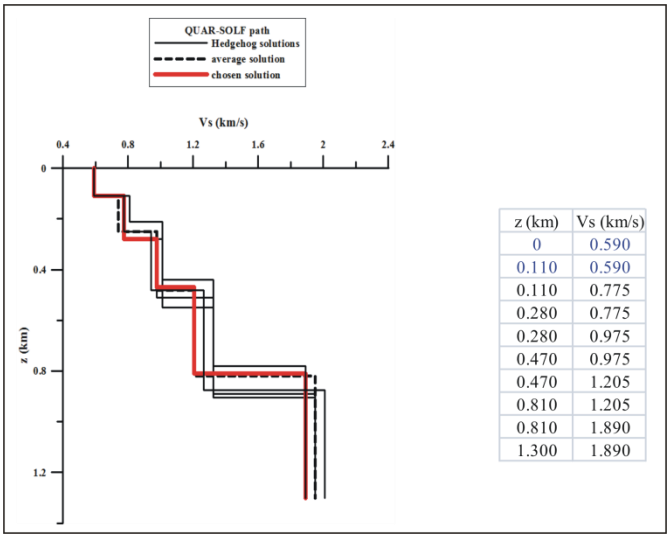

Fig.5.24 *– Set of solutions obtained from the inversion of the average group velocity dispersion curve relative to QUAR-SOLF path. The chosen solution is evidenced by the red line: this model, characterized by the minimum r.m.s., is presented in the table on the right. The black dotted line indicates the average solution.*

5.1.25 SOLF-SMN path

The starting model (Tab.5.25) used in the inversion of the average group velocity dispersion curve relative to the SOLF-SMN path (Fig.3.49D) is defined by 7 independent parameters (3 thickness and 4 V_S values) and by two different values of V_P/V_S ratio: 2

associated to the fixed, first and second inverted layers, and 1.8 to the third and fourth inverted layers. The explored thickness is 2 km.

SOLF-SMN path			
Parameters		**Step**	**Range of variability**
h (km)	0.040		
	0.190	0.040	0.019-0.309
	0.330	0.040	0.169-0.499
	0.480	0.060	0.299-0.699
V_S (km/s)	0.550		
	0.720	0.050	0.579-0.899
	1.055	0.055	0.899-1.209
	1.300	0.085	0.909-1.549
	1.895	0.095	1.559-2.079
V_P/V_S	2	for fixed, 1st and 2nd inverted layers	
	1.8	for 3rd and 4th inverted layers	

Tab.5.25 *– Starting model used in the inversion of the average group velocity dispersion curve relative to SOLF-SMN path (inverted parameters are in black, fixed parameters are in blue).*

The obtained solution set consists of 4 solutions (Fig.5.25): the model characterized by the minimum r.m.s. presents V_S values increasing from 0.77 to 1.99 km/s, at a depth of 0.98 km.

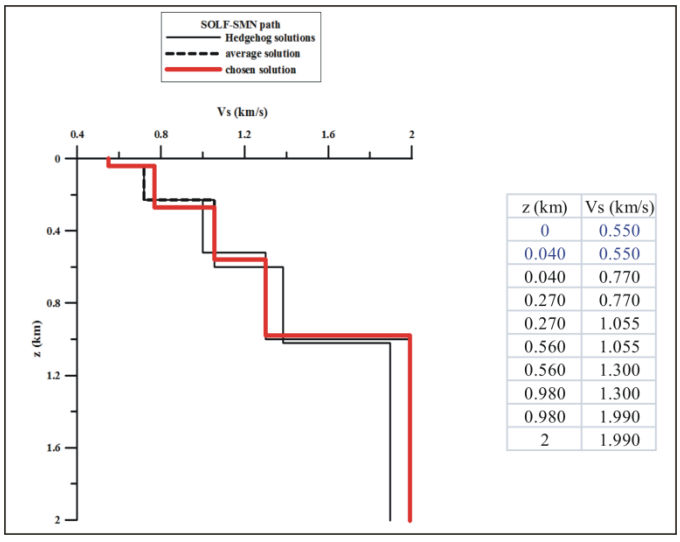

Fig.5.25 *– Set of solutions obtained from the inversion of the average group velocity dispersion curve relative to SOLF-SMN path. The chosen solution is evidenced by the red line: this model, characterized by the minimum r.m.s., is presented in the table on the right. The black dotted line indicates the average solution.*

Chapter 6

V_S MODELS AT ISCHIA

6.1 Hedgehog non-linear inversion of average dispersion curves

Hedgehog non-linear inversion has been performed for all the 13 average group velocity dispersion curves obtained at Ischia (see 4.3 section). Average group velocity dispersion curves are in 0.64-2.22 s period range (Fig.4.17) that allows to explore a maximum depth of 2 km.

Starting models of the inversion have been parameterized based on stratigraphic and volcanological data (Penta and Conforto, 1951; Capaldi et al., 1976; Forcella et al., 1981; 1983) for V_S and thickness values, and the gravimetric and aeromagnetic interpretative models (Nunziata and Rapolla, 1987) beside the Nafe-Drake empirical relation (Fowler, 1995) for density values.

As regards the V_P/V_S ratio, after a set of tests made varying it between 1.8 and 3.0, with 0.1 step, I have accepted as a suitable value the one that or maximizes the number of solutions, keeping all other values of the parameterization unchanged, or improves the resolution of the parameters (smaller step). The suitable V_P/V_S ratio turned out to be in the range 1.8-2.0 depending on the path.

In the parameterization, each layer is defined by V_S and thickness values considered as independent parameters, V_P as dependent parameter, density and V_P/V_S ratio as fixed parameters based on the preliminary tests. The starting models are characterized by the presence of a layer at the top of the investigated structure defined by thickness and V_S fixed values (indicated by the blue colour in the following tables).

In the following sections starting models and the obtained set of solutions are presented for each paths. As for Campi Flegrei, chosen solutions are characterized by the minimum r.m.s.

6.1.1 ISCH-NEG path

The starting model (Tab.6.1) used in the inversion of the average group velocity dispersion curve relative to ISCH-NEG path (Fig.4.5E) is defined by 7 independent parameters (3 thickness and 4 V_S values) and a V_P/V_S ratio value of 1.9 for the fixed and the inverted layers. The explored thickness is 1.4 km.

ISCH-NEG path			
Parameters		**Step**	**Range of variability**
h (km)	0.100		
	0.085	0.020	0.009-0.231
	0.315	0.065	0.049-0.491
	0.335	0.065	0.159-0.541
V_S (km/s)	0.550		
	0.670	0.060	0.549-0.991
	0.970	0.065	0.649-1.171
	1.355	0.080	0.999-1.649
	1.785	0.065	1.089-1.991
V_P/V_S	1.9	for all the layers	

Tab.6.1*– Starting model used in the inversion of the average group velocity dispersion curve relative to ISCH-NEG path (inverted parameters are in black, fixed parameters are in blue).*

The obtained solution set consists of 4 solutions (Fig.6.1): the model characterized by the minimum r.m.s. presents V_S values increasing from 0.67 to 1.785 km/s, at a depth of 0.835 km.

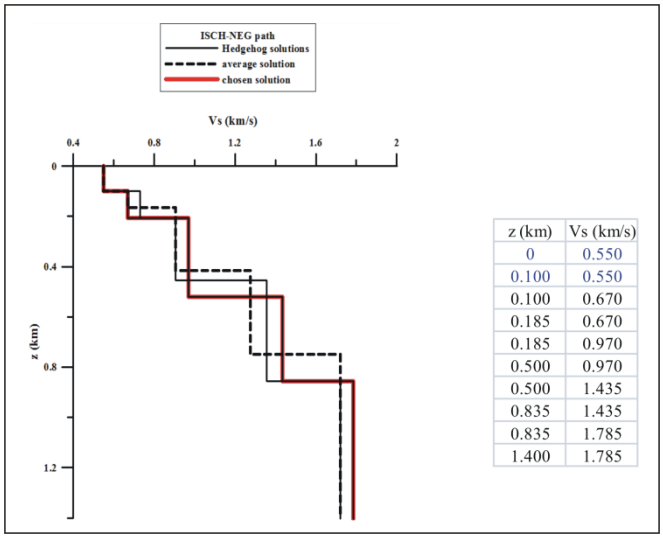

Fig.6.1 *– Set of solutions obtained from the inversion of the average group velocity dispersion curve relative to ISCH-NEG path. The chosen solution is evidenced by the red line: this model, characterized by the minimum r.m.s., is presented in the table on the right. The black dotted line indicates the average solution.*

6.1.2 ISCH-NPL path

The starting model (Tab.6.2) used in the inversion of the average group velocity dispersion curve relative to ISCH-NPL path (Fig.4.6F) is defined by 5 independent parameters (2 thickness and 3 V_S values) and a V_P/V_S ratio value of 1.8 for the fixed and the inverted layers. The explored thickness is 0.7 km.

ISCH-NPL path			
Parameters		**Step**	**Range of variability**
h (km)	0.100		
	0.130	0.020	0.089-0.171
	0.310	0.040	0.229-0.391
V_S (km/s)	0.380		
	0.515	0.010	0.494-0.536
	0.900	0.080	0.559-2.201
	1.430	0.135	1.159-1.701
V_P/V_S	1.8	for all the layers	

Tab.6.2– *Starting model used in the inversion of the average group velocity dispersion curve relative to ISCH-NPL path (inverted parameters are in black, fixed parameters are in blue).*

The obtained solution set consists of 3 solutions (Fig.6.2): the model characterized by the minimum r.m.s. presents V_S values increasing from 0.525 to 1.43 km/s, at a depth of 0.54 km.

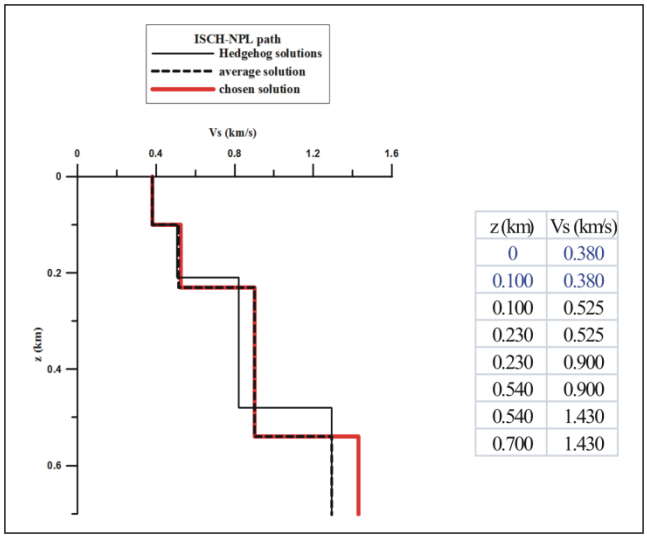

Fig.6.2 *– Set of solutions obtained from the inversion of the average group velocity dispersion curve relative to ISCH-NPL path. The chosen solution is evidenced by the red line: this model, characterized by the minimum r.m.s., is presented in the table on the right. The black dotted line indicates the average solution.*

6.1.3 SPL-WTES path

The starting model (Tab.6.3) used in the inversion of the average group velocity dispersion curve relative to SPL-WTES path (Fig.4.7E) is defined by 5 independent parameters (2 thickness and 3 V_S values) and a V_P/V_S ratio value of 1.8 for the fixed and the inverted layers. The explored thickness is 0.9 km.

SPL-WTES path			
Parameters		**Step**	**Range of variability**
h (km)	0.090		
	0.190	0.055	0.049-0.339
	0.135	0.080	0.009-0.339
V_S (km/s)	0.620		
	0.935	0.050	0.791-1.091
	1.155	0.090	0.959-1.421
	2.050	0.130	1.009-2.399
V_P/V_S	1.8	for all the layers	

Tab.6.3– *Starting model used in the inversion of the average group velocity dispersion curve relative to SPL-WTES path (inverted parameters are in black, fixed parameters are in blue).*

The obtained solution set consists of 6 solutions (Fig.6.3): the model characterized by the minimum r.m.s. presents V_S values increasing from 0.985 to 1.92 km/s, at a depth of 0.39 km.

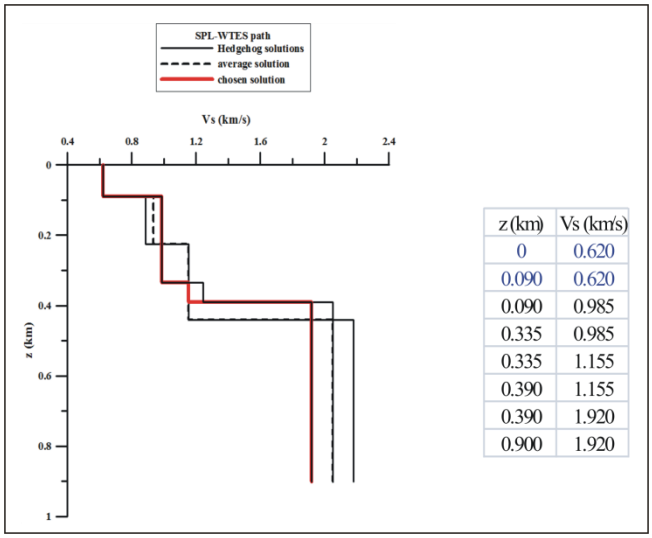

Fig.6.3 *– Set of solutions obtained from the inversion of the average group velocity dispersion curve relative to SPL-WTES path. The chosen solution is evidenced by the red line: this model, characterized by the minimum r.m.s., is presented in the table on the right. The black dotted line indicates the average solution.*

6.1.4 SUC-NFOR path

The starting model (Tab.6.4) used in the inversion of the average group velocity dispersion curve relative to SUC-NFOR path (Fig.4.8E) is defined by 5 independent parameters (2 thickness and 3 V_S values) and a V_P/V_S ratio value of 1.9 for the fixed and the inverted layers. The explored thickness is 0.9 km.

SUC-NFOR path			
Parameters		**Step**	**Range of variability**
h (km)	0.050		
	0.195	0.035	0.099-0.561
	0.295	0.060	0.099-0.581
V_S (km/s)	0.420		
	0.590	0.030	0.449-0.951
	0.890	0.040	0.549-1.591
	1.410	0.080	1.139-1.661
V_P/V_S	1.9	for all the layers	

Tab.6.4– *Starting model used in the inversion of the average group velocity dispersion curve relative to SUC-NFOR path (inverted parameters are in black, fixed parameters are in blue).*

The obtained solution set consists of 4 solutions (Fig.6.4): the model characterized by the minimum r.m.s. presents V_S values increasing from 0.59 to 1.41 km/s, at a depth of 0.6 km.

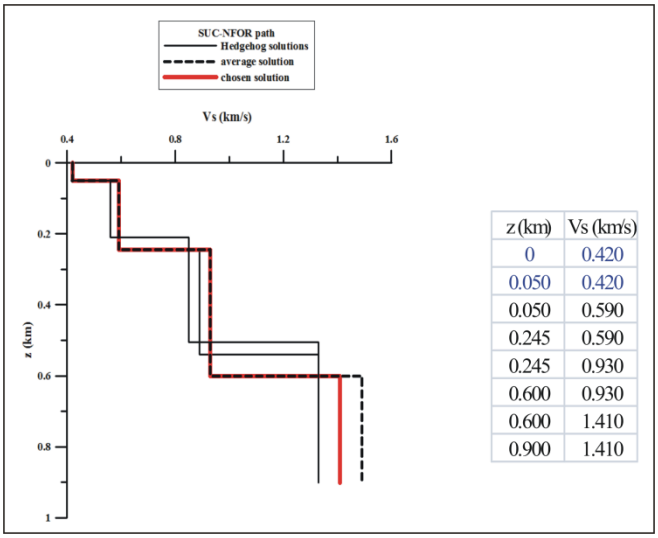

Fig.6.4 *– Set of solutions obtained from the inversion of the average group velocity dispersion curve relative to SUC-NFOR path. The chosen solution is evidenced by the red line: this model, characterized by the minimum r.m.s., is presented in the table on the right. The black dotted line indicates the average solution.*

6.1.5 ISC-ETES path

The starting model (Tab.6.5) used in the inversion of the average group velocity dispersion curve relative to ISC-ETES path (Fig.4.9G) is defined by 5 independent parameters (2 thickness and 3 V_S values) and a V_P/V_S ratio value of 1.8 for the fixed and the inverted layers. The explored thickness is 0.8 km.

ISC-ETES path			
Parameters		**Step**	**Range of variability**
h (km)	0.070		
	0.175	0.020	0.011-0.399
	0.280	0.065	0.056-0.799
V_S (km/s)	0.570		
	0.790	0.045	0.449-0.999
	1.250	0.065	0.759-1.699
	1.730	0.075	1.201-1.969
V_P/V_S	1.8	for all the layers	

Tab.6.5– *Starting model used in the inversion of the average group velocity dispersion curve relative to ISC-ETES path (inverted parameters are in black, fixed parameters are in blue).*

The obtained solution set consists of 4 solutions (Fig.6.5): the model characterized by the minimum r.m.s. presents V_S values increasing from 0.745 to 1.805 km/s, at a depth of about 0.5 km.

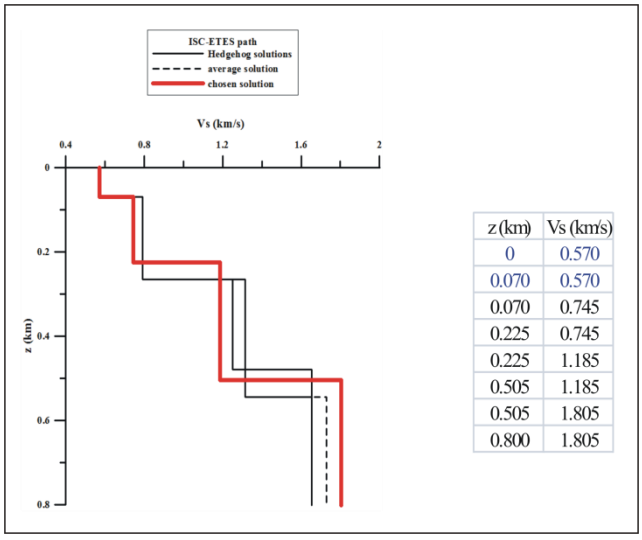

Fig.6.5 *– Set of solutions obtained from the inversion of the average group velocity dispersion curve relative to ISC-ETES path. The chosen solution is evidenced by the red line: this model, characterized by the minimum r.m.s., is presented in the table on the right. The black dotted line indicates the average solution.*

6.1.6 ISC-NEG path

The starting model (Tab.6.6) used in the inversion of the average group velocity dispersion curve relative to ISC-NEG path (Fig.4.10E) is defined by 7 independent parameters (3 thickness and 4 V_S values) and a V_P/V_S ratio value of 1.8 for the fixed and the inverted layers. The explored thickness is 1.5 km.

ISC-NEG path			
Parameters		**Step**	**Range of variability**
h (km)	0.070		
	0.100	0.045	0.011-0.239
	0.250	0.080	0.056-0.549
	0.195	0.095	0.054-0.779
V_S (km/s)	0.590		
	0.680	0.068	0.539-0.859
	1.200	0.090	0.959-1.439
	1.310	0.120	1.001-1.769
	2.100	0.080	1.801-2.259
V_P/V_S	1.8	for all the layers	

Tab.6.6– *Starting model used in the inversion of the average group velocity dispersion curve relative to ISC-NEG path (inverted parameters are in black, fixed parameters are in blue).*

The obtained solution set consists of 5 solutions (Fig.6.6): the model characterized by the minimum r.m.s. presents V_S values increasing from 0.68 to 2.18 km/s, at a depth of 0.6 km.

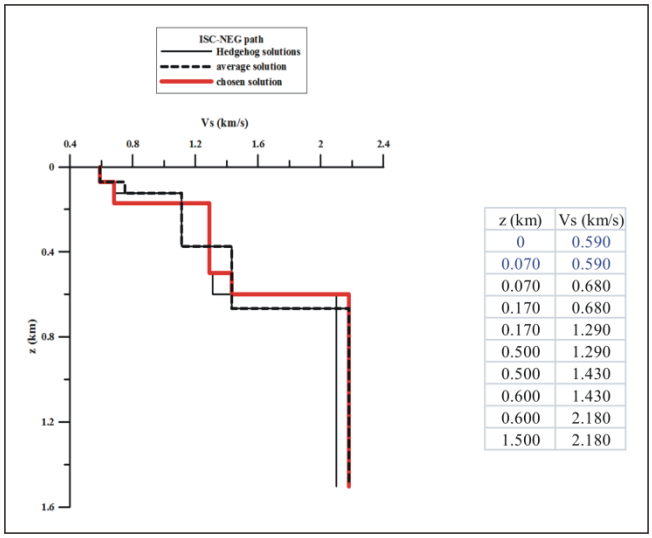

Fig.6.6 *– Set of solutions obtained from the inversion of the average group velocity dispersion curve relative to ISC-NEG path. The chosen solution is evidenced by the red line: this model, characterized by the minimum r.m.s., is presented in the table on the right. The black dotted line indicates the average solution.*

6.1.7 ISC-PER path

The starting model (Tab.6.7) used in the inversion of the average group velocity dispersion curve relative to ISC-PER path (Fig.4.11G) is defined by 5 independent parameters (2 thickness and 3 V_S values) and a V_P/V_S ratio value of 1.8 for the fixed and the inverted layers. The explored thickness is 0.9 km.

ISC-PER path			
Parameters		**Step**	**Range of variability**
h (km)	0.100		
	0.190	0.040	0.011-0.299
	0.430	0.080	0.056-0.699
V_S (km/s)	0.600		
	0.750	0.060	0.549-0.899
	1.100	0.065	0.759-1.399
	1.560	0.080	1.401-1.719
V_P/V_S	1.8	for all the layers	

Tab.6.7– *Starting model used in the inversion of the average group velocity dispersion curve relative to ISC-PER path (inverted parameters are in black, fixed parameters are in blue).*

The obtained solution set consists of 4 solutions (Fig.6.7): the model characterized by the minimum r.m.s. presents V_S values increasing from 0.75 to 1.48 km/s, at a depth of 0.72 km.

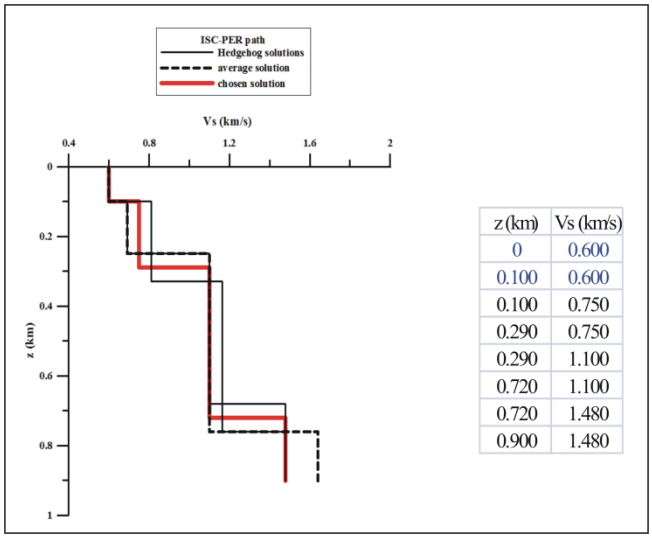

Fig.6.7 *– Set of solutions obtained from the inversion of the average group velocity dispersion curve relative to ISC-PER path. The chosen solution is evidenced by the red line: this model, characterized by the minimum r.m.s., is presented in the table on the right. The black dotted line indicates the average solution.*

6.1.8 ISC-SAN path

The starting model (Tab.6.8) used in the inversion of the average group velocity dispersion curve relative to ISC-SAN path (Fig.4.12G) is defined by 5 independent parameters (2 thickness and 3 V_S values) and a V_P/V_S ratio value of 1.8 for the fixed and the inverted layers. The explored thickness is 1.1 km.

ISC-SAN path			
Parameters		**Step**	**Range of variability**
h (km)	0.060		
	0.250	0.025	0.059-0.399
	0.445	0.025	0.109-0.554
V_S (km/s)	0.550		
	0.850	0.020	0.461-0.999
	1.480	0.050	1.025-1.699
	2.320	0.060	2.136-2.499
V_P/V_S	1.8	for all the layers	

Tab.6.8– *Starting model used in the inversion of the average group velocity dispersion curve relative to ISC-SAN path (inverted parameters are in black, fixed parameters are in blue).*

The obtained solution set consists of 3 solutions (Fig.6.8): the model characterized by the minimum r.m.s. presents V_S values increasing from 0.83 to 2.26 km/s, at a depth of 0.73 km.

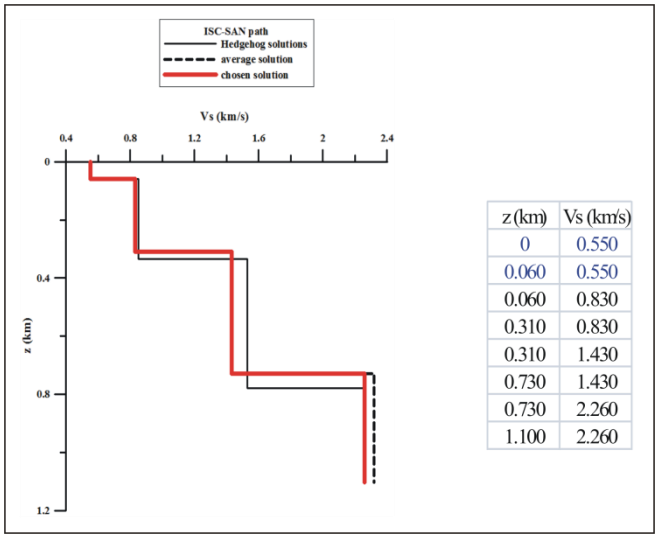

Fig.6.8 *– Set of solutions obtained from the inversion of the average group velocity dispersion curve relative to ISC-SAN path. The chosen solution is evidenced by the red line: this model, characterized by the minimum r.m.s., is presented in the table on the right. The black dotted line indicates the average solution.*

6.1.9 NEG-ETES path

The starting model (Tab.6.9) used in the inversion of the average group velocity dispersion curve relative to NEG-ETES path (Fig.4.4E) is defined by 7 independent parameters (3 thickness and 4 V_S values) and a V_P/V_S ratio value of 1.8 for the fixed and the inverted layers. The explored thickness is 2 km.

NEG-ETES path			
Parameters		**Step**	**Range of variability**
h (km)	0.050		
	0.080	0.027	0.009-0.454
	0.250	0.065	0.056-0.429
	0.410	0.082	0.109-0.759
V_S (km/s)	0.550		
	0.590	0.080	0.426-0.829
	1.344	0.064	1.101-1.535
	1.530	0.060	1.351-1.709
	2.320	0.097	1.121-2.689
V_P/V_S	1.8	for all the layers	

Tab.6.9– *Starting model used in the inversion of the average group velocity dispersion curve relative to NEG-ETES path (inverted parameters are in black, fixed parameters are in blue).*

The obtained solution set consists of 4 solutions (Fig.6.9): the model characterized by the minimum r.m.s. presents V_S values increasing from 0.59 to 2.32 km/s, at a depth of about 0.8 km.

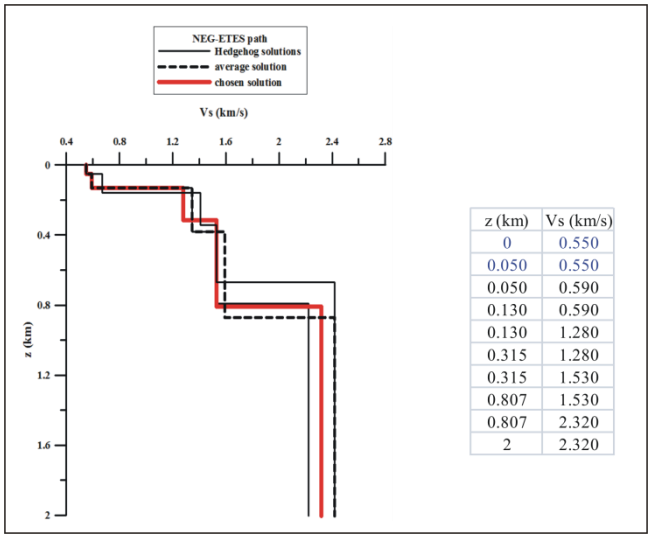

Fig.6.9 *– Set of solutions obtained from the inversion of the average group velocity dispersion curve relative to NEG-ETES path. The chosen solution is evidenced by the red line: this model, characterized by the minimum r.m.s., is presented in the table on the right. The black dotted line indicates the average solution.*

6.1.10 NEG-SAN path

The starting model (Tab.6.10) used in the inversion of the average group velocity dispersion curve relative to NEG-SAN path (Fig.4.13E) is defined by 7 independent parameters (3 thickness and 4 V_S values) and a V_P/V_S ratio value of 1.8 for the fixed and the inverted layers. The explored thickness is 1.5 km.

NEG-SAN path			
Parameters		**Step**	**Range of variability**
h (km)	0.090		
	0.130	0.045	0.009-0.254
	0.240	0.077	0.009-0.449
	0.310	0.090	0.109-0.694
V_S (km/s)	0.640		
	0.830	0.084	0.601-1.079
	1.220	0.090	1.001-1.539
	1.470	0.120	1.209-1.799
	2.490	0.100	2.221-2.689
V_P/V_S	1.8	for all the layers	

Tab.6.10– *Starting model used in the inversion of the average group velocity dispersion curve relative to NEG-SAN path (inverted parameters are in black, fixed parameters are in blue).*

The obtained solution set consists of 5 solutions (Fig.6.10): the model characterized by the minimum r.m.s. presents V_S values increasing from ~0.75 to 2.39 km/s, at a depth of ~0.78 km.

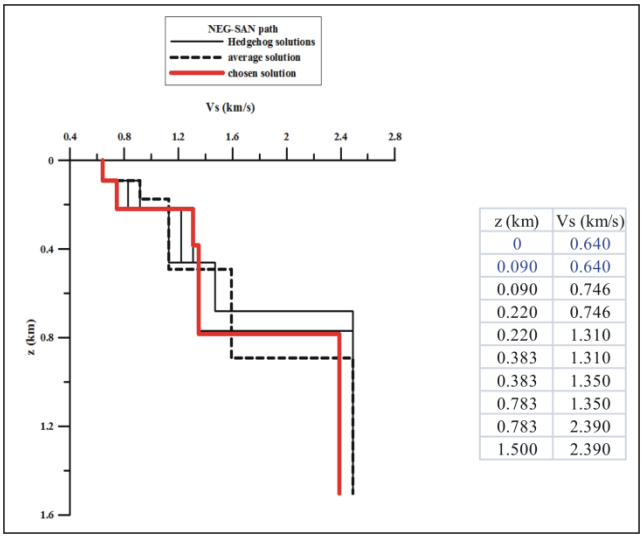

Fig.6.10 *– Set of solutions obtained from the inversion of the average group velocity dispersion curve relative to NEG-SAN path. The chosen solution is evidenced by the red line: this model, characterized by the minimum r.m.s., is presented in the table on the right. The black dotted line indicates the average solution.*

6.1.11 NEG-SFOR path

The starting model (Tab.6.11) used in the inversion of the average group velocity dispersion curve relative to NEG-SFOR path (Fig.4.14E) is defined by 5 independent parameters (2 thickness and 3 V_S values) and a V_P/V_S ratio value of 1.8 for the fixed and the inverted layers. The explored thickness is 0.7 km.

NEG-SFOR path			
Parameters		**Step**	**Range of variability**
h (km)	0.070		
	0.135	0.060	0.011-0.287
	0.120	0.050	0.019-0.549
V_S (km/s)	0.660		
	0.950	0.055	0.792-1.109
	1.095	0.065	0.871-1.394
	1.660	0.050	1.401-1.809
V_P/V_S	1.8	for all the layers	

Tab.6.11– *Starting model used in the inversion of the average group velocity dispersion curve relative to NEG-SFOR path (inverted parameters are in black, fixed parameters are in blue).*

The obtained solution set consists of 3 solutions (Fig.6.11): the model characterized by the minimum r.m.s. presents V_S values increasing from ~1 to 1.61 km/s, at a depth of 0.335 km.

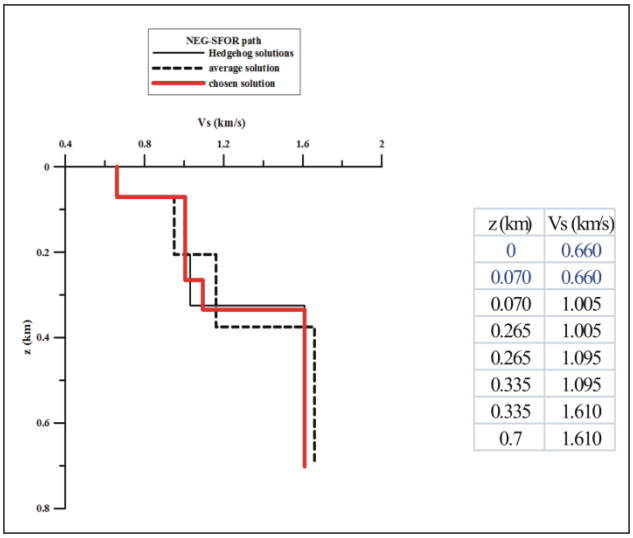

Fig.6.11 *– Set of solutions obtained from the inversion of the average group velocity dispersion curve relative to NEG-SFOR path. The chosen solution is evidenced by the red line: this model, characterized by the minimum r.m.s., is presented in the table on the right. The black dotted line indicates the average solution.*

6.1.12 PER-SFOR path

The starting model (Tab.6.12) used in the inversion of the average group velocity dispersion curve relative to PER-SFOR path (Fig.4.15E) is defined by 5 independent parameters (2 thickness and 3 V_S values) and a V_P/V_S ratio value of 1.8 for the fixed and the inverted layers. The explored thickness is 1 km.

PER-SFOR path			
Parameters		**Step**	**Range of variability**
h (km)	0.180		
	0.090	0.041	0.009-0.540
	0.475	0.070	0.049-0.950
V_S (km/s)	0.850		
	1.260	0.085	0.949-1.419
	1.670	0.070	1.479-1.939
	2.100	0.090	1.850-2.599
V_P/V_S	1.8	for all the layers	

Tab.6.12– *Starting model used in the inversion of the average group velocity dispersion curve relative to PER-SFOR path (inverted parameters are in black, fixed parameters are in blue).*

The obtained solution set consists of 4 solutions (Fig.6.12): the model characterized by the minimum r.m.s. presents V_S values increasing from 1.345 to 2.1 km/s, at a depth of about 0.63 km.

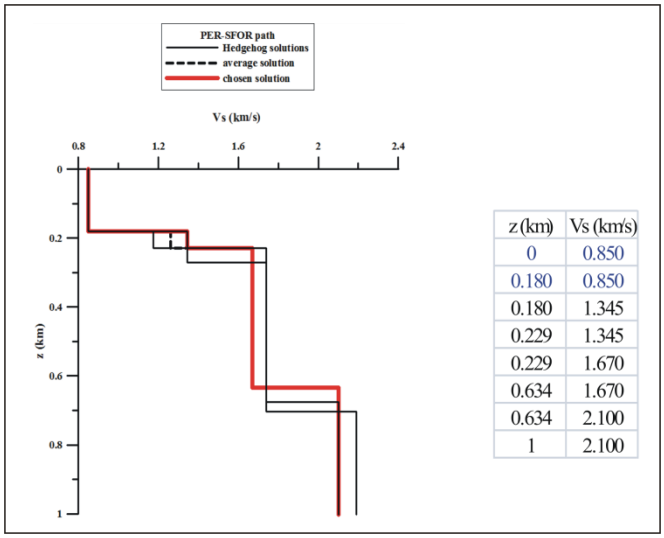

Fig.6.12 *– Set of solutions obtained from the inversion of the average group velocity dispersion curve relative to PER-SFOR path. The chosen solution is evidenced by the red line: this model, characterized by the minimum r.m.s., is presented in the table on the right. The black dotted line indicates the average solution.*

6.1.13 SFOR-ISC path

The starting model (Tab.6.13) used in the inversion of the average group velocity dispersion curve relative to SFOR-ISC path (Fig.4.16G) is defined by 7 independent parameters (3 thickness and 4 V_S values) and a V_P/V_S ratio value of 1.8 for the fixed and the inverted layers. The explored thickness is 1.6 km.

SFOR-ISC path			
Parameters		**Step**	**Range of variability**
h (km)	0.080		
	0.180	0.035	0.059-0.299
	0.150	0.045	0.049-0.549
	0.360	0.050	0.109-0.554
V_S (km/s)	0.650		
	0.775	0.040	0.661-0.899
	1.100	0.045	0.999-1.319
	1.390	0.050	1.125-1.539
	2.100	0.065	1.576-2.229
V_P/V_S	1.8	for all the layers	

Tab.6.13– *Starting model used in the inversion of the average group velocity dispersion curve relative to SFOR-ISC path (inverted parameters are in black, fixed parameters are in blue).*

The obtained solution set consists of 5 solutions (Fig.6.13): the model characterized by the minimum r.m.s. (which is coincident with the average solution) presents V_S values increasing from 0.735 to 2.165 km/s, at a depth of 0.735 km.

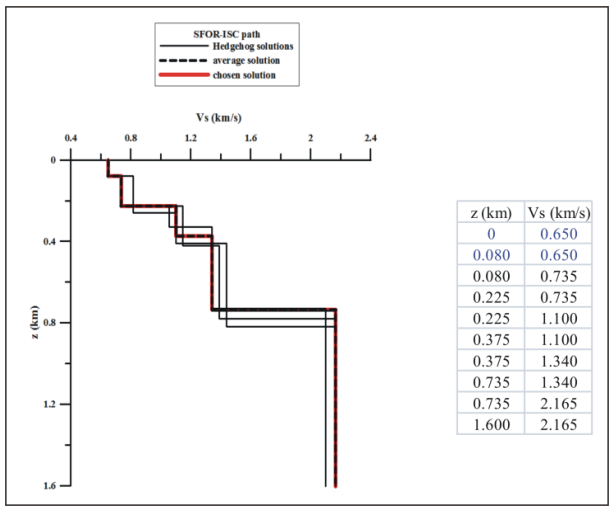

Fig.6.13 *– Set of solutions obtained from the inversion of the average group velocity dispersion curve relative to SFOR-ISC path. The chosen solution is evidenced by the red line: this model, characterized by the minimum r.m.s. and coincident with the average solution (black dotted line), is presented in the table on the right.*

Chapter 7

GEOLOGICAL INTERPRETATION OF THE V_S MODELS

7.1 Interpretation of the V_S models at Campi Flegrei

V_S models obtained from the Hedgehog non-linear inversion of the average group velocity dispersion curves along the 27 paths at Campi Flegrei (Fig.7.1) and chosen according to the minimum r.m.s. criterion as representative of each analysed path (see chapter 5) are interpreted here on the basis of the available geological and geophysical data.

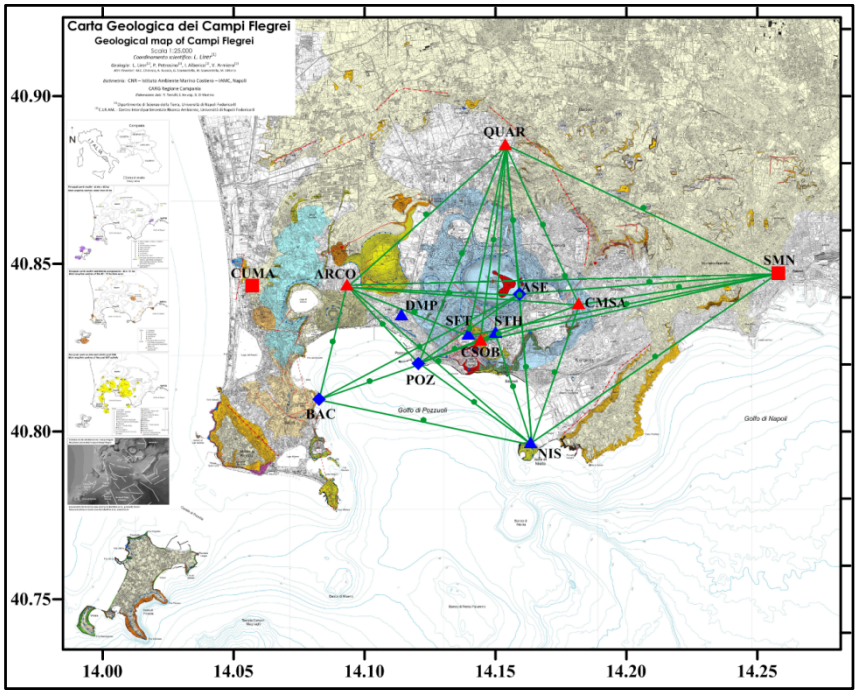

Fig.7.1 *– Paths crossing Campi Flegrei area (green lines) for which V_S models have been obtained from the non-linear inversion with the Hedgehog method of the average group velocity dispersion curves. V_S models are attributed below the path midpoints (green dots).*

Geological information are provided by the stratigraphies of deep boreholes located in the central area of Campi Flegrei (i.e. CF23 deep drilling (Penta, 1954)) and in the Mofete and San Vito areas (AGIP, 1987) (see 1.1.1 section).

The main features of the shallow structures of Campi Flegrei are the presence of thick light materials filling the caldera (Nunziata and Rapolla, 1981; AGIP, 1987; Fedi et al., 1991; Judenherc and Zollo, 2004) and the presence of low velocity layers and high V_P/V_S ratio values related to the circulation of hydrothermal fluids in the central sector of the Phlegraean area (Aster and Meyer, 1988; Vanorio et al., 2005; Battaglia et al., 2008; Dello Iacono et al., 2009).

All the V_S profiles obtained below Campi Flegrei are shown in Fig.7.2. Three trends can be distinguished: *i)* models characterized by very low V_S values, relative to the paths crossing the Gulf of Pozzuoli (BAC-NIS, BAC-POZ and POZ-NIS paths (Fig.7.1)); *ii)* models characterized by the presence of a low velocity layer at about 0.5 km depth (BAC-ARCO, BAC-POZ, NIS-STH, POZ-ASE, POZ-CMSA and POZ-NIS paths (Fig.7.1)); *iii)* all the other models characterized by higher V_S values, relative to the paths crossing the onshore part of Campi Flegrei (Fig.7.1).

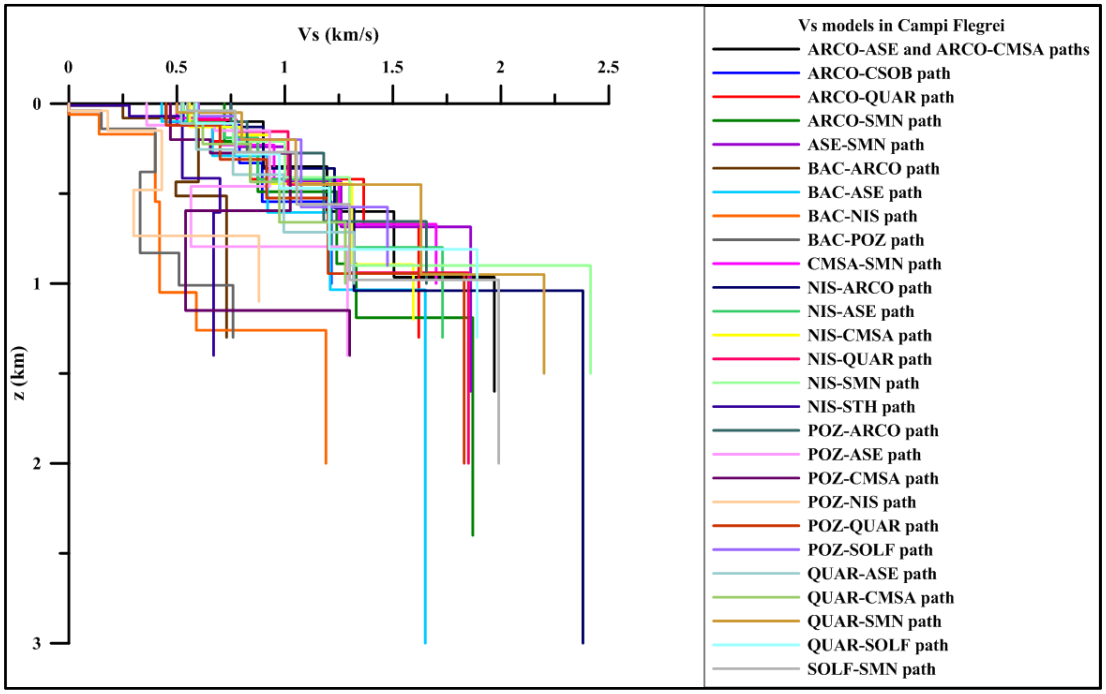

Fig.7.2 *- V_S models chosen as representative of the 27 paths crossing Campi Flegrei.*

Since these 1-D Vs profiles are average models representative of the medium between the two stations located at the edges of each path, Vs profiles are attributed below the midpoint of each path (Fig.7.1). In this way an irregular grid composed by the 27 midpoints has been created in order to easily represent and examine the distribution of V_S and V_P/V_S ratio values in the investigated area.

Two sets of images have been reconstructed to represent the V_S and V_P/V_S ratio pattern (Figs.7.3-7.4 respectively) at regular interval of 0.25 km from the sea level to 1.25 km depth. In the 0-1 km depth range I have the greatest density of midpoints (i.e. the grid is composed by all the 27 midpoints up to 0.75 km depth and by 26 midpoints at 1 km level), while 19 V_S profiles have reached the depth of 1.25 km. At greater depth the only 11 V_S profiles have reached the depth of 1.5 km and 7 models have explored 2 km depth. So

contour lines of V_S and V_P/V_S ratio are drawn up to depths of 1.25 km, and only the values at the midpoints are shown at greater depths (Figs.7.3-7.4).

The V_S difference between the offshore (Gulf of Pozzuoli and along the coastline) and the onshore areas is evident on the relative maps (Fig.7.3). At 0.25 km depth a homogeneous distribution of V_S values ranging from 0.7 to 1 km/s characterizes the Phlegraean area, while lower V_S values (ranging from 0.4 to 0.7 km/s) are present in the Gulf of Pozzuoli. A particular feature is the extension of this low velocity region in the area east of the town of Pozzuoli. At 0.5 km depth low V_S values are still present in the offshore sector, while in the onshore sector two zones are identified: an inland area with V_S higher than 1 km/s and an area characterized by V_S ranging from 0.7 to 1 km/s, extending along the coastline. Inside this latter region, an area characterized by lower V_S values is recognized: it is located in correspondence of the Solfatara crater and is present up to 1 km depth. At greater depths the lower V_S velocities are confined to the centre of the Gulf of Pozzuoli (Fig.7.3). Moreover, V_S higher than 2 km/s are identified in the eastern (along the Posillipo hill) and north-eastern sectors.

Also the pattern of the V_P/V_S ratio values (Fig.7.4) shows a strong difference between the Gulf of Pozzuoli and the inland area. In the shallow 0.75 km depth the offshore area is characterized by very high V_P/V_S ratio values (ranging from 2.7 to 3), which slightly decrease moving toward the coast (from 2.4 to 2.7). The inland area presents lower V_P/V_S values: it can be distinguished an intermediate band identified by values ranging from 2.1 to 2.4 and an inner sector characterized by quite “normal” V_P/V_S ratios (values ranging from 1.8 to 2). At greater depth (1 km and 1.25 km levels) this ”normal” region extends toward the coastline, while the Gulf of Pozzuoli is still characterized by very high V_P/V_S ratio values. At the bottom of the investigated depth (1.5 km and 2 km levels) the whole inland area presents V_P/V_S ratio values ranging from 1.8 to 2, while in the gulf a high value (2.5) is still present (Fig.7.4).

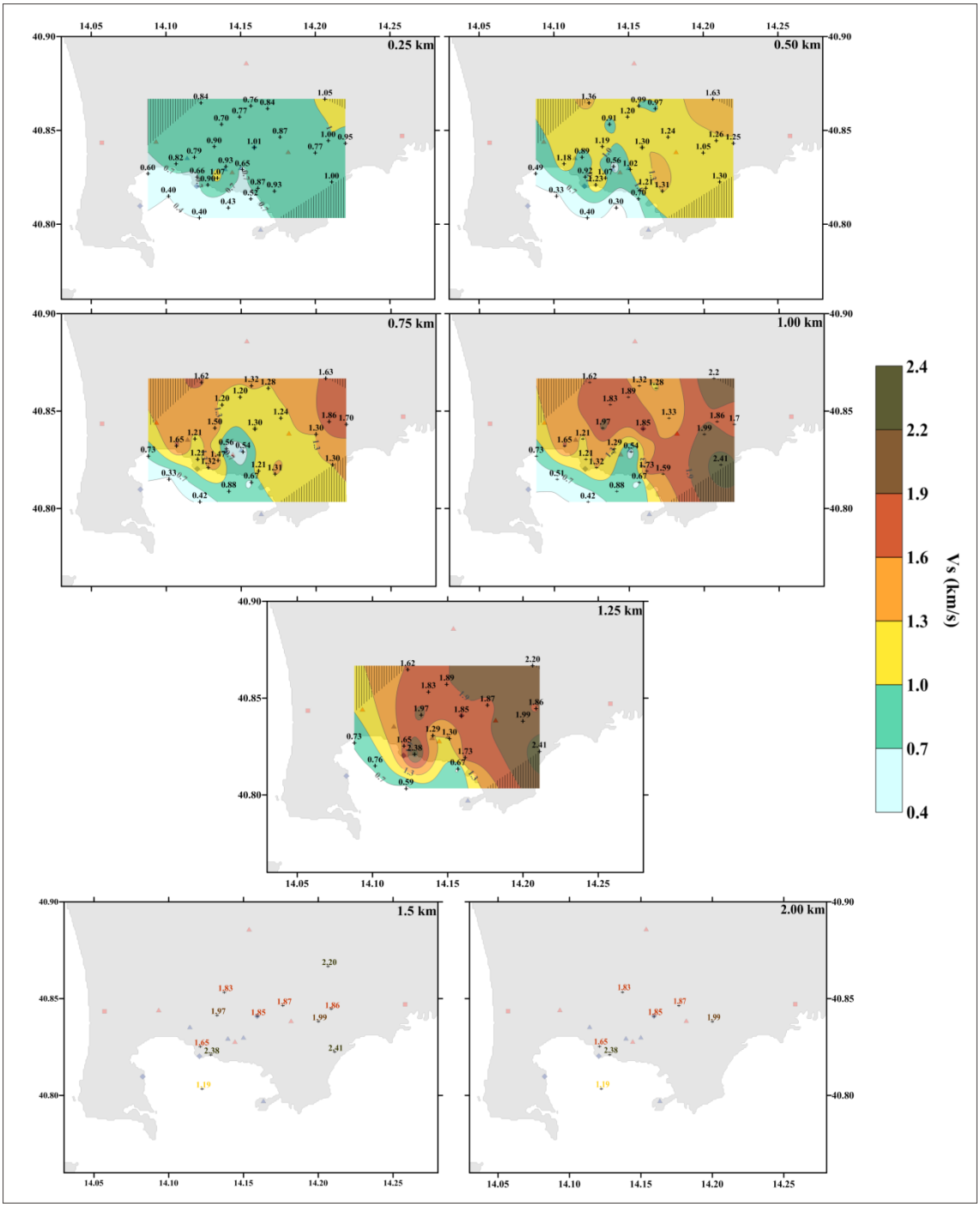

Fig.7.3 *– Horizontal slices representing the distribution of V_S values in the uppermost 2 km of the crust in the Campi Flegrei area. From the sea level to 1.25 km depth slice interval is 0.25 km, at greater depth 0.5 km. V_S contour line interval is 0.3; shaded areas at the edges of the slices correspond to the areas where no data are available.*

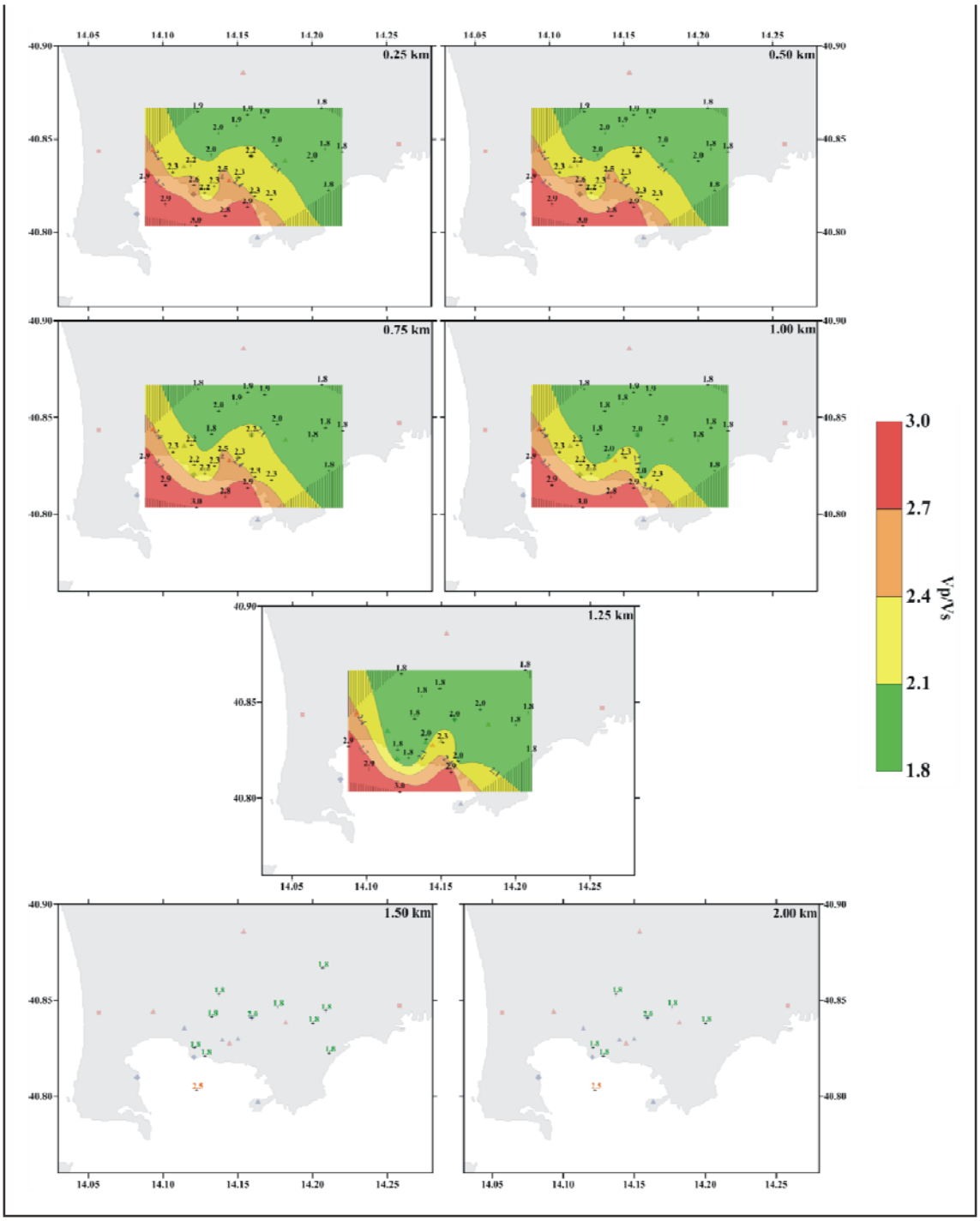

Fig.7.4 *– Horizontal slices representing the distribution of V_P/V_S ratio values in the uppermost 2 km of the crust in the Campi Flegrei area. From the sea level to 1.25 km depth slice interval is 0.25 km, at greater depth 0.5 km. V_P/V_S ratio contour line interval is 0.3; shaded areas at the edges of the slices correspond to the areas where no data are available.*

V_S and V_P/V_S ratio maps show an interesting correspondence between low V_S and high V_P/V_S ratio areas. In particular the Gulf of Pozzuoli is characterized by both V_S velocities lower than 0.7 km/s persisting up to 1 km depth and V_P/V_S ratio values higher than 2.7 up to 1.25 km of depth. This feature is also observed east of the town of Pozzuoli, where the 2.4-2.6 V_P/V_S value is observed in correspondence of the Solfatara crater in the shallow

0.75 km depth, and low V_S are present up to 1 km depth. Instead the inland area is characterized by both V_S values higher than 1 km/s and quite "normal" V_P/V_S ratio (1.8-2 range) since the shallower structures.

The distribution of V_S can be compared with the 3-D V_S and V_P/V_S ratio models proposed by Aster and Meyer (1988) for the uppermost 3 km of the crust in the Campi Flegrei (see Fig.1.24 in 1.1.5 section). The comparison can be done at 1 km depth where the tomography has the best resolution (Fig.7.5). The location of the minimum V_S and high V_P/V_S ratio region identified by my velocity models is partially coincident with the low velocity and high V_P/V_S ratio area recognized by the authors in the central area of the caldera. The minimum value of 1.35 km/s proposed by Aster and Meyer (1988), in correspondence of the town of Pozzuoli (Fig.7.5B), agrees with the 1.32 km/s V_S value retrieved by my model (Fig.7.5A). Also a good agreement is found as regards the 2.2 V_P/V_S ratio value (Fig.7.5C-D). Instead a strong disagreement exists about the extension of the minimum V_S and high V_P/V_S ratio region east of the town of Pozzuoli, and mostly in the Gulf of Pozzuoli, where my models evidence the presence of V_S lower than 0.7 km/s and V_P/V_S ratio of 2.8-3 (Figs.7.5A-B).

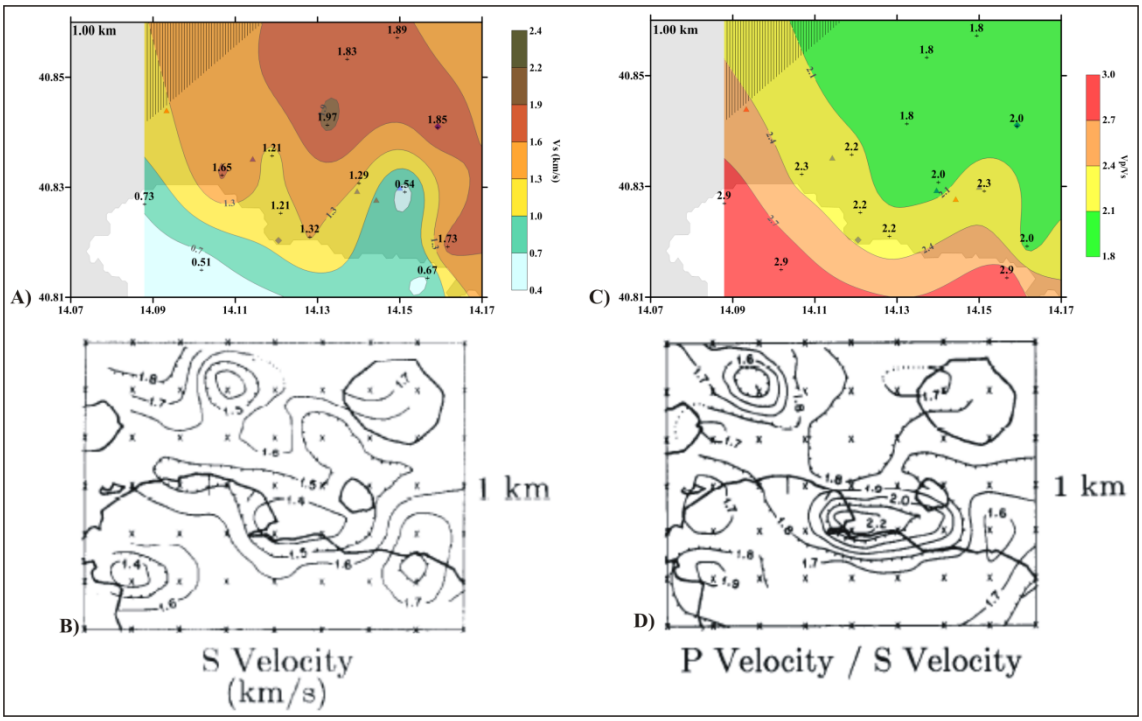

Fig.7.5 *– Comparison between V_S (A) and V_P/V_S ratio (C) distributions at 1 km depth obtained in this study and the 3-D V_S (B) and V_P/V_S ratio (D) models obtained by Aster and Meyer (1988).*

Likewise the comparison between the V_P/V_S ratio distribution obtained in this study and the model proposed by Battaglia et al. (2008) can be done only at 1 km depth (Fig.7.6).

The match is not so good as regards the location of the highest V_P/V_S ratio values, since my model shows a wide maximum extending in the Gulf of Pozzuoli (Fig.7.6B), while the authors' model shows a more restricted maximum region centred on the town of Pozzuoli (Fig.7.6A). Instead a good agreement is found in the inland sector (Fig.7.6A-B).

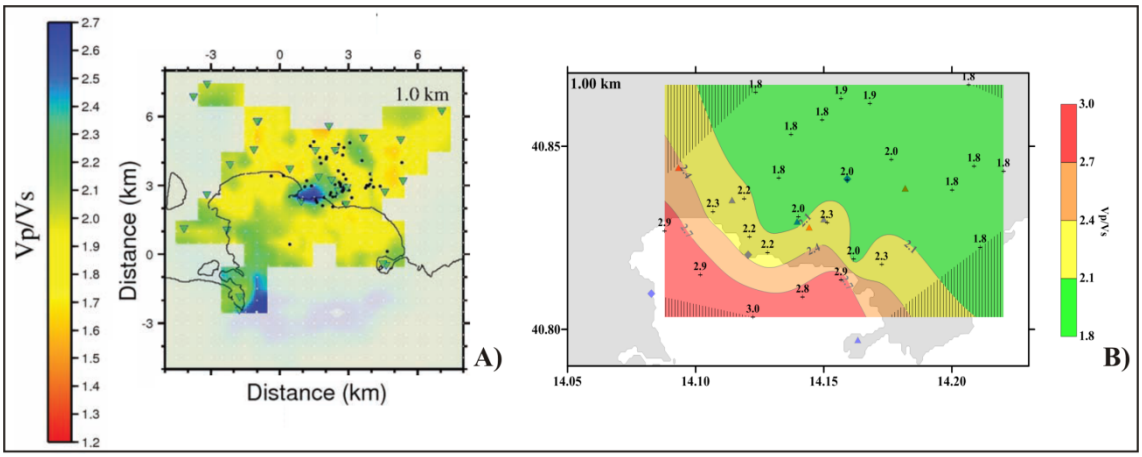

Fig.7.6 *– Comparison between V_P/V_S ratio values distribution at 1 km depth obtained in this study (B) and the V_P/V_S ratio model after Battaglia et al. (2008) (A).*

7.1.1 Seismo-stratigraphic model of the Gulf of Pozzuoli

According to the two strongly different areas identified by the distribution of V_S and V_P/V_S ratio values, three seismo-stratigraphic sections have been drawn across the Gulf of Pozzuoli and the inland area.

The seismo-stratigraphic section across the Gulf of Pozzuoli consists of two portions, one NW-SE, correlating the V_S models obtained below the paths BAC-ARCO, BAC-POZ, and the other one, SW-NE, correlating the V_S models obtained below the paths POZ-NIS, NIS-STH and NIS-CMSA. The two sections cross at the midpoint of the path BAC-NIS in the gulf (Fig.7.7).

V_S model relative to the NIS-CMSA path has been also included in the section, even if the relative midpoint is not located offshore but in the Bagnoli area, in order to evidence the variations from the centre of the gulf to the coastal area.

The main feature along the section is the presence of a very thick shallow layer characterized by V_S values lower than 0.7 km/s, which reaches a depth of 0.5 km in the western sector of the gulf and deepens up to 1.3 km toward the centre of the Pozzuoli bay. This layer is also characterized by low densities (on average 1.7 g/cm^3) and very high V_P/V_S ratio values, which range from 2.8 to 3 in the uppermost 1.25 km depth and are 2.5 at 1.5 km depth (Fig.7.4). According to other authors (e.g. Aster and Meyer, 1988; Vanorio

et al., 2005; Battaglia et al., 2008; Dello Iacono et al., 2009), the shallower structure of the gulf of Pozzuoli consists of soils and highly fractured rocks with a high percentage of liquid water-filled cracks (see 1.1.5 section).

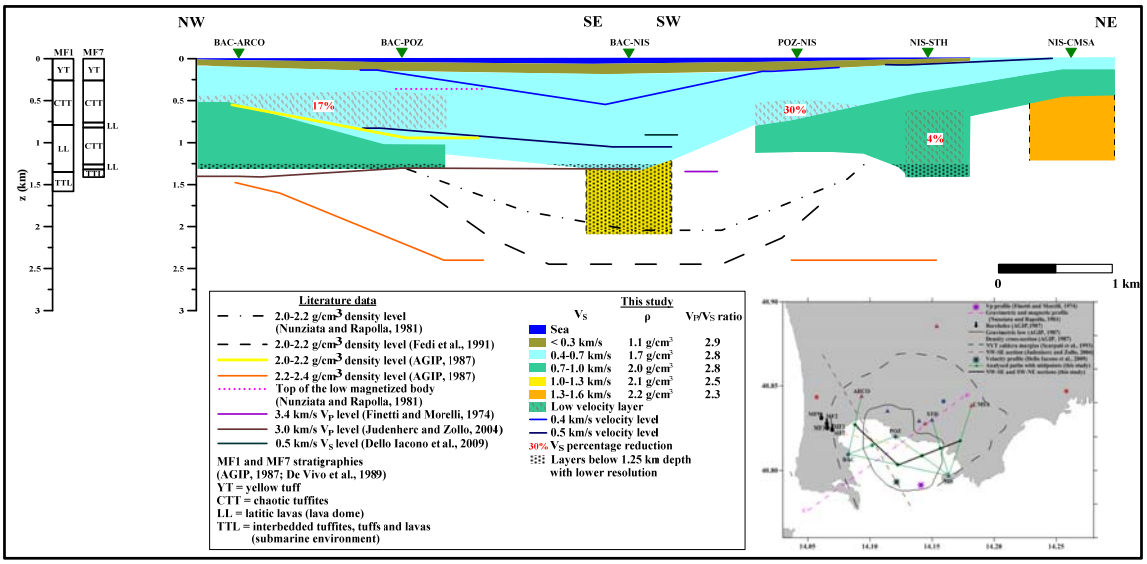

Fig.7.7 *– Seismo-stratigraphic section across the Gulf of Pozzuoli through the midpoints of the paths located in the map.*

The section is almost entirely located in the Bouguer anomaly low (Fig.7.7), so the presence of such a layer up to depths greater than 1 km can be related with the light and altered material filling the caldera as proposed by Nunziata and Rapolla (1981) and Fedi et al. (1991). Instead, a disagreement exists with the model proposed by AGIP (1987) and built on the Mofete drilling stratigraphies. The 2.0-2.2 g/cm^3 density discontinuity attributed to the transition from the loose sediments to the more compact material is deeper than 1.3 km.

The velocity decrease below the BAC-ARCO and BAC-POZ paths can be reasonably attributed to the anomalous high thermal state of the area, as testified by the high temperatures measured in the Mofete boreholes (see Fig.1.5 in 1.1.1 section). Its depth is also in agreement with the top of the low magnetized layer because of thermochemical alteration (Nunziata and Rapolla, 1981). As regards the eastern sector of the gulf, a stronger V_S reduction (30%) is found below the POZ-NIS path, while a light (4%) reduction is below the NIS-STH path. Taking into account the presence of the demagnetized body (Nunziata and Rapolla, 1981) in the gulf, it is reasonable to relate also this low velocity layer to the presence of high temperatures.

A further comparison can be done with the V_P models of the Gulf of Pozzuoli provided by Finetti and Morelli (1974) and Judenherc and Zollo (2004) according to which in the

central part of the bay at about 1.3 km depth V_P values of 3.4 km/s and 3.0 km/s respectively have been retrieved (Fig.7.7). The corresponding V_P model below the BAC-NIS path (since this path crosses the centre of the gulf and reaches the maximum investigated depth below the gulf) has been computed starting from the obtained V_S model and using the assigned V_P/V_S ratio values (see 5.1.8 section). A sharp increase in V_P values from ~1.8 to ~3.0 km/s is shown by BAC-NIS V_P model at about 1.3 km depth. So the depth of the shallowest discontinuity identified by Finetti and Morelli (1974) and Judenherc and Zollo (2004) agrees with mine. Moreover a particular agreement is found in the centre of the gulf with the velocity of the volcanic filling material (V_P=3 km/s) retrieved by Judenherc and Zollo (2004).

A very good agreement exists with the V_S values of ~0.5 km/s obtained from V_P measurements and V_P/V_S ratio of 3.7±0.9 found in the Gulf of Pozzuoli (Dello Iacono et al., 2009). This comparison lets to hypothesize that the maximum thickness of the light sediments is in the centre of the bay, and rises to ~0.9 km in the south, between Miseno and Nisida, to 0.5 km onshore in the west and 0.2 km onshore in the east.

Lastly, a comparison with the V_S model of the Gulf region proposed by Guidarelli et al. (2002) (see Fig.1.25a-d in 1.1.5 section) cannot be done as the former is referred to an area that includes both offshore and onshore sectors. Anyway, my V_S models offshore in the gulf are about 20% lower.

7.1.2 Seismo-stratigraphic model of the central-eastern area of Campi Flegrei

A SW-NE seismo-stratigraphic section has been drawn from the Gulf of Pozzuoli toward the eastern sector of the Campi Flegrei, correlating the V_S models below BAC-POZ, BAC-ASE, NIS-ARCO, POZ-SOLF, POZ-ASE, POZ-CMSA, NIS-QUAR, ARCO-SMN, SOLF-SMN, ASE-SMN and CMSA-SMN paths (Fig.7.8).

This section allows to observe the lateral variations from the central area to the eastern sector of the Phlegraean caldera.

It can be observed that the layer with the lowest V_S values (i.e. 0.4-0.7 km/s range) is thinner and thinner moving from the gulf (1 km thick beneath the BAC-POZ path) to inland (about 0.3 km beneath the POZ-CMSA path), up to disappearing beneath the NIS-ARCO and ARCO-SMN paths. If we take into account the stratigraphic sequence of the CF23 borehole (Penta, 1954), drilled by SAFEN east of the Solfatara crater (Fig.7.8), this

layer can be associated to tuffaceous and pyroclastic material. It should be the topmost incoherent portion of the tuffaceous sequence with V_S in the range 0.7-1 km/s.

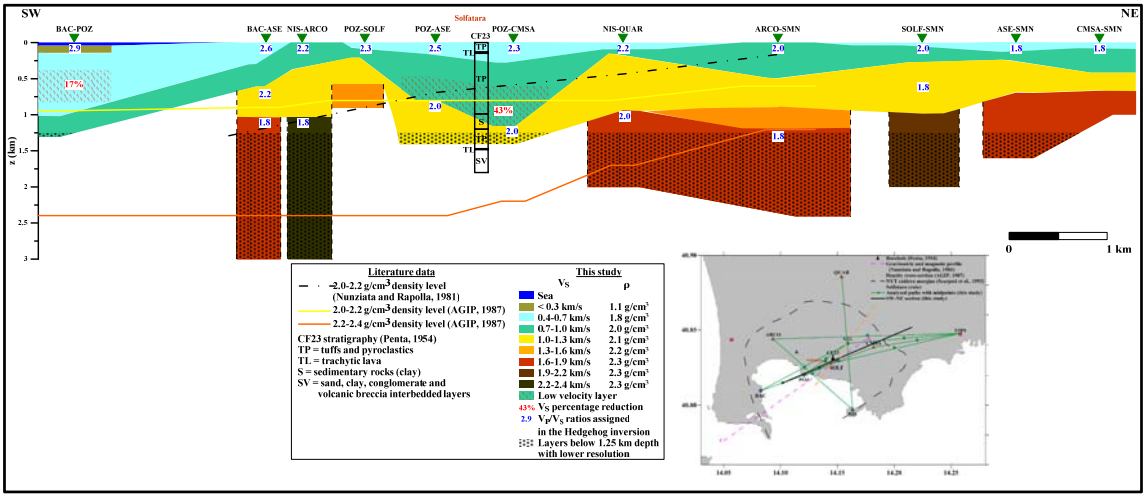

Fig.7.8 *– Seismo-stratigraphic section across the central-eastern sector of the Campi Flegrei through the midpoints of the paths located in the map.*

Deeper, a layer with V_S in the range 1-1.3 km/s is present only beneath the paths crossing the inland area. In particular it rises to about 0.25 km depth in correspondence of the NIS-ARCO, POZ-SOLF and NIS-QUAR paths, while it deepens beneath the POZ-ASE and POZ-CMSA paths reaching 1.4 km depth. In correspondence of these two latter paths, crossing the Solfatara crater (Fig.7.8), a low velocity (43% reduction) layer is detected at depths from 0.5 km to about 1 km, also characterized by high V_P/V_S ratios of 2.3-2.5.

The presence of low V_S and high V_P/V_S ratios is consistent with the hydrothermal environment of the Solfatara where intense fumarolic activity occurs with temperature of 150-164° C (Chiodini and Marini, 1998). Water vapour is the main component of the fumarolic effluents, followed by CO_2, H_2S, N_2, H_2 and CH_4. Moreover, the isotopic composition of H_2O, CO_2 and He suggests the involvement of large portion of magmatic fluids (Chiodini et al., 2003 and references therein).

The top of the layers with V_S ranging from 1.6 to 2.4 km/s is on average at 1 km depth and uprises to about 0.7 km depth beneath ASE-SMN and CMSA-SMN paths (Fig.7.8). This discontinuity is comparable with the sharp increase of V_S to ~1.4 km/s at about 1.2 km depth retrieved by Guidarelli et al. (2002) in more extended area (the Astroni region, see Fig.1.25a-c in 1.1.5 section).

Lastly it is evident the disagreement with the interpretative gravity models as regards the depth of the 2.0-2.2 g/cm^3 density level.

7.1.3 Seismo-stratigraphic model of the northern area of Campi Flegrei

A SW-NE seismo-stratigraphic section has been drawn in the northern area of the Campi Flegrei, correlating the V_S profiles relative to the ARCO-QUAR, POZ-QUAR, QUAR-SOLF, QUAR-ASE, QUAR-CMSA and QUAR-SMN paths (Fig.7.9).

A thin layer with an average thickness of 0.2 km and V_S of 0.4-0.7 km/s has been recognized in the shallowest portion of the section, lying on stiffer material. The midpoint of the ARCO-QUAR path is coincident with the location of the SV3 drilling (AGIP 1987; De Vivo et al., 1989) (Fig.7.9), but the description of the lithotypes is too generic to be used for the volcanological attribution to the seismic layers.

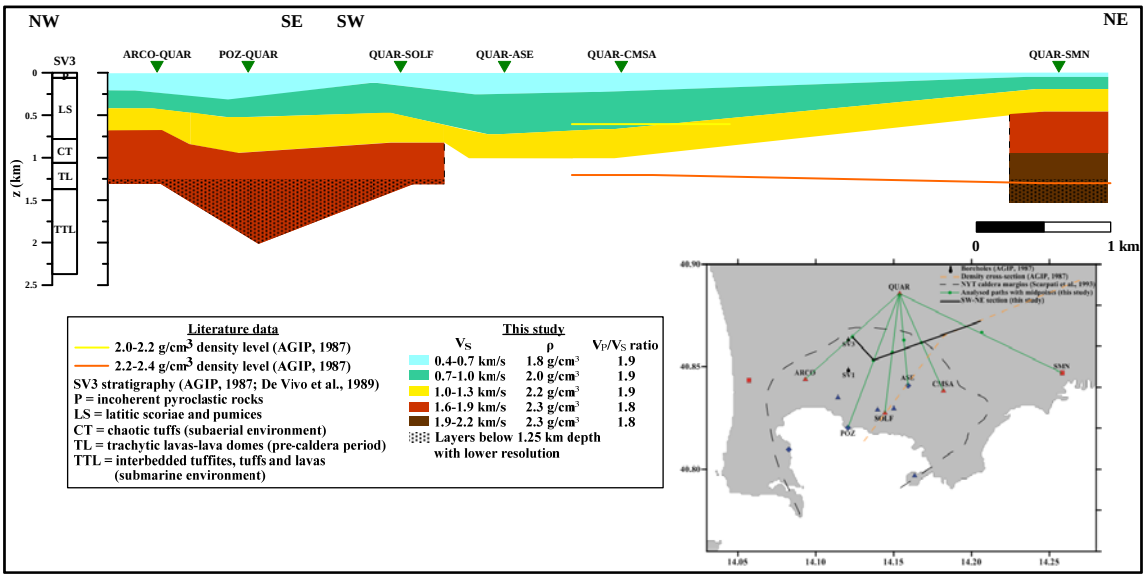

Fig.7.9 *– Seismo-stratigraphic section across the northern sector of the Campi Flegrei through the midpoints of the paths located in the map.*

An interesting difference can be recognized between the two inland sections: the morphology of the seismo-stratigraphic discontinuities shows a more regular trend in the northern area than the central-eastern sector (Fig.7.8). This latter section crosses the area of the Campi Flegrei which has been interested by the greatest event of the recent volcanism (see 1.1.2 section) and has been affected by the maximum uplift during the 1969-1972 and 1982-1984 bradyseismic crisis (see Fig.1.3 and 1.1.4 section). In fact the greatest irregularity in the morphology of the seismo-stratigraphic sequence is observable in the central portion of the central-eastern section, from BAC-ASE to NIS-QUAR path. Instead, moving toward NE (i.e. toward the edge of the caldera), the layers assume a more regular trend.

The northern area of Campi Flegrei is quite laterally homogeneous. If we take into account the SV3 drilling stratigraphy, the V_S of 1.6-1.9 km/s might be attributed to subaerial chaotic tuffs and trachytic lavas.

It is also remarkable the rising trend of the 0.7-1 and 1-1.3 km/s layers moving toward NE, that is toward the edge of the Phlegraean caldera (Fig.7.9). The QUAR-SMN path, which is entirely located outside the depressed area, shows a very thin cover layer (only 0.05 km) and two important discontinuities at depths of 0.45 km, with V_S of 1.6 km/s, and of 0.95 km, with V_S of 2.2 km/s (Fig.7.9). This pattern is very similar to that found in the urban area of Napoli (Nunziata et al., 2012) (see Fig.3.2 in 3.2.1 section).

In the northeastern portion of the section a good agreement is found with the 2.0-2.2 g/cm^3 density discontinuity (AGIP, 1987). The depth of this discontinuity is shallower (about 0.5 km depth) than that in the centre of the Gulf of Pozzuoli (at about 1.3 km depth) (Fig.7.7).

Moreover, the northeastern section is characterized by "normal" V_P/V_S ratio (1.8-2 range) from the surface down to the maximum investigated depth (2 km) (Fig.7.4). All these features let to hypothesize an improvement of the mechanical qualities of the medium moving from the centre to the edges of the depressed area.

7.2 Interpretation of the V_S models at Ischia

V_S models obtained from the Hedgehog non-linear inversion of the average group velocity dispersion curves along the 13 paths crossing the island of Ischia (Fig.7.10) and chosen according to the minimum r.m.s. criterion as representative of each analysed path (see chapter 6) are interpreted here on the basis of the available geological and geophysical data. As already said in 1.2.4 section, unfortunately the only existing data are represented by the drillings in the Citara area (Penta and Conforto, 1951) and the interpretation of gravity and magnetic data (Nunziata and Rapolla, 1987; Paoletti et al., 2009).

V_S models are attributed to the midpoint of each analysed path (Fig.7.10), but, because of the significant altitude differences between the edges of the paths, they are referred to the height of the midpoints (Fig.7.11).

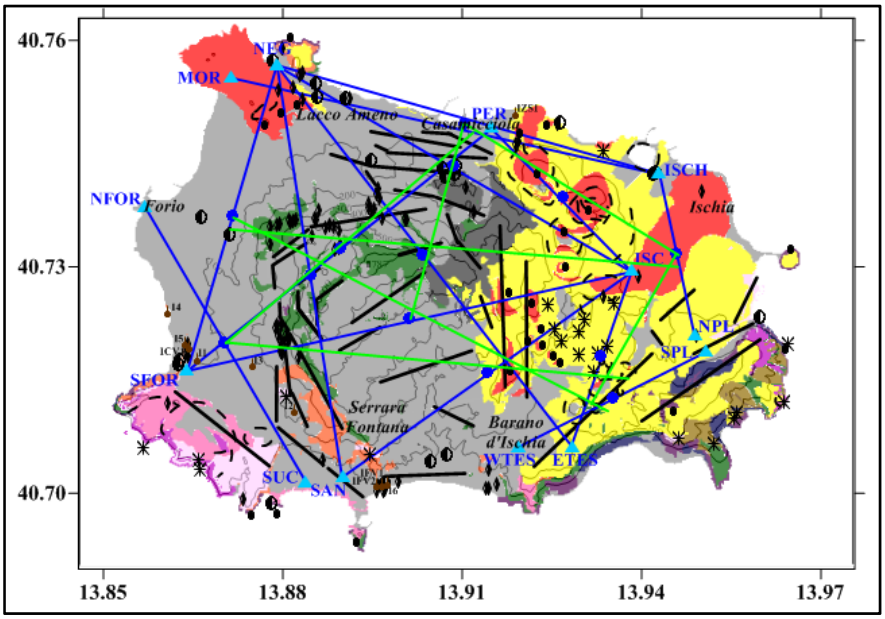

Fig.7.10 *– Paths crossing the island of Ischia (blue lines) for which V_S models have been obtained from the non-linear inversion with the Hedgehog method of the average group velocity dispersion curves. V_S models are attributed to the path midpoints (blue dots). Green lines are the traces of the seven seismo-stratigraphic sections drawn in this study (see the legend of the simplified geological map of Ischia in Fig.1.32).*

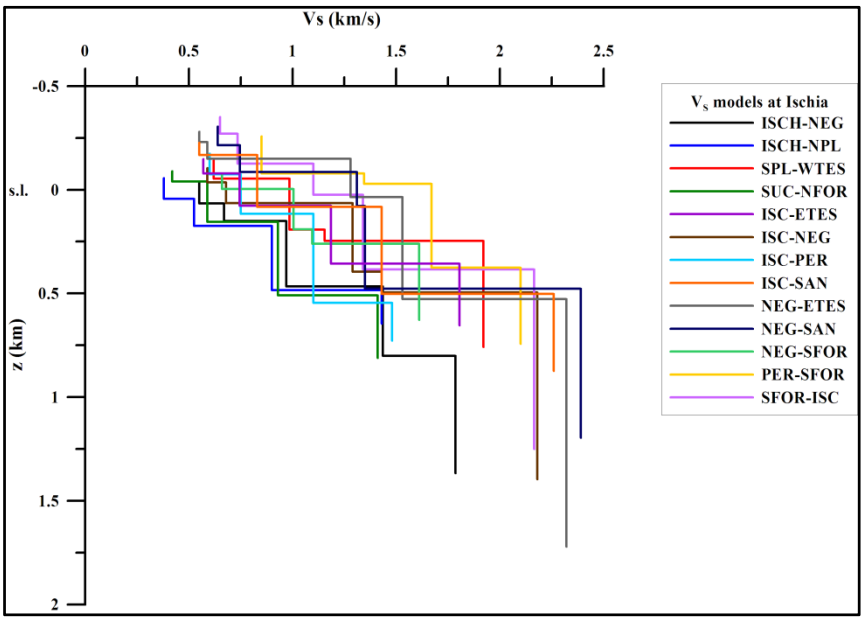

Fig.7.11 *- V_S models chosen as representative of the 13 paths crossing Ischia island. They are referred to the path midpoint height on sea level.*

Comparing the 13 V_S profiles it can be noted that the models relative to the paths crossing the edges of the island (i.e. ISCH-NEG, ISCH-NPL and SUC-NFOR paths) are characterized by V_S values lower than those crossing the central area of the island. This feature suggests the hypothesis of the existence of significant lateral heterogeneities between the different sectors of the island, even if all the V_S profiles show an evident velocity increase at about 0.5 km b.s.l..

On the basis of the V_S measured in the Neapolitan area (Nunziata et al., 2004; 2012) (see 3.2.1 and 4.2.1 sections), since measurements of shear wave velocities are missing at Ischia, and observing the V_S values shown by the 13 models obtained in this study, five ranges of shear wave velocity have been individuated: $0.38 \leq V_S \leq 0.60$ km/s, $0.60 < V_S \leq 0.85$ km/s, $0.85 < V_S \leq 1.40$ km/s, $1.40 < V_S \leq 2.00$ km/s and $2.00 < V_S \leq 2.40$ km/s. Then V_S models have been transformed in seismo-stratigraphic columns representative of each analysed path. Seven seismo-stratigraphic sections have been drawn that cross the whole island in N-S and W-E directions (Fig.7.10). A fundamental constrain is represented by the stratigraphic sequences reconstructed at the Citara area (Penta and Conforto, 1951). As we can see in Fig.7.10, this area has been investigated by the SUC-NFOR path and its midpoint is very close to the I1 and I3 boreholes. In particular the V_S model relative to the SUC-NFOR path is compared and correlated with the stratigraphy of the deepest I3 borehole (see Fig.1.34 in 1.2.1 section) (Fig.7.12).

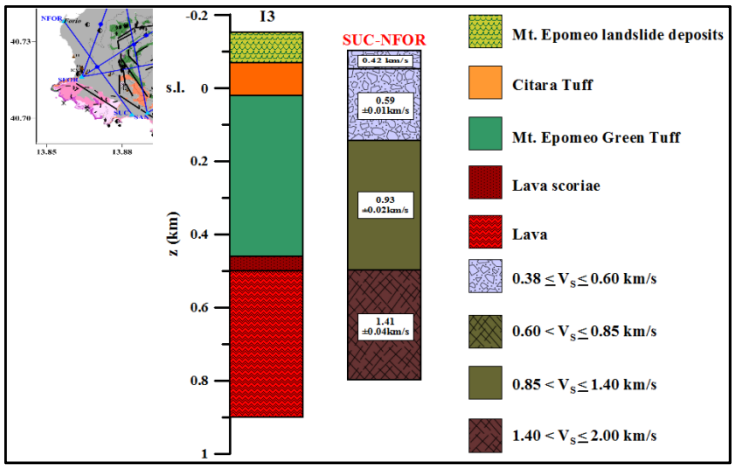

Fig.7.12 *– Correlation between the seismo-stratigraphic column reconstructed for the SUC-NFOR path and the I3 stratigraphic sequence (Penta and Conforto, 1951).*

The shallower layer characterized by V_S lower than 0.6 km/s shows a thickness comparable with the width of the landslide deposits and Citara Tuff, so the lowest velocity might be associated to the cover material. The 0.35 km thickness of the body with V_S of 0.85-1.40 km/s seems to be consistent with the ~0.4 km thickness of Mt. Epomeo Green Tuff. The stratigraphy of the I3 borehole shows lava scoriae and lava at 0.5 km depth, whereas the SUC-NFOR V_S model shows an increase to the 1.40-2.00 km/s velocity range. This range may be attributed to altered and fractured lavas, while the higher V_S range (i.e. 2-2.4 km/s) may be associated to the compact facies of the lava (Fig.7.12).

In the light of this correlation between the V_S layers and the available stratigraphic sequence (Penta e Conforto, 1951), I try to give a geological interpretation of the seismic sections drawn for the whole island (Fig.7.10).

Four W-E sections, Perrone-Ischia (PER-ISC in Fig.7.13a), North Forio-Ischia (NFOR-ISC in Fig.7.13b), North Forio-Testaccio (NFOR-TES in Fig.7.13c) and South Forio-Testaccio (SFOR-TES in Fig.7.13d), and three N-S sections, South Forio-Perrone (SFOR-PER in Fig.7.14a), centre of the island-Perrone (CENTRE-PER in Fig.7.14b) and Ischia-Testaccio (ISC-TES in Fig.7.14c), have been drawn in order to give a view of the shallow structures moving in the N-S and W-E direction, respectively.

Observing these sections a particular feature is immediately noticeable: the seismo-layers show an almost symmetric trend both in N-S and W-E directions (Figs.7.13-7.14). Moving from the centre to the edges of the island the seismo-layers, outcropping beneath the central paths, deepen toward the border sectors. Moreover a cover layer with V_S values varying from 0.38 to 0.60 km/s has been recognized below the paths crossing the edges of the island. In particular it has been retrieved moving toward north along the CENTRE-PER section (Fig.7.14b), east along the whole PER-ISC section (Fig.7.13a) and the eastern portion of the NFOR-ISC section (Fig.7.13b), where this layer deepens reaching a thickness of 0.2 km in correspondence of the ISCH-NPL path (Fig.7.13a-b). In the eastern sector of the island this layer could be related to the pyroclastic material erupted during the recent volcanism (10 ka) as shown by the geological map of Ischia (see 1.2.2 section) (Fig.7.10). Since in the western area of Ischia the 0.38-0.60 km/s layer identified only by the SUC-NFOR model has been related to the landslides deposits and the Citara Tuff (as explained before), it might be deduced that this reworked material and the recent volcanics have very similar V_S values.

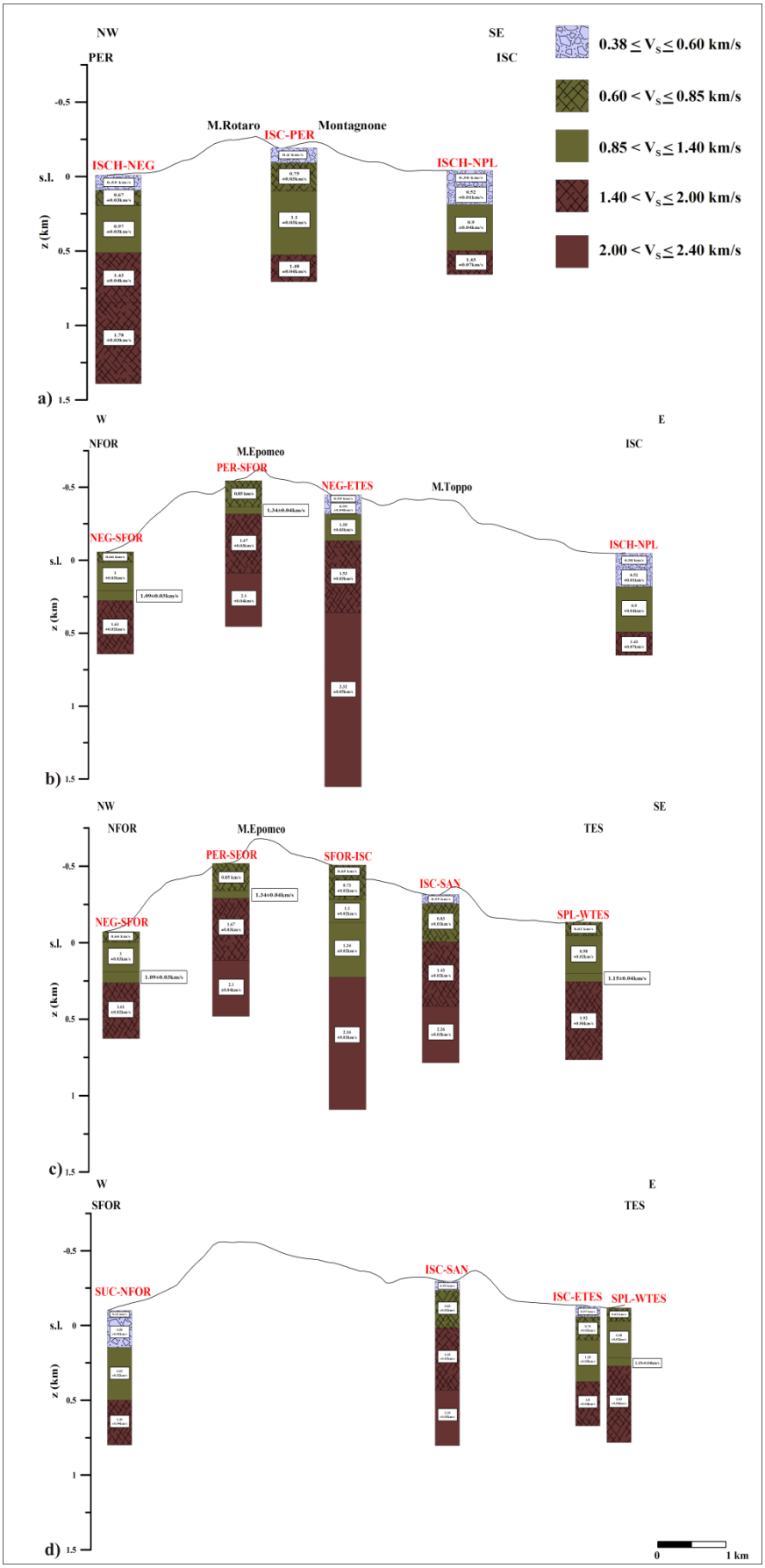

Fig.7.13 *– Seismo-stratigraphic sections crossing Ischia in W-E direction (green lines in Fig.7.10): PER-ISC (a), NFOR-ISC (b), NFOR-TES (c) and SFOR-TES (d).*

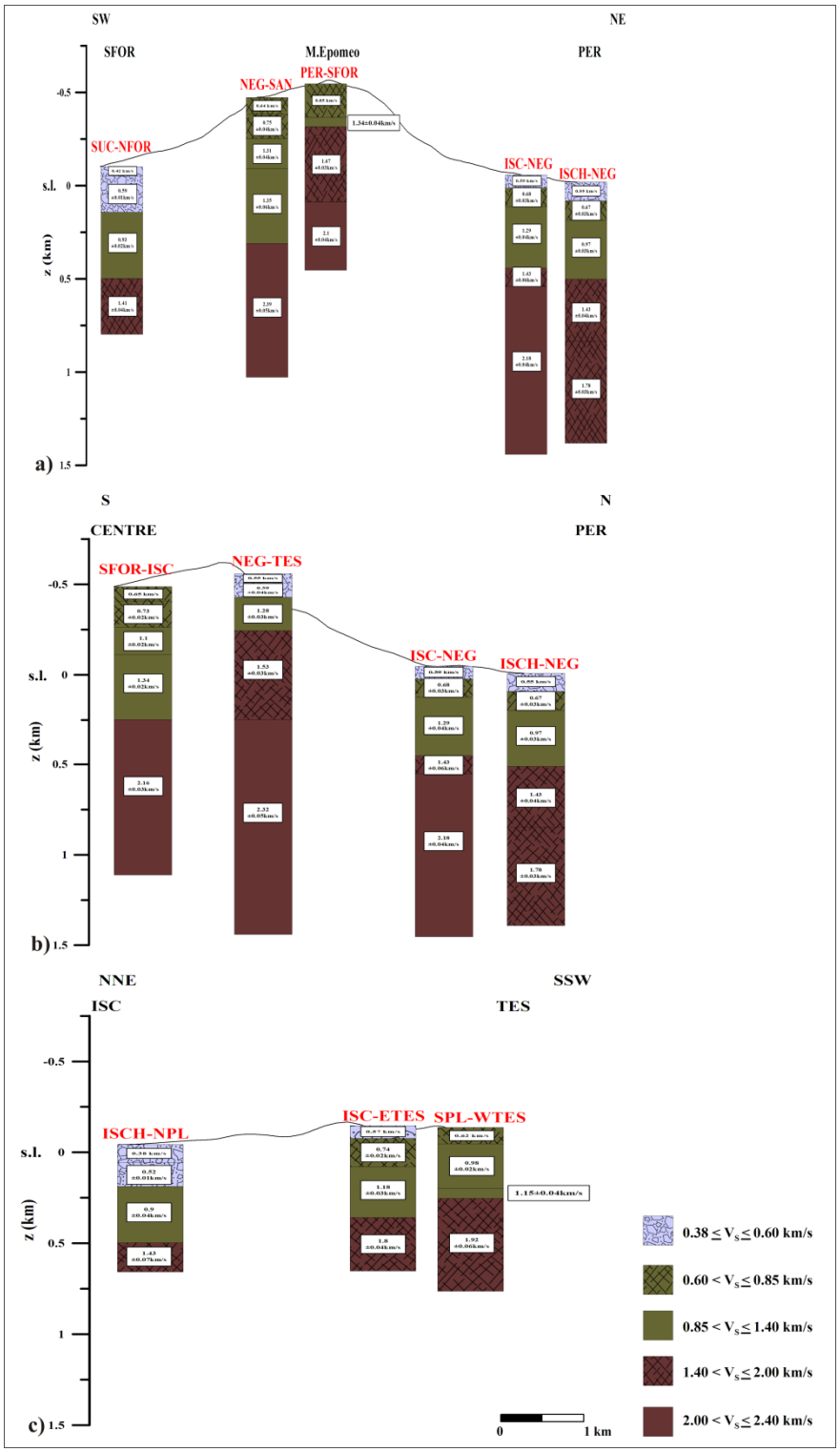

Fig.7.14 *– Seismo-stratigraphic sections crossing Ischia in N-S direction (green lines in Fig.7.10): SFOR-PER (a), CENTRE-PER (b) and ISC-TES (c).*

In the central area of Ischia, nearby the Mt. Epomeo, the first layer is characterized by velocities ranging from 0.60 to 0.85 km/s, as shown by the NFOR-ISC (Fig.7.13b), NFOR-TES (Fig.7.13c), SFOR-PER (Fig.7.14a) and CENTRE-PER (Fig.7.14b) sections. It overlays the higher V_S body (0.85-1.40 km/s) which has been correlated to the Green Tuff

according to the I3 stratigraphy. Since in the central area the Green Tuff is outcropping (see Fig.1.32), the 0.60-0.85 km/s seismo-layer might be related to the altered and fractured facies of the Green Tuff, while the higher range (0.85-1.40 km/s) is compatible with the compact facies. These two seismo-layers can be followed in N-S and W-E directions suggesting the presence of these volcanic products beneath the more recent volcanics with a thickness of about 0.4 km both in the northern (Figs.7.13a-7.14b) and eastern sector (Fig.7.13b-d), similarly to the western area (Fig.7.13d).

The midpoint of the PER-SFOR path is in correspondence of the top of the Mt. Epomeo (Fig.7.10), where Vezzoli (1988) shows the presence of a 0.2-0.3 km thick Green Tuff layer lying on lavas. The seismo-stratigraphic model relative to the PER-SFOR path agrees with this data showing a total thickness of about 0.2 km for both the facies of the Green Tuff (Fig.7.13b-c). Moreover, the 1.40-2.00 km/s V_S range could be related to the lava.

A body with higher V_S values, in the 2.00-2.40 km/s range, has been identified at depths varying from 0.4 to 0.6 km b.s.l. in the central area (Fig.7.13b-c and Fig.7.14a-b).

Nunziata and Rapolla (1987) hypothesized the presence of the basement at 0.6 km depth at the centre of Ischia, by assuming a density contrast of 0.3 g/cm^3 between the basement material and the pyroclastic sediments. Moreover, Maino and Tribalto (1971) assigned a density value of 2.5 g/cm^3 to the trachytic lava to which a V_S value of about 2.5 km/s corresponds according to the Nafe-Drake empirical relation (Fowler, 1995). In the light of these considerations, it might be reasonable correlate the 2.00-2.40 km/s body with the lava basement, while the lower range (1.40-2.00 km/s) could represent the altered and fractured facies of the lava or the deeper portion of the tuff layer which might be affected by thermal alteration due to the uprising of this lava material. Furthermore the deepening of this high V_S layer is extremely evident in my seismo-stratigraphic models as, moving toward the edges of the island, it should be at depths greater than those investigated (Fig.7.13-7.14). This result is in a good agreement with the deepening trend of the basement toward north and south delineated by Nunziata and Rapolla (1987) and with the disappearance of the lava material in I6 borehole drilled at Maronti in the southern area of Ischia (Penta and Conforto, 1951) (Fig.1.34).

The deepening trend of the seismo-layers from the centre to the edges of the island, recognized along the W-E NFOR-ISC (Fig.7.13b) and SFOR-TES (Fig.7.13d) sections, is consistent with the structural setting of Ischia: a central uplifted area where the Mt. Epomeo raises and a graben extending in the central-eastern part of the island bordered by NNE and N trending fracture systems (Capaldi et al., 1976) (see 1.2.1 section). Likewise in

the central-northern area the differences of the layer depth moving along the northern flank of the Mt. Epomeo (CENTRE-PER section (Fig.7.14b)) may be related to the presence of a ENE-WSW to E-W striking fault system (Vezzoli, 1988; Molin et al., 2003) (Fig.7.10). The same observation can be done as regards the ISC-ETES and SPL-WTES paths (Fig.7.14c) which cross the south-eastern sector of Ischia: the V_S models present a deepening of the seismo-layers in SSW-NNE direction which probably might be related to the presence of a NE-SW extending fault (Fig.7.10).

Conclusions

One-Dimensional shear wave velocity models have been defined in the upper crust of Campi Flegrei and Ischia volcanic areas through the non-linear inversion of the group velocity dispersion curves of Rayleigh surface waves fundamental mode extracted from the seismic noise cross-correlation functions (Green functions) between two receivers.

The cross-correlation analysis of noise recordings along 50 paths in the Phlegraean area has provided satisfactory and successful results since monthly cross-correlation functions computed for most of the paths are stable in terms of frequency content and waveforms. I could compute the group velocity dispersion curve of Rayleigh wave fundamental mode below 46 paths, but I didn't invert the average dispersion curves with high error bars and those not statistically sounded as computed between two monthly dispersion curves. A total of 25 paths have resulted reliable to perform the Hedgehog non-linear inversion and get V_S profiles vs. depth.

The cross-correlation analysis of noise recordings along 14 paths at Ischia has shown that the noise wavefield is very complex with many sources acting in different frequency ranges and at different scales. In fact, most of the computed NCF are characterized by a low signal-to-noise ratio and a strong contribution at very low frequencies. Nevertheless average dispersion curves have been computed for 13 paths (since an average dispersion curve has been computed for the ISCH-NEG and ISCH-MOR paths) but with error bars higher than those computed at Campi Flegrei, and inverted to get V_S models.

The V_S models (Hedgehog solutions with the minimum error) have been attributed to the midpoint of the paths and interpreted on the basis of literature data.

The distribution of the V_S velocities in the Campi Flegrei area shows a strong difference between the Gulf of Pozzuoli, where very low velocities and very high V_P/V_S ratio values are present down to 1.3 km depth, and the inland area characterized by higher V_S values and decreasing V_P/V_S ratio values moving toward the inner sector. It comes out a more complex setting in the Gulf of Pozzuoli and in the central area than in the northern sector characterized by a quite laterally homogeneous setting.

A funnel-shaped caldera model turns out in the Gulf of Pozzuoli where the 0.4-0.7 km/s layer, with density of 1.7 g/cm^3, deepens to 1.3 km depth and the 1.0-1.3 km/s layer, with density of 2.1 g/cm^3, deepens to the maximum investigated depth of 2 km. This model is in agreement with the interpretation of gravity anomalies after Nunziata and Rapolla (1981) and Fedi et al. (1991), and contradicts that given by AGIP (1987) based on the assumption

of the stratigraphies of Mofete drillings. Moreover, the agreement of the V_P seismic discontinuity at 1.3 km depth (by assuming the V_P/V_S ratios used in the inversion) with other studies (Finetti and Morelli, 1974; Judenherc and Zollo, 2004) is a validation test of the NCF method.

At 0.4-0.5 km depth a low velocity layer with high V_P/V_S ratios of 2.8-2.9 and low density (1.7 g/cm^3) has been detected both in the western (17% V_S reduction) and the eastern (30%) sector of the Gulf of Pozzuoli: it can be related to the anomalous high thermal state of the area, as testified by the high temperatures measured in the Mofete boreholes. Its depth is also in agreement with the top of the demagnetized body (western sector) (Nunziata and Rapolla, 1981).

A 43% velocity reduction, with a 2.3-2.5 V_P/V_S ratio, has been detected from 0.5 to about 1 km depth at inland, in the central-eastern sector of Campi Flegrei in correspondence of the Solfatara crater, where high temperature fumaroles are present (Chiodini et al., 2003 and references therein).

The layer with the lowest V_S value (0.4-0.7 km/s) is thinner and thinner moving from the gulf to the inland area, where it reaches an average thickness of 0.2 km. The top of the layers with higher V_S values, ranging from 1.6 to 2.4 km/s, has been retrieved at depth of about 1 km in the central area and 0.7-0.8 km in the northern area. The rising trend of the high V_S layers and the existence of "normal" V_P/V_S ratio (1.8-2 range) in the inner sector of Campi Flegrei let to hypothesize an improvement in the mechanical qualities of the medium moving from the centre to the edge of the depressed area.

At Ischia a deepening trend of the seismo-layers has been recognized moving from the centre to the edges of the island both in N-S and in W-E direction.

In the central area, beneath the Mt. Epomeo, a 0.2 km thick layer characterized by V_S increasing from 0.6 to 1.4 km/s has been identified. It has been related to the Green Tuff (from the fractured to the compact facies) according to the stratigraphic reconstructions (Penta and Conforto, 1951; Vezzoli, 1988). This layer can be retrieved at greater depth in the western, northern and eastern areas, where it shows a thickness of about 0.4 km and is overlaid by the landslide deposits and the recent volcanics which, instead, are characterized by low V_S ranging from ~0.4 to 0.6 km/s.

In the central area at depth varying from 0.4 to 0.6 km b.s.l. a body with higher V_S values, belonging to the 2.00-2.40 km/s range, has been identified. It has been related to the lava basement in agreement with the retrievement of the basement at 0.6 km depth in the

hypothesis of a 0.3 g/cm^3 density contrast between the basement material and the pyroclastic sediments (Nunziata and Rapolla, 1987). The basement deepens moving toward the edges of the island where the 2.00-2.40 km/s layer hasn't been retrieved.
Decreasing velocity layers haven't been identified at Ischia: this may be due to the small size of the high temperature areas, lower than data resolution.

In the light of the obtained results a marked difference emerges between the V_S models proposed for Campi Flegrei and Ischia. Generally the uppermost 1.7 km depth b.s.l. investigated at Ischia are characterized by higher V_S values, recognizable from the surface, than those retrieved in the Campi Flegrei. At Ischia a quite simple geological setting has been recognized with a deepening of the structures from the centre to the edges of the island which may be correlated to the existence of several fault systems. On the contrary the uppermost 2-3 km of the crust investigated in the Campi Flegrei show strong difference between the offshore and the onshore areas and the co-existence in a restricted area of different geological and thermal settings.

The results of this study are an important contribution to the knowledge of Campi Flegrei and Ischia volcanic areas. In the future, noise or earthquake recordings at greater distances could be analysed to infer structural models at greater depths, by using both regional and these local dispersion data.

Acknowledgements

At the end of this very important and formative three years course I wish to thank all the people who have given a contribution to the accomplishment of this work.

First of all I wish to thank sincerely my supervisor, the Professor Concettina Nunziata, for trusting me. She has been a fundamental, helpful and constant guide during the last three years, instilling in me courage and passion for research activity. All my best thanks are addressed to her and I hold her in high esteem. I hope that I didn't disappoint her expectations.

I wish to thank heartily Maria Rosaria and Rossana, my "fellow-travellers". A great and friendly collaboration is grown day by day with them on the basis of respect and continuous comparison. Their support has been essential and helpful for me, mostly in hard moments.

Special thanks are also addressed to Alessia, Danila, Luca and Mimmo: helping and guiding them in their degree thesis works have given to me the possibility of growing and ripening.

I wish to thank the INGV-OV, in particular Dr. Luca D'Auria, for kindly providing us the seismic noise recordings at Campi Flegrei. Moreover, thanks to the Archeological Park of Cuma and all the inhabitants of Ischia island for allowing us to execute seismic noise measurements. Particular thanks are addressed to the Iannotta family and the staff of the Negombo thermal park for their disposability.

Lastly thanks to the Professor Vincenzo Del Gaudio for his disposability, interesting advices and constructive review.

References

Acocella V. and Funiciello R. (1999) - *The interaction between regional and local tectonics during resurgent doming: the case of the island of Ischia, Italy* - J. Volcanol. Geoth. Res., 88, pp. 109-123.

Acocella V., Cifelli F., Funiciello R. (2001) - *The control of overburden thickness on resurgent domes: insights from analogue models* - J. Volcanol. Geoth. Res., 111, pp. 137-153.

AGIP (1981) - *Italia, Carta Magnetica, Anomalie del Campo Magnetico Residuo.*

AGIP (1987) - *Modello geotermico del sistema flegreo (sintesi)* - Servizi Centrali per l'Esplorazione, SERG-MESG. San Donato, pp. 23.

Aiello G., Cicchella A.G., Di Fiore V., Marsella E. (2011) - *New seismostratigraphic data of the Volturno Basin (northern Campania, Tyrrhenian margin, southern Italy): implications for tectonostratigraphy of the Campania and Latium sedimentary basins* - Ann. Geophys., 54(3), pp. 265-283.

Aiello G., Marsella E., Passaro S. (2012) - *Stratigraphic and structural setting of the Ischia volcanic complex (Naples Bay, Southern Italy) revealed by submarine seismic reflection data* - Rend. Fis. Acc. Lincei, 23, pp. 387-408, doi 10.1007/s12210-012-0204-2.

Alessio M., Bella F., Improta S., Belluomini G., Cortesi C., Turi B. (1971) - *University of Rome Carbon-14 Dates IX* - Radiocarbon, 13(2), pp. 395-411.

Alessio M., Bella F., Improta S., Belluomini G., Cortesi C., Turi B. (1973) - *University of Rome Carbon-14 Dates X* - Radiocarbon, 15(1), pp. 165-178.

Alessio G., Esposito E., Ferranti L., Mastrolorenzo G., Porfido S. (1996) - *Correlazione tra sismicità ed elementi strutturali nell'isola di Ischia* - II Quaternario, 9(1), pp. 303-308.

Amadei G., Maino A., Tribalto G. (1971) - *Risultati delle misure gravimetriche di raffittimento effettuate nei Campi Flegrei (Napoli)* - Boll. Serv. Geol. Ital., 92, pp. 73-85.

Armienti P., Barberi F., Bizouard H., Ciocchiatti R., Innocenti F., Metrich N., Rosi M., Sbrana A. (1983) - *The Phlegraean Fields: Magma evolution within a shallow chamber* - J. Volcanol. Geoth. Res., 17, pp. 289-311.

Aster R.C. and Meyer R.P. (1988) - *Three-dimensional velocity structure and hypocenter distribution in the Campi Flegrei caldera, Italy* - Tectonophysics, 149, pp. 195-218.

Aster R.C. and Meyer R.P. (1989) - *Determination of shear and compressional wave velocity variations and hypocentral locations in a rapidly inflating caldera: the Campi Flegrei* - Phys. Earth Planet. In., 55, pp. 313-325.

Aster R.C., Meyer R.P., De Natale G., Zollo A., Martini M., Del Pezzo E., Scarpa R., Iannaccone G. (1992) - *Seismic investigation of Campi Flegrei Caldera* - Volcanic Seismology. Proc. Volcanol. Series, vol. III., Springer Verlag, New York.

Auger E., Gasparini P., Virieux J., Zollo A. (2001) - *Seismic evidence of an extended magmatic sill under Mt. Vesuvius* - Science, 294, pp. 1,510-1,512.

Barberi F., Innocenti F., Lirer L., Munno R., Pescatore T., Santacroce R. (1978) - *The Campanian Ignimbrite: a major prehistoric eruption in the Neapolitan area (Italy)* - B. Volcanol., 41(1), pp. 1-22.

Barberi F., Innocenti F., Luongo G., Nunziata C., Rapolla A., Scandone P. (1979) - *Analysis and synthesis of the geological, geophysical and volcanological data about the Neapolitan area and its geothermal potentiality* - EUR 6386, 2.

Barberi F., Corrado G., Innocenti F., Luongo G. (1984) - *Phlegraean Fields 1982-1984: brief chronicle of a volcano emergency in a densely populated* area - B. Volcanol., 47, pp. 175-185.

Barberi F., Cassano E., La Torre P., Sbrana A. (1991) - *Structural evolution of Campi Flegrei caldera in light of volcanological and geophysical data* - J. Volcanol. Geoth. Res., 48, pp. 33-49.

Barra D., Cinque A., Italiano A., Scorziello R. (1992a) - *Il Pleistocene superiore marino di Ischia: paleoecologia e rapporti con l'evoluzione tettonica recente* - Studi Geologici Camerti, 1, pp. 231-243.

Barra D., Cinque A., Italiano A., Scorziello R. (1992b) - *La serie marina olocenica di Cafieri (isola d'Ischia): implicazioni vulcano-tettoniche e geomorfologiche* - Il Quaternario, 5(1), pp. 17-26.

Bartole R. (1984) - *Tectonic structures of Latian-Campanian shelf (Tyrrhenian sea)* - Boll. Ocean. Teor. Appl., 2, pp. 197-230.

Bartole R., Savelli D., Tramontana M., Wezel F. (1984) - *Structural and sedimentary features in the Tyrrhenian margin of Campania, Southern Italy* - Mar. Geol., 55, pp. 163-180.

Battaglia J., Zollo A., Virieux J., Dello Iacono D. (2008) - *Merging active and passive data sets in traveltime tomography: the case study of Campi Flegrei caldera (Southern Italy)* - Geophys. Prospect., 56, pp. 555-573, doi:10.1111/j.1365-2478.2007.00687.x.

Battaglia M., Troise C., Obrizzo F., Pingue F., De Natale G. (2006) - *Evidence for fluid migration as the source of deformation at Campi Flegrei caldera (Italy)* - Geophys. Res. Lett., 33:L01307, doi:10.1029/2005GL024904.

Belkin H.E., De Vivo B., Lima A., Torok K. (1996) - *Magmatic (silicate/sulfur-rich/CO_2) immiscibility and zirconium and rare-earth element enrichment from alkaline magma chamber margins: evidence from Ponza island, Pontine Archipelago* - Eur. J. Mineral., 8, pp. 1,401-1,420.

Bellucci F., Woo J., Kilburn C.R.J., Rolandi G. (2006) - *Ground deformation at Campi Flegrei, Italy: implications for hazard assessment* - In: Troise C., De Natale G., Kilburn C.R.J. (eds), Mechanisms of activity and unrest at large calderas, Geol. Soc. London Spec. Publ., 269, pp. 141-157.

Bensen G.D., Ritzwoller M.H., Barmin M.P., Levshin A.L., Lin F., Moschetti M.P., Shapiro N.M., Yang Y. (2007) - *Processing seismic ambient noise data to obtain reliable broad-band surface wave dispersion measurements* - Geophys. J. Int., 169, pp. 1,239-1,260.

Berrino G., Corrado G., Luongo G., Toro B. (1984) - *Ground deformation and gravity changes accompanying the 1982 Pozzuoli uplift* - B. Volcanol., 47, pp. 187-200.

Berrino G, Corrado G, Riccardi U. (1998) - *Sea gravity data in the Gulf of Naples: a contribution to delineate the structural pattern of Vesuvian* area - J. Volcanol. Geoth. Res., 82, pp. 139-150.

Bianchi R., Cordini A., Federico C., Giberti G., Lanciano P., Pozzi J.P., Sartoris G., Scandone R. (1987) - *Modelling of surface ground deformation in volcanic areas: the 1970-1972 and 1982-1984 crises of Campi Flegrei, Italy* - J. Geophys. Res., 92(B13), pp. 14,139-14,150.

Bodnar R.J., Cannatelli C., De Vivo B., Lima A., Belkin H.E., Milia A. (2007) - *Quantitative model for magma degassing and ground deformation (bradyseism) at Campi Flegrei, Italy: implications for future eruptions* - Geology, 35(9), pp. 791-794, doi:10.1130/G23653A.1.

Bonafede M. (1991) - *Hot fluid migration: an efficient source of ground deformation. Application to the 1982-85 crisis at Campi Flegrei, Italy* - In: Luongo G., Scandone R. (Eds.), Campi Flegrei, J. Volcanol. Geoth. Res., 48, pp. 187-198.

Bonafede M., Dragoni M., Quareni F. (1986) - *Displacement and stress fields produced by a centre of dilatation and by a pressure source in visco-elastic half-space: application to the study of ground deformation and seismic activity at Campi Flegrei, Italy* - Geophys. J. Roy. Astr. S., 87, pp. 455-485.

Boschi E., Guidoboni E., Ferrari G., Mariotti D., Valensise G., Gasperini P. (2000) - *Catalogue of Strong Italian Earthquakes* - Ann. Geofis., 43, pp. 268.

Boyadzhiev G., Brandmayr E., Pinat T., Panza G.F. (2008) - *Optimization for non-linear inverse problems* - Rend. Lincei, 19, pp. 17-43.

Brown R.J., Orsi G., de Vita S. (2008) - *New insights into Late Pleistocene explosive volcanic activity and caldera formation on Ischia (southern Italy)* - B. Volcanol., 70, pp. 583-603.

Bruni P., Chelini W., Sbrana A., Verdiani G. (1985) - *Deep exploration of the S.Vito area (Pozzuoli-NA) - Well S.Vito 1* - In: A.S. Strub and P. Ungemach (Editors), European Geothermal Update, Proc. Third Int. Seminar, pp. 390-406.

Bruno P.P., de Alteriis G., Florio G. (2002) - *The western undersea section of the Ischia volcanic complex (Italy, Tyrrhenian sea) inferred by marine geophysical* data - Geophys. Res. Lett., 29(9), pp. 1-4.

Buchner G. (1986) - *Eruzioni vulcaniche e fenomeni vulcano-tettonici di età preistorica e storica nell'isola d'Ischia* - Eruptions Volcaniques, Tremblemants de Terre et Vie des Hommes dans la Campanie Antique: Centre J. Bérard, Inst. Fr. de Naples, Naples, Italy, 7, pp. 145-188.

Buchner G., Italiano A., Vita-Finzi C. (1996) - *Recent uplift of Ischia, southern Italy* - In: Mc Guire W.J., Jones A.P., Neuberg J. (Eds.), Volcano Instability on the Earth and Other Planets, Geol. Soc. Spec. Publ., London, 110, pp. 249-252.

Caliro S., Chiodini G., Moretti R., Avino R., Granirei D., Russo M., Fiebig J. (2007) - *The origin of the fumaroles of La Solfatara (Campi Flegrei, South Italy)* - Geochim. Cosmochim. Acta, 71, pp. 3,040-3,055.

Calligaris D., Morelli C., Pisani M., (1972) - *Rilievo gravimetrico e magnetico* - Quad. Ric. Sci., 83, pp. 72-81.

Cannatelli C., Lima A., Bodnar R.J., De Vivo B., Webster J.D., Fedele L. (2007) - *Geochemistry of melt inclusions from the Fondo Riccio and Minopoli 1 eruptions at Campi Flegrei (Italy)* - Chem. Geol., 237, pp. 418-432.

Capaldi G., Civetta L., Gasparini P. (1976) - *Volcanic history of the island of Ischia (South Italy)* - B. Volcanol., 40(1), pp. 11-22.

Carella R. and Guglielminetti M. (1983) - *Multiple reservoirs in the Mofete fields, Naples, Italy* - 9th Workshop on Geothermal Reservoir Engineering, Stanford, pp. 12.

Carlino S. (2012) - *The process of resurgence for Ischia Island (southern Italy) since 55 ka: the laccolith model and implications for eruption forecasting* - B. Volcanol., 74 (5), pp. 947-961.

Carlino S., Cubellis E., Luongo G., Obrizzo F. (2006) - *On the mechanics of caldera resurgence of Ischia Island (southern Italy)* - In: Troise C., De Natale G., Kilburn C.R.J. (Eds.), Mechanisms of Activity and Unrest at Large Calderas, Geol. Soc. London Spec. Publ., 269, pp. 181-193.

Carlino S., Cubellis E., Marturano A. (2010) - *The catastrophic 1883 earthquake at the island of Ischia (southern Italy): macroseismic data and the role of geological conditions* - Nat. Hazards, 52, pp. 231-247.

Carrara E., Iacobucci F., Pinna E., Rapolla A. (1973) - *Gravity and magnetic survey of the Campanian volcanic area, S. Italy* - Boll. Geofis. Teor. Appl., 15(57), pp. 39-51.

Carrara E., Iacobucci F., Pinna E., Rapolla A. (1974) - *Interpretation of gravity and magnetic anomalies near Neaples , Italy, using computer technique* - B. Volcanol., 38(2), pp. 458-467.

Casertano L., Oliveri A., Quagliariello M.T. (1976) - *Hydrodynamics and geodynamics in the Phlegraean Fields area of Italy* - Nature, 264, pp. 161-164.

Cassignol C. and Gillot P.Y. (1982) - *Range and effectiveness of unspiked potassium-argon dating: experimental ground work and application* - In: G.S. Odin (Editor), Numerical Dating in Stratigraphy, Wiley, New York, NY, pp. 160.

Chiesa S., Cornette Y., Forcella F., Gillot P.Y., Pasquarè G., Vezzoli L. (1985) - *Carta geologica dell'isola d'Ischia - CNR, Progetto Finalizzato Geodinamica,* Roma.

Chiesa S., Civetta L., De Lucia M., Orsi G., Poli S. (1987) - *Volcanological evolution of the island of Ischia* - In: De Girolamo P. (Ed.), The volcanoclastic rocks of Campania (southern Italy), Rend. Acc. Sci. Fis. e Mat. In Napoli, Spec. Issue, pp. 69-83.

Chiodini G. and Marini L. (1998) - *Hydrothermal gas equilibria: the H_2O-H_2-CO_2-CO-CH_4 system* - Geochim. Cosmochim. Ac., 62(15), pp. 2673-2687.

Chiodini G., Frondini F., Cardellini C., Granieri D., Marini L., Ventura G. (2001) - *CO_2 degassing and energy release at Solfatara Volcano, Campi Flegrei, Italy* - J. Geophys. Res., 106, pp. 16,213-16,221.

Chiodini G., Todesco M., Caliro S., Del Gaudio C., Macedonio G., Russo M. (2003) - *Magma degassing as a trigger of bradyseismic events: The case of Phlegrean Fields (Italy)* - Geophys. Res. Lett., 30(8), 1434, doi:10.1029/2002GL016790.

Chiodini G., Avino R., Brombach T., Caliro S., Cardellini C., de Vita S., Frondini F., Granirei D., Marotta E., Ventura G. (2004) - *Fumarolic and diffuse soil degassing West of Mount Epomeo, Ischia,* Italy - J. Volcanol. Geoth. Res., 133, pp. 291-309.

Ciani A., Gantar C., Morelli C. (1960) - *Rilievo gravimetrico sullo zoccolo epicontinentale dei mari italiani* - Boll. Geofis. Teor. Appl., 2(6), pp. 289-373.

Cinque A., Rolandi G., Zamparelli V. (1984) - *L'estensione dei depositi marini olocenici nei Campi Flegrei in relazione alla vulcano-tettonica* - Boll. Soc. Geol. Ital., 104(2), pp. 327-348.

Civetta L., Carluccio E., Innocenti F., Sbrana A., Taddeucci G. (1991a) - *Magma chamber evolution under the Phlegraean Fields during the last 10 ka: Trace element and isotopic data* - Eur. J. Mineral., 3, pp. 415-428.

Civetta L., Gallo G., Orsi G. (1991b) - *Sr- and Nd-isotope and trace element constraints on the chemical evolution of the magmatic system of Ischia (Italy) in the last 55 ka* - J. Volcanol. Geoth. Res., 46, pp. 213-230.

Civetta L., Orsi G., Pappalardo L., Fisher R.V., Heiken G.H., Ort M. (1997) - *Geochemical zoning, mixing, eruptive dynamics and depositional processes-the Campanian Ignimbrite, Campi Flegrei, Italy* - J. Volcanol. Geoth. Res., 75, pp. 183-219.

Civetta L., D'Antonio M., de Lorenzo S., Di Renzo V., Gasparini P. (2004) - *Thermal and geochemical constraints on the 'deep' structure of Mt. Vesuvius* - J. Volcanol. Geoth. Res., 133, pp. 1-12.

Corrado G., Guerra I., Lo Bascio A., Luongo G., Rampoldi F. (1977) - *Inflation and microearthquake activity of Phlegraean Fields, Italy* - B. Volcanol., 40 (3), pp. 169-188.

Cortini M. and Barton C.C. (1993) - *Non linear forecasting analysis of inflation-deflation patterns of an active caldera (Campi Flegrei, Italy)* - Geology, 21, pp. 239-242.

Cortini M., Cilento L., Rullo A. (1991) - *Vertical ground movements in the Campi Flegrei caldera as a chaotic dynamic phenomenon* - J. Volcanol. Geoth. Res., 48, pp. 103-114.

Costanzo M.R. - *Modelli delle velocità sismiche di taglio della struttura crostale profonda della Piana Campana mediante cross-correlazione di rumore sismico,* Dottorato di Ricerca in Scienza della Terra XXIV ciclo - Novembre, 2011.

Costanzo M.R. and Nunziata C. (2014) - *Lithospheric V_S models below the Campanian Plain (Italy) by integrating Rayleigh wave dispersion data from noise cross-correlation functions and earthquake recordings* - in press.

Cubellis E., Di Donna G., Luongo G., Mazzarella A. (2002) - *Simulating the mechanism of magmatic processes in the Campi Flegrei area (southern Italy) by the Lorenz equations* - J. Volcanol. Geoth. Res., 115, pp. 339-349.

D'Antonio M. (2005) - *Calderas and magmatic feeding systems: examples from Campi Flegrei (southern Italy)* - Acta Vulcanol., 17, pp. 53-66.

D'Antonio M., Civetta L., Di Girolamo P. (1999a) - *Mantle source heterogeneity in the Campanian Region (South Italy) as inferred from geochemical and isotopic features of mafic volcanic rocks with shoshonitic affinity* - Miner. Petrol., 67, pp. 163-192.

D'Antonio M., Civetta L., Orsi G., Pappalardo L., Piochi M., Carandente A., de Vita S., Di Vito M.A., Isaia R., Southon J. (1999b) - *The present state of the magmatic system of the Campi Flegrei caldera based on the reconstruction of its behaviour in the past 12* ka - J. Volcanol. Geoth. Res., 91, pp. 47-268.

D'Antonio M., Tonarini S., Arienzo I., Civetta L., Di Renzo V. (2007) - *Components and processes in the magma genesis of the Phlegrean Volcanic District, southern Italy* - Geol. Soc. Am. Spec. Pap., 418, pp. 203-220.

D'Antonio M., Tonarini S., Arienzo I., Civetta L., Dallai L., Moretti R., Orsi G., Andria M., Trecalli A. (2013) - *Mantle and crustal processes in the magmatism of the Campania region: inferences from mineralogy, geochemistry, and Sr-Nd-O isotopes of young hybrid volcanics of the Ischia island (South Italy)* - Contrib. Mineral. Petr., 165, pp. 1,173-1,194, doi:10.1007/s00410-013-0853.

D'Argenio B., Pescatore T.S., Scandone P. (1973) - *Schema geologico dell'Appennino Meridionale* - Accad. Naz. Lincei Quad., 183, pp. 49-72.

D'Erasmo G. (1931) - *Studio geologico dei pozzi profondi della* Campania - Boll. Soc. Nat. Napoli, 43, pp. 15-143.

Danyushevsky L.V. and Lima A. (2001) - *Relationships between Campi Flegrei and Mt. Somma volcanism: evidence from melt inclusions in clinopyroxene phenocrysts from volcanic breccias* xenoliths - Miner. Petrol., 73, pp. 107-119.

de Alteriis G. and Toscano F. (2003) - *Introduzione alla geologia dei mari circostanti le isole flegree di Ischia, Procida e Vivara* - AA.VV., "Ambiente marino costiero e territorio delle isole flegree (Ischia, Procida e Vivara) e Golfo di Napoli: Risultati di uno studio multidisciplinare, Monografia Accademia di Scienze Matematiche, Fisiche e Naturali, Liguori Ed., Naples, pp. 77.

De Lorenzo S., Gasparini P., Mongelli F., Zollo A. (2001a) - *Thermal state of the Campi Flegrei caldera inferred from seismic attenuation tomography* - J. Geodyn., 32, pp. 467-486.

De Lorenzo S., Zollo A., Mongelli F. (2001b) - *Source parameters and three-dimensional attenuation structure from the inversion of microearthquake pulse width data: Q_P imaging and inferences on the thermal state of the Campi Flegrei caldera (southern Italy)* - J. Geophys. Res., 106, pp. 16,265-16,286.

De Natale G., Ferraro A., Zollo A., Virieux J. (1995) - *Accurate fault mechanisms of a 1984 earthquake swarm at Campi Flegrei caldera (Italy), during an unrest episode: Implications for volcanological research* - J. Geophys. Res., 100(B12), pp. 24,167-24,185, doi: 10.1029/95JB00749.

De Natale G., Troise C., Pingue F., Mastrolorenzo G., Pappalardo L., Battaglia L., Boschi E. (2006) - *The Campi Flegrei caldera: unrest mechanisms and hazard* - In: Troise C., De Natale G., Kilburn C.R.J. (eds) Mechanisms of activity and unrest at large calderas, Geol. Soc. London Spec. Publ., 269, pp. 159-171.

De Nisco G. and Nunziata C. (2011) - *V_s profiles from noise cross correlation at local and small scale* - Pure Appl. Geophys., 168, pp. 509-520, doi: 10.1007/s00024-010-0119-8.

de Vita S., Orsi G., Civetta L., Carandente A., D'Antonio M., Deino A., di Cesare T., Di Vito M.A., Fisher R.V., Isaia R., Marotta E., Necco A., Ort M., Pappalardo L., Piochi M., Southon J. (1999) - *The Agnano–Monte Spina eruption (4100 years BP) in the restless Campi Flegrei caldera (Italy)* - J. Volcanol. Geoth. Res., 91, pp. 269-301.

de Vita S., Sansivero F., Orsi G., Marotta E. (2006) - *Cyclical slope instability and volcanism related to volcano-tectonism in resurgent calderas: the Ischia island (Italy) case study* - Eng. Geol., 86, pp. 148-165.

de Vita S., Sansivero F., Orsi G., Marotta E., Piochi M. (2010) - *Volcanological and structural evolution of the Ischia resurgent caldera (Italy) over the past 10 k.y.* - In: Groppelli G. and Viereck- Goette L. (eds), Stratigraphy and Geology of Volcanic Areas, Geol. Soc. Am. Spec. Pap., 464, pp. 193-241.

De Vivo B. and Lima A. (2006) - *A hydrothermal model for ground movements (bradyseism) at Campi Flegrei, Italy* - In: De Vivo B. (Ed.), Volcanism in the Campania Plain. Vesuvius, Campi Flegrei, Ignimbrites, Developments in Volcanology, Elsevier, 9, pp. 289-317.

De Vivo B., Belkin H.E., Barbieri M., Chelini W., Lattanzi P., Lima A., Tolomeo L. (1989) - *The Campi Flegrei (Italy) geothermal system: a fluid inclusion study of the Mofete and San Vito fields* - J. Volcanol. Geoth. Res., 36, pp. 303-326.

De Vivo B., Torok K., Ayuso R.A., Lima A., Lirer L. (1995) - *Fluid inclusion evidence for magmatic/saline/CO_2 immiscibility and geochemistry of alkaline xenoliths from Ventotene Island, Italy* - Geochim. Cosmochim. Acta, 59(14), pp. 2,941-2,953.

De Vivo B., Rolandi G., Gans P.B., Calvert A., Bohrson W.A., Spera F.J., Belkin H.E. (2001) - *New constraints on the pyroclastic eruptive history of the Campanian volcanic Plain (Italy)* - Miner. Petrol., 73, pp. 47-65.

De Vivo B, Petrosino P., Lima A., Rolandi G., Belkin H.E. (2010) - *Research progress in volcanology in the Neapolitan area, southern Italy: a review and some alternative* views - Miner. Petrol., 99, pp. 1-28.

Deino A.L., Orsi G., Piochi M., de Vita S. (2004) - *The age of the Neapolitan Yellow Tuff caldera-forming eruption (Campi Flegrei caldera-Italy) assessed by $^{40}Ar/^{39}Ar$ dating method* - J. Volcanol. Geoth. Res., 133, pp. 157-170.

Del Gaudio C., Ricco C., Equino I., Brandi G., Serio C., Siniscalchi V. (2005) - *Misure di livellazione di precisione e dati tiltmetrici per il controllo delle deformazioni del suolo ai Campi Flegrei* - INGV-Osservatorio Vesuviano. Open File Report http://www.ov.ingv.it.

Del Gaudio C., Aquino I., Ricciardi G.P., Ricco C., Scandone R. (2010) - *Unrest episodes at Campi Flegrei: A reconstruction of vertical ground movements during 1905-2009* - J. Volcanol. Geoth. Res., 195, pp. 48-56.

Della Vedova B., Bellani S., Pellis G., Squarci P. (2001) - *Deep temperatures and surface heat flow distribution* - In: Vai G. B. and Martini I. P. (eds), Anatomy of an Orogen: the Apennines and Adjacent Mediterranean Basins, Dordecht: Kluwer Academic, pp. 65-76.

Dello Iacono D., Zollo A., Vassallo M., Vanorio T., Judenherc S. (2009) - *Seismic images and rock properties of the very shallow structure of Campi Flegrei caldera (southern Italy)* - B. Volcanol., 71, 275-284, doi 10.1007/s00445-008-0222-1.

Derode A., Larose E., Tanter M., de Rosny J., Tourim A., Campillo M., Fink M. (2003) - *Recovering the Green's function from field-field correlations in an open scattering medium* - J. Acoust. Soc. Am., 113, pp. 2,973-2,976.

Di Filippo G., Lirer L., Maraffi S., Capuano M. (1991) - *L'eruzione di Astroni nell'attività recente dei Campi Flegrei* - Boll. Soc. Geol. Ital., 110, pp. 309-331.

Di Girolamo P. (1968) - *Petrografia dei tufi Campani: Il processo di pipernizzazione (Tufo-Tufo pipernoide-Piperno)* - Rend. Acc. Sci. Fis. Mat. Napoli, 5, pp. 4-25.

Di Girolamo P. (1970) - *Differenziazione gravitativa e curve isochimiche nell'Ignimbrite Campana* - Rend. Soc. It. Mineral. Petr., 26, pp. 547-588.

Di Girolamo P. and Rolandi G. (1975) - *Vulcanismo sottomarino latitebasaltico-latitico (serie potassica) nel Canale d'Ischia (Campania)* - Rend. Acc. Sci. Fis. Mat. Napoli, 42, pp. 561-596.

Di Girolamo P. and Stanzione D. (1973) - *Lineamenti geologici e petrologici dell'isola di Procida* - Rend. Soc. It. Mineral. Petr., 29, pp. 82-125.

Di Girolamo P., Ghiara M.R., Lirer L., Munno R., Rolandi G., Stanzione D. (1984) - *Vulcanologia e petrologia dei Campi Flegrei* - Boll. Soc. Geol. Ital., 103, pp. 349-413.

Di Napoli R., Aiuppa A., Bellomo S., Busca L., D'Alessandro W., Gagliano Candela E., Longo M., Pecoraino G., Valenza M. (2009) - *A model for Ischia hydrothermal system: evidences from the chemistry of thermal groundwaters* - J. Volcanol. Geoth. Res., 186, pp. 133-159.

Di Vito M., Lirer L., Mastrolorenzo G., Rolandi G., Scandone R. (1985) - *Volcanological map of Campi Flegrei* - Ministero Protezione Civile, Università di Napoli, Naples, Italy.

Di Vito M.A., Lirer L., Mastrolorenzo G., Rolandi G. (1987) - *The Monte Nuovo eruption (Campi Flegrei, Italy)* - B. Volcanol., 49, pp. 608-615.

Draeger C. and Fink M. (1995) - *One-channel time reversal in chaotic cavities: Theoretical limits* - J. Acoust. Soc. Am., 105, pp. 611-617.

Dvorak J.J. and Mastrolorenzo G. (1991) - *The mechanism of recent vertical crustal movements in Campi Flegrei caldera, Southern Italy* - Geol. Soc. Am. Spec. Pap., 263.

Dvorkin J., Mavko G., Nur A. (1999) - *Overpressure detection from compressional- and shear-wave data* - Geophys. Res. Lett., 26, pp. 3,417-3,420.

Dziewonski A., Bloch S., Landisman M. (1969) - *A technique for the analysis of transient seismic signals* - Bull. Seism. Soc. Am., 59, pp. 427-444.

Dzurisin D. and Newhall C.G. (1984) - *Recent ground deformation and seismicity at Long Valley (California), Yellowstone (Wyoming), the Phlegrean Fields (Italy), and Rabaul (Papua New Guinea)* - US Geological Survey, Open-File Report, OF 84-0939, pp. 784-829.

Esposito R., Bodnar R.J., De Vivo B., Lima A., Fedele L., Shimizu N., Belkin H.E., Hunter J. (2009) - *Volatile evolution of magma associated with the Solchiaro eruption in the Phlegrean volcanic District* - ECROFI XX, Granada, Spain, pp. 75-76.

Fedi M., Nunziata C., Rapolla A. (1991) - *The Campania-Campi Flegrei area: a contribution to discern the best structural model from gravity interpretation* - J. Volcanol. Geoth. Res., 48, 51-59.

Ferrucci F., Hirn A., Virieux J., De Natale G., Mirabile L. (1992) - *P-SV conversions at a shallow boundary beneath Campi Flegrei caldera (Naples, Italy): evidence for the magma chamber* - J. Geophys. Res., 97, pp. 15,351-15,359.

Fevola F., Fusi N., Mirabile L. (1993) - *Rilievi di sismica monocanale ad alta risoluzione: aspetti dell'evoluzione geomorfologica del Golfo di Napoli* - Ann. Ist. Univ. Nav. Napoli, 60, pp. 61-67.

Finetti I. and Morelli C. (1974) - *Esplorazione sismica a riflessione dei Golfi di Napoli e Pozzuoli* - Boll. Geofis. Teor. Appl., 16(62-63), pp. 175-222.

Fisher R.V., Orsi G., Ort M.H., Heiken G. (1993) - *Mobility of a large volume pyroclastic flow-emplacement of the Campanian ignimbrite, Italy* - J. Volcanol. Geoth. Res., 56, pp. 205-220.

Florio G., Fedi M., Cella F., Rapolla A. (1999) - *The Campanian Plain and Phlegrean fields: structural setting from potential field data* - J. Volcanol. Geoth. Res., 91, pp. 361-379.

Forcella F., Gnaccolino M., Vezzoli L. (1981) - *Stratigrafia e sedimentologia dei depositi piroclastici affioranti nel settore sud-occidentale dell'isola d'Ischia* - Riv. Ital. Paleontol. S., 87, pp. 329-366.

Forcella F., Gnaccolino M., Vezzoli L. (1983) - *I depositi piroclastici del settore sud-orientale dell'isola d'Ischia (Italia)* - Riv. Ital. Paleontol. S., 89, pp. 135-170.

Foulger G.R., Julian B.R., Pitt A.M., Hill D.P., Malin P.E., Shalev E. (2003) - *Three-dimensional crustal structure of Long Valley caldera, California, and evidence for the migration of CO_2 under Mammoth Mountain* - J. Geophys. Res. 108, pp. 2,147-2,163, doi:10.1029/2000JB000041.

Fournier R.O. (1999) - *Hydrothermal processes related to movement of fluid from plastic into brittle rock in the magmatic-epithermal environment* - Econ. Geol., 94(8), pp. 1,193-1,212.

Fowler C.M.R. (1995) - *The Solid Earth. An introduction to Global Geophysics* - Cambridge Univ. Press.

Fusi N., Mirabile L., Camerlenghi A., Ranieri G. (1991) - *Marine geophysical survey of the Gulf of Napoli (Italy): relationships between submarine volcanic activity and sedimentation* - Mem. Soc. Geol. Ital., 47, pp. 95-114.

Gaeta F.S., De Natale G., Peluso F., Mastrolorenzo G., Castagnolo D., Troise C., Pingue F., Mita D.G., Rossano S. (1998) - *Genesis and evolution of unrest episodes at Campi Flegrei caldera: the role of thermal fluid dynamical processes in the geothermal system* - J. Geophys. Res., 103, pp. 921-933.

Gillot P.Y., Chiesa S., Pasquarè G., Vezzoli L. (1982) - *33.000 yr K/Ar dating of the volcano-tectonic horst of the isle of Ischia, Gulf of Naples* - Nature, 229, pp. 242-245, http://dx.doi.org/10.1038/299242a0.

Goldstein P., Dodge D., Firpo M., Minner L. (2003) - *SAC2000: signal processing and analysis tools for seismologists and engineers.* In: Lee W.H.K., Kanamori H., Jennings P.C., Kisslinger C. (Eds.), Invited contribution to "The IASPEI International Handbook of Earthquake and Engineering Seismology", Academic Press, London.

Guerra I., Lo Bascio A., Luongo G., Nazzaro A. (1972) - *Rapporto sulla sorveglianza sismica nell'area di Pozzuoli (marzo 1970-ottobre 1971)* - CNR, Quaderni Ric. Sc., n. 83.

Guidarelli M, Saraò A., Panza G.F. (2002) - *Surface wave tomography and seismic source studies at Campi Flegrei (Italy)* - Phys. Earth Planet. In., 134, pp. 157-173.

Guidarelli M., Zille A., Saraò A., Natale M., Nunziata C., Panza G.F. (2006) - *Shear-wave velocity models and seismic sources in Campanian volcanic areas: Vesuvius and Phlegraean Fields* - In: Dobran F. (ed) Vesuvius, Elsevier, 6, pp. 287-309.

Haubrich R.A., Munk W., Snodgrass F.E. (1963) - *Comparative spectra of microseisms and swell* - Bull. Seism. Soc. Am., vol. 53, pp. 27-37.

Hill D.P., Pollitz F., Newhall C. (2002) - *Earthquake-volcano interactions* - Phys. Today, November, pp. 41-47.

Ippolito F. and Rapolla A. (1982) - *L'energia geotermica in Campania* - Fonti Energetiche Alternative, Fondazione Politecnica per il Mezzogiorno, Franco Angeli Ed, Milano, pp. 57-106.

Ippolito F., Ortolani F., Russo M. (1973) - *Struttura marginale tirrenica dell'Appennino Campano: reinterpretazione di dati di antiche ricerche di idrocarburi* - Mem. Soc. Geol. Ital., XII, pp. 227-250.

Isaia R., D'Antonio M., Dell'Erba F., Di Vito M., Orsi G. (2004) - *The Astroni volcano: the only example of close eruptions within the same vent area during the recent history of the Campi Flegrei caldera (Italy)* - J. Volcanol. Geoth. Res., 133, pp. 171-192.

Ito H., De Vilbiss J., Nur A. (1979) - *Compressional and shear waves in saturated rock during water-steam transition* - J. Geophys. Res., 84, pp. 4,731-4,735.

Judenherc S. and Zollo A. (2004) - *The Bay of Naples (southern Italy): constraints on the volcanic structures inferred from a dense seismic survey* - J. Geophys. Res., 109, B10312, doi:10.1029/2003JB002876.

Karnik V. (1969) - *Seismicity of the European area* - Geophys. Monograph Series, vol. 13, pp. 139-144.

Kastens K., Mascle J., Auroux C., Bonatti E., Broglia C., Channell J.E.T., Curzi P., Emeis K.C., Glason G., Hasegawa S., Hieke W., Mascle G., McCoy F., McKenzie J., Mendelson J., Mueller C., Rehault J.P., Robertson A., Sartori R., Sprovieri R., Torii M. (1986) - *Young Tyrrhenian Sea evolved very quickly* - Geotimes, 31(8), pp. 11-14.

Kastens K., Mascle J., Auroux C., Bonatti E., Broglia C., Channell J.E.T., Curzi P., Emeis K.C., Glacon G., Asegawa S., Hieke W., Mascle G., McCoy F., McKenzie J., Mendelson G., Muller C., Rehault J.P., Robertson A., Sartori R., Sprovieri R., Torii M. (1988) - *ODP Leg 107 in the Tyrrhenian Sea: insights into passive margin and back-arc basin* evolution - Geol. Soc. Am. Bull., 100, pp. 1,140-1,156.

Knopoff L. and Panza G.F. (1977) - *Resolution of upper mantle structure using higher modes of Rayleigh waves* - Ann. Geophys., 30, pp. 491-505.

Kolinsky P. (2004) - *Surface waves dispersion curves of Eurasian earthquakes: the SVAL program* - Acta Geodyn. Geomater., 1(2), pp. 165-185.

Larose E., Derode A., Campillo M., Fink M. (2004) - *Imaging from one-bit correlations of wideband diffuse wave fields* - J. Appl. Phys., 95, pp. 8,393-8,399.

Lee A.W. (1935) - *On the direction of approach of microseismic waves* - Proc. R. Soc. Lond. A, Math. Phys. Eng. Sci., 149, pp. 183-199.

Levshin A.L., Pisarenko V., Pogrebinsky G. (1972) - *On a frequency-time analysis of oscillations* - Ann. Geophys., 28, pp. 211-218.

Levshin A.L., Ratnikova L.I., Berger J. (1992) - *Peculiarities of surface wave propagation across Central Eurasia* - Bull. Seism. Soc. Am., 82, pp. 2,464-2,493.

Lima A., Danyushevsky L.V., De Vivo B., Fedele L. (2003) - *A model for the evolution of the Mt. Somma-Vesuvius magmatic system based on fluid and melt inclusion investigations* - In: De Vivo B., Bodnar R.J. (eds), Melt inclusions in volcanic systems: methods, applications and problems. Series: Developments in Volcanology 5, Elsevier, Amsterdam, pp. 1-272.

Lima A., De Vivo B., Fedele L., Sintoni M.F. (2006) - *Influence of hydrothermal processes on geochemical variations between 79 AD and 1944 AD Vesuvius eruptions* - In: De Vivo B. (ed), Volcanism in the Campania Plain: Vesuvius, Campi Flegrei, Ignimbrites, Elsevier, 9, Developments in Volcanology, pp. 235-247.

Lima A., De Vivo B., Spera F.J., Bodnar R.J., Milia A., Nunziata C., Belkin H.E., Cannatelli C. (2009) - *Thermodynamic model for uplift and deflation episodes (bradyseism) associated with magmatic-hydrothermal activity at the Campi Flegrei (Italy)* - Earth-Sci. Rev., 97, pp. 44-58.

Lin F., Ritzwoller M.H., Townend J., Savage M., Bannister S. (2007) - *Ambient noise Rayleigh wave tomography of New Zealand* - Geophys. J. Int., 18, doi:10.1111/j.1365-246X.2007.03414.x.

Lirer L., Luongo G., Scandone R. (1987) - *On the volcanological evolution of Campi Flegrei* - EOS. Trans. Am. Geophys. Union, 68, pp. 226-234.

Lirer L., Petrosino P., Alberico I., Armiero V., Chirosca M.C., Ruocco A., Scamardella G., Scamardella M., Vittoria M., Tonielli R., Innangi S., Di Martino G. (2010) - *Carta Geologica dei Campi Flegrei (scala 1:25000)* - Progetto CARG Regione Campania, Coordinamento scientifico: Lirer L., CNR-IAMC Napoli, Dipartimento di Scienze della Terra Università di Napoli Federico II, C.I.R.A.M.

Lobkis O.I. and Weaver R.L. (2001) - *On the emergence of the Green's function in the correlations of a diffuse field* - J. Acoust. Soc. Am., 110, pp. 3,011-3,017.

Longuet-Higgins M.S. (1950) - *A theory of the origin of microseisms* - Phil. Trans. R. Soc. Lond. A, 243, pp. 1-35.

Lowenstern J.B. and Hurwitz S., (2007) - *Monitoring a supervolcano in repose: heat and volatile flux at the Yellowstone caldera* - Elements, 4, pp. 35-40.

Macedonio G. and Tammaro U. (2005) - *Attività di Sorveglianza dell'Osservatorio Vesuviano* - Rendiconto anno 2003. INGV-Osservatorio Vesuviano. http://www.ov.ingv.it/.

Maino A. and Tribalto G. (1971) - *Rilevamento gravimetrico di dettaglio dell'isola d'Ischia (Napoli)* - Boll. Ser. Geol. It., 92, pp. 109-123.

Maino A., Segre A.G., Tribalto G., (1964) - *Rilevamento gravimetrico dei Campi Flegrei e dell'isola d'Ischia* - Ann. Oss. Vesuv., 5, pp. 229-312.

Mangiacapra A., Moretti R., Rutherford M., Civetta L., Orsi G., Papale P. (2008) - *The deep magmatic system of the Campi Flegrei caldera (Italy)* - Geophys. Res. Lett., 35, L21304, pp. 6.

Manzo M., Ricciardi G.P., Casu F., Ventura G., Zeni G., Borgstrom S., Berardino P., Del Gaudio C., Lanari R. (2006) - *Surface deformation analysis in the Ischia Island (Italy) based on spaceborne radar interferometry* - J. Volcanol. Geoth. Res., 151, pp. 399-416.

Mercalli G. (1884) - *L'isola d'Ischia ed il terremoto del 28 luglio 1883* - Memorie R. Istituto Lombardo, cl. Sc. Mat. Nat., 15, pp. 99-154.

Milia A. (1999) - *Aggrading and prograding infilling of a peri-Tyrrhenian basin: Naples Bay, Italy* - Geo-Marine Lett., 19, pp. 237-244.

Milia A. and Torrente M.M. (1999) - *Tectonics and stratigraphic architecture of a pery-Tyrrhenian half-graben (Bay of Naples Italy)* - Tectonophysics, 315, pp. 297-314.

Milia A. and Torrente M.M. (2000) - *Fold uplift and syn-kinematic strata architectures in a region of active transtensional tectonics and volcanism, Eastern Tyrrhenian Sea* - Geol. Soc. Am. Bull., 112, pp. 1,531-1,542.

Milia A. and Torrente M.M. (2003) - *Late Quaternary Volcanism and transtensional tectonics in the Bay of Naples, Campanian continental margin, Italy* - Miner. Petrol., 79, pp. 49-65.

Milia A. and Torrente M.M. (2007) - *The influence of paleogeographic setting and crustal subsidence on the architecture of ignimbrites in the Bay of Naples (Italy)* - Earth Planet. Sc. Lett., 263, 192-206.

Milia A. and Torrente M.M. (2011) - *The possible role of extensional faults in localizing magmatic activity: a crustal model for the Campanian Volcanic Zone (eastern Tyrrhenian Sea, Italy)* - J. Geol. Soc., 168, pp. 471-484, doi: 10.1144/0016-76492010-121.

Milia A., Torrente M.M., Giordano F. (2000) - *Active deformation and volcanism offshore Campi Flegrei, Italy: new data from high resolution seismic reflection profiles* - Mar. Geol., 171, pp. 61-73.

Milia A., Torrente M.M., Russo M., Zuppetta A. (2003) - *Tectonics and crustal structure of the Campania continental margin: relationships with volcanism* - Miner. Petrol., 79, pp. 33-47.

Milia A., Torrente M.M., Giordano F., Mirabile L. (2006) - *Rapid changes of the accommodation space in the Late Quaternary succession of Naples Bay, Italy: the influence of volcanism and tectonics.* In: De Vivo B. (Ed.), Volcanism in the Campania Plain: Vesuvius, Campi Flegrei and Ignimbrites. Series "Developments in Volcanology", vol. 9. Elsevier, pp. 53-68.

Mogi K. (1958) - *Relations between the eruptions of various volcanoes and the deformations of the ground surfaces around the* - B. Earthq. Res. I. Tokyo, 36, pp. 99-134.

Molin P., Acocella V., Funiciello R. (2003) - *Structural, seismic and hydrothermal features at the border of an active intermittent resurgent block: Ischia island (Italy)* - J. Volcanol. Geoth. Res., 121, pp. 65-81.

Morhange C., Marriner N., Laborel J., Todesco M., Oberlin C. (2006) - *Rapid sea level movements and noneruptive crustal deformations in the Phlegrean Fields caldera, Italy* - Geology, 34, pp. 93-96.

Moschetti M.P., Ritzwoller M.H., Shapiro N.M. (2007) - *Surface wave tomography of the western United States from ambient seismic noise: Rayleigh wave group velocity maps* - Geochem., Geophys., Geosys., 8, Q08010, doi:10.1029/2007GC001655.

Newhall C.G. and Dzurisin D. (1988) - *Historical unrest at large calderas of the world* - US Geol. Surv. Bull., 1855, pp. 1-598.

Nunziata C. (2005) - *Metodo FTAN per profili dettagliati di Vs* - Geologia Tecnica e ambientale (Journal of technical and environmental geology), rivista trimestrale dell'Ordine Nazionale dei Geologi, 3, pp. 25-43. On line www.consiglionazionalegeologi.it

Nunziata C. (2010) - *Low shear-velocity zone in the Neapolitan-area crust between the Campi Flegrei and Vesuvio volcanic area* - Terra Nova, 22, pp. 208-217.

Nunziata C. and Rapolla A. (1981) - *Interpretation of gravity and magnetic data in the Phlegraean Fields geothermal area, Naples, Italy* - J. Volcanol. Geoth. Res., 9, pp. 209-225.

Nunziata C. and Rapolla A. (1987) - *A gravity and magnetic study of the volcanic island of Ischia, Naples (Italy)* - J. Volcanol. Geoth. Res., 31, pp. 333-344.

Nunziata C., Natale M., Panza G.F. (2004) - *Seismic characterization of neapolitan soils* - Pure Appl. Geophys., 161(5-6), pp. 1,285-1,300.

Nunziata C., Natale M., Luongo G., Panza G.F. (2006) - *Magma reservoir at Mt. Vesuvius: size of the hot, partially molten, crust material detected deeper than 8 km* - Earth Planet Sc. Lett., 242, pp. 51-57.

Nunziata C., De Nisco G., Panza G.F. (2009) - *S-waves profiles from noise cross correlation at small scale* - Eng. Geol., 105(3-4), pp. 161-170.

Nunziata C., De Nisco G., Costanzo M.R. (2012) - *Active and passive experiments for S-wave velocity measurements in urban areas.* In: Earthquake Research and Analysis - New Frontiers in Seismology, Dr Sebastiano D'Amico (Ed.), ISBN: 978-953-307-840-3, InTech.

Oliveri del Castillo A. and Quagliariello M. T. (1969) - *Sulla genesi del bradisismo flegreo* - Atti Assoc. Geofis. Ital., 4, pp. 1-4.

Orsi G. and Scarpati C. (1989) - *Stratigrafia e dinamica eruttiva del Tufo Giallo Napoletano* - Boll. GNV, 2, pp. 917-930.

Orsi G., Civetta L., Aprile A., D'Antonio M., de Vita S., Gallo G., Piochi M. (1991a) - *The Neapolitan Yellow Tuff: eruptive dynamics, emplacement mechanism and magma evolution of a phreatoplinian-to-plinian eruption* - In: G. Orsi e M. Rosi (Editors), Large Ignimbrite Eruptions of the Phlegraean Fields Caldera: The Neapolitan Yellow Tuff and The Campanian Ignimbrite. I.A.V.C.E.I., Commision on Explosive Volcanism, Naples, Sept. 1-8, Guideb., pp. 76-115.

Orsi G., Gallo G., Zanchi A. (1991b) - *Simple-shearing block resurgence in caldera depressions. A model from Pantelleria and Ischia* - J. Volcanol. Geoth. Res., 47, pp. 1-11.

Orsi G., D'Antonio M., de Vita S., Gallo G. (1992) - *The Neapolitan Yellow Tuff, a large-magnitude trachytic phreatoplinian eruption: eruptive dynamics, magma withdrawal and caldera collapse* - J. Volcanol. Geoth. Res., 53, pp. 275-287.

Orsi G., De Vita S., Piochi M. (1994) - *Ischia: a volcanic Island* - In: IAS 15th reg meet fieldtrip guidebook, pp. 107-123.

Orsi G., Civetta L., D'Antonio M., Di Girolamo P., Piochi M. (1995) - *Step-filling and development of a three-layers magma chamber: the Neapolitan Yellow Tuff case history* - J. Volcanol. Geoth. Res., 67, pp. 291-312.

Orsi G., De Vita S., Di Vito M. (1996a) - *The restless, resurgent Campi Flegrei nested caldera (Italy): constraints on its evolution and configuration* - J. Volcanol. Geoth. Res., 74, pp. 179-214.

Orsi G., Piochi M., Campajola L., D'Onofrio A., Gialanella L., Terrasi F. (1996b) - *^{14}C geochronological constraints for the volcanic history of the island of Ischia (Italy) over the last 5,000 years* - J. Volcanol. Geoth. Res., 71, pp. 249-257.

Orsi G., Civetta L., Del Gaudio C., de Vita S., Di Vito M.A., Isaia R., Petrazzuoli S.M., Ricciardi G.P., Ricco C. (1999a) - *Short-term ground deformations and seismicity in the resurgent Campi Flegrei caldera (Italy): an example of active block-resurgence in a densely populated area* - J. Volcanol. Geoth. Res., 91, pp. 415-451.

Orsi G., Patella D., Piochi M., Tramacere A. (1999b) - *Magnetic modeling of the Phlegraean Volcanic District with extension to the Ponza archipelago, Italy* - J. Volcanol. Geoth. Res., 91, pp. 345-360.

Ortolani F. and Aprile F. (1978) - *Nuovi dati sulla struttura profonda della Piana Campana ad est del fiume Volturno* - Boll. Soc. Geol. Ital., 97, pp. 591-608.

Pabst S., Wörner G., Civetta L., Tesoro R. (2008) - *Magma chamber evolution prior to the Campanian Ignimbrite and Neapolitan Yellow Tuff eruptions (Campi Flegrei, Italy)* - B. Volcanol., 70, pp. 961-976.

Panza G.F. (1981) - *The resolving power of seismic surface waves with respect to crust and uppermantle structural models*. In: R. Cassinis (ed.), The solution of the inverse problem in geophysical interpretation, Plenum Publishing Corporation, pp. 39-77.

Panza G.F., Peccerillo A., Aoudia A., Farina B. (2007) - *Geophysical and petrological modelling of the structure and composition of the crust and upper mantle in complex geodynamic settings: The Tyrrhenian Sea and surroundings* - Earth-Sci. Rev., 80, pp. 1-46.

Paoletti V., Di Maio R., Cella F., Florio G., Motschka K., Roberti N., Secomandi M., Supper R., Fedi M., Rapolla A. (2009) - *The Ischia volcanic island (Southern Italy): Inferences from potential field data interpretation* - J. Volcanol. Geoth. Res., 179, pp. 69-86.

Paoletti V., D'Antonio M., Rapolla A. (2013) - *The structural setting of the Ischia Island (Phlegrean Volcanic District, Southern Italy): Inferences from geophysics and geochemistry* - J. Volcanol. Geoth. Res., 249, pp. 155-173.

Pappalardo L., Piochi M., D'Antonio M., Civetta L., Petrini R. (2002) - *Evidence for multi-stage magmatic evolution during the past 60 kyr at Campi Flegrei (Italy) deduced from Sr, Nd and Pb isotope* data - J. Petrol., 43, pp. 1,415-1,434.

Parascandola A. (1947) - *I fenomeni bradisismici del Serapeo di Pozzuoli, Napoli* - Privately published, pp. 156.

Penta F., (1954) - *Ricerche e studi sui fenomeni esalativi-idrotermali e il problema delle forze endogene* - Ann. Geofis., 7(3), pp. 317-408.

Penta F. and Conforto B. (1951) - *Risultati di sondaggi e di ricerche geominerarie nell'isola d'Ischia dal 1939 al 1943, nel campo del vapore, delle acque termali e delle 'forze endogene' in generale* - Ann. Geofis., 4, pp. 159-191.

Perrotta A., Scarpati C., Luongo G., Morra V. (2006) - *The Campi Flegrei caldera boundary in the city of Naples* - In: De Vivo B. (Ed.), Volcanism in the Campania Plain: Vesuvius, Campi Flegrei and Ignimbrites. Elsevier, pp. 85-96.

Pescatore T., Diplomatico G., Senatore M.R., Tramutoli M., Mirabile L. (1984) - *Contributi allo studio del Golfo di Pozzuoli: aspetti stratigrafici e strutturali* - Mem. Soc. Geol. Ital., 27, pp. 133-149.

Peterson J. (1993) - *Observation and modeling of background seismic noise* - US Geol. Surv. Open-File Rept., Albuquerque.

Pierce K.L., Cannon K.P., Meyer G.A., Trebesch M.J., Watts R. (2002) - *Post-glacial inflation-deflation cycles, tilting and faulting in the Yellowstone caldera based on Yellowstone lake shorelines* - U.S. Geol. Survey Open-File Report 02-0142.

Pingue F., De Martino P., Obrizzo F., Serio C., Tammaro U. (2006) - *Stima del campo di spostamento ai Campi Flegrei da dati CGPS e di livellazione di precisione nel periodo maggio 2004 - marzo 2006* - INGV-Osservatorio Vesuviano. Open File Report http://www.ov.ingv.it.

Piochi M., Civetta L., Orsi G. (1999) - *Mingling in the magmatic system of Ischia (Italy) in the past 5 ka* - Miner. Petrol., 66, pp. 227-258.

Poli S., Chiesa S., Gillot P.Y., Gregnanin A., Guichard F. (1987) - *Chemistry versus time in the volcanic complex of Ischia (Gulf of Naples, Italy): evidence of successive magmatic* cycles - Contrib. Mineral. Petr., 95(3), pp. 322-335.

Rampoldi R. (1972) - *Risultati delle osservazioni sismografiche effettuate dal giugno 1970 al luglio 1971* - CNR, Quaderni Ric. Sc. n. 83.

Rapolla A., Paoletti V., Secomandi M. (2010) - *Seismically-induced landslide susceptibility evaluation: application of a new procedure to the island of Ischia, Campania Region, Southern Italy* - Eng. Geol., 114, pp. 10-25.

Rittmann A. (1930) - *Geologie der Insel Ischia* - Zeitschrift fur Vulkanologie (Erganzungsband VI), Berlin, pp. 268.

Rittmann A. (1948) - *Origine e differenzazione del magma ischitano* - Bull. Suisse Minerai. Petrogr., 28, pp. 643.

Rittmann A. and Gottini V. (1980) - *L'isola d'Ischia. Geologia Bollettino* - Ser. Geol. Ital. 101, pp. 131-274.

Rittmann A., Vighi L., Falini V., Ventriglia V., Nicotera P. (1950) - *Rilievo geologico dei Campi Flegrei* - Boll. Soc. Geol. Ital., 69, pp. 117-362.

Rolandi G., Bellucci F., Heizler M.T., Belkin H.E., De Vivo B. (2003) - *Tectonic controls on the genesis of ignimbrites from the Campanian Volcanic Zone, southern Italy* - Miner. Petrol., 79, pp. 3-31.

Romeo G. and Braun T. (2006) - *Appunti di sismometria.*

Rosi M. and Santacroce R. (1984) - *Volcanic hazard assessment in the Phlegraean Fields: a contribution based on stratigraphic and historical data* - B. Volcanol., 47(2), pp. 359-370.

Rosi M. and Sbrana A. (1987) - *Phlegrean Fields* - CNR, Quad. Ric. Sci., 114, pp. 1-175.

Rosi M., Sbrana A., Principe C. (1983) - *The Phlegrean Fields: structural evolutions, volcanic history and eruptive mechanism* - J. Volcanol. Geoth. Res., 17, pp. 273-288.

Rosi M., Vezzoli L., Aleotti P., De Censi M. (1996) - *Interaction between caldera collapse and eruptive dynamics during the Campanian Ignimbrite eruption, Phlegraean Fields, Italy* - B. Volcanol., 57, pp. 541-554.

Sbrana A., Fulignati P., Marianelli P., Boyce A. J., Cecchetti A. (2009) - *Exhumation of an active magmatic-hydrothermal system in a resurgent caldera environment: the example of Ischia (Italy)* - J. Geol. Soc., London, 166, pp. 1,061-1,073.

Scandone R., Bellucci F., Lirer L., Rolandi G. (1991) - *The structure of the Campanian plain and the activity of the Neapolitan Volcanoes* - J. Volcanol. Geoth. Res., 48(1-2), pp. 1-31.

Scandone R., Giacomelli L., Fattori Speranza F. (2006) - *The volcanological history of the volcanoes of Napoli: a review* - In: De Vivo B. (ed), Volcanism in the Campania Plain: Vesuvius, Campi Flegrei, Ignimbrites, Elsevier, Developments in Volcanology, 9, pp. 1-26.

Scarascia S. (1972) - *Carta aeromagnetica dell'area dei Campi Flegrei-Pozzuoli* - Quad. Ric. Sci., 83, pp. 209-217.

Scarpati C., Cole P., Perrotta A. (1993) - *The Neapolitan Yellow Tuff - A large volume multiphase eruption from Campi Flegrei, Southern Italy* - B. Volcanol., 55, pp. 343-356.

Scherillo A. and Franco E. (1960) - *Rilevamento stratigrafico del territorio comunale di* Napoli - Boll. Soc. Nat., Napoli, 69, pp. 255-262.

Sepe V., Atzori S., Ventura G. (2007) - *Subsidence due to crack closure and depressurization of hydrothermal systems: a case study from Mt Epomeo (Ischia Island, Italy)* - Terra Nova, 19(2), pp. 127-132.

Shapiro N.M. and Campillo M. (2004) - *Emergence of broadband Rayleigh waves from correlations of the ambient seismic noise* - Geophys. Res. Lett., 31, L07614, doi:10.1029/2004GL019491.

Shapiro N.M. and Ritzwoller M.H. (2002) - *Monte-Carlo inversion for a global shear velocity model of the crust and upper mantle* - Geophys. J. Int., 151, pp. 88-105.

Signorelli S., Vaggelli G., Francalanci L., Rosi M. (1999) - *Origin of magmas feeding the Plinian phase of the Campanian Ignimbrite eruption, Phlegraean Fields (Italy): Constraints based on matrix-glass and glass-inclusion compositions* - J. Volcanol. Geoth. Res., 91, pp. 199-220.

Smith R.L. and Bailey R.A. (1968) - *Resurgent cauldrons* - In: R.R. Coats, R.L. Hay and C.A. Anderson (Editors), Studies in Volcanology, Geol. Soc. Am. Mem., 116, pp. 613-662.

Tanimoto T. and Artru-Lambin J. (2006) - *Interaction of Solid Earth, Atmosphere & Ionosphere.*

Tibaldi A. and Vezzoli, L. (1998) - *The space problem of caldera resurgence: an example from Ischia Island, Italy* - Geologische Rundschau, 87, pp. 53-66.

Tibaldi A. and Vezzoli L. (2000) - *Late Quaternary monoclinal folding induced by caldera resurgence at Ischia, Italy* - Geol. Soc. Sp., 169, pp. 103-113.

Tibaldi A. and Vezzoli L. (2004) - *A new type of volcano flank failure: the resurgent caldera sector collapse, Ischia, Italy* - Geophys. Res. Lett., 31, L14605 http://dx.doi.org/10.1029/2004GL020419, 2004.

Tinti S., Chiocci F.L., Zambinoni F., Pagnoni G., de Alteriis G. (2011) - *Numerical simulation of the tsunami generated by a past catastrophic landslide on the volcanic Island of Ischia, Italy* - Mar. Geophys. Res., 32, pp. 287-297.

Troise C., De Natale G., Pingue F., Obrizzo F., De Martino P., Tammaro U., Boschi E. (2007) - *Renewed ground uplift at Campi Flegrei caldera (Italy): new insight on magmatic processes and forecast* - Geophys. Res. Lett., 34, L03301.

Valyus V.P., Keilis-Borok V.I., Levshin A.L. (1968) - *Determination of the velocity profile of the upper mantle in Europa* - Doklady Akad. Nauk SSSR, 185(8), pp. 564-567.

Vanorio T., Virieux J., Capuano P., Russo G. (2005) - *Three-dimensional seismic tomography from P wave and S wave microearthquake travel times and rock physics characterization of the Campi Flegrei Caldera* - J. Geophys. Res., 110, B03201, doi:10.1029/2004GL003102.

Vezzoli L. (1988) - *Island of Ischia* - Quaderni de La Ricerca Scientifica, 114 (10), CNR, Progetto Finalizzato Geodinamica 10, Roma, pp. 133.

Vezzoli L., Principe C., Malfatti J., Arrighi S., Tanguy J.C., Le Goff M. (2009) - *Modes and times of caldera resurgence: The <10 ka evolution of Ischia Caldera, Italy, from high-precision archaeomagnetic dating* - J. Volcanol. Geoth. Res., 186, pp. 305-319.

Weaver R.L. (2005) - *Information from seismic noise* - Science, 307, pp. 1,568-1,569.

Wohletz K., Orsi G., de Vita S. (1995) - *Eruptive mechanism of the Neapolitan Yellow Tuff interpreted from stratigraphic, chemical and granulometric data* - J. Volcanol. Geoth. Res., 67, pp. 263-290.

Wulf S., Kraml M., Brauer A., Keller J., Negendank J.F.W. (2004) - *Tephrochronology of the 100 ka lacustrine sediment record of Lago Grande di Monticchio (southern Italy) –* Quatern. Int., 122, pp. 7-30.

Yang Y., Ritzwoller M.H., Levshin A.L., Shapiro N.M. (2007) - *Ambient noise Rayleigh wave tomography across Europe* - Geophys. J. Int., 168, pp. 259-274.

Yao H., Van der Hilst R.D., de Hoop M.V. (2006) - *Surface-wave tomography in SE Tibet from ambient seismic noise and two-station analysis - I. Phase velocity maps* - Geophys. J. Int., 166, pp. 732-744, doi: 10.1111/j.1365–246X.2006.03028.x.

Zamora M., Sartoris G., Chelini W. (1994) - *Laboratory measurements of ultrasonic wave velocities in rocks from the C. F. volcanic system and their relation to other field data* - J. Geophys. Res., 99, 13,553-13,561.

Zollo A., Judenherc S., Auger E., D'Auria L., Virieux J., Capuano P., Chiarabba C., de Franco R., Makris J., Michelini A., Musacchio G. (2003) - *Evidence for the buried rim of Campi Flegrei caldera from 3-d active seismic imaging* - Geophys. Res. Lett., 30(19), doi:10.1029/2003GL018173.

Zollo A., Maercklin N., Vassallo M., Dello Iacono D., Virieux J., Gasparini P. (2008) - *Seismic reflections reveal a massive melt layer under Campi Flegrei volcanic* field - Geophys. Res. Lett., 35, L12306.